

This electronic thesis or dissertation has been downloaded from the King's Research Portal at <https://kclpure.kcl.ac.uk/portal/>



Image-based computational modelling of coronary autoregulation with the primary aim of improving risk stratification of Alagille's syndrome patients prior to liver transplantation

Da Silva Nogueira Vieira, Miguel

Awarding institution:
King's College London

The copyright of this thesis rests with the author and no quotation from it or information derived from it may be published without proper acknowledgement.

END USER LICENCE AGREEMENT



Unless another licence is stated on the immediately following page this work is licensed

under a Creative Commons Attribution-NonCommercial-NoDerivatives 4.0 International

licence. <https://creativecommons.org/licenses/by-nc-nd/4.0/>

You are free to copy, distribute and transmit the work

Under the following conditions:

- Attribution: You must attribute the work in the manner specified by the author (but not in any way that suggests that they endorse you or your use of the work).
- Non Commercial: You may not use this work for commercial purposes.
- No Derivative Works - You may not alter, transform, or build upon this work.

Any of these conditions can be waived if you receive permission from the author. Your fair dealings and other rights are in no way affected by the above.

Take down policy

If you believe that this document breaches copyright please contact librarypure@kcl.ac.uk providing details, and we will remove access to the work immediately and investigate your claim.

KING'S COLLEGE LONDON

Doctoral Thesis

**Image-based computational modelling
of coronary autoregulation with the primary aim of
improving risk stratification of Alagille's syndrome
patients prior to liver transplantation**

Author:

Supervisors:

JOSÉ MIGUEL

PROFESSOR CARLOS ALBERTO FIGUEROA, Ph.D.

DA SILVA NOGUEIRA VIEIRA

PROFESSOR REZA RAZAVI, M.D.

Nº1523329

A thesis submitted in fulfilment of the requirements

for the degree of Doctor of Philosophy

DIVISION OF IMAGING SCIENCE & BIOMEDICAL ENGINEERING

SCHOOL OF MEDICINE

December 2018

KING'S
College
LONDON



The copyright of this thesis rests with the author and no quotation from it or information derived from it may be published without proper acknowledgement.

ABSTRACT

Alagille's syndrome (ALGS) is a rare multisystemic disorder that usually presents in the first year of life with progressive and debilitating liver failure symptoms. Approximately 20 to 30% of ALGS children require liver transplantation in early infancy for end-stage liver disease. When compared to other paediatric indications for liver transplantation, ALGS patients have worst post-operative outcomes. These have been ascribed to concomitant congenital heart disease (CHD) and in particular to peripheral pulmonary artery stenosis (PPS), which is present in the majority of patients. PPS, particularly if not treated appropriately and in a timely fashion, results in persistent right ventricular (RV) hypertension and progressive maladaptive ventricular as well as vascular remodelling (i.e. initially RV hypertrophy, and later RV dilation and systolic impairment as well as increased pulmonary stiffness). In turn, this may place these patients at high risk of RV ischaemia and pump failure particularly during the critical stage of the liver graft reperfusion, which is often accompanied with a marked systemic hypotension and corresponding coronary perfusion pressure drop. Currently, an hybrid X-ray/magnetic resonance guided catheterisation study (XMR) with dobutamine stress is used, pre-operatively, to identify those ALGS patients that are deemed to be at high risk of right heart failure (RHF). By measuring the systemic/pulmonary pressures and resistance, as well as the cardiac output response to dobutamine, clinicians hope to replicate some of the haemodynamics events of liver transplantation, such as the expected increase in heart rate and myocardial metabolic demand. While the adequate response to dobutamine stress has been described to be an increase in cardiac output of at least 40%, a key limitation of this workup is a failure to account for the systemic hypotension and corresponding coronary perfusion pressure drop that occurs during liver transplantation. By neglecting this, the risk of RV ischaemia leading to RHF might not be adequately

predicted. However, studying the coronary responses in ALGS children to identify those deemed to be at high risk of RV ischaemia during liver transplantation presents several ethical and methodological challenges.

In this PhD research we have designed an innovative experimental setup using recently developed imaging and computational modelling techniques that could be used to reproduce *in silico* some of the haemodynamic events of liver transplantation and investigate coronary autoregulation in ALGS patients.

Two main computational methods were used: (1) the coupled multidomain momentum method to combine a three-dimensional (3D) portion of the vascular anatomy (i.e. the aorta, coronaries and proximal pulmonary arteries branches) segmented from the XMR, to zero-dimensional (0D) lumped parameter networks (LPNs) representing the heart chambers and the non-segmented systemic and pulmonary vasculature; and (2) a coronary autoregulation control method that adjusted the coronary microcirculation resistance to increase the coronary blood flow (CBF) and thus matched the left and right ventricular metabolic demands, which in turn were computed from the patient-specific ventricular pressure-volume (PV) loops extracted from the XMR data.

As highly detailed images of the small coronaries of an ALGS child were to be segmented to create the 3D systemic domain of the patient-specific computational model (PSCM), several studies were concomitantly conducted aiming to improve the conventional one-dimensional (1D) respiratory-navigated (NAV) T2-prepared coronary magnetic resonance angiography (CMRA) sequence. We first tested the feasibility of a recently developed two-dimensional (2D) image-navigated (iNAV) CMRA sequence (Study 1) in healthy volunteers and in an adult patient cohort with CHD. We showed that the novel navigation scheme resulted in faster scan acquisitions and improved coronary image quality compared to the conventional 1D NAV. This was followed by a validation of the technique against gold standard invasive X-ray coronary angiography for screening significant coronary artery disease in an adult patient cohort (Study 2). We then replaced the conventional T2 preparation magnetisation scheme by an inversion recovery (IR) approach to improved blood-background differentiation, and acquired the 2D iNAV CMRA in a paediatric CHD cohort following the injection of gadobenate dimeglumine (Study 3). This is a high-relaxivity contrast agent, with a long half-life thus providing higher and longer

intravascular signal ideal for CMRA. We showed that our methodology improved significantly image quality in small children with high heart rates. Finally, this sequence design was incorporated in Study 6 to provide the high resolution radiation-free anatomic data of the coronaries and proximal systemic and pulmonary arteries of a six year-old ALGS child with associated pulmonary vascular disease (i.e. increased pulmonary arterial pressure despite treated PPS) undergoing pre-liver transplantation risk assessment. This data was segmented using a custom-made software developed by our team (CRIMSON) to produce the 3D domains of the closed-loop 0D-3D multi-domain PSCM.

Two separate studies were carried out in parallel, one in a sample of hypertrophic cardiomyopathy (HCM) patients (Study 4), and another in a mixed cohort of middle-aged twins and aortic coarctation patients (Study 5), both involving the evaluation of CMR-derived methodologies to provide parameters such as left atrial volumes/elastance and vascular stiffness, respectively, that were used in the parametrisation of the PSCM. In Study 4, we studied the different components of left atrial (LA) function (the reservoir, conduit and booster pump function) using phasic volume changes and tissue-tracking, and showed that this robust methodology could improve disease staging. In Study 5, we developed and evaluated a novel tool for automated extraction of the thoracic aorta length from different CMR sequences to streamline pulse wave velocity calculation.

The aforementioned measures together with other imaging and invasive data obtained during the clinical XMR study (e.g. intraventricular volumes and pressure, aortic and pulmonary flow, pressure and resistance) were used to calibrate the different components of the PSCM (e.g. the LPNs resistance and capacitance) and replicated the rest and dobutamine stress haemodynamics (Study 6). We demonstrated that at rest, due to abnormally high RV afterload, CBF in the right coronary artery (RCA) territory occurred mainly in diastole, akin to the left coronary artery. This abnormal profile was even more pronounced during dobutamine stress. We then modelled a generalised vasodilation, similar to that occurring immediately post-transplant (post-reperfusion syndrome, PRS) by imposing a 31% drop in the mean arterial pressure through manual adjustment of the resistor components in the systemic arterial bed LPNs. Our computational model predicted that the heart would be unable to maintain adequate RCA perfusion in the face of such reduced aortic perfusion pressure, despite a major reduction in coronary resistance. This study provided a mechanistic

insight into how abnormal ventricular-vascular coupling (high RV afterload resulting in extravascular compressive resistance) could translate into RV ischaemia during the critical stage of liver reperfusion, eventually leading to pump failure, a result not expected given the adequate cardiac output increase ($> 40\%$) during the clinical XMR dobutamine stress study. We hypothesise that this impaired coronary autoregulation and RV myocardial oxygen demand-supply imbalance could be related to the unfavourable ALGS post-transplant outcomes described in the literature when compared to other paediatric liver transplantation indications.

This research shows great promise not only for the application of the novel 2D iNAV IR-CMRA sequence in paediatric CHD imaging but also for the use of the different imaging and computational methods to study CBF autoregulation in ALGS patients with pulmonary vascular disease. The PSCM presented could be an appealing option to refine pre-transplant risk assessment of these patients. On the one hand, there is a scarcity of strong medical evidence due to the low prevalence of the disease and the constraints of studying the coronary circulation in children. On the other hand, there is a great need to personalise medical management given the limitations of current pre-operative diagnostic workup. As the ethical and methodological constraints preclude direct invasive validation of these results, obtaining PSCM in other ALGS patients and correlating them to transplantation outcomes could enable clinical translation.

ACKNOWLEDGEMENTS

*"(...) "What makes the desert beautiful," said the little prince,
"is that somewhere it hides a well. (...)"*

In "Le Petit Prince"

Antoine de Saint Exupéry (1900 – 1944)

I would like to show my deepest appreciation for all that have made this research possible. Risking neglecting important contributions to my work, I would like to express my gratitude to Professor Figueroa, for all the support throughout this PhD, for the unique insight into the mechanics of the human circulation and for teaching me the fundamentals of computational modelling applied to cardiovascular medicine. As a Cardiologist and clinical researcher this was an enlightening endeavour!

I am thankful and honoured for Professor Razavi's pertinent guidance throughout my research. It was his landmark work nearly twenty years ago that inspired this research!

I would also like to thank Christopher Arthurs for his critical help with the computational simulations and Desmond Dillon-Murphy for his help using CRIMSON.

My appreciation to Professor Gerald Greil and Professor Tarique Hussain with whom this journey started.

Finally, to my family, as all the efforts would have been impossible and in vain without you.

December 2018

PUBLICATIONS AND PRESENTATIONS

Peer-reviewed journals publications arising from this thesis:

First Author

1. *Patient-Specific Image-Based Computational Modeling in Congenital Heart Disease: A Clinician Perspective.*

Vieira SM, Hussain T, Figueroa CA.

Journal of Cardiol Ther 2015 December 2(5): 273-278. doi: 10.17554/j.issn.2309-6861.2015.02.96.

2. *Improved coronary magnetic resonance angiography using gadobenate dimeglumine in pediatric congenital heart disease.*

Vieira MS, Henningsson M, Dedieu N, Vassiliou VS, Bell A, Mathur S, Pushparajah K, Figueroa CA, Hussain T, Botnar R, Greil GF.

Magn Reson Imaging. 2018 Jun;49:47-54. doi: 10.1016/j.mri.2017.12.023.

3. *Patient-specific modeling of right coronary circulation vulnerability post-liver transplant in Alagille's syndrome*

Vieira MS, Arthurs CJ, Hussain T, Razavi R, Figueroa CA.

PLoS ONE November 2018 13(11):e0205829. doi: 10.1371/journal.pone.0205829.

Co-Author

1. *Whole-heart coronary MR angiography using image-based navigation for the detection of coronary anomalies in adult patients with congenital heart disease.*
Henningsson M, Hussain T, **Vieira MS**, Greil GF, Smink J, Ensbergen GV, Beck G, Botnar RM.
J Magn Reson Imaging. 2016 Apr;43(4):947-55. doi: 10.1002/jmri.25058.
2. *Left Atrial Performance in the Course of Hypertrophic Cardiomyopathy: Relation to Left Ventricular Hypertrophy and Fibrosis.*
Kowallick J, **Vieira MS**, Kutty S, Lotz J, Hasenfuss G, Chiribiri A, Schuster A.
Invest Radiol. 2017 Mar;52(3):177-185. doi: 10.1097/RLI.0000000000000326.
3. *Aortic length measurements for pulse wave velocity calculation: manual 2D vs automated 3D centreline extraction.*
van Engelen A, **Vieira MS**, Rafiq I, Cecelja M, Schneider T, de Bliet H, Hussain T, Botnar R, Alastruey J, Figueroa A.
J Cardiovasc Magn Reson. 2017 Mar 8;19(1):32. doi: 10.1186/s12968-017-0341-y.
4. *Diagnostic performance of image navigated coronary CMR angiography in patients with coronary artery disease.*
Henningsson M, Shome J, Bratis K, **Vieira MS**, Nagel E, Botnar RM.
J Cardiovasc Magn Reson. 2017 Sep 11;19(1):68. doi: 10.1186/s12968-017-0381-3.
5. *Arterial stiffening is a heritable trait associated with arterial dilation but not wall thickening: a longitudinal study in the twins UK cohort.*
Cecelja M, Jiang B, Keehn L, Hussain T, **Vieira MS**, Phinikaridou A, Greil G, Spector TD, Chowienczyk P.
Eur Heart J 2018 Jun 21;39(24):2282-2288. doi: 10.1093/eurheartj/ehy165.

International Conferences presentations arising from this thesis:

1. *Whole-heart contrast enhanced coronary magnetic resonance angiography using respiratory image based navigation in patients with congenital heart disease.*

Vieira MS, Henningsson M, Dedieu N, Rafiq I, Botnar R, Bell Aaron, Mathur S, Pushparajah K, Hussain T, Greil GF. (2015) *J Cardiovasc Magn Reson*, 17 (Suppl 1).
<http://www.jcmr-online.com/supplements/17/S1>

18th Annual SCMR Scientific Sessions, Nice, France on 4-7 February 2015. Silva Vieira, M J .

2. *Image-based multiscale, multidomain computational modelling of pulmonary biomechanics.*

Vieira MS, Arthurs CJ, Dillon-Murphy D, Khlebnikov R, Figueroa CA.

<http://www.eccomas.org/space/1/7/proceedings---congresses>

ECCOMAS (European Congress on Computational Methods in Applied Sciences and Engineering) Conference, 5-10 June 2016, Crete, Greece, 5-10th June

3. *A patient-specific MRI-based 3D computational modeling study of RCA flow changes during vasodilator therapy in pulmonary arterial hypertension.*

Vieira MS, Arthurs CJ, Velasco-Forte M, Ruijsink B, K Pushparajah K, Figueroa CA.

https://c.ymcdn.com/sites/scmr.org/resource/resmgr/2017_Meeting/SCMR.Abstract.Supplement.FIN.pdf

20th Annual SCMR Scientific Sessions, Washington, USA, 1-4th February 2017.

*“Because strait is the gate,
and narrow is the way,
which leadeth unto life,
and few there be that find it.”*

The Gospel of Mathew, New Testament (7:14)

CONTENTS

<i>Abstract</i>	3
<i>Acknowledgements</i>	7
<i>Publications And Presentations</i>	8
<i>Contents</i>	12
<i>List of Figures</i>	16
<i>List of Tables</i>	18
<i>List of Equations</i>	20
<i>Units Conversion</i>	21
1. Thesis Outline	22
2. Introduction	24
2.1. Research Rationale	25
2.1. Clinical Background: Alagille’s Syndrome	26
2.1.1. Overview.....	26
2.1.2. Genetics And Epidemiology.....	26
2.1.3. Clinical Manifestations	27
2.1.4. Diagnosis.....	29
2.1.5. Prognosis.....	30
2.1.6. Treatment	31
2.1.7. Liver Transplantation.....	32
2.2. Patient-Specific Computational Modelling in Paediatric Congenital Heart Disease	38

2.2.1. Background: Unmet Needs In The Care Of Paediatric Congenital Heart Disease.....	38
2.2.2. Diagnostic Methodologies In Paediatric Congenital Heart Disease.....	39
2.2.3. New Paradigm of Predictive Personalised Medicine For Paediatric Congenital Heart Disease...	40
2.2.4. Fundamental Concepts For Image-Based Computational Modelling.....	41
2.3. Coronary Circulation.....	50
2.3.1. Coronary Anatomical Arrangement.....	50
2.3.2. Myocardial Metabolism	51
2.3.3. Coronary Blood Flow.....	51
3. Coronary Magnetic Resonance Angiography	62
3.1. Study 1: 2D iNAV CMRA Feasibility Study	63
3.1.1. Background	63
3.1.2. Material and Methods	70
3.1.3. Results.....	73
3.1.4. Discussion	78
3.1.5. Limitations	79
3.1.6. Conclusions.....	80
3.2. Study 2: 2D iNAV CMRA In Coronary Artery Disease Patients	80
3.2.1. Background	80
3.2.2. Material and Methods	81
3.2.3. Results.....	86
3.2.4. Discussion	90
3.2.5 Limitations	92
3.2.6. Conclusions.....	93
3.3. Study 3: 2D iNAV CMRA In Paediatric Patients With Congenital Heart Disease.....	93
3.3.1. Background	93
3.3.2. Material and Methods	96
3.3.3. Results.....	100
3.3.4. Discussion	107
3.3.5. Clinical Significance.....	111
3.3.6. Limitations	112
3.3.7. Conclusions.....	113
4. CMR Imaging Biomarkers.....	115
4.1. Overview	116
4.2. Study 4: Left Atrial Performance In The Course Of Hypertrophic Cardiomyopathy	118

4.2.1. Background	118
4.2.2. Material and Methods	121
4.2.3. Results.....	125
4.2.4. Discussion	132
4.2.5. Clinical Significance.....	135
4.2.6. Limitations	136
4.2.7. Conclusions.....	137
4.3. Study 5: Aortic Length Measurements For Pulse Wave Velocity Calculation: Manual 2D Versus Automated 3D Centreline Extraction	138
4.3.1. Background	138
4.3.2. Material And Methods	141
4.3.3. Results.....	148
4.3.4. Discussion	154
4.3.5. Clinical Significance.....	156
4.3.6. Limitations	157
4.3.7. Conclusions.....	158
5. Patient-Specific Computational Modelling	160
5.1. Study 6: Patient-specific Modelling Of Right Coronary Circulation Vulnerability Post-liver Transplant In Alagille’s Syndrome.....	161
5.1.1. Background	161
5.1.1.1. Coronary Autoregulation In Alagille’s Syndrome	162
5.1.2. Material And Methods	167
5.1.3. Results.....	190
5.1.4. Discussion	195
5.1.5. Limitations	204
5.1.6. Conclusion.....	206
6. Future Work.....	207
6.1. Coronary Magnetic Resonance Angiography	208
6.2. Imaging Biomarkers	209
6.2.1. Study 4: Left Atrial Performance In The Course Of Hypertrophic Cardiomyopathy	209
6.2.2. Study 5: Aortic Length Measurements For PWV Calculation: Manual 2D versus Automated 3D Centreline Extraction.....	210

6.3. Patient-specific Computational Modelling	212
<i>Abbreviations</i>	<i>214</i>
<i>Co-Author Publications</i>	<i>218</i>
<i>References.....</i>	<i>219</i>

LIST OF FIGURES

<i>Figure 1</i>	29
<i>Figure 2</i>	42
<i>Figure 3</i>	44
<i>Figure 4</i>	44
<i>Figure 5</i>	45
<i>Figure 6</i>	45
<i>Figure 7</i>	47
<i>Figure 8</i>	48
<i>Figure 9</i>	49
<i>Figure 10</i>	58
<i>Figure 11</i>	66
<i>Figure 12</i>	69
<i>Figure 13</i>	73
<i>Figure 14</i>	74
<i>Figure 15</i>	76
<i>Figure 16</i>	76
<i>Figure 17</i>	77
<i>Figure 18</i>	83
<i>Figure 19</i>	86
<i>Figure 20</i>	87
<i>Figure 21</i>	88
<i>Figure 22</i>	89
<i>Figure 23</i>	90
<i>Figure 24</i>	99
<i>Figure 25</i>	101
<i>Figure 26</i>	104
<i>Figure 27</i>	104
<i>Figure 28</i>	105

<i>Figure 29</i>	106
<i>Figure 30</i>	107
<i>Figure 31</i>	117
<i>Figure 32</i>	124
<i>Figure 33</i>	130
<i>Figure 34</i>	130
<i>Figure 35</i>	131
<i>Figure 36</i>	140
<i>Figure 37</i>	142
<i>Figure 38</i>	144
<i>Figure 39</i>	150
<i>Figure 40</i>	152
<i>Figure 41</i>	168
<i>Figure 42</i>	171
<i>Figure 43</i>	173
<i>Figure 44</i>	173
<i>Figure 45</i>	174
<i>Figure 46</i>	175
<i>Figure 47</i>	176
<i>Figure 48</i>	177
<i>Figure 49</i>	183
<i>Figure 50</i>	184
<i>Figure 51</i>	185
<i>Figure 52</i>	188
<i>Figure 53</i>	189
<i>Figure 54</i>	190
<i>Figure 55</i>	192
<i>Figure 56</i>	193
<i>Figure 57</i>	194
<i>Figure 58</i>	195
<i>Figure 59</i>	199
<i>Figure 60</i>	202

LIST OF TABLES

<i>Table 1</i>	30
<i>Table 2</i>	72
<i>Table 3</i>	74
<i>Table 4</i>	75
<i>Table 5</i>	77
<i>Table 6</i>	85
<i>Table 7</i>	86
<i>Table 8</i>	89
<i>Table 9</i>	99
<i>Table 10</i>	101
<i>Table 11</i>	102
<i>Table 12</i>	103
<i>Table 13</i>	103
<i>Table 14</i>	126
<i>Table 15</i>	127
<i>Table 16</i>	129
<i>Table 17</i>	132
<i>Table 18</i>	143
<i>Table 19</i>	148
<i>Table 20</i>	149
<i>Table 21</i>	151
<i>Table 22</i>	151
<i>Table 23</i>	153
<i>Table 24</i>	170
<i>Table 25</i>	178
<i>Table 26</i>	179
<i>Table 27</i>	179
<i>Table 28</i>	182

<i>Table 29</i>	182
<i>Table 30</i>	186
<i>Table 31</i>	191
<i>Table 32</i>	192

LIST OF EQUATIONS

<i>Equation 1</i>	41
<i>Equation 2</i>	41
<i>Equation 3</i>	51
<i>Equation 4</i>	58
<i>Equation 5</i>	59
<i>Equation 6</i>	59
<i>Equation 7</i>	98
<i>Equation 8</i>	98
<i>Equation 9</i>	122
<i>Equation 10</i>	123
<i>Equation 11</i>	123
<i>Equation 12</i>	123
<i>Equation 13</i>	139
<i>Equation 14</i>	174
<i>Equation 15</i>	177
<i>Equation 16</i>	178
<i>Equation 17</i>	178
<i>Equation 18</i>	179
<i>Equation 19</i>	180
<i>Equation 20</i>	180
<i>Equation 21</i>	180
Equation 22	180
<i>Equation 23</i>	180
<i>Equation 24</i>	181
<i>Equation 25</i>	181
<i>Equation 26</i>	181

UNITS CONVERSION

	SI Units	Units in text (1 unit)	Equivalent Conversions
Pressure	$\text{Kg m}^{-1} \text{s}^{-2}$	1 mmHg	133.332 Pa
Flow	$\text{m}^3 \text{s}^{-1}$	1 $\text{mm}^3 \text{s}^{-1}$	0.001 ml/s
Wall shear stress	Pa	Pa	-

Kg, kilograms; m, metres; mm, millimetres; Pa, Pascal; s, seconds; SI, International System.

1

THESIS OUTLINE

The structure of this thesis is as follows: in Chapter 2 we begin by discussing the rationale for this thesis project - the need to understand the role of coronary autoregulation impairment as a possible cause of right heart failure (RHF) in Alagille's Syndrome (ALGS) children undergoing liver transplantation. This is followed by a literature review of ALGS, from the known pathogenetic mechanisms of the disease, to its natural history, the current diagnostic and management strategies, including the need for a thorough pre-liver transplantation cardiovascular risk assessment. Subsequently, a discussion of the dramatic haemodynamic events occurring during liver reperfusion (post-reperfusion syndrome, PRS) is presented and why these patients have worst surgical outcomes compared to other diseases, focusing on the complex coronary microcirculatory responses motivating this research. Given the technical difficulties and ethical limitations of studying coronary haemodynamics in ALGS patients, we then discuss the need for experimental computational techniques. This introduces the next section describing fundamental concepts for image-based computational modelling and the overall design of the framework used in this research thesis to study coronary autoregulation in an ALGS child. In the final part of the Chapter 2, we review the physiology of coronary autoregulation and some of the mathematical models developed for *in silico* experiments, including the one used in the main research study of this thesis (Study 6). In Chapter 3 we describe the work conducted to develop and validate a new coronary CMR sequence (Studies 1-3) for improved imaging of small children with congenital heart disease (CHD). In Chapter 4 we described two complementary research studies using CMR tools: one assessing LA function in hypertrophic cardiomyopathy (HCM) patients to provide incremental disease staging (Study 4); the other concerning a new automated aortic centreline extraction tool to streamline CMR pulse wave velocity (PWV) calculation (Study 5). The tools developed in these different studies were applied in the parametrisation of the patient-specific computational model (PSCM) of an ALGS child being considered for liver transplantation (Study 6 – Chapter 5). At the beginning of Chapters 3, 4 and 5 a brief introductory background is followed by the methods, results, discussion and main conclusions of each study, along with a summary of the limitations. Chapter 6 details suggestions on how this work might lead to future research and address some of the limitations mentioned.

2

INTRODUCTION

This chapter will: (1) examine the clinical background of Alagille's syndrome including the known pathogenetic mechanisms, the epidemiology of the disease, the clinical manifestations, diagnostic evaluation, prognosis and clinical management; (2) introduce the new paradigm of predictive personalised medicine using patient-specific computational modelling, fundamental physics concepts as well the typical image-based modelling workflow; (3) describe the coronary circulation physiology and different models of coronary blood flow autoregulation, including the one used in this thesis, and how computational modelling can be applied to risk-stratify ALGS patients prior to liver transplantation. The fundamental concepts of this thesis will address will be introduced.

2.1. RESEARCH RATIONALE

The initial interest of this thesis was to investigate the interplay between the coronary circulation, the right ventricle (RV) and the pulmonary circulation in children with Alagille's Syndrome (ALGS), and its possible role in the evolution to right heart failure (RHF). ALGS is a rare multi-organ disorder that usually manifests as childhood cholestasis. It is associated with congenital heart disease (CHD), in particular to some form of pulmonary vascular disease (PVD), which has been related to the worst outcomes seen in ALGS children that undergo liver transplantation for end-stage hepatic failure. Predicting pre-operatively the risk of RHF secondary to associated PVD and chronic high RV afterload is therefore of paramount importance as this is the main cause of morbidity and mortality (Marino et al., 1992; Tonelli et al., 2013; Kamath et al., 2012b). As in other more common CHDs that course with PVD, it is thought that sustained RV hypertension triggers compensatory RV structural (e.g. RV hypertrophy, RVH) and metabolic changes that ultimately render the myocardium prone to microvascular ischaemia [i.e. in the absence of coronary epicardial disease] (Gomez et al., 2001; Szabó et al., 2006; Pokreisz et al., 2007; van Wolferen et al., 2008; Warnes, 2009; Champion et al., 2009). Although the evolution of RV pathology, from a normal to a compensated (hypertrophied) and then a decompensated state in the setting of increased afterload is still poorly understood, recent research suggests that the RV microvasculature is a key modulator (Pokreisz et al., 2007; Champion et al., 2009; Hsu et al., 2016).

To untangle the contribution of the different pathophysiologic mechanisms involved in adverse RV remodelling we need to account for the complex nature of ventriculo-arterial-coronary coupling. This means that we need to study, as a coupled system, the interplay between the RV, the coronary circulation (and in particular its microvascular compartment where the metabolic blood flow control occurs) and the pulmonary arterial circulation upstream, which is the RV afterload and in turn affects the ventricular performance (i.e. increases the workload and thus the O₂ demand-supply balance). This has proven to be difficult with *in vivo* experiments, often using animal models in highly controlled settings, with surgically induced pulmonary arterial hypertension (PAH), thus precluding exploration of the effect of long term adverse pulmonary remodelling on the ventricular and coronary haemodynamics (Lowensohn et al., 1976; Vlahakes et al., 1981; Bruinsma et al., 1988; Hoffman and Spaan, 1990; Zong et al., 2002, 2005).

In response to the limitations of *in-vivo* studies, several mathematical coronary blood flow (CBF) models have been proposed (Miyashiro and Feigl, 1995; Dankelman et al., 1989; Arciero et al., 2008; Kim et al., 2010). However, most have been devoted to the study of the left ventricle (LV). Therefore, a novel *in silico* experimental model, accounting for the complex ventriculo-arterial-coronary pathophysiological coupling could allow to investigate mechanisms underlying RHF in ALGS children as well as in PVD associated with other CHDs, and open the possibility of developing targeted therapies (Haddad et al., 2010).

Motivated by a need to understand the coronary autoregulation and abnormal RV-coronary-pulmonary artery cross-talk in ALGS and how it can predispose to RHF during liver transplantation, we have developed of a translational research project for personalisation of coronary haemodynamic computations during a virtual transplantation setup, using recent advances in imaging and computational technology, as well as multi-physics mathematical models. We proceed to describe the clinical and scientific background behind this research.

2.2. CLINICAL BACKGROUND: ALAGILLE’S SYNDROME

2.2.1. OVERVIEW

ALGS also known as Alagille-Watson’s syndrome or arteriohepatic dysplasia is a rare multi-systemic developmental disorder. It was first reported by Alagille *et al.* in 1969 (Alagille et al., 1969), who described the classic constellation present in up to 80-90% of cases: neonatal liver disease due to paucity of interlobular bile ducts resulting in cholestasis, congenital cardiovascular malformations (e.g. peripheral pulmonary artery stenosis, PPS), dysmorphic facies, skeletal (butterfly-like vertebral arch defects) and ophthalmic abnormalities [e.g. posterior embryotoxon] (Emerick et al., 1999).

2.2.2. GENETICS AND EPIDEMIOLOGY

ALGS is a polymalformative disorder transmitted in an autosomal dominant pattern. The genetics behind the ALGS phenotype is an area of active research. Recent advances in paediatric hepatology, molecular genetics and developmental biology, have mapped this autosomal dominant disorder to mutations in the Notch signalling pathway, which is involved in the embryologic development of the majority of organs in humans (Li et al., 1997;

Turnpenny and Ellard, 2012). This intercellular signalling pathway is required for lineage commitment, cell specification, and maintenance of progenitor cells during embryogenesis, adult cell population renewal, as well as response to injury (Li et al., 1997; Turnpenny and Ellard, 2012). In the majority of cases (up to ~90 %), mutations involve the *Jagged1* gene located in the short arm of chromosome 20 (20p12-jagged-1 locus), which encodes a critical transmembrane ligand (JAG1) that activates the Notch signalling cascade (Lindsell et al., 1995). More than four hundred JAG1 mutations have been identified in ALGS patients with up to 60% being sporadic [new in the proband] (Kamath et al., 2010a). In a small minority of ALGS cases, the *NOTCH2* gene is involved, which encodes one of the Notch receptors (McDaniell et al., 2006; Leonard et al., 2014). Some authors have proposed that mutations in the *Jagged1* gene lead to a truncated ligand that results in an inability of the *Jagged1*-Notch complex to undergo endocytosis in the signal-sending cell. This mechanism is essential for activation of the Notch pathway and its disruption impairs differentiation and/or cell migration during foetal vascular development (Ponio et al., 2007).

ALGS has high penetrance but variable expression (variable phenotypic severity) (Turnpenny and Ellard, 2012). Dhorne-Pollet *et al.* (Dhorne-Pollet et al., 1994) analysed 33 families (43 probands) and concluded that penetrance was approximately 94%. However, 26 individuals (including 11 siblings) presented only minor forms of the disease. Because of this phenotypic variability, ranging from subclinical disease to life-threatening manifestations, ALGS prevalence, reported to be of 1:70,000 newborns (based on the presence of neonatal live disease), is thought to be largely underestimated (Leonard et al., 2014; Saleh et al., 2016).

2.2.3. CLINICAL MANIFESTATIONS

As discussed in the previous section, the phenotypic expression can vary dramatically even in patients with known identical mutations and encompasses at least eight organ system (Emerick et al., 1999). In the large majority of patients (approximately 85%), the disease usually presents in the first three to six months of life with cholestasis or obstruction in bile flow (Kamath et al., 2010c). Cholestasis in ALGS is “intrahepatic”, due to an embryonic derangement of the intrahepatic ducts architecture. Paucity of bile ducts in liver biopsies is in fact a defining feature of ALGS and results in a compromise of the bile flow and elimination of lipophilic compounds (e.g. bilirubin, anions, cations), which accumulate in

blood (cholestasis). Cholestasis is commonly profound and manifests clinically as jaundice, pruritus (the most severe of any chronic liver disease disturbing sleep, daily activities, and cognitive development), xanthomas on the extensor surfaces of the extremities, and failure to thrive due to fat malabsorption. In up to 70% of ALGS patients, liver disease will progress to cirrhosis with portal hypertension. For unclear reasons, ALGS cholestasis has a unique clinical picture: it typically worsens until school age (around the age of five) and then, in nearly half of the children, it improves or stabilises (Lykavieris et al., 2001).

Laboratory findings include conjugated hyperbilirubinaemia, raised plasma bile acids, elevated liver enzymes (with a disproportionately increased gamma-glutamyltranspeptidase), high cholesterol and triglycerides levels (Gottrand et al., 1995). The increased plasma bile acid levels and cholesterol are the cause of the severe, often debilitating pruritus and disfiguring xanthomas, that dominate the early clinical picture.

Malnutrition and developmental delay are common and multifactorial. They are thought to be related with the primary defect in the *Jagged1* gene, skeletal involvement, fat malabsorption/steatorrhea and insufficient caloric intake due to liver disease, and cardiac disease (Wasserman et al., 1999).

In the majority of ALGS patients (90–97%), some form of structural cardiovascular disease (typically right-sided heart lesions) is present (Table 1) and symptomatic (e.g. failure to thrive, restlessness, dyspnoea). The pulmonary vasculature is most commonly involved and PPS is a hallmark feature of the condition, present in about two thirds of individuals. Tetralogy Fallot is the most common complex cardiac defect seen (7–16%). Other cardiac malformations that have been described in ALGS include atrial and ventricular septal defects, congenital aortic valve stenosis, and aortic coarctation, in order of decreasing frequency (Saleh et al., 2016).

In addition to classic pulmonary artery abnormalities, vascular malformations involving the intracranial vessels, the aorta and renal arteries are also a well-established feature of ALGS (Kamath et al., 2004). Although they can be incidental findings, these vascular lesions account for significant morbidity and mortality.

2.2.4. DIAGNOSIS

Classically, the diagnosis of ALGS in a proband, typically a young child with cholestasis (Figure 1) was established if bile duct paucity (an increased portal tract-to-bile duct ratio) was present on a liver biopsy and accompanied by at least three of the following clinical criteria (Alagille et al., 1987): characteristic facies, posterior embryotoxon, cardiac defects (usually PPS), and vertebral abnormalities (usually butterfly vertebrae). Recent observations of abnormalities involving the kidneys (Kamath et al., 2012a) and peripheral vasculature (Kamath et al., 2004) have led to an expansion of the phenotypic criteria (Table 1).

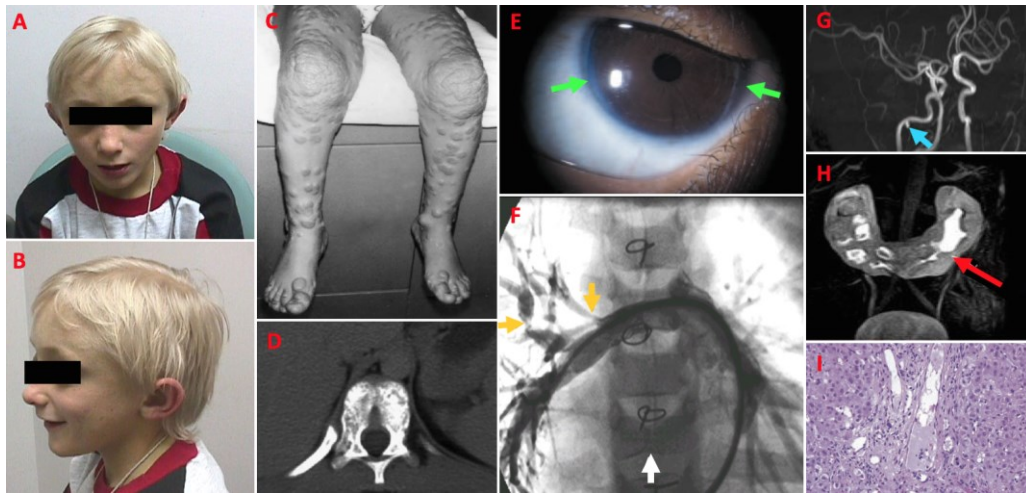


Figure 1

Panels A and B: ALGS characteristic facies: prominent forehead, hypertelorism and pointed chin giving the overall appearance of an inverted triangle. **Panel C:** Extensive disfiguring cutaneous xanthomas in a 4-year-old child with ALGS. **Panel D:** Computed tomography (CT) scan image depicting a butterfly vertebra (failure of fusion of the lateral halves of the vertebral body) in an ALGS patient. **Panel E:** Posterior embryotoxon (central thickening and displacement of the Schwalbe line). **Panel F:** Pulmonary arteriogram showing multiple stenosis (yellow arrows) in an ALGS patient with prior surgery for tetralogy of Fallot; white arrow points to a butterfly vertebra. **G:** External carotid artery aneurysm in a 17-year-old with ALGS found by routine screening. **Panel H:** Horseshoe kidney in an ALGS patient. **Panel I:** Liver biopsy specimen from an infant with ALGS with bile duct paucity (portal tract is shown without any identifiable interlobular bile). Adapted from *Suchy FJ, Sokol RJ, Balistreri WF. Liver Disease in Children. 4th ed. Cambridge University Press; 2014 and Alagille syndrome - The Childhood Liver Disease Research Network. (n.d.). Retrieved October 7, 2018, from <https://childrennetwork.org/For-Physicians/Alagille-Syndrome-Information-for-Physicians>.*

In addition to the variable expression, somatic/germline mosaicism is also thought to be frequent (Giannakudis et al., 2001; Turnpenny and Ellard, 2012). This results in a lack of genotype–phenotype correlation, which poses important diagnostic challenges as even individuals from the same family and sharing an identical mutation might not present the

same phenotype. Despite these limitations, molecular genetic testing is currently available and may provide valuable non-invasive confirmation, particularly in milder cases (Samejima et al., 2007).

System involved	Clinical Features	Frequency
Hepatic	Cholestasis	87-100%
	Jaundice due to conjugated hyperbilirubinemia	66-85%
	Pruritus	59-88%
	Cirrhosis	44 -95%
	Xanthomas	30-42%
Cardiac	Structural changes	90–97%
	Pulmonary stenosis	60–67%
	Tetralogy of Fallot	7–16%
Facial	Prominent forehead	20–97%
	Hypertelorism	
	Pointed chin	
Ophthalmologic	Saddle nose with a bulbous tip	78-89%
	Posterior embryotoxon	
Skeletal	Hemivertebra	33-93%
	Butterfly vertebra	
Renal	Ureteropelvic obstruction	39%
	Renal tubular acidosis	
Vascular	Intracranial (aneurysms, Moyamoya disease)	9-15%
	Aortic (coarctation and aneurysm)	
	Renal artery stenosis	

Table 1

Summary of the clinical features and reported frequency among individuals with ALGS (Emerick et al., 1999; Subramaniam et al., 2011).

With the availability of a genetic diagnosis, the role of liver biopsy as part of the routine clinical care, considerations about genetic counselling and prenatal testing, as well as a review of ALGS incidence are needed (Leonard et al., 2014). In addition, the identification of carriers of a JAG1 mutation but with minimal or atypical clinical manifestations, has led some authors to suggest that ALGS might represent the “tip of the iceberg” of JAG1 mutation–associated disease (Kamath et al., 2003, 2010b).

2.2.5. PROGNOSIS

The overall prognosis and risk mortality depends on the severity of organ involvement. In up to 50% of those who present in infancy, cholestasis leads to chronic liver failure that may progress to cirrhosis with portal hypertension complications [e.g. ascites,

variceal bleeding, infections, and hypersplenism] (Hoffenberg et al., 1995). An estimated 20 to 30% of those children will require liver transplantation before school age, while the remaining stabilise with well-compensated chronic liver disease and eventual good hepatic outcome (Emerick et al., 1999; Lykavieris et al., 2001; Kamath et al., 2010b; Squires et al., 2014). Possible early childhood predictive markers (clinical, biochemical and biopsy) of later hepatic outcomes have been identified, and highlight the importance of aggressive medical management of cholestasis in the early years to avoid the need for liver transplantation (Kamath et al., 2010b).

As previously mentioned, for unclear reasons, up to 50% of children with ALGS show spontaneous improvement in cholestasis, with little residual hepatic disease (Lykavieris et al., 2001). Moreover, in some ALGS patients, pruritus and/or deforming xanthomas can severely impact the child's quality of life despite a relatively preserved liver function (Squires et al., 2014). This unique natural history of ALGS liver disease adds additional difficulties in optimising the care of these patients.

In addition to liver disease, early mortality is usually due to cardiac disease, while later mortality is often caused by vascular accidents [intracranial haemorrhage may affect up to 15% of individuals, with 30% to 50% of those events being fatal] (Emerick et al., 1999; Kamath et al., 2004).

2.2.6. TREATMENT

Early aggressive medical control of cholestasis and its debilitating and disfiguring pruritus and xanthomas is crucial, as it increases the survival of the native liver (Kamath et al., 2010b, 2010c). In addition to conservative management (e.g. adequate skin hydration and trimming the fingernails), several drugs have been studied for the treatment of pruritus (e.g. cholestyramine works by stimulating bile flow, bile acid-binding resins and antihistamines for symptomatic relief) with modest success (Kamath et al., 2010b). Xanthomas tend to occur with serum cholesterol levels greater than 500 mg/dL, and typically appear on the extensor surfaces of the hands or areas of friction, such as the gluteal area. Although they can be disfiguring, they are not considered painful and generally do not require surgery. The marked hypercholesterolemia of ALGS does not appear to carry an increased risk of cardiovascular disease as it is mainly due to high levels of lipoprotein-X, which resists oxidation and thus

protects against premature atherosclerosis (Nagasaka et al., 2005). Therefore, there is no specific threshold for lipid-lowering therapy.

Malnutrition and growth failure also require aggressive treatment. A tailored and supervised diet with carbohydrate supplementation to improve overall caloric deficit, together with formulas supplemented with medium-chain triglycerides and individual fat-soluble vitamins (due to malabsorption of long-chain fat) are key (Kamath et al., 2010b).

Management of the cardiac disease is lesion specific (e.g. surgical repair of tetralogy of Fallot with ventricular septal defect closure and relief of the right ventricle outflow tract obstruction). Percutaneous techniques (i.e. balloon dilatation and stent implantation) have been successfully used in PPS (Saidi et al., 1998). There are also anecdotal cases of heart–lung transplantation in combination with liver transplantation for selected cases in the extreme spectrum of ALGS (Gandhi et al., 2002).

Management of ALGS systemic vasculopathy remains controversial as there are no longitudinal data about the risks and benefits of diagnosing and treating asymptomatic lesions (Kamath et al., 2010b). If in symptomatic or progressive cerebral vascular disease (e.g. Moyamoya disease which is associated with a high risk of recurrent stroke) the benefits of early surgical intervention usually outweigh the associated risks, in other cases, such benefits are not as clear (Kamath et al., 2004; Emerick et al., 2005).

2.2.7. LIVER TRANSPLANTATION

Children with ALGS constitute approximately 4 to 5.3% of those requiring a liver transplant (Englert et al., 2006; Arnon et al., 2010). The unpredictable natural history of ALGS, not predictable by genotype, and the multisystemic involvement adds complexity to transplantation decisions. If the majority of patients can be treated conservatively, in approximately 20 to 30% of cases orthotopic liver transplantation is the only option for end-stage liver failure. Given the variable nature of liver disease, the indications for liver transplantation in ALGS are likewise not uniform and controversial, spanning from those associated with cirrhosis (e.g. portal hypertension) to those associated with impairment of quality of life [e.g. growth failure and refractory metabolic bone disease due to fat-soluble vitamin deficiency and/or intractable pruritus] (Englert et al., 2006; Shneider, 2012). As an example, refractory pruritus, although not a life-threatening condition, is the most common

indication for liver transplantation in ALGS. Consequently, the approach to a patient being considered for liver transplantation must be taken thoughtfully, with attention to the multi-system/extrahepatic nature of ALGS, in particular to associated cardiovascular disease, which can complicate the intraoperative and anaesthetic care. As we will discuss in the following sections, these contributors to pre and post-transplant morbidity/mortality shape the focus of pre-transplantation evaluation and planning.

2.2.7.1. LIVER TRANSPLANTATION SURGICAL PROCEDURE

In general, the transplant procedure is associated with rapid and severe haemodynamics changes, particularly after the occlusion of the vascular supply to the liver (clamping of the inferior vena and portal vein), which results in splanchnic congestion and reduction of cardiac preload (the anhepatic or ischaemic phase of the transplant). A decline in cardiac output in the order of 20-30% is commonly observed even with volume loading prior to vascular cross-clamping or with the use of modern techniques [e.g. use of extracorporeal bypass to limit the decrease in venous return] (Ozier and Klinck, 2008). An unbalanced coagulation system can result in sudden blood loss and aggravate the haemodynamic instability, particularly in patients with poor cardiac reserve.

In addition, the reperfusion of the newly transplanted liver is often associated with a transient period of haemodynamic instability related to the sudden release of vasoactive mediators into the systemic circulation (Ozier and Klinck, 2008). This is characterised by a decrease in myocardial contractility and systemic vascular resistance, and a moderate increase in pulmonary arterial pressure (PAP) and pulmonary artery wedge pressure (PAWP). In adult series, up to 50% of liver transplant recipients can have a severe decrease in mean arterial pressure (MAP; $\geq 30\%$ to the value at the end of the anhepatic phase), for at least one minute and within five minutes of reperfusion (Chui et al., 2000; Hilmi et al., 2008; Paugam-Burtz et al., 2009). Aggarwal and co-workers (Aggarwal et al., 1987) first described this clinical picture as post-reperfusion syndrome (PRS), a dramatic cardiovascular and metabolic derangement that markedly increases the recipient's perioperative morbidity and mortality (Siniscalchi et al., 2010; Paugam-Burtz et al., 2009). It is plausible that similar events may occur in ALGS children undergoing liver transplantation, although this has not been widely reported.

2.2.7.2. HIGH RISK OF LIVER TRANSPLANT COMPLICATIONS IN ALGS

Pre-transplant mortality in AGS is related to cardiac disease as often as it is to hepatic disease itself (Emerick et al., 1999; Shneider, 2012). Indeed, approximately 10 to 15% of all deaths in ALGS children with end-stage liver disease are cardiac related (Marino et al., 1992; Englert et al., 2006; Arnon et al., 2010; Kamath et al., 2012). Moreover, several studies have shown that in those patients undergoing liver transplantation, cardiopulmonary disease is predictive of post-transplant mortality in ALGS (Emerick et al., 1999; Arnon et al., 2010; Kamath et al., 2012b).

When compared to other causes of neonatal-childhood cholestasis such as biliary atresia (BA), the survival rate of age-matched ALGS patients during and following liver transplantation is significantly lower (Hoffenberg et al., 1995; Arnon et al., 2010; Kamath et al., 2012). A review of the United Network for Organ Sharing (UNOS) transplantation database (United States) including 11,467 children who received a liver transplant between October/1987 and May/2008 showed that 461 (4.0%) had ALGS versus 3056 (26.7%) with BA: the one- and five-year patient survival was approximately 7% lower in ALGS (Arnon et al., 2010); furthermore, the early mortality (at 14 and 30 days) as well as the early graft failure were significantly worst in ALGS (Arnon et al., 2010). A retrospective review and analysis of 91 children with ALGS from the Studies in Paediatric Liver Transplantation Registry (SPLIT) also observed a worst 1-year post-transplant mortality rate for ALGS (13%) compared to a matched cohort of children with BA (4%), with a significant number of these deaths occurring in the first 30 days after transplantation and due to systemic manifestations of ALGS (such as cardiac disease) not addressed by liver transplantation (Kamath et al., 2012b).

The pre- and post-transplant cardiovascular mortality in ALGS has been specifically attributed to RHF and circulatory collapse (Marino et al., 1992; Tzakis et al., 1993; Png et al., 1999; Smithson et al., 2014). PPS is thought to be the common denominator. It has been postulated that PPS results in chronic pressure overload and induces detrimental RV remodelling: compensatory hypertrophy initially and eventually dilation and systolic function impairment (Tzakis et al., 1993; Png et al., 1999; Pokreisz et al., 2007). Due to its remarkable ability to adapt to pressure and volume load (Warnes, 2009), RV dysfunction is often overlooked and may only become clinically apparent during transplantation. ALGS

children may appear to have a compensated physiology at “basal” conditions, but are at great risk of RHF and its inherent mortality, as well as that related to congestive hepatopathy (“backward” congestion) during and immediately post-transplantation. Passive hepatic venous congestion secondary to RHF promotes further ischaemic injury to new-liver resulting in release of vasoactive mediators into the systemic circulation thus contributing to circulatory failure (Ford et al., 2015).

Another concern is related to ventricular interdependence since the systemic-like RV pressures can be transmitted to the LV, independently of neural, humoral, or circulatory effects (Santamore and Dell’Italia, 1998), and cause LV underfilling. This will further compromise systemic perfusion and thus the graft and recipient outcomes (Lazar et al., 1993; Png et al., 1999).

Besides the aforementioned problems, some ALGS patients may also have a cirrhotic cardiomyopathy characterised by myocardial (eccentric) hypertrophy, impaired diastolic relaxation, increased cardiac output and peripheral vasodilatation. This is known to affect nearly 70% of BA patients and is associated with a high risk of post-transplantation mortality, but limited data is available in ALGS (Desai et al., 2011). Finally, two distinct pulmonary vascular disorders, hepato-pulmonary syndrome (HPS) and porto-pulmonary hypertension (POPH) may also occur, both with major clinical implications for liver transplantation (Krowka et al., 2016). HPS is characterised by the triad of liver disease, pulmonary vascular dilation, and impaired oxygenation resulting from a right-to-left shunt (Krowka et al., 2016). It has been reported to occur in up to 22.2% of ALGS patients (Lee et al., 2013). POPH is defined by an elevated mean PAP (≥ 25 mmHg at rest), PAWP ≤ 15 mmHg and raised pulmonary vascular resistance (PVR, > 3 Wood units). It is another complication that can occur in ALGS children presenting for a liver transplant evaluation, although its prevalence is not well known (Condino et al., 2005; Krowka et al., 2016; Galie et al., 2016;).

2.2.7.3. PRE-OPERATIVE CARDIOVASCULAR ASSESSMENT

Following a report showing that ALGS had nearly 20% higher mortality than all other children from the same unit, Tzakis and co-workers (Tzakis et al., 1993) were the first to recommend a thorough pre-operative cardiac assessment to recognise those patients who are likely to be at a high risk because of their cardiovascular disease. Then, besides routine blood

tests, ALGS patients were assessed by echocardiography alone, provided that the pulmonary artery systolic pressure (PASP) estimated by Doppler echocardiography was normal (Tzakis et al., 1993; Razavi et al., 2001). However, on the one hand, echocardiography often failed to visualise the distal branch pulmonary arteries, requiring invasive angiography for adequate assessment of the distal vasculature. On the other hand, the shortcomings of PASP Doppler calculations (see Figure 2), such as assumption of planar blood flow, user-dependent plane misalignment during ultrasound beam interrogation, absence of tricuspid regurgitation jet, often required invasive confirmation (Janda et al., 2011; Greiner et al., 2014).

Currently, pre-operative cardiovascular evaluation is usually performed in specialised centres by a multidisciplinary team and involves a thorough history and physical examination, together with: pulse oximetry; routine haematology/biochemistry tests (e.g. complete blood count, blood typing, coagulation testing, serum creatinine/urea with estimation of the glomerular filtration rate, electrolytes and liver function tests); electrocardiography (ECG); and a comprehensive echocardiography study. Further testing often includes: arterial blood gas analysis to screen for hypoxaemia; contrast echocardiogram with agitated saline for detection of intrapulmonary shunting; CMR for accurate assessment of cardiac volumes, possible shunts and anatomic assessment of the central pulmonary arteries; right heart invasive catheterisation for accurate systemic/pulmonary pressure and resistance measurements; and, less commonly, a lung perfusion scanning with peripheral vein injection of Technetium (^{99m}Tc) macroaggregated albumin for detection and quantification of intrapulmonary vascular dilatations. Despite these improvements in pre-transplant assessment, the variable nature of the disease and the multi-systemic involvement make the determination of a cardiovascular contraindication to liver transplantation in children with ALGS complex (Ovaert et al., 2001).

In our institution, all ALGS children with suspected pulmonary vasculopathy being considered for a liver transplantation undergo a hybrid X-ray/magnetic resonance guided study (XMR) with dobutamine stress. This comprehensive exam comprises: a baseline CMR scan with 3D anatomic data, rest cines for function and cardiac volumes assessment as well as rest flows (aorta and pulmonary arteries) to rule out a shunt; an XMR right heart catheterisation for systemic/pulmonary pressure and resistance measurements (often pre and post inhaled nitride oxide, a pulmonary vasodilator, to assess for the reversibility of the

pulmonary vascular disease); and a dobutamine stress CMR (DSCMR) scan with acquisition of cines and flows. This XMR program pioneered by our institution (Muthurangu et al., 2004) allows: (1) to accurately assess pulmonary vascular resistance by combining pulmonary blood flow measurements and invasive catheterisation; (2) to use dobutamine stress pre-transplant to unmask abnormal ventricular physiologic responses and therefore assess the risk of early RHF post-transplant; (3) to reduce radiation burden associated with conventional X-ray guided right heart catheterisation studies, particularly when faced with the need for repetitive investigations. In addition, the acquisition of advanced high-resolution functional and morphologic CMR data with concomitant central pressure monitoring. As it will be discussed in Study 6 of this thesis, we have used this rich and unique information to parameterise our computational simulations.

2.2.7.4. XMR STUDY WITH DOBUTAMINE STRESS

Razavi and co-workers (Razavi et al., 2001) have proposed XMR with dobutamine stress to risk stratify ALGS patients undergoing liver transplantation. Using dobutamine as an inotropic vasodilator they have tried to replicate the haemodynamic conditions following reperfusion of the transplanted liver by inducing peripheral vasodilatation and increasing the cardiac output. They have found that the patients' haemodynamic response to dobutamine could predict their ability to increase the cardiac output in the immediate post-transplant period to meet the demands of generalised vasodilatation occurring with liver reperfusion (Razavi et al., 2001).

Dobutamine is a synthetic catecholamine and, at low doses, it has mainly an inotropic effect on the myocardium through beta-1 receptors. At higher doses it has a chronotropic effect and induces a mild peripheral vasodilatation through its action on beta-2 and alpha-receptors, with little effects on PVR (Schranz et al., 1982; Westfall and Westfall, 2011). In their protocol, they used a graded dobutamine infusion starting at 10 $\mu\text{g}/\text{kg}/\text{minutes}$ up to 20 $\mu\text{g}/\text{kg}/\text{minutes}$. Among the fifteen ALGS children included in their original report, a significant decrease in the systemic vascular resistance was only observed with the higher dose of 20 $\mu\text{g}/\text{kg}/\text{minutes}$ and this was established as the target dose for a diagnostic test.

Razavi *et al.* found a wide variation in the cardiac output response to dobutamine infusion, independently of baseline RV pressures conventionally used to assess ALGS

patients. They proposed this dynamic test as a more physiological measure of the heart's ability to cope with the large haemodynamic changes associated with liver transplantation, and concluded that patients with a maximal increase in cardiac output of less than 40% following dobutamine stress were at higher risk of complications during liver transplantation. If suitable, they should be considered for treatment of their PPS (Razavi et al., 2001; Squires et al., 2014).

However, a major limitation of dobutamine stress is that it does not account for all key haemodynamic events during liver transplantation: while the test might reproduce the increase in heart rate (HR) and myocardial metabolic demand, it fails to account for the severe systemic vasodilation and for the corresponding coronary perfusion pressure drop during transplantation. Furthermore, the general guideline of 40% increase in cardiac output during dobutamine stress CMR (DSCMR) might not guarantee adequate coronary perfusion for all ALGS patients, particularly during PRS. It is unlikely that adequate collection of data on coronary blood flow (CBF) in ALGS children during liver transplantation is feasible, ethically or clinically. In this PhD thesis, we have developed an image-based computational methodology that is able to simulate some of the haemodynamics of liver reperfusion and evaluate the adequacy of the coronary responses. In the next sections, we introduce the paradigm of patient-specific computational modelling for studying patients with CHD that was applied to our patient. Finally, we discuss fundamental aspects of the coronary circulation and the cross-talk between cardiac myocardium, the coronary vasculature and the pulmonary circulation motivating the experiments of the main study of this thesis (Study 6).

2.3. PATIENT-SPECIFIC COMPUTATIONAL MODELLING IN PAEDIATRIC CONGENITAL HEART DISEASE

2.3.1. BACKGROUND: UNMET NEEDS IN THE CARE OF PAEDIATRIC CONGENITAL HEART DISEASE

In the last 60 years, due to successful paediatric cardiology programs (with improved early diagnosis) and paediatric cardiac surgery breakthroughs, we have witnessed a remarkable improvement in the life expectancy of paediatric patients with CHD, including in ALGS patients (Kamath et al., 2012b). While before only 20% survived until adulthood,

nowadays over 85% of patients do (Reid et al., 2006). These improvements in the diagnosis and surgical treatment have also resulted in an increasing prevalence of CHD in the general population, some with residual, palliated, complex defects in addition to associated comorbidities (e.g. coronary artery disease, PVD), further stressing the need for personalised care (Opotowsky et al., 2009).

A significant concern in paediatric CHD patients, including in those with ALGS, is related to the development of PVD, a progressive disease associated with high morbidity and mortality despite the availability of advanced vasodilator therapy (Manes et al., 2014; Kozlik-Feldmann et al., 2016). In the 2007 Euro Heart Survey the prevalence of PAH in adults with CHD was of 5 to 10% (Engelfriet et al., 2007). More recent data estimates that approximately 3 to 10% of children with CHD will develop PVD (van Riel et al., 2014), but with improvements in their care and thus their life expectancy, this number is expected to rise in the coming years (Diller and Gatzoulis, 2007).

Despite major advances in the care of paediatric CHD (including in ALGS), the clinical decision-making process is still based on consensus opinion of experts, small prospective and retrospective studies, or registries. Not surprisingly, the majority of the recommendations for the management of CHD patients have the lowest evidence level (level C) (Warnes et al., 2008; Silversides et al., 2010; Baumgartner et al., 2010). Additionally, the safety and effectiveness of most medical treatments and/or procedures have not been formally studied in children. Although largely off-label, clinicians have often use medicines and treatments based on what is known to work in adults, which may pose a risk to a particularly vulnerable subset of patients. Not only the pharmacokinetic and pharmacodynamic properties of certain drugs may differ considerably in children from their adult counterparts, but also extrapolating empirical data on treatments from cohorts of patients with similar conditions might not reflect the response of the individual subject.

2.3.2. DIAGNOSTIC METHODOLOGIES IN PAEDIATRIC CONGENITAL HEART DISEASE

Imaging plays a crucial role in the understanding of complex anatomic malformations and the resultant pathophysiologic adaptations in paediatric CHD, underpinning an initial clinical diagnosis. The remarkable improvements in the diagnostic assessment of the past

decades as well as the accuracy of treatment decisions rely more and more on precise and detailed information provided by the multiple sophisticated imaging modalities available (Warnes et al., 2008; Baumgartner et al., 2010; Valsangiacomo Buechel et al., 2015). Moreover, multidimensional image data provides the ability to customise biomechanical and physiological parameters to a particular patient's anatomy, while integrating models of cardiac and vascular physiology. These integrative models of cardiovascular pathophysiology are key to understand the spectrum of paediatric CHD and associated conditions (e.g. PVD), as well as for treatment planning. Nevertheless, in the overall diagnostic workup of certain defects and/or diseases, clinicians still rely on the gold-standard information from invasive but riskier haemodynamic assessment (O'Byrne et al., 2015; Stefanescu Schmidt et al., 2017). That is the case of cardiac output, pulmonary pressure and resistance quantification in patients with known or suspected cardiac shunts or PVD.

However, gold standard invasive methods for measuring cardiac output like Fick's and thermodilution techniques are not devoid of errors (e.g. thermodilution method tends to overestimate the cardiac output in the presence of low outputs) and make key assumptions on the physiologic state of the subject (e.g., cumbersome oxygen consumption measurement is usually replaced by an assumed fixed value in Ficks' methodology). Additionally, these methodologies can only provide physiological assessment at a limited number of spatial locations (e.g. pressure is usually measured at a reference point of the patient's cardiovascular system).

2.3.3. NEW PARADIGM OF PREDICTIVE PERSONALISED MEDICINE FOR PAEDIATRIC CONGENITAL HEART DISEASE

In response to these limitations, a new paradigm of “predictive personalised medicine” postulates the use of computational tools that integrate patient-specific medical imaging (as well as other measurements) to simulate and quantify physiologic and pathophysiologic function of the cardiovascular system. The ultimate goal is to perform a subject-specific haemodynamic assessment and, when applicable, to predict the outcome of alternative treatment plans for an individual patient. In the next sections, we introduce fundamental concepts for patient-specific computational modelling (PSCM) and describe the typical workflow.

2.3.4. FUNDAMENTAL CONCEPTS FOR IMAGE-BASED COMPUTATIONAL MODELLING

2.3.4.1. FROM ENGINEERING TO PATIENT-SPECIFIC COMPUTATIONAL MODELLING

In general, a model is an approximation of the reality that helps to understand function. In engineering, modelling has traditionally relied on using complex partial differential equations (e.g. Navier-Stokes equations) to describe certain physical phenomenon. These equations can be solved either analytically or numerically. Analytical solutions (e.g. Poiseuille's law) can be obtained under a series of simplified conditions on the physics and geometry (for instance, steady flow in a perfectly cylindrical rigid tube), and provide a closed-form solution for the quantity of interest. These assumptions (e.g. non-deformable tubes) entail obvious limitations when applied to dynamic problems/systems such as the human circulation. Moreover, when the combination of physics and anatomy is complex (for instance, turbulent 3D flow through a stenotic vessel), there are no analytical solutions that can accurately describe the physics. For example, in pulmonary stenosis, flow is highly complex and significant viscous losses occur as blood moves through the stenotic area. Under these conditions, the simplified Bernoulli's law (Equation 2), commonly used in echocardiography and which assumes no viscous dissipation, is fundamentally flawed (see Equation 1). This is particularly critical for the estimation of pulmonary pressures for screening and the diagnosis of pulmonary vasculopathy in paediatric patients with CHD, including ALGS patients (Figure 2). Therefore, an accurate, non-invasive estimation of metrics such as pressure gradients, wall shear stress (WSS) may only be obtained by solving complex partial differential equations (e.g. Navier-Stokes), using numerical techniques and high performance computing (HPC).

$$\Delta P = \frac{1}{2} \sigma (v_2^2 - v_1^2) + (dv/dt)dx + R(v)$$

Equation 1

$$\Delta P = 4 \times v_2^2$$

Equation 2

The Bernoulli's equation (Equation 1) calculates the pressure difference or gradient (ΔP) across an obstruction by taking into account the velocity proximal to a stenosis (v_1), the velocity in the stenotic jet (v_2), the density of blood (σ), the acceleration of blood through the orifice (dv/dt), and the viscous losses [$R(v)$]. This formula has been simplified for practical use in Doppler-echocardiography and only uses the maximal velocity along

the ultrasound beam, thus allowing a quick conversion of velocity difference obtained by tracing the spectral Doppler to instantaneous pressure gradient. This simplified equation (Equation 2) assumes that viscous losses and acceleration effects are negligible. In addition, the simplified Bernoulli equation ignores the proximal flow velocity (v_1), a reasonable assumption when velocity is <1 meters/seconds. Because of all these assumptions, it is imperative that accurate measurement of v_2 is obtained by good alignment of the Doppler probe (due to the squaring of v_2 , a 10% error will result in a 20% error in the pressure estimated). Although this simplification is reasonable for the restrictive orifices, it is not fully accurate for flow through valves, where more than half of the pressure drop is typically due to inertial forces.

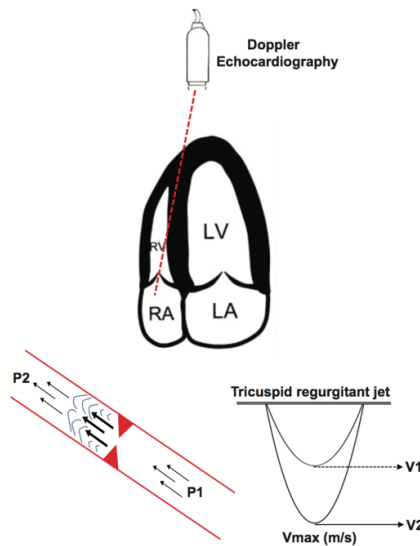


Figure 2

Whenever the maximal velocity of a tricuspid regurgitant (TR) jet (V_2 velocity profile) can be sampled by Doppler-echocardiography, an estimate of the pulmonary artery systolic pressure (PASP) can be made and used to screen PVD in paediatric CHD. This is done by calculating the right atria (RA) to RV pressure gradient using the modified Bernoulli equation (Equation 2) and then adding an assumed RA pressure according to inferior vena cava (IVC) diameter and its variation with respiratory movements (as pressure from the RA is transmitted to the IVC). This equation can also be applied to calculate the pressure gradient or difference (between P_2 and P_1) across a vessel/valve stenosis. However, for estimation of the PSAP, in addition to the error introduced by the estimated RA pressure, the inaccurate alignment of the ultrasound and thus underestimation of the peak velocity, this calculation assumes planar blood flow. Furthermore, although Doppler echocardiography is the best imaging modality in terms of temporal resolution, it cannot resolve a velocity map on a randomly oriented anatomic plane. Not surprisingly, the accuracy and reliability of some of these measurements is often debated. LA, left atrium. LV, left ventricle. RA, right atrium. RV, right ventricle.

In the following, we provide an overview of several fundamental closed-form solutions that are commonly used to gain basic insight into the mechanics of blood flow and vessel wall dynamics. Then, we provide an overview of the computational modelling workflow that we have used in the main study of this thesis (Study 6).

2.3.4.2. FUNDAMENTAL SOLUTIONS FOR BLOOD FLOW AND CARDIOVASCULAR MECHANICS ANALYSIS IN PAEDIATRIC CONGENITAL HEART DISEASE

The cardiovascular circulation can be described as closed-loop pulsatile system. At every cardiac cycle the heart pumps blood throughout the systemic and pulmonary circulations. In turn, the movement of blood through the vascular system can be described mathematically as that of an incompressible fluid (with constant or shear-dependent viscosity) governed by the Navier-Stokes equations, which describe the conservation of linear momentum and mass. The Navier-Stokes equations describe the fluid motion in three spatial dimensions, due to forces such as pressure gradients, viscous losses, acceleration, and gravity. Because of their non-linear character, obtaining a solution to these equations requires the use of HPC and numerical methods. A number of simplifications to the 3D Navier-Stokes equations have been utilised to describe flow and pressure under much simpler terms.

The Windkessel Model

One of the most commonly used simplified models of the circulation (lumped-parameter network, LPN) consists of electric analogues of the circulation. The Windkessel model described by Otto Frank in the late 19th century, was the first LPN model. It describes the heart and the systemic arterial system as a closed hydraulic circuit (Frank, 1990). In this analogy, the circuit contained a water pump connected to a chamber, filled with water except for a pocket of air (Figure 3). As it is pumped, the water compresses the air, which in turn pushes the water out of the chamber. Windkessel models are frequently used to represent the workload of the heart during the cardiac cycle, to characterise parameters such as arterial compliance, peripheral resistance and as a mean to derive aortic flow or arterial pressure from image data.

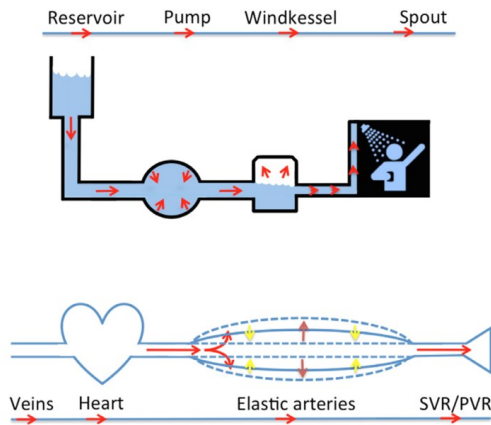


Figure 3

Representation of the Windkessel model of the human circulation with the correspondent and equivalent hydraulic system. The Windkessel is similar to a water pump connected to a chamber, filled with water but with a pocket of air. As the water is pumped, it compresses the air, pushing water out of the chamber. SVR, systemic vascular resistance. PVR, pulmonary vascular resistance.

LPN models can have different designs: from 2-element models that take into account the arterial compliance and total peripheral resistance, to 3 or 4-element models that provide a finer description of the distal vascular bed.

Poiseuille's Law

Another commonly used simplified model of the circulation is given by Poiseuille's law (Figure 4 and Figure 5). Poiseuille's law provides an analytical solution for the Navier-Stokes equations under the assumptions of steady-flow in a symmetric, cylindrical vessel, in the absence of gravity, and under a constant pressure gradient. Poiseuille's law relates flow to a constant pressure gradient and a resistance that is directly proportional to the vessel length (L), the blood viscosity (μ), and inversely proportional to the fourth power of the vessel radius (r).

$$Q = \frac{\pi r^4 \Delta P}{8 \mu L} \quad \rightarrow \quad \text{Resistance} = \frac{8 \mu L}{\pi r^4}$$

The diagram shows a blue cylindrical vessel. The length is labeled 'L', the radius is labeled 'r', and the viscosity is labeled ' μ '. A red arrow labeled 'Q' points to the right, indicating the direction of flow. Below the vessel, a pressure difference ΔP is shown between two points, P1 (high-pressure) and P2 (low-pressure).

Figure 4

Poiseuille's Law for an hydraulic system, describing the behaviour of fluids through pipes, can be used to describe the flow of blood through the arteries. Poiseuille's law describes the rate of flow (Q or the volume of fluid passing a certain point along the tube per unit of time) in terms of the fluid's viscosity, the vessel's radius and length, and the pressure difference along the tube. Resistance is directly proportional to viscosity and inversely proportional to the fourth power of the radius. Q, flow; r, radius; ΔP , pressure difference (P1 high-pressure to P2 low-pressure); μ , blood viscosity; L, length of the tube.

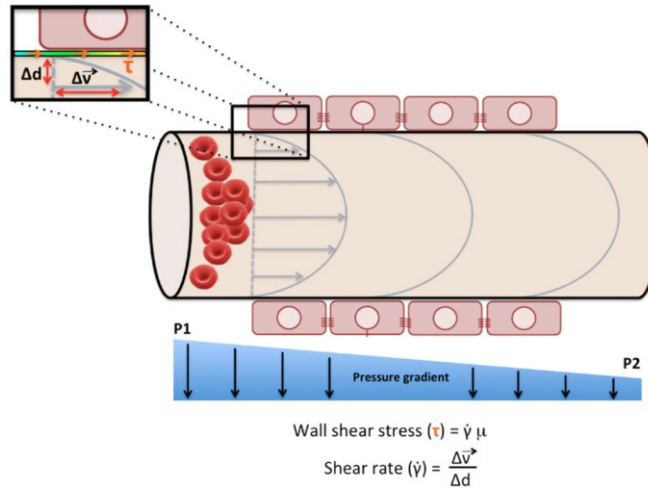


Figure 5

Schematic of a longitudinal section of a tube representing an idealised arterial vessel. Poiseuille's analytical solution for an incompressible (no change of volume) Newtonian fluid (constant viscosity) assumes constant flow (no acceleration) in a rigid (non-deformable) cylindrical tube, with constant cross-sectional area and a constant pressure gradient driving the flow. Under these assumptions, Poiseuille's solution produces a parabolic velocity profile as depicted in the figure, with a zero velocity at the vessel wall boundary and maximum axial velocity at the centre of the vessel. Because of these assumptions, there are obvious limitations to its use for the understanding of biofluids and vessel wall mechanics. Nevertheless, such analytical solutions allow us to derive important parameters that have been correlated with important clinical outcomes (e.g. tensile stress and risk of aneurysm rupture, endothelial shear stress and coronary atherosclerotic plaque and vascular remodelling). The shear rate at the inner wall of a Newtonian fluid flowing within a pipe is given by the ratio between the linear fluid velocity (v) and the diameter of the pipe (d). Wall shear stress is related to the shear rate by multiplying it by the fluid viscosity (μ).

Laplace's Law

Laplace's law is another commonly used analytical solution. It applies to cylindrical (vessels) or spherical (ventricular chamber) geometries, whether the material has linear or non-linear mechanical properties and irrespective of wall thickness. It states that wall stress is directly proportional to the product of the luminal pressure and the radius and inversely proportional to the wall thickness (Figure 6).

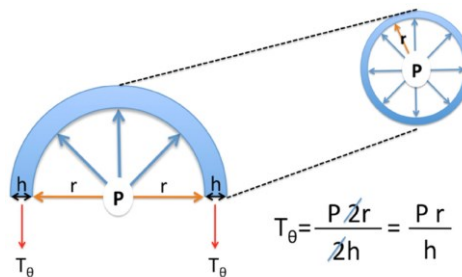


Figure 6

A schematic of Laplace's law. T_{θ} , wall tensile (circumferential) stress; P , transmural pressure; r , radius; h , wall thickness.

All these solutions do not suffice in complex anatomical and physiological configurations. For these, no analytical solutions can be accurately applied and one must resort to advance tools such as computational fluid dynamics (CFD) to describe the physics at hand.

2.3.4.3. COMPUTATIONAL FLUID DYNAMICS IN PAEDIATRIC CONGENITAL HEART DISEASE

CFD is a discipline that uses numerical methods and algorithms to solve the Navier-Stokes equations of conservation of mass and momentum in order to describe and solve fluid problems. Although it was first used in engineering areas such as chemical, aerospace/aeronautic and the automotive industry, it has recently emerged as a valuable tool in biomedical engineering (Tu et al., 2013). The ever-increasing CFD applications in cardiovascular research span from understanding the pathophysiology of certain diseases, acquired or congenital, the development of new and improved medical devices, to the optimisation of existing surgical procedures through computational simulations, resulting in enhanced efficiency and lower costs (Nichols et al., 2005).

In paediatric CHD, there is a growing body of evidence showing the usefulness of CFD for planning complex cardiovascular interventions (Migliavacca et al., 2000; Migliavacca and Dubini, 2005; Hsia et al., 2011; DeCampli et al., 2012; Pennati, 2013; Arbia et al., 2014; Marsden and Esmaily-Moghadam, 2015). The use of these CFD-based methodologies is particularly appealing in the study of rarer conditions such as ALGS, or diseases affecting vulnerable patients (e.g. children with poorly compensated CHD), where recruiting enough patients to provide robust clinical evidence may not be feasible or where collection of adequate clinical data may be problematic. In addition, CFD-based methods may provide unique patient-specific mechanistic insights into complex congenital malformations. Moreover, they offer a unique opportunity to integrate and augment current imaging modalities and to provide tailored and predictive information that can help medical diagnosis, prognostication as well as therapeutic/interventional planning. These can be interpreted as an extra piece of evidence upon which clinicians can support their management decisions. In the next section, we describe the specific steps of the computational simulation workflow that were also used in Study 6.

2.3.4.4. A WORKFLOW FOR CLINICIANS

The typical workflow for CFD-based patient-specific modelling (used in Study 6) is presented in (Figure 7). The first step is the acquisition of accurate patient information on anatomy as well as physiology using the most appropriate available imaging and/or invasive data. In the research developed for this PhD thesis, XMR was the imaging methodology used as it allowed simultaneous acquisition of imaging, flow and pressure data used to specify the computational model and the boundary conditions for the Navier-Stokes equations.

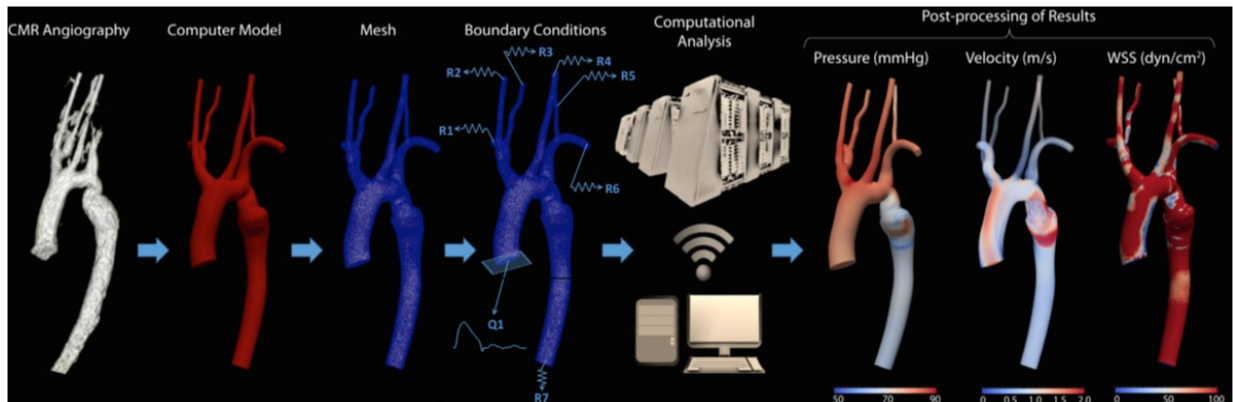


Figure 7

Example of a CFD simulation on an aortic coarctation case. The acquired raw data (in this case coronary magnetic resonance angiography, CMRA) was segmented to produce the 3D geometry of the model that was then meshed. After assigning the boundary conditions (Q1, inflow boundary condition given for instance by 2D phase-contrast CMR at the aortic valve; R1- R7 outlet resistors), the computational analysis was performed using a HPC. This enabled to map pressure, flow (velocity) and wall shear stress in any point of the 3D model. Of note, only by solving the Navier-Stokes equations can the complex flow patterns and pressures shown in the post-stenotic aneurysm be accurately assessed.

After the acquisition of the image data, the next step is the construction of an anatomical model of the region of interest (e.g. aorta, coronaries, pulmonary arteries). This involves contouring the walls of the vessels and/or chambers to be included in the computational analysis using 2D or 3D segmentation techniques. The surfaces of the extracted geometry can be defined using either analytical functions such as b-splines (see panel A Figure 8) or discrete surface triangulations that provide a faceted approximation of the surface of the model (see panel B of Figure 8). Analytical representations make it possible to create a computer aided design prototype of the anatomical model. On the other hand, surface triangulations are lightweight and can be used to make 3D-printed prototypes of the anatomy.

Several manual to semi-automated computer software solutions are available to perform image segmentation and create the geometric model, with variable degree of user-interaction. Generally speaking, direct-3D segmentation methods (see panel B Figure 8) require a smaller user interaction and work well when high-quality image data is available. These direct-3D methods usually produce a discrete surface triangulation representation of the anatomy (Dillon-Murphy et al., 2016). Conversely, 2D segmentation methods (used in Study 6) involve a higher degree of user interaction, but make it possible to handle noisier data (Wang et al., 1999a). The end result is an analytical (e.g., non-uniform rational b-spline, NURBS) representation of the model (see panel A Figure 8). Analytical models have a significant advantage in CFD simulation over discrete models as they effectively have an unlimited resolution. Conversely, discretised models have a limited resolution given by the point density of the faceted representation of the boundary.

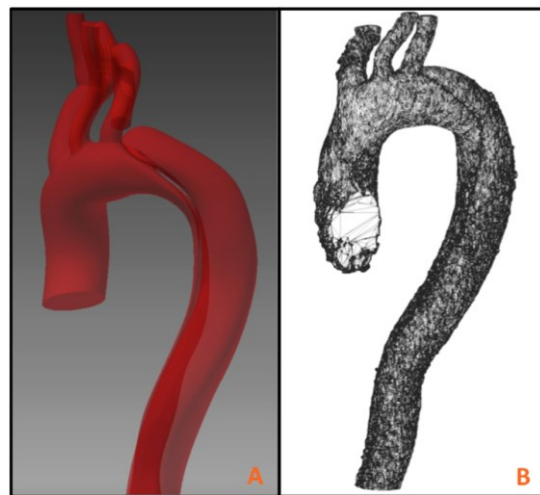


Figure 8

Two different representations of the same anatomical model of a type B aortic dissection. **Panel A** depicts a smooth, analytical representation of the segmentation given by NURBS, obtained using 2D segmentation and lofting techniques. **Panel B** shows a surface triangulation of the same data, obtained with direct-3D segmentation techniques. NURBS, non-uniform rational b-spline.

Once the geometry of the model is defined, it must be discretised into a computational mesh. The volume of the geometry is broken down into a collection of cells (or elements) and nodes (or points). The elements can be of different shapes such as tetrahedral or hexahedral. The equations of motion are then discretised and solved in every element and node of the mesh. Since the mesh has typically hundreds of thousands of elements, the

resulting problem has a large number of unknowns, and must be solved using a powerful HPC. For instance, in 3D-CFD Navier-Stokes simulations, every node of the mesh contains four unknowns: the scalar value of pressure, and the three different components of the velocity field.

In the computational modelling paradigm, it is critical to ensure that the obtained numerical solution is “grid-independent”: This means that the same solution can be obtained in different meshes, thereby attaining spatial and temporal convergence. A good computational modelling practice is therefore to perform mesh-independence studies, where solutions are obtained in finer and finer computational grids until no change is observed between repeated simulations (Taylor and Figueroa, 2009). Figure 9 illustrates an example of different meshes used for mesh-independence analysis in a thoracic aortic flow problem.

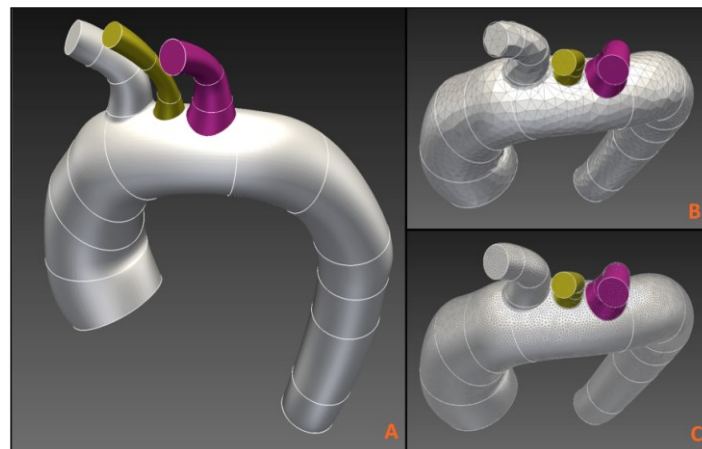


Figure 9

Panel A. Analytical representation of a thoracic aorta segmentation obtained from a 3D steady-state free precession CMR dataset. **Panel B.** Coarse computational grid created by assigning a large tetrahedron size. **Panel C.** Refined computational grid created by reducing the tetrahedral element size used in Panel B.

Once the mesh is created, one must define the so-called “boundary conditions” for every face of the computational model. These conditions are given by measurements (e.g., data on flow, pressure, wall motion, cardiac function) that provide information for quantities such as cardiac output, flow splits, and microcirculatory resistance. A commonly used approach is to specify flow waveforms at the inflow faces of the computational model, and Windkessel models at the outflow faces. The vessel walls can be modelled as rigid (e.g., a zero velocity is used as a boundary condition) or assigned elastic properties derived from wall motion data.

The final step in the simulation workflow involves obtaining the numerical solution for the equations representing the laws of fluid dynamics (e.g. Navier-Stokes) at each point of the computational model using HPC and powerful algorithms. Once the solution is obtained, it is post-processed to visualise fields such as velocity, pressure, WSS, etc. (see Figure 7). Ultimately, CFD provides a high-resolution description of the 3D physics of flow (e.g. 3D velocities and pressures at every point of the computational grid) by having a small number of physiological measurements (e.g. imaging-derived flow, catheter-derived pressure) at a limited number of locations.

We now proceed to discuss relevant physiological and physics concepts to understand how we modelled the coronary circulation of an ALGS child being considered for liver transplantation in order to gain insight into how the RV would handle a state of coronary hypoperfusion during liver transplantation.

2.4. CORONARY CIRCULATION

2.4.1. CORONARY ANATOMICAL ARRANGEMENT

Compared to other circulatory systems, the coronary circulation has some particular features. It is uniquely designed to maintain adequate delivery of oxygen and nutrients to the organ that generates the pressure necessary to drive blood throughout the entire circulatory system. The coronary vasculature has also a special anatomical arrangement: on the one hand, the large epicardial coronary arteries serve an “obligatory” conduit function as they divide over the heart’s surface into small tributaries that penetrate into the myocardium to perfuse all the heart’s layers; on the other hand, the cardiac muscle has nearly eight times the capillary density of the skeletal muscle and the majority (approximately 70%) of the coronary vascular resistance occurs in vessels < 170 microns (μm) in diameter (Chilian et al., 1989; Tune, 2014). This renders the endocardium particularly vulnerable to ischaemia given that it is not only the furthest away from the epicardial conduit arteries, but is also subject to greater intramyocardial compressive forces and higher levels of myocardial oxygen consumption [MVO₂] (Bell and Fox, 1974). Also, the contraction of the LV generates compressive forces that affect the CBF by changing the coronary wall tension (Duncker and Bache, 2008).

2.4.2. MYOCARDIAL METABOLISM

The heart's MVO₂ is mainly determined by the HR, the myocardial contractility and the ventricular (pressure-volume) workload (Braunwald, 1971; Suga, 1990; Tune et al., 2004; Duncker and Bache, 2008). Critically, the heart has the highest per gram oxygen consumption of all organs in the body and has a limited anaerobic capacity, extracting approximately 70–80% of the oxygen delivered by the coronary circulation, under physiological “resting” conditions (Tune et al., 2004). Such limited myocardial oxygen extraction reserve renders the heart predominantly dependent on CBF to maintain normal cardiac output and blood pressure (Tune, 2014).

2.4.3. CORONARY BLOOD FLOW

From a mere physical point a view, CBF is directly proportional to the arterial pressure gradient across the coronary vasculature and inversely proportional to coronary vascular resistance (i.e. Ohm's Law of the circulation - Equation 3).

$$Q = \frac{P}{R}$$

Equation 3

Ohm's Law for electric circuits states that current (I) through an ideal conductor is directly proportional to the voltage difference between two points (ΔV) divided by resistance (R) (i.e. $I = \Delta V / R$). A simplified analogy can be used to explore the relation between blood flow (Q), pressure (P) and resistance (R).

Poiseuille further expanded these concepts by introducing determinants of vascular resistance and showing the dominant influence of vessel radius on blood flow, as expressed in his classic formula (see Figure 4). However, extending these determinants of blood flow to the heart and the coronary circulation and studying them *in vivo* is quite complex. Firstly, Poiseuille's equation assumes long, straight tubes (as blood vessels), a Newtonian fluid (e.g., water, not blood which is non-Newtonian), and steady, laminar flow conditions. Secondly, more recent evidence suggests that blood flow *in vivo* is more accurately related to the internal diameter of the resistance arterioles raised to the third power (Mayrovitz and Roy, 1983). Finally, CBF is tightly regulated by a complex variety of mechanisms including: (1) coronary perfusion pressure; (2) diastolic time fraction; (3) extravascular compressive forces; (4) local metabolic factors; (5) endothelial-derived neuro-and humoral mediators; (6) arterial

oxygen tension and content (Ardehali and Ports, 1990; Tune et al., 2004; Duncker and Bache, 2008).

Even though many different mechanisms can markedly affect myocardial perfusion, CBF to the normal heart is most closely coupled to the rate of myocardial metabolism (Tune, 2014). In practice, MVO_2 is used as a surrogate measure of the myocardial metabolism since the heart relies almost exclusively on the oxidative phosphorylation of substrates for energy production (Braunwald, 1971). We proceed to describe postulated control systems that modulate CBF to match the MVO_2 .

2.4.3.1. MVO_2 AND FEEDFORWARD-FEEDBACK CORONARY AUTOREGULATION AT REST AND STRESS

Under physiologic conditions, there is a close match between myocardial oxygen demand and supply (Tune et al., 2004), and the oxygen delivered by the coronary circulation can be defined by the product of CBF and arterial blood oxygen content (Klabunde, 2011). This match is achieved by the combined action of intrinsic and extrinsic control systems that modify the coronary resistance to ensure rapid and accurate adjustment of CBF in response to changes in MVO_2 (Miyashiro and Feigl, 1995). These postulated control systems broadly fall into two categories: those operating via a feedforward and those that acting via a feedback loop.

At the onset of exercise or other situations of stress (e.g. pain, surgery), sympathetic activation and circulating catecholamines result in a beta-adrenoceptor mediated increase in HR, blood pressure and myocardial contractility (Heusch, 2011). The resulting increase in MVO_2 (that may be as much as fivefold from the resting state) is matched by an increased CBF through metabolic coronary vasodilation (Feigl, 1983; Tune et al., 2004). A feedforward anticipative control loop has been proposed to trigger coronary vasodilation to forestall any expected myocardial oxygen demand-supply imbalance (Miyashiro and Feigl, 1995; Feigl, 1998; Gorman et al., 2000; Tune et al., 2004). By controlling both alpha and beta-adrenoceptors, the feedforward loop adjusts the proximal and microvascular coronary resistances and, possibly to some extent, the coronary vascular compliance (Feigl, 1998; Gorman and Feigl, 2012). If the activation of coronary vascular beta-adrenoceptors by neuronal and humoral catecholamines (parasympathetic) induces vasodilation, the activation

of alfa-adrenoceptors (sympathetic) results in vasoconstriction. Epicardial vasoconstriction is mostly mediated by alfa-1-adrenoceptors, while that of the resistive microcirculation is largely dependent on alfa-2-adrenoceptors and to, a minor extent, on alfa-1-adrenoceptors (Heusch, 2011).

Notably, an alfa-adrenoceptor-mediated coronary vasoconstriction at the onset of exercise/stress is a well-documented phenomenon (Feigl, 1998), although it seems rather “paradoxical” when CBF must increase to meet the large increase in MVO_2 (Heusch, 1990). Even if this sympathetic vasoconstriction is only modest, as compared to the cutaneous or skeletal muscle circulation (Mark et al., 1972), and in a normal coronary circulation under stress conditions metabolic vasodilation prevails, it competes and limits CBF increase such that myocardial oxygen extraction must also be higher to match the myocardial oxygen demand (Heusch, 2011). One proposed explanation for this alfa-adrenergic vasoconstriction is that it helps to maintain a uniform transmural CBF, particularly to the ischaemia-susceptible endocardium during exercise-induced tachycardia, by reducing systolic retrograde coronary flow (Feigl, 1987). In fact, CBF to the inner layer of the LV begins in diastole and is stopped by the large compressive forces acting on subendocardial vessels during systole (Heineman and Grayson, 1985). The tachycardia of exercise exacerbates this problem as it shortens diastole. Scaramucci first recognised the reversal of CBF during systole (retrograde flow) and the potential for the heart to limit its own blood supply by the myocardial systolic compression of the coronary vasculature (Scaramucci, 1695; Tune, 2014). However, there is no clear consensus on whether these coronary effects caused by alpha-adrenoceptor stimulation are beneficial or deleterious to the myocardial endo/epicardium flow ratio and metabolism (Heusch, 2011). In fact, available experimental studies, mostly in dogs and proof-of-concept clinical studies (Buffington and Feigl, 1983; Chilian and Ackell, 1988; Seitelberger et al., 1988), have consistently demonstrated that coronary vasoconstriction persists and contributes to myocardial ischaemia, and there is an improved subendocardial CBF with alfa-blockade (Heusch, 2011).

There is also evidence that the coronary microcirculation exhibits an heterogeneous response to adrenergic receptor stimulation so that feedforward alfa-vasoconstriction predominantly affects vessels of diameter $>100\ \mu\text{m}$, whereas feedforward beta-vasodilation occurs in vessels of diameter $<100\ \mu\text{m}$ (Chilian et al., 1989).

In addition to the feedforward loop, a feedback control system has also been proposed, responsible for monitoring and countering of any myocardial oxygen demand-supply imbalance and thus fine-tuning the feedforward loop response (Feigl, 1998). The precise physiological mechanisms underlying these control systems are poorly understood, but it is clear that they are complex, highly integrative, and non-linear, which complicates their study *in vivo* (Arthurs et al., 2016).

2.4.3.2. MODELLING THE PHYSIOLOGICAL MECHANISMS OF CORONARY BLOOD FLOW AUTOREGULATION

The coronary circulation exhibits an intrinsic tendency to maintain CBF at a constant rate, despite changes in (aortic) perfusion pressure, in order to satisfy the heart's metabolic requirements, a mechanism known as autoregulation (Crea et al., 2014). As highlighted in the previous section, the study of the physiological mechanisms of coronary autoregulation is complicated by the number of integrative pathways involved and the coupling of CBF, myocardial metabolism, aortic pressure and the peripheral vascular bed. For example, on the one hand, arterial pressure is the result of the cardiac output and the peripheral resistance, but it is also the afterload for the LV and thus an important variable determining myocardial metabolism and CBF. On the other hand, metabolic-mediated CBF is directly proportional to the arterial pressure gradient across the coronary vasculature and any perturbation of the heart and/or peripheral circulation ultimately influences CBF via alterations in cardiac workload. Since many of the integrative pathways have chronotropic and inotropic cardiac effects that alter cardiac output and myocardial metabolism, it is difficult to separate the direct action of autonomic activation on the coronary vessels from the indirect effects in coronary (aortic) perfusion pressure and local metabolic control, using only animal models.

To try to answer this conundrum, theoretical and data-based CBF regulation models have been developed since the early 1990s. More recently, multiscale 3D computational simulation has emerged as a promising tool for quantifying flow and pressure within the cardiovascular system. As we have describe, this powerful methodology may enable investigations of the coronary microcirculation that would be otherwise difficult or impossible *in vivo*, and may be used to make predictions of the adequacy of autoregulatory coronary responses to different physiological environments (e.g. exercise/stress). Over the

next sections, we review of CBF autoregulation models previously developed that provided crucial concepts to the one used in this PhD research.

2.4.3.3. PREVIOUS CORONARY BLOOD FLOW MODELS

Miyashiro and Feigl (Miyashiro and Feigl, 1995) developed a feedforward and feedback CBF control model, adopting a concept of metabolic error signal to represent the oxygen demand-supply mismatch. Their model manipulated coronary vascular resistance to maintain the balance between metabolism and flow. Importantly, they noticed that the speed and accuracy of the flow response to changes in MVO_2 could be improved by adding a stronger beta-adrenergic feedforward control or weakening the alpha-feedback control. Furthermore, a greater feedback gain increased the speed of the flow response but at the cost of higher instability, a penalty that could be addressed by including a time delay in the alpha-feedforward loop. However, Miyashiro and Feigl imposed flow directly upon the system, and their model was not designed to respond to historical oxygen supply deficits such as that occurring in reactive hyperaemia.

Dankelman *et al.* (Dankelman et al., 1989) proposed a mathematical model of CBF regulation that adjusted coronary resistance (by altering the smooth muscle tone) in response to changes in myocardial oxygen partial pressure, to study the dynamic responses of the coronary circulation to a perturbation (e.g. change in HR). The model predictions were tested in open-chest goats with cannulated left main coronary arteries. Sudden changes in HR were induced by pacing, thus introducing transients modifications in MVO_2 , and by perfusing alternately with constant pressure or constant flow. They noted that coronary resistance adjustments to changes in MVO_2 took longer to complete at high constant perfusion pressure than at low, and at constant flow, the response took longer still. In subsequent work in goats, they observed that at constant MVO_2 , step changes in pressure or flow induced a change in the coronary resistance that took longer to complete when the step was an increase as opposed to a decrease. Because their model was not able to reproduce this fast and slow coronary adjustment to a perturbation, they later refined it (Dankelman et al., 1990), and found that the intramyocardial compliance with varying venous resistance or the “vascular waterfall” model with a small compliance could explain the fast phase (Downey and Kirk, 1975). Briefly, this “vascular waterfall” model postulates that during systole, the coronary segments

downstream from the maximal resistance point are partially collapsed by the local intramyocardial pressure, which is equal to LV pressure at the endocardium, and decreases linearly to zero at the epicardium. Together with the relatively large microvascular compliance reported for the heart (intravascular volume of ~12 millilitres/100 grams), this “vascular waterfall” is necessary to explain observations of reversal of CBF (retrograde flow) and increases in coronary venous outflow during systole (Spaan et al., 1981a, 1981b). Dankelman *et al.* later observed similar dynamic responses in the coronary circulation of dogs. However, in contrast to their observations in goats, the coronary resistance adjustments in dogs were faster and the directional sensitivity of the responses to perfusion pressure or flow steps was absent (Dankelman et al., 1992).

Using a 0D model of a generic vascular bed with different compartments representing the capillaries, large and small arterioles, and venules, Arciero *et al.* (Arciero et al., 2008) performed a mechanistic study of the metabolic, myogenic, and shear stress control systems. They proposed a mechanism of flow regulation where red blood cells, acting as oxygen saturation sensors, release adenosine triphosphate (ATP), which triggered an upstream response signal leading to arteriolar dilation. They also assumed an exponential decay of the signal in the upstream direction, with a constant length of approximately one centimetre (cm). Their sophisticated model adjusted the resistances of the vessels in each compartment by adjusting their nominal diameters in response to a combination of shear, myogenic, and metabolic inputs. However, the model did not include a feedforward control and is not suitable for investigating coronary responses during high levels of oxygen demand (e.g. exercise/pharmacological stress). Nevertheless, it has confirmed prior observations that metabolic control is by far the most important mechanism and the overall determinant of CBF.

In their landmark study, Kim *et al.* (Kim et al., 2010) have designed a model for CBF control applied as a boundary condition for 3D multidomain Navier-Stokes simulations (including two LPN heart models representing the left and right sides of the heart). The model adjusted CBF in response to changes in myocardial oxygen demand. In addition, the coronary outlet boundary conditions were constructed to account for ventricular contraction through incorporation of the myocardial pressure. Although, their experiments realistically simulated temporal behaviours of the heart, coronary vascular beds, and arterial system during exercise

of healthy subjects, they have not included a feedback loop in their model, resulting in changes in myocardial oxygen demand being converted directly and, apparently instantaneously, into changes in coronary resistance.

2.4.3.4. STRUCTURAL MODELS OF THE CORONARY ARTERIES AND OF MYOCARDIAL PERFUSION

Alternatively, some researchers have created structural models of the coronary circulation. It is worth to mention the efforts of Mynard and Nithiarasu (Mynard and Nithiarasu, 2008), who have provided some insight into the interaction between the pumping performance of the ventricle, arterial haemodynamics and CBF. They have modelled the extravascular compression of the subendocardial vessels by the contracting myocardium, using a combined 0D (microvascular beds) and 1D (major conduit arteries) LPN approach, and applying a time-varying external pressure, proportional to ventricular pressure, to the distal part of the coronary vessel. Later, they further refined their approach to consider the transmural CBF distribution with a multi-layered 0D model, with different extravascular compression forces (Mynard et al., 2010), as well as different levels of coronary resistance (i.e. subepicardial, midwall, and subendocardial) (Mynard et al., 2014). They validated the multiscale coronary circulation model with high-fidelity measurements of adult sheep and newborn lambs, and using allometric scaling (a powerful technique for predicting physiological parameters over a wide range of body sizes across species or during maturation) they performed a detailed CBF waveform analysis during normal growth.

2.4.3.5. DYNAMIC CORONARY FLOW CONTROL MODEL FOR COMPUTATIONAL SIMULATIONS

Arthurs and co-workers (Arthurs et al., 2016) have recently proposed a 0D LPN coronary flow control model (CFCM) representing the mechanisms of the feedforward-feedback hypothesis described above (Figure 10). This is a model capable of dynamically adjusting the coronary resistance and could be part of a controlled boundary condition at the coronary outlets of a 3D Navier-Stokes simulation of haemodynamics. Validated using 0D-3D CFD simulation and clinical data from an adult patient, it is able to realistically reproduce the coronary haemodynamics, including the beat-to-beat CBF patterns at rest and

hyperaemia. Importantly, it has the ability to predict the expected changes in CBF during a perturbation introduced in the model (e.g. a decrease in blood pressure as occurring during PRS), a sophistication key to the main study of this thesis.

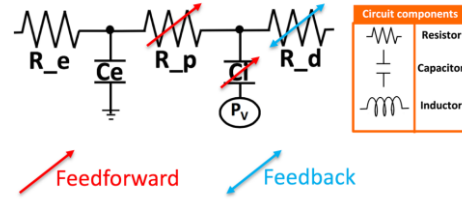


Figure 10

0D LPN model of the coronary microcirculation with the different circuit components. The extravascular compression experienced by the intramyocardial coronary vasculature is modelled by passing the ventricular pressure (P_v) to one node of the intramyocardial vessels capacitor (C_i). This capacitor, together with the epicardial (R_e), proximal (R_p) and distal (R_d) microvascular resistances experiences adjustment by the control system. The total resistance of the circuit is given by $R_e + R_p(t) + R_d(t)$ ($N \cdot s \cdot cm^{-5}$) of the circuit; this represents coronary vasoconstriction or vasodilation in the physiological system. C_e , epicardial vessel capacitor.

The proposed CFCM is based on coronary physiological observations and assumes that:

- (1) CBF closely follows myocardial oxygen demand and control oscillations that occur whenever the system is perturbed (e.g. stress/exercise);
- (2) The CBF is primarily controlled via the feedback loop, which evaluates and rapidly acts to counter any discrepancy (i.e. error signal) in myocardial oxygen demand and supply by adjusting coronary resistances;
- (3) All changes in the amount of oxygen extracted by the myocardium are solely the result of changes in CBF (i.e. coronary venous blood oxygen content and myocardial oxygen extraction per unit volume of blood delivered to the myocardium are constant);
- (4) The historical myocardial oxygen “deficit” is taken into account by the control system, so that any oxygen “debts” that may have arisen are timely “repaid”. A hypothetical concept of myocardial hunger (H) was adopted reflecting the total myocardial oxygen deficit (the error signal) derived from the mismatch in the oxygen demand-supply ratio, calculated from Equation 4 and Equation 5:

$$h(t) = MVO_2(t) - \gamma Q_{cor}(t) \quad [\text{units } (cm^3/s)]$$

Equation 4

where $h(t)$ (cm³/s), the instantaneous myocardial oxygen deficit at time $t(s)$, is the difference between $MVO_2(t)$ (cm³/s), the instantaneous myocardial oxygen demand, and $Q_{cor}(t)$ (cm³/s), the volumetric CBF and γ , the coronary-extractible blood oxygen content volume proportion, from where we derive the total myocardial oxygen deficit or $H(t)$,

$$H(t) := \int_0^t h(\tau) d\tau \quad \text{units [cm}^3\text{].}$$

Equation 5

This error signal is the basis for the feedback metabolic control loop. As the principal site of metabolic control in the coronary circulation occurs in those vessels of diameter < 100 μm (Jones et al., 1995), in the model this was assigned to the R_d component of the coronary circuit (Figure 10).

Furthermore, the model also lumps together other feedback mechanisms such as myogenic (related to changes in circumferential stress that are detected and countered by the smooth myocytes) and shear-dependent responses [related to local increases in vessel WSS that are detected by endothelial cells and signalled to the vascular smooth muscle to trigger vasodilation] (Cornelissen et al., 2002; Westerhof et al., 2006).

The combination of the two previous formulations (Equation 6) describes how the CFCM adjusts the coronary resistance to match oxygen requirements, thus acting to drive H to zero:

$$\frac{dS(t)}{dt} \bar{P}_{cor} = \underbrace{k_{fb} \gamma^{-1} H(t) + g \gamma^{-1} \frac{dH(t)}{dt}}_{\text{Feedback: Damped oscillations of myocardial hunger}} + \underbrace{\gamma^{-1} \frac{dMVO_2(t)}{dt}}_{\text{Feedforward: Oxygen demand}}$$

Equation 6

where the coronary resistance $\frac{dS(t)}{dt} \bar{P}_{cor}$ is dependent on two feedback error signals – the total historical myocardial hunger $H(t)$, and the instantaneous myocardial oxygen deficit $\frac{dH(t)}{dt}$. The constants k_{fb} and g are the feedback gain and the damping coefficient,

respectively. The premise for introducing this damping coefficient streams from prior work by Canty and Klocke (Canty and Klocke, 1985). In a dog model, they have demonstrated that following a severe drop in coronary perfusion pressure, while maintaining aortic pressure to avoid changing cardiac workload and thus changes in MVO_2 , CBF profile was that of an harmonic damped oscillator (Arthurs et al., 2016). In the CFCM, this harmonic-type control of the CBF was added to the neural feedback loop thus permitting to account for historical oxygen supply inadequacies.

In summary, the parameters dynamically adjusted in the LPN circuit are the resistances R_p and R_d . The R_p approximates the resistance of coronary vessels of diameter $>100 \mu m$ and thus experiences feedforward vasoconstriction. R_d approximates the resistance in microvessels of diameter $<100 \mu m$ and experiences both beta-feedforward vasodilation and metabolic feedback control. As there was no dynamic control model available in the literature to describe the behaviour of intramyocardial vessel compliance (C_i), this parameter was adjusted manually.

Given that the myocardial oxygen requirements are related to the cardiac workload, the MVO_2 was computed from the area enclosed by a time-varying ventricular pressure-volume (P-V) loop, in turn determined by the 0D-heart model. Although Arthurs *et al.* have applied these considerations only to the LV, the same approach could be used for the RV. In the main study of this PhD thesis (Study 6), we have added further complexity to this coronary autoregulation model to include metabolic inputs from both the LV and RV. This LPN model was part of a closed-loop 0D-3D multidomain computational simulation to investigate coronary autoregulation in an ALGS patient undergoing cardiovascular risk assessment prior to liver transplantation.

In the next Chapters we described different research subprojects conducted to support the computational modelling workflow of the main project (Study 6 – Chapter 5), from the construction of the 3D anatomical models of the aorta, pulmonary arteries and coronary vessel tree, to the material properties of the 3D domains of the PSCM, and the inlet and outlets boundary conditions:

(1) Studies 1 to 3 (Chapter 3) - developing a novel image-based navigator coronary magnetic resonance angiography (CMRA) sequence to improve coronary imaging in both adults (with coronary artery disease and CHD) and children with CHD (this sequence was

then used to acquire the high resolution anatomic data that was segmented and constituted the computational 3D domains of our PSCM);

(2) Study 4 (Chapter 4) - investigating the role of left atrial (LA) function as a biomarker of disease progression in hypertrophic cardiomyopathy (HCM) patients (the CMR-based methodology evaluated and the knowledge acquired were utilised for boundary condition specification of the atrial volumes and atrial elastance of the 0D heart LPN of Study 6);

(3) Study 5 (Chapter 4) - improving CMR-derived assessment of pulse wave velocity (PWV) by developing an algorithm for automated tracking of the aorta centreline in different sequences (this research provided knowledge and the tools used for determination of the stiffness prescribed to the 3D domains of Study 6 PSCM);

3

CORONARY MAGNETIC

RESONANCE ANGIOGRAPHY

This chapter describes the validation of a new image-based navigator CMRA technique in volunteers/adult patients with CHD (Study 1), patients with suspected coronary artery disease (Study 2) and finally in paediatric CHD (Study 3). This sequence was used to provide the high quality anatomic data that was segmented to create the 3D domains of the computational model of an ALGS child used in Study 6 (Chapter 5).

3.1. STUDY 1: 2D INAV CMRA FEASIBILITY STUDY

3.1.1. BACKGROUND

Coronary magnetic resonance angiography (CMRA) has evolved substantially since it was first reported that it could visualise the ostia of the coronary arteries in the late 1980's (Lieberman et al., 1984; Paulin et al., 1987). The first preclinical CMRA studies were published in 1993 and 1994, following the development of a new group of fast MRI pulse sequences in 1991 (Edelman et al., 1991; Manning and Edelman, 1993; Manning et al., 1993; Duerinckx and Urman, 1994). If early approaches were based on 2D breath-hold vectorcardiogram (VCG) triggered segmented sequences (Manning and Edelman, 1993; Manning et al., 1993), 3D free-breathing methods have become the standard approach as they permit larger anatomic coverage with higher signal-to-noise ratio (SNR). Initially, targeted techniques were applied by prescribing a 3D volume with the axial plane centred in the left or the right coronary arteries (LCA or RCA) origins. These were later replaced by simpler whole-heart techniques, where an axial or coronal 3D volume covering the entire heart was sampled in a single acquisition (Stuber et al., 1999b; Bi et al., 2006). This not only facilitated sequence planning but also provided a more complete anatomical coverage, particularly useful for segmental analysis of CHD.

Since these landmark works, 3D CMRA has been performed using both gradient recalled echo or gradient echo (GRE) and steady-state free precession (SSFP) sequences. GRE sequences result in more homogenous blood pool signal, but they are heavily dependent on the inflow of unsaturated protons. This effect often leads to signal loss when coronary artery flow is slow or stagnant and thus prevents accurate assessment of the coronary lumen (Nezafat et al., 2008). Conversely, SSFP sequences are relatively insensitive to inflow saturation effects and provide intrinsically higher SNR because of its balanced gradients and improved blood-myocardium contrast, in turn due to its T1/T2 weighting. As a result, SSFP has progressively become the sequence of choice for CMRA at 1.5 T (Maintz et al., 2004).

Currently CMRA is a well-established technique for the evaluation of the origin and proximal course of the coronary arteries in paediatric patients with CHD with the advantage of avoiding radiation exposure of cardiac CT and invasive angiography studies (Bunce et al., 2003; Kilner et al., 2010; Tangcharoen et al., 2011; Valsangiacomo Buechel et al., 2015). It is typically acquired during free-breathing using a VCG triggered 3D SSFP readout and a

whole-heart technique. Despite major advances in the technique, imaging the coronary arteries in children is a formidable challenge. Unlike other vascular structures, in order to obtain high quality diagnostic images of the small and relatively tortuous coronary arteries, compensation for the significant physiological motions (cardiac and respiratory) that they are subject to is of paramount importance.

Cardiac-induced motion artefacts

The first major difficulty of CMRA is related to blurring resulting from bulk cardiac motion due, on the one hand, to cardiac contraction/relaxation during the cardiac cycle, and on the other hand, to superimposed diaphragmatic and chest wall movement during ventilation.

Overall coronary artery motion is minimal during isovolumic relaxation and at mid diastole, immediately before atrial systole (diastasis). Therefore, synchronisation of acquisition with QRS detection is required to limit data sampling to the most quiescent phase of the RR interval and thus reduce scan time (Wang et al., 1999b).

To define the optimal data acquisition window a high temporal resolution cine orthogonal to the long axis of the proximal/mid RCA and of the LAD is often used, although semi-automated tools have been also developed (Jahnke et al., 2005; Sakuma et al., 2005). As the duration of the diastasis period is inversely related to the HR, the acquisition window needs to be adapted to each patient's HR/diastasis interval (Jahnke et al., 2006). In children and young adults there is another challenge: sinus arrhythmia is a frequent finding, leading to significant HR variability. This can further increase the acquisition duration and lead to image degradation (Tangcharoen et al., 2008). Real-time arrhythmia rejection algorithms have been proposed to correct for HR variability and improve CMRA image quality, but at the cost of increasing acquisition duration (Leiner et al., 2005; Roes et al., 2008).

Respiratory-induced motion artefacts

The second major challenge for CMRA is to adequately compensate for respiratory motion to reduce ghosting artefacts arising from the patient's respiratory movements. With each inspiration there is chest wall expansion and the diaphragm may descend up to 30 mm, both resulting in an anterior rotation and inferior displacement of the heart (Wang et al.,

1995). Several approaches have been proposed to minimise the impact of the patient's respiratory movements in the CMRA image quality, including sustained end-expiratory breath-holding, chest wall respiratory bellows (a belt containing a displacement transducer placed around the upper abdomen), respiratory navigators, fat navigators, and self-gating methods.

Sustained end-expiratory breath-holds were used in initial 2D CMRA methods (Edelman et al., 1991). If breath-holding approaches were simpler to implement in compliant patients, the anatomic coverage, spatial resolution and temporal acquisition window were limited by the ability of the patient to adequately sustain a prolonged apnoea (of at least 15-20 seconds). In addition, to overcome the frequent slice registration errors, related to variable end-expiratory diaphragmatic positions or diaphragmatic drift during breath-holds (Taylor et al., 1997; Holland et al., 1998), substantial image oversampling (up to fivefold) was often required to allow differentiation of gaps in vessel continuity from signal loss caused by coronary stenoses (Danas et al., 1997). This further increased acquisition duration and has precluded wider use of breath-holding approaches particularly in paediatrics.

Diaphragmatic respiratory navigators were first proposed by Ehman and Felmlee (Ehman and Felmlee, 1989) for abdominal MRI. They have been adapted for CMRA studies, with the respiratory navigator often positioned at the right hemi-diaphragm dome as shown in Figure 11 (Stuber et al., 1999c), and a 1D navigator echo, representing the superior-inferior movements of the diaphragm, tracked across the entire data acquisition. Other interfaces that accurately reflect respiratory motion (e.g. the left hemidiaphragm, the anterior chest wall, the anterior free wall of the left ventricle) have also been proposed, but the right hemi-diaphragm has become the preferred option (McConnell et al., 1997).

As respiratory induced motion of the heart is dominated by a global translation in the superior-inferior axis and is linearly correlated to the diaphragm movement, minimisation of respiratory artefacts can be achieved by tracking this interface. Wang and co-workers have observed a nearly constant linear relationship between the movement of the diaphragm and that of the heart, with a ratio between cardiac and diaphragmatic displacement of ~ 0.6 for the RCA and ~ 0.7 for the LCA at end-expiration (Wang et al., 1995). Although there is some subject variability, this offers the possibility of prospective navigator gating with real-time tracking of the lung-liver interface along the foot-head (FH) direction, and estimating

respiratory induced motion using an empirical correction factor (typically 0.6). The sequence of events is as follows: before data collection the position of diaphragm is determined and the slice position is shifted in real time to appropriately adjust the spatial coordinates; when the navigator indicates that the “interface” (i.e., diaphragm position) falls within a user-defined window, the data is used for image reconstruction, otherwise it is discarded. In summary, CMRA with real-time navigator tracking has enabled longer free-breathing acquisitions, without the time constraints imposed by breath-holding approaches, while minimising registration errors and achieving superior spatial resolution (isotropic) as well as high blood pool-to-myocardium contrast, key aspects for diagnostic CMRA (Stuber et al., 1999c).

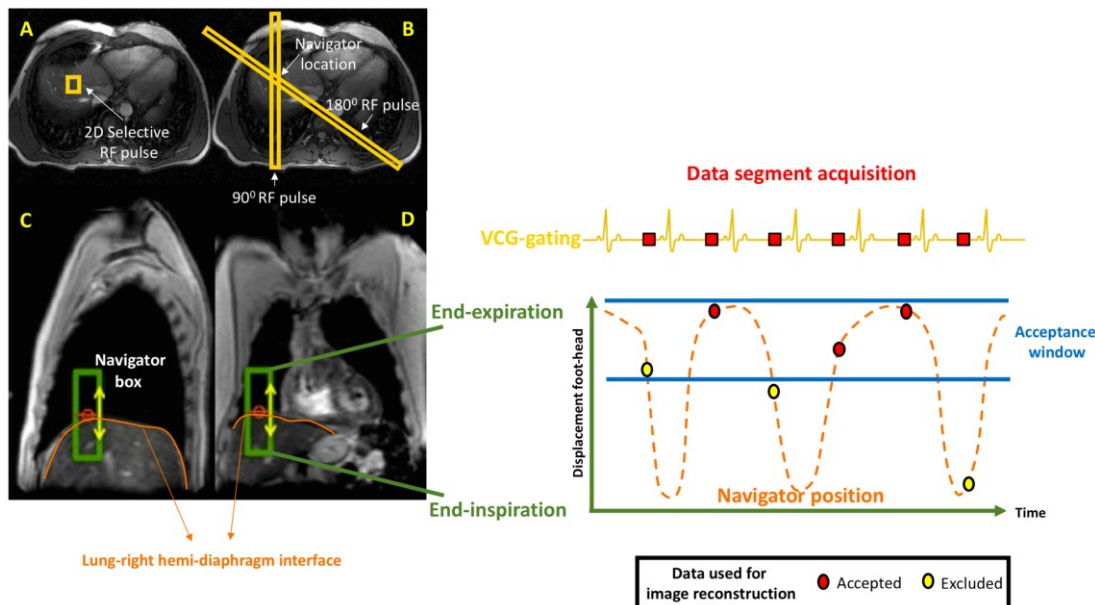


Figure 11

Vectorcardiogram (VCG) gated 3D steady-state free precession (SSFP) with a 1D respiratory-navigator (1D NAV) placed at the lung-right hemi-diaphragm interface. Planning of 1D NAV position is usually performed in an axial plane at the right-hemidiaphragm dome using either a 2D selective RF “pencil beam” excitation pulse (A) or a spin-echo approach with obliquely aligned 90° excitation and 180° refocusing RF pulses (B). The 1D NAV, with a readout in foot-head direction position is confirmed in the sagittal (C) and coronal plane (D). The 1D NAV will capture the displacement of the lung-liver interface along the foot-head direction over time and enable compensation of the respiratory induced coronary motion artefacts. The CMRA data used for image reconstruction is usually limited to the mid diastolic diastasis and the most end-expiratory position of the navigator (acceptance window). RF, radiofrequency.

Limitations of diaphragmatic 1D respiratory-navigated CMRA

If, as we have described, the use of a diaphragmatic 1D respiratory navigator allows prospective gating and slice tracking, and can reduce the respiratory motion artefacts by

assuming a “fixed” superior–inferior correction factor of 0.6 (with no left–right or anterior–posterior correction), it neglects a large inter-subject variability (Taylor et al., 1999; Keegan et al., 2002) and is susceptible to hysteresis [i.e. a certain diaphragm position corresponds to different heart positions for inspiration and expiration] (Danas et al., 1999). Moreover, due to the simplicity of the underlying 1D translational motion model, real-time tracking implementations typically require a small diaphragmatic gating windows (5 mm) that result in navigator efficiencies below 50% (Danas et al., 1997). The resulting images are often of suboptimal quality to allow accurate segmentation of the coronary tree, particularly in small children, such as those with ALGS, our subject of interest. If setting a narrow respiratory gating window allows to shorten the range of acceptable motion to end-expiration, this comes at the expenses of increasing the acquisition duration as the scan efficiency is further reduced (Oshinski et al., 1996). Such trade-off between image quality and scan efficiency can result in long scanning times, unpredictable and often non-diagnostic image quality secondary to respiratory motion artefacts. This has limited CMRA widespread clinical application for paediatric and even adult coronary imaging.

To overcome these limitations a number of refinements have been proposed: the use of multiple navigator locations (McConnell et al., 1997); the use of a subject-specific tracking factor (Moghari et al., 2012); the use of leading navigators (acquired to directly track motion due to respiration) and trailing navigators (that interpolate readings between two navigators and help to improve the accuracy of motion estimation) to enable respiratory motion compensation over a prolonged acquisition window (Wu et al., 2013); epicardial fat navigators (Nguyen et al., 2008) and the use of navigators for affine motion correction (i.e. 3D translations and rotations of the heart) that permit the use of larger navigator windows, hence higher navigator efficiency (Nehrke and Börnert, 2005). In addition to these refinements, it has also been proposed that the heart itself be tracked (Stehning et al., 2005; Lai et al., 2008; Piccini et al., 2012). These promising tools are discussed in the next sections.

Self-navigation Methods

In self-navigation methods, the respiration induced heart motion is estimated from the acquired data itself by repeatedly sampling the centre-of-mass/central k-space (Stehning et al., 2005) or by profile-shift detection (Lai et al., 2008), with no need for a heart-diaphragm

tracking factor or a 1D navigator echo. As with 1D navigator echo approaches, self-navigation methods typically perform motion correction only in the FH direction, although the signal can be spatially encoded in more than one dimension to measure respiratory motion with additional degrees of freedom. This allows to compensate for rigid (such as translational) but also non-rigid (deformation) motion of the heart (Henningsson et al., 2013). The additional implementation of advanced correction approaches applied to the respiratory cycle have further reduced the scan time, but they usually require cumbersome offline post-processing (Schmidt et al., 2011; Pang et al., 2014; Aitken et al., 2015; Cruz et al., 2017). There is another important limitation of these self-navigator techniques: signal from static structures within the excited volume can contaminate the heart motion measured in the 1D projections. For instance, chest wall motion, which displays high signal due to its proximity to the receiver coils and is different from that of the heart, can be superimposed onto the 1D projections thus reducing the precision of the navigator (Lai et al., 2008).

Image-based Navigation Methods

In response to the aforementioned problems of the self-navigation methods and to account for more complex cardiac motion, several 2D and 3D image-based navigators (iNAVs) have been developed (Gurney et al., 2007; Scott et al., 2011; Henningsson et al., 2013; Wu et al., 2013; Moghari et al., 2014; Kawaji et al., 2014; Luo et al., 2017). Image-based methods generally involve the acquisition of a low-resolution 2D or 3D image of the heart at every beat (either before or after the CMRA data acquisition), which provides real-time coordinates of the heart's position and thus improves motion estimation. Similar to self-navigation approaches, iNAV can be implemented with a much larger gating window, or it can be removed entirely, thereby increasing the scan efficiency and promising shorter and predictable scan times. But, compared to self-navigation, the major advantage of iNAV methods is the isolation of signals from the moving heart from those of the more static chest wall (Gurney et al., 2007; Scott et al., 2011). This enables respiratory-induced cardiac motion to be directly derived via (rigid or affine) image-registration of the iNAVs, at different respiratory positions, to improve motion estimation.

In contrast to most iNAV approaches so far, our research group has recently proposed a new 2D iNAV where, at every cardiac cycle, the startup profiles of the SSFP sequence,

primarily used to catalyse the magnetisation towards the steady-state, were increased and encoded to create a 2D projection of the heart (Figure 12). Compared to the 1D respiratory navigator methods previously described, our method has shown to produce a more accurate estimation of the respiratory-induced cardiac motion (Henningsson et al., 2012). Besides a higher navigator phase encoding resolution, an additional benefit of increasing the number of startup profiles in the 2D iNAV was an improvement in T2 contrast. This is a desirable effect in CMRA as it suppresses the signal from the myocardium and cardiac veins, allowing for better delineation of the coronary arteries (Shea et al., 2002; Henningsson et al., 2012).

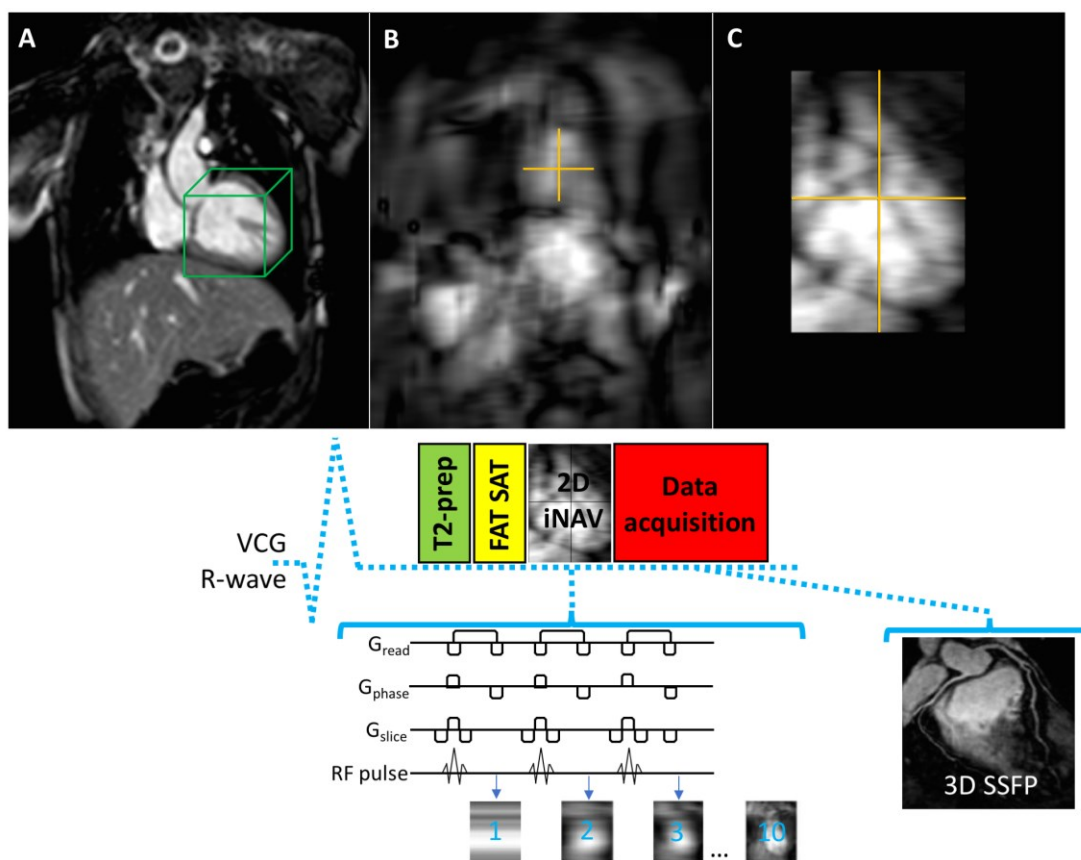


Figure 12

Diagram of 2D image-based navigator (iNAV) using the startup echoes of a 3D Steady-State Free Precession (SSFP) sequence with T2 and fat saturation (FAT SAT) pre-pulses. An iNAV region of interest (ROI) centred on the heart was defined using the local shim volume (green box, panel A) used to reduce the local magnetic field inhomogeneities. The 2D iNAV was generated by adding phase encoding gradients (G_{phase}) to the startup echoes, using a high-low profile order. The number of startup echoes produced by the radiofrequency (RF) pulses (in our study 10 startup echoes were used) was proportional to the 2D iNAV phase encoding resolution. The first acquired 2D iNAV ROI was then used as reference, to which all subsequent iNAVs were registered using normalised cross-correlation that in turn provided translational motion information. The 2D translational correction was applied to the CMRA k-space raw data by modulating its phase.

If initial *in vivo* experiments in healthy adult patients were encouraging (Henningsson et al., 2012), the 2D iNAV was still limited to translational motion correction in two directions (FH and left-right, LR). Therefore, we hypothesise that the addition of respiratory gating could help to minimise respiratory artefacts from non-homogeneous 3D heart motion that occurs between end-expiration and end-inspiration (Shechter et al., 2003). Furthermore, since the navigator was acquired with a rectilinear (Cartesian) sampling scheme of the k-space and used a fast registration algorithm, it could be implemented with a prospective inline motion correction.

In this study, we proposed to test the feasibility of a 2D iNAV CMRA sequence with inline correction and respiratory bellows gating and assess whether it can improve image quality compared to the conventional 1D NAV CMRA, prone to unpredictable scan durations and low gating efficiency as described before. This “conventional” free-breathing 3D whole-heart CMRA sequence has been used in our institution for the segmental analysis of cardiovascular morphology of CHD patients. It is also part of the protocol of a pioneer XMR cardiac catheterisation program developed by Razavi and co-workers (Razavi et al., 2003; Muthurangu et al., 2004; Pushparajah et al., 2015). Performed in a specially designed hybrid suite, such XMR studies combine X-ray and CMR guided cardiac catheterisations in a single procedure allowing simultaneous acquisition of invasive pressures and CMR derived anatomy, ventricular function and quantification of flow. If image quality could be improved, this seemed the ideal approach to acquire the high quality anatomic data (i.e. of the aorta, its major branches, the coronary and central pulmonary arteries), as well as the detailed invasive pressure and flow measurements required to inform Study 6 computational framework for CBF analysis (Chapter 5).

3.1.2. MATERIAL AND METHODS

3.1.2.1. CMR IMAGING PROTOCOL

Healthy Volunteers Cohort

To test the feasibility and usefulness of the new 2D iNAV with inline correction and respiratory bellows gating, we first scanned nine healthy adult volunteers (mean age of 32 ± 6 years, seven male and two female) with no general contraindications to CMR. For each

volunteer, one 1D NAV scan and two 2D iNAV scans, one without (iNAV_C) and one with bellows gating (iNAV_{C+G}) were randomly acquired.

All experiments were performed on a Philips Achieva 1.5 Tesla clinical CMR scanner (Philips Healthcare, Best, The Netherlands) using a 32-channel receiver coil. The CMRA employed in the three navigator strategies consisted of a whole-heart 3D SSFP sequence used in our institution to obtain morphological information for segmental analysis in adult patients with CHD. It includes T2 preparation pre-pulses and fat suppression, and is acquired in a coronal orientation with a readout in the FH direction, a LR phase encoding direction and an anterior-posterior (AP) slice encoding direction. The following parameters were used: repetition time/echo time (TR/TE) = 3.7/1.86 milliseconds (ms), flip angle = 70°, field-of-view (FoV) = 320 x 320 x 120 mm³, acquired isotropic spatial resolution = 1.5 x 1.5 x 1.5 mm³, parallel imaging acceleration (SENSE) factor of 2. The data acquisition was synchronised with the VCG to coincide with the most quiescent cardiac phase. The optimal cardiac rest-period was determined from an axial high-temporal resolution four-chamber cine scan acquired prior to the CMRA scan. Single-phase studies were acquired and the longest rest period of the heart coinciding with the late-systolic or diastolic-phase images was determined primarily by evaluating the movement of the right coronary artery (RCA) in the atrio-ventricular groove as described before (Sakuma et al., 2005). A diaphragmatic tracking factor of 0.6 was used in conjunction with a fixed 6 mm end-expiratory respiratory gating window.

With regard to the 2D iNAV, ten startup echoes were used to generate the heart projection images in each cardiac cycle. This resulted in a phase encoding resolution of 9.6 mm.

Adult Congenital Heart Disease Patients Cohort

We then prospectively recruited patients who underwent a whole-heart 3D SSFP CMRA scan using a conventional 1D NAV as part of their clinical examination. An additional CMRA scan was acquired using the proposed 2D iNAV approach with respiratory bellows gating. The order of the two CMRA scans was randomised for each patient.

Both studies were approved by the institutional ethics committee and written consent was obtained from all participants.

3.1.2.2. DATA ANALYSIS

Healthy Volunteers Cohort

To assess the usefulness of the respiratory bellows in each healthy volunteer we compared the position of the two 2D iNAV CMRA scans, the acquisition duration and the resulting coronary image quality.

The CMRA scan acquisition duration was retrospectively measured using the scanner log file. For the quantitative assessment of the coronary arteries, each dataset was reformatted using a dedicated and validated software ["Soap-Bubble", Philips Medical Systems, Best, The Netherlands] (Etienne et al., 2002; Makowski et al., 2011). This custom-made validated tool facilitates multiplanar reformats of CMRA datasets, while also providing vessel length and diameter for objective quantitative comparison (see Figure 13). Furthermore, the local vessel wall sharpness (VWS), an objective metric of the quality of the vessel wall visualisation, can be obtained by means of a Deriche filtering algorithm for edge detection (Deriche, 1990). This algorithm calculates the local magnitude change in signal intensity of the vessel wall using a first-order derivative of the input image. To facilitate interpretation of the results, this is then provided as single VWS value normalised for the entire vessel path (a higher percentage of magnitude change at the edge is consistent with a superior sharpness). This algorithm is also the basis of the semi-automated vessel-tracking tool that enables the user to identify the vessel borders of the specified coronary segment.

For the qualitative assessment, two observers, blinded to the motion correction method used, independently reviewed the proximal RCA, left anterior descending artery (LAD), and left circumflex artery (LCX) of each dataset and scored the CMRA images, according to Table 2 criteria.

Qualitative score	Coronary Images
0	Uninterpretable visualisation due to excessive motion artefacts
1	Poor visualisation with severe motion artefacts
2	Good visualisation with moderate motion artefacts
3	Very good visualisation with mild motion artefacts
4	Excellent visualization with no motion artefacts

Table 2
CMRA images qualitative score.

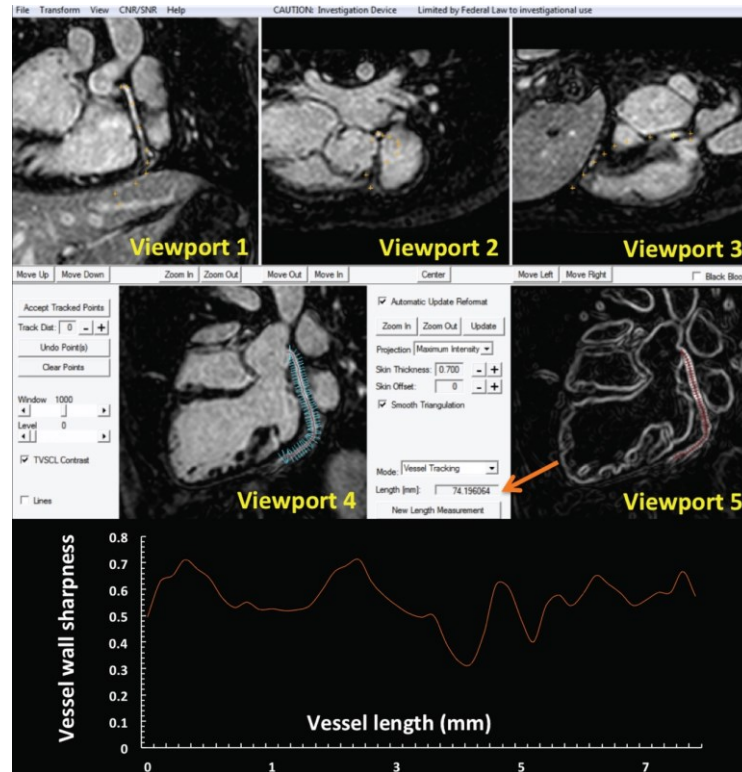


Figure 13

Soap-Bubble user interface. A reformatted CMRA image is generated (viewport 4) after manually tracking in three orthogonal views (viewports 1 to 3) the coronary artery path (yellow crosses). The vessel length is measured along the user-specified points in the reformatted coronary artery as described by Etienne A *et al.*

Adult Congenital Heart Disease Patients Cohort

We compared the acquisition duration and the coronary image quality (quantitative and qualitative parameters, as detailed for the healthy volunteer study) for both the conventional 1D NAV and the 2D iNAV_(C+G) CMRA scans.

3.1.3. RESULTS

Healthy Volunteers Cohort

The acquisition duration of the 2D iNAV_C and the 2D iNAV_{G+C} CMRA scan was 4.43 ± 0.37 and 7.30 ± 1.01 minutes, respectively ($p < 0.05$). While on average the use of respiratory bellows gating increased the scan time by a factor of approximately 1.6, it reduced the amount of extreme respiratory positions in most volunteers. The average total displacements for the 2D iNAV_C was 7.2 ± 5.6 mm and 5.2 ± 3.7 mm for the 2D iNAV_{G+C}

($p < 0.05$). Plots of the measured FH and LR displacements for 2D iNAV_C and 2D iNAV_{G+C} scans for all volunteers recruited are shown in Figure 14.

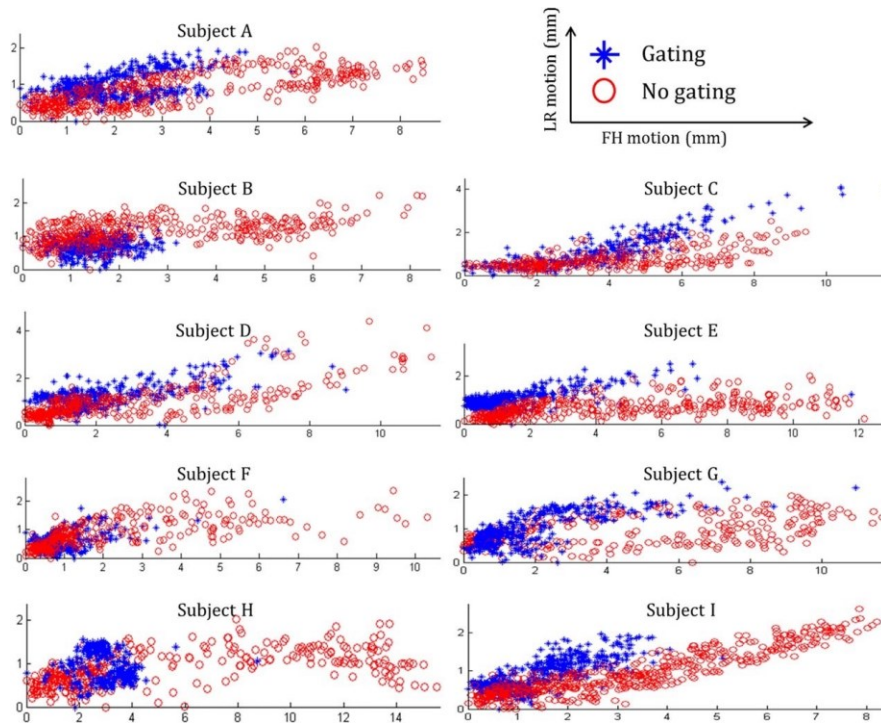


Figure 14

Respiratory motion in foot-head (FH) and left-right (LR) direction as measured by the 2D iNAV for all nine subjects (A-I) with (blue data points) and without (red data points) respiratory bellows gating. The 2D iNAV values have been normalised such that end-expiration occurs at position 0 and inspiratory positions have positive values. The same number of data points (accepted shots) was obtained for both scans.

The average VWS and visual scores for the different coronary arteries obtained using the different motion compensation approaches are detailed Table 3.

	Coronary	2D iNAV _C	2D iNAV _{G+C}	<i>p</i> value
VWS	LAD	57.3 ± 8.2	61.7 ± 6.3	<0.05
	LCX	55.5 ± 7.8	61.5 ± 5.3	<0.05
	RCA	70.1 ± 4.9	67.15 ± 5.3	0.23
Visual Score (median / 25 th / 75 th)	LAD	3 / 4 / 2	4 / 4 / 3	<0.05
	LCX	2 / 3 / 2	3 / 4 / 3	<0.05
	RCA	3 / 4 / 3	4 / 4 / 3	0.05

Table 3

Healthy volunteers CMRA vessel wall sharpness (VWS) quantitative results (mean ± standard deviation) and visual score qualitative results (median, 25th and 75th percentiles).

Adult Congenital Heart Disease Patients Cohort

Thirty adult patients with CHD (mean age of age 28 ± 9 years, 18 male and 12 female) were prospectively recruited. In one patient the CMRA scan was aborted due to extremely low scan efficiency of the 1D NAV (less than 15% of the data within the respiratory gating window). In the remaining 29 patients (97%) CMRA was successfully acquired and these were included in the final analysis. The main diagnosis of the patients included in the study is summarised in Table 4.

Diagnosis	N° of patients (N=29)
Aortic coarctation	7
Tetralogy of Fallot	4
Bicuspid aortic valve	3
Transposition of great vessels	3
Ventricular septal defect	2
Ebstein's anomaly	2
Pulmonary autograft replacement	2
Fontan procedure	2
Anomalous pulmonary vein	1
Valve replacement	1
Dilation of the ascending aorta	1
Patent ductus arteriosus	1

Table 4
Main clinical diagnosis.

Three patients (10%) had congenital anomalies of the coronary arteries, including one case of dual LAD supply, one with a left main originating from the RCA ostium and one with a LAD arising from the RCA ostium (Figure 15). Representative coronary reformats from three patients are shown in Figure 16.

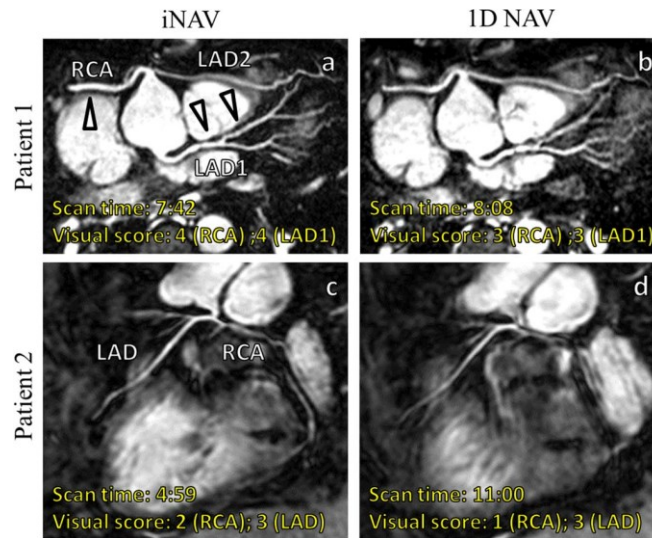


Figure 15

Reformatted whole-heart CMRA images acquired with the 2D image-based navigator (iNAV) and the conventional 1D diaphragmatic navigator (1D NAV) from a 32-year-old man with a type IV dual left anterior descending (LAD) coronary artery (**panels a and b**); and a 24-year-old female with situs inversus, dextrocardia and aortic coarctation, with an anomalous origin of the LAD from the RCA ostium (**panels c and d**). Arrows highlight coronary segments with improved visualisation. LAD, left anterior descending artery. RCA, right coronary artery.

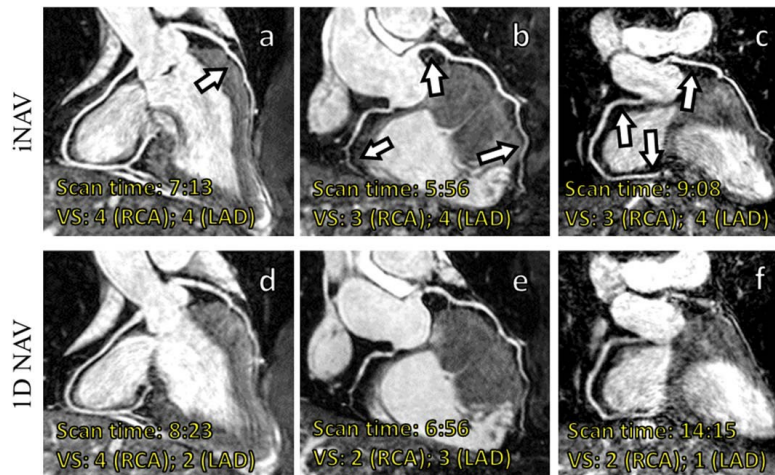


Figure 16

CMRA from three patients using the 2D image-based navigation (iNAV) and the diaphragmatic navigator (1D NAV): 24-year-old male with bicuspid aortic valve (**panels a and d**), 40-year-old male with aortic coarctation (**panels b and e**), 26-year-old male with pulmonary autograft replacement (**panels c and f**). Arrowheads highlight coronary segments with improved visualisation. LAD, left anterior descending artery. RCA, right coronary artery. VS, visual score.

The average scan acquisition duration was 7.57 ± 1.34 minutes for the 2D iNAV_{G+C} and 9.15 ± 3.02 minutes for the 1D NAV ($p < 0.01$). Compared to the 1D NAV approach, the proposed 2D iNAV_{G+C} reduced CMRA scan duration in the majority of the patients

(75%). In five patients (18%) with irregular breathing, acquisition duration was reduced by more than 5 minutes.

Mean values and standard deviation for the VWS, as well as the median, 25th and 75th percentiles for the visual score, for both navigator approaches are shown in Table 5. The 2D iNAV_{G+C} resulted in improved VWS in both RCA ($p < 0.05$) and LAD ($p < 0.05$) but not in the LCX ($p = 0.17$).

	Coronary	1D NAV	2D iNAV _{G+C}	<i>p</i>
VWS	LAD	58.3 ± 9.5	63.2 ± 6.7	<0.05
	LCX	54.0 ± 8.6	57.0 ± 7.6	0.17
	RCA	60.2 ± 11.4	65.3 ± 6.6	<0.05
Visual Score (median / 25th / 75th)	LAD	3 / 2 / 3	3 / 3 / 4	<0.001
	LCX	3 / 2 / 3	3 / 2 / 4	0.07
	RCA	3 / 3 / 4	4 / 3 / 4	<0.001

Table 5

Quantitative (mean ± standard deviation) and qualitative results (median, 25th and 75th percentiles).

There was high inter-observer correlation ($r=0.9616$; $p < 0.0001$) and agreement for the VWS measurements (Figure 17), with an average difference of 0.37% (95% confidence intervals of 4.42 to 5.16).

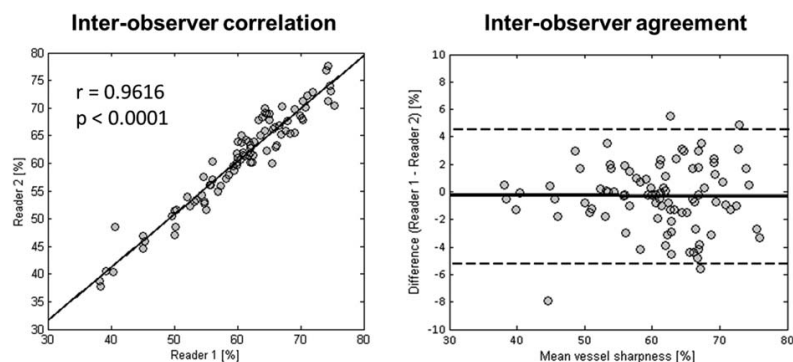


Figure 17

Inter-observer variability of coronary vessel wall sharpness (VWS) measurements. The inter-observer correlation was high ($r=0.9616$; $p < 0.0001$), with a good inter-observer agreement (average difference of 0.37% with a 95% confidence interval of 4.42% to 5.16%).

3.1.4. DISCUSSION

In this feasibility study, we evaluated a novel image-based navigation approach together with conventional respiratory bellows gating. The preliminary results in healthy volunteer demonstrated the usefulness of respiratory bellows gating in combination with the 2D iNAV algorithm to improve coronary image quality, at the expense of increasing the CMRA acquisition time. The use of respiratory bellows gating reduced the amount of measured respiratory motion, except in one volunteer, where significant respiratory drift was noticed. This exemplifies a common cause of failed or aborted CMRA scans when using the conventional 1D NAV approach, due to the insensitivity of the bellows gating to respiratory drift.

We then compared the performance of the 2D iNAV in combination with bellows gating to the conventional diaphragmatic navigator (1D NAV), with a fixed 6 mm gating window and a tracking factor of 0.6, in 29 adult patients with known CHD. The proposed 2D iNAV approach resulted in improved image quality (both in terms of subjective qualitative as well as objective quantitative measurements) in the LAD and RCA, compared to the conventional 1D NAV. Interestingly, lower SNR was seen in the LCX. Together with the RCA, this artery is subject to greater motion displacement during the cardiac cycle (Schmidt et al., 2009), particularly at high HRs. However, compared to the RCA, the LCX is often of smaller calibre (Li et al., 1995) and at a larger distance from the receiver coil, which could explain our results. Importantly, this improvement in coronary imaging quality using the 2D iNAV approach was attained with a concomitant reduction in the scanning duration.

A further important advantage of the 2D iNAV method compared to the 1D NAV was that no dedicated scan planning was required for the navigator acquisition, thereby simplifying the CMRA scan preparation. The improved performance and ease-of-use of the 2D iNAV could help streamline CMRA so that it is included in clinical CMR protocols together with cines, tissue characterisation and ischaemia assessment. The use of this technique may also benefit the diagnostic performance of CMRA to detect significant coronary artery disease (CAD), although this was not assessed in this study.

In recent years, there has been an increased interest in self-navigated (Piccini et al., 2012; Pang et al., 2014) and image-based respiratory navigation (Henningsson et al., 2012; Wu et al., 2013; Moghari et al., 2014; Aitken et al., 2015) for whole-heart CMRA. However,

most available evidence has been limited to small studies in healthy subjects. The use of 1D self-navigation has recently been reported in 105 patients (55% male; mean age 23 ± 12 years) with CHD (Monney et al., 2015). Although no head-to-head comparison with the 1D NAV approach was made, the reported success rate of 1D self-navigation ($>90\%$ scans with diagnostic quality) compared favourably with the conventional approach (Sørensen et al., 2004; Hussain et al., 2012). In our study, a direct comparison between 2D iNAV and the conventional 1D NAV was made and clearly demonstrated improved image quality and scan efficiency with the former approach. Compared with the 1D self-navigation approaches, the proposed 2D iNAV has two main advantages: it avoids “contamination” by signal from static surrounding thoracic structures that may be included in the FoV; it also enables correction of respiratory motion in the LR direction.

3.1.5. LIMITATIONS

We acknowledge a number of limitations of this study. The small number of patients precluded any analysis on the ability of the proposed approach to improve diagnosis or add clinically relevant information about the underlying CHD. We have used a 6 mm gating window for the 1D NAV method, which is slightly larger than the 5 mm window normally adopted. The spatial resolution was also lower (1.5 mm^3 isotropic) compared with conventional CMRA, when the aim is to detect coronary stenosis (approximately $1\text{--}1.3 \text{ mm}^3$). However, in our institution, these were the standard settings for whole-heart imaging in patients with CHD and provided a good trade-off between image quality (when the primary interest is the visualisation of the great vessels and the course of proximal coronary arteries) and scanning time.

As respiratory gating could not be performed with the 2D iNAV (i.e., labelling measured k-space data as accepted or rejected), external respiratory bellows signal was used to this end. This was due to the limitation of one-way communication between the spectrometer and reconstruction computer. Thus, all acquired data (including 2D iNAV and 3D CMRA) was sent to the reconstruction computer and used for image reconstruction. As a further consequence, arrhythmia rejection was incompatible with the implemented 2D iNAV, an option that may be particularly important for image-based navigation as the motion is measured on the heart and arrhythmic events may be erroneously interpreted as respiratory

motion. However, an advantage of using respiratory bellows to perform the gating is that the scan becomes less sensitive to respiratory drift, a common source of low gating efficiency and aborted scans in the 1D NAV with a fixed gating window.

Additionally, currently, the respiratory motion correction implemented can only be performed in the FH and LR direction, and AP motion is thereby neglected. AP motion has been shown to be substantial in many studies, and is often cited as larger than LR motion. Respiratory gating may be used to effectively minimise AP motion artefacts. Alternatively, the need for respiratory gating may be removed altogether by incorporating advanced correction strategies [e.g. affine (Pang et al., 2014; Henningsson et al., 2014) or non-linear correction (Schmidt et al., 2011)] in an inline implementation, but at the cost of complex and computationally intensive post-processing steps. In contrast, the post-processing of the proposed 2D iNAV methodology can be performed in real-time, with no additional user interaction.

3.1.6. CONCLUSIONS

In this preliminary work, we have shown the feasibility of image-based respiratory navigation with bellows gating for CMRA. Compared to the conventional diaphragmatic navigator, the proposed methodology resulted in improved CMRA image quality in a small sample of healthy volunteers and adult patients with CHD, while significantly reducing scan time (Henningsson et al., 2016).

3.2. STUDY 2: 2D iNAV CMRA IN CORONARY ARTERY DISEASE PATIENTS

3.2.1. BACKGROUND

In addition to its role in CHD, CMR is also a comprehensive and well-established diagnostic and prognostic tool in ischaemic heart disease, allowing, in a single study, qualitative and quantitative assessment of both global and regional myocardial contraction, inducible ischaemia and fibrosis/necrosis (von Knobelsdorff-Brenkenhoff and Schulz-Menger, 2012, 2015). Furthermore, whole-heart CMRA has been shown to have a high negative predictive value thus being a good diagnostic tool to rule out significant CAD (Kato

et al., 2010). A combined coronary artery imaging, myocardial perfusion and late gadolinium enhancement (LGE) study is thus an attractive non-invasive, ionising radiation free first-line test and a gate keeper for invasive X-ray coronary angiography (Klein et al., 2008; Assomull et al., 2011).

In practice, and in spite of substantial technological advances, the clinical use of CMRA for the detection of CAD remains limited. Two of the most important limiting factors are long and unpredictable acquisition times resulting in image degradation (e.g. coronary blurring and ghosting artefacts), and relatively low spatial resolution when compared to CT and invasive angiography (Danas et al., 2004; Yang, Q, et al., 2009; Henningsson et al., 2013).

By directly tracking the respiratory motion of the heart, our recently developed 2D iNAV approach could reduce the acquisition time as it increases the accuracy of respiratory heart motion estimation (Henningsson et al., 2012, 2016). Furthermore, it reduces operator dependence as it does not require any dedicated respiratory navigator scan planning and could be implemented with inline correction for efficient respiratory gating (Henningsson et al., 2018). As a result, higher spatial resolution and/or slab coverage could be achieved in a clinically acceptable time.

In this study, we have evaluated the diagnostic performance of the 2D iNAV CMRA used in Study 1, together with constant respiratory efficiency using single end-expiratory threshold (CRUISE) motion compensation, to rule out significant CAD by comparing its results with the gold standard invasive X-ray coronary angiography.

3.2.2. MATERIAL AND METHODS

3.2.2.1. STUDY POPULATION

Consecutive patients referred for CMR were considered for inclusion in this prospective pilot study. Patients were excluded if they had: (1) any implanted cardiovascular electronic device over the region of interest (even if CMR conditional) that could cause any susceptibility artefact and reduce image quality; and (2) any contraindication to adenosine (e.g. known or suspected moderate to severe bronchoconstrictive or bronchospastic lung disease) or to gadolinium contrast agent (e.g. severe renal failure with an estimated

glomerular filtration rate < 30 millilitres/minutes/ m^2). The study was approved by the local institutional ethics committee and all participants provided written informed consent.

3.2.2.2. CMR IMAGING PROTOCOL

All experiments were performed on a 1.5 Tesla clinical CMR scanner (Achieva, Philips Healthcare, Best, The Netherlands) using a 32-channel receiver coil. The protocol consisted of multi-slice cine stack in short and long-axis, first-pass stress and rest perfusion, multi-slice LGE stack in short and long-axis and the 2D iNAV CMRA. The contrast medium (gadobutrol, Gadovist®, Bayer AG, Leverkusen, Germany) was administered by bolus injection (0.1 ml/kg) at the time of the stress and rest perfusion as described before [total dose of 0.2 ml/kg] (Kramer et al., 2013). The CMRA acquisition was performed after the rest perfusion acquisition, to avoid the higher HR immediately following the stress scan, and before the LGE sequences. No specific patient preparation was performed for the CMRA scan, such as administration of beta-blockers to reduce the HR or nitroglycerin to dilate and thus improve coronary visualisation.

The CMRA consisted of a VCG-triggered whole heart 3D SSFP sequence acquired in coronal orientation to exclude the chest wall and minimise respiratory motion artefacts. The following imaging parameters were used: isotropic spatial resolution with an acquired voxel size of $1.3 \times 1.3 \times 1.3$ mm³, TR/TE = 3.9/1.95 ms, flip angle = 70°, and parallel imaging acceleration factor (SENSE) = 2.5 (in-plane phase encoding direction). Subject-specific trigger delays and acquisition windows were used to minimise cardiac motion as described before (Sakuma et al., 2005). To improve CMRA blood-to-myocardium contrast, T2 (TE = 35 ms) and fat suppression pre-pulses were used.

The 2D iNAV was acquired using ten startup echoes of the SSFP sequence, as previously described (Henningsson et al., 2012). The geometry shim box, used to improve the magnetic field homogeneity, was also utilised to define the region of interest (ROI) encompassing the entire heart. This ROI was then tracked in the FH and LR directions and the first acquired navigator served as a reference to which all subsequent 2D iNAVs were registered, using normalised cross-correlation. A 2D translational motion correction was applied to the CMRA k-space raw data by modulating its phase. In addition, a CRUISE motion compensation was implemented (Henningsson et al., 2018) for inline respiratory

gating, by estimating the respiratory induced heart motion directly from the 2D iNAV. This algorithm aims to ensure that the CMRA segmented k-space is acquired in the most end-expiratory positions, where its longer duration and lower diaphragm velocities are associated with higher scan efficiency (Taylor et al., 1997). It assumes a fixed gating efficiency of 50%, resulting in half of the acquired data being discarded and re-measured. The measured respiratory positions in the FH direction are then added to a sorted list in which high values correspond to end-expiration and low values correspond to end-inspiration. In the first half of the acquisition, all the CMRA data is stored and the sorted list is populated. During the second half of the acquisition, the CMRA k-space segment associated with the lowest value (end-inspiration) is discarded and re-measured. In addition, the algorithm discards any measured position outside the temporary gating window and re-measures it over the following cardiac cycle. The result is a gradual narrowing of the accepted respiratory motion range as an increasing number of CMRA k-space segments are acquired closer to end-expiration. The 2D iNAV correction and gating were performed in real-time on the scanner, with no additional post-processing required. A simplified example of the CMRA acquisition using the CRUISE gating algorithm is illustrated in Figure 18 (Henningsson et al., 2018).

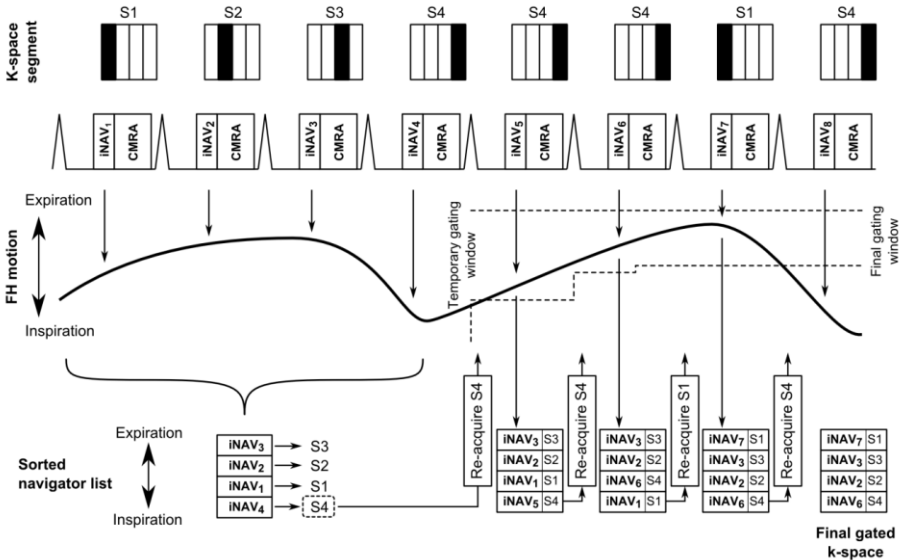


Figure 18

Proposed respiratory gating algorithm (CRUISE) for CMRA acquisition consisting of four k-space segments (S1-4). During the first half of the scan the image-navigators (iNAV) positions are added to a sorted list based in the foot-head (FH) motion of the heart, from expiration to inspiration, each iNAV associated with a k-space segment. During the second half of the scan, the k-space segment associated with the most inspiratory iNAV is re-measured, and the new iNAV position is added to the sorted list if within the temporary gating window. This

gating window is defined by the most inspiratory iNAV position in the sorted list. This results in a gradually narrowing of the temporary gating window as all expiratory iNAVs are obtained and added to the sorted list. If the re-measured iNAV position is outside the gating window, as in the last cardiac cycle, the k-space segment is ignored.

3.2.2.3. DATA ANALYSIS

All CMRA datasets were reformatted using a dedicated software ("Soap-Bubble", Philips Medical Systems, Best, The Netherlands) (Etienne et al., 2002; Makowski et al., 2011). Segmentation of the visualised RCA, LAD, and LCX was performed in order to objectively and subjectively assess CMRA image quality using VWS measurements and a visual score.

VWS was calculated for the first 4 cm of all coronary arteries. VWS was assessed by an expert for the entire patient data. On 10 randomly selected datasets, three months later, VWS was re-assessed by the same expert to establish the intra-observer variability. A second expert performed VWS measurements on 10 randomly selected patient datasets to evaluate inter-observer variability.

The visual score used to assess the image quality of each coronary artery segment (Table 6) was based on Kim *et al.* study (Kim et al., 2001) assessing the diagnostic performance of CMRA in a cohort of adult patients with suspected CAD scheduled for invasive X-ray coronary angiography. The nine coronary segment model used in previous CMRA studies was adopted (He et al., 2016), with the following segments individually scored: the left main (LM) artery; the proximal, mid and distal LAD; the proximal and mid LCX; the proximal, mid and distal RCA. The visual scoring was performed independently by two experts, blinded to the patient's clinical information and the invasive X-ray coronary angiography results. A visual score of 2 or higher was considered of diagnostic quality. Coronary segments were excluded from the analysis if they had stents or if the diameter was less than 1.5 mm. Significant coronary stenosis was visually defined as a luminal narrowing of more than 50% in each of the nine segments described. Disagreements between the two readers were settled with a consensus reading. The findings from the diagnostic reading of the coronary segments were compared to the gold standard invasive X-ray coronary angiography that was performed within six months of the CMRA scan. Diagnostic performance of the CMRA was assessed using an intention-to-treat approach, with the likelihood of stenosis graded according to the following scale: 1 – absent, 2 – probably

absent, 3 – possibly present, 4 – probably present and 5 – definitely present (Kato et al., 2010).

Qualitative score	Coronary Images
0	Coronary artery not visible
1	Coronary artery visible but with marked blurring
2	Coronary artery visible with moderate blurring
3	Coronary artery visible with mild blurring
4	Coronary artery visible with sharp edges

Table 6
Visual score used to assess CMRA image quality.

3.2.2.4. STATISTICAL ANALYSIS

All statistical analyses were performed using MATLAB (The Mathworks Inc., Natick, MA USA) statistics toolbox. Continuous variables are presented as mean \pm standard deviation, while categorical variables are presented as median, 75th percentile, 25th percentile. For the continuous variables (VWS and acquisition time) a two-tailed Student's *t*-test was performed to evaluate statistical significance. For the categorical variable (visual score) a Wilcoxon signed rank test was performed to evaluate statistical significance. A *p* value smaller than 0.05 was considered statistically significant.

Inter-observer agreement for the visual scores was performed using Cohen's kappa coefficient: poor agreement if < 0.4 , good agreement if ≥ 0.4 and $0.75 \leq$, and excellent agreement if > 0.75 . In addition, the mean difference and standard deviation for continuous variables were calculated to assess the intra and inter-observer variability.

The different coronary segments were grouped into proximal (LM, proximal LAD, LCX and RCA), middle (middle LAD, LCX and RCA) and distal (distal LAD and RCA) to enable comparison of the visual scores according to the vascular territory. This analysis was performed through a Kruskal-Wallis one-way analysis of variance. If a statistically significant difference was found, *post hoc* multiple Mann Whitney U tests were performed with a $p < 0.017$ considered statistically significant due to the Bonferroni correction for multiple comparisons ($0.05/3 = 0.017$).

To evaluate whether patient variables such as age, HR, and body mass index (BMI) were correlated with VWS, a bivariate analysis was performed. A linear regression model was constructed, and the Pearson's correlation coefficient calculated to investigate if these

variables could predict coronary VWS. The coronary VWS was averaged across the RCA, LAD and LCX for each patient to obtain a single value.

3.2.3. RESULTS

A total of 31 consecutive patients were recruited for the study. Relevant clinical characteristics are summarised in Table 7.

Characteristics (N=31)	
Age (years)	56.4 ± 14.7
Gender	24 (77.4%)
Average heart rate	66.4 ± 10.9
BMI (kg/m ²)	27.3 ± 4.0
Coronary risk factors	
Hypertension	17 (55.8%)
Hyperlipidaemia	13 (41.9%)
Smoker	10 (32.2%)

Table 7

Patients characteristics. Kg, kilograms. M, meters.

In total, out of a possible 279 coronary segments, 26 segments (8 proximal, 9 middle and 9 distal segments) were excluded due to stents (N=8) or diameter less than 1.5 mm (N=18), resulting in a total of 253 coronary segments analysed (example of an excluded patient is shown in Figure 19).

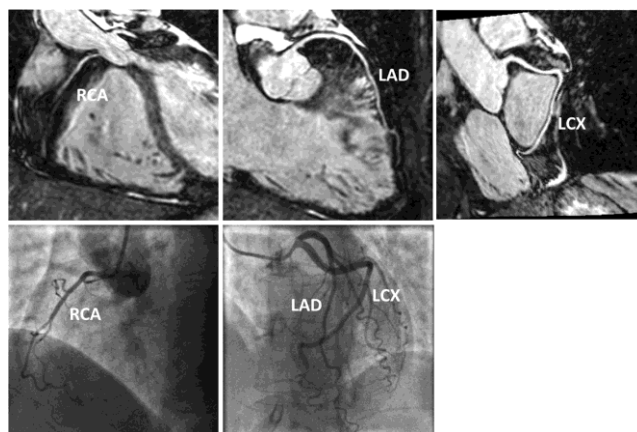


Figure 19

CMRA datasets from a patient with no obstructive coronary artery disease (CAD) but a non-dominant right coronary artery (RCA) precluding analysis of mid and distal segments of the vessel. Corresponding invasive

X-ray coronary angiography from the same patient is also shown for illustrative comparison (bottom row). LAD, left anterior descending artery; LCX, left circumflex artery.

The CMRA acquisition duration for the 31 patients was 7.21 ± 0.28 minutes. In the majority of cases (N=25, 81%), a diastolic CMRA acquisition was performed: average HR of 63 ± 15 beats per minute (bpm); acquisition window of 118 ± 38 ms; imaging time of 7.13 ± 0.18 minutes. In the remaining (N=6, 19%), a systolic acquisition was done: average HR of 78 ± 12 bpm; acquisition window of 85 ± 22 ms; imaging time of 8.30 ± 0.33 minutes.

3.2.3.1. CMRA IMAGE QUALITY

The distribution of the qualitative visual scores of the different 253 coronary arteries segments (proximal, mid and distal) is shown in Figure 20. Diagnostic image quality, defined as having a visual score of ≥ 2 , was obtained in 98% of all proximal coronary segments (113/115), 94% of middle segments (79/84), and 91% of distal coronary segments (49/54). The majority (75%) of the total non-diagnostic segments occurred in two patients that had significant arrhythmia throughout the CMRA acquisition. In these two cases, non-diagnostic image quality was found in 9 out of 18 coronary segments.

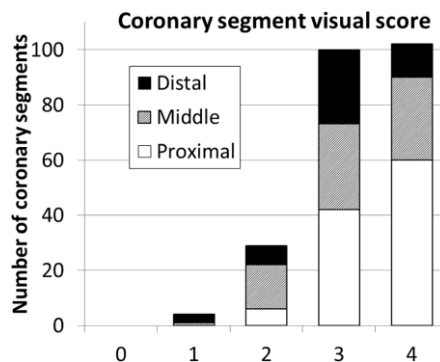


Figure 20

The visual scores (0-5) attributed to each coronary segment (proximal, mid and distal) of the entire study cohort are presented. A score of 0 was considered a non-visible coronary segment, while at the other end a score of 5 represented a visible segment with sharp edges. Visual scores of 2 or higher were considered to be of diagnostic image quality. As the graph shows, there were no proximal or mid coronary segments with non-diagnostic image quality.

The Kruskal-Wallis test, comparing the distributions of the visual scores for the proximal, middle and distal coronary arteries segments, revealed a statistically significant difference ($p < 0.01$). A *post-hoc* analysis using the Mann-Whitney U test showed a

statistically significant difference in the median, 25th and 75th percentiles of the visual scores for proximal and mid segments (proximal: 4 / 4 / 3 versus mid: 3 / 4 / 3; $p < 0.01$) and proximal and distal segments (proximal: 4 / 4 / 3 versus distal: 3 / 3 / 3; $p < 0.001$). Overall, there was a good agreement between observers for the visual score, with a kappa coefficient of 0.71.

Coronary VWS was 56.2 ± 7.2 in the LAD, 51.9 ± 6.9 in the LCX, and 53.9 ± 9.5 in the RCA. There was good intra- and inter-observer agreement for the VWS, with an intra-observer mean difference of -0.05% (95% confidence interval of 1.8% to -1.9%) and inter-observer mean difference of 0.23% (95% confidence interval of 3.2% to -2.8%).

The correlation analysis between patient characteristics and coronary VWS is shown in Figure 21. None of the variables such as age, BMI or HR, known to correlated with CMRA image quality, predicted coronary VWS in the multiple regression analysis.

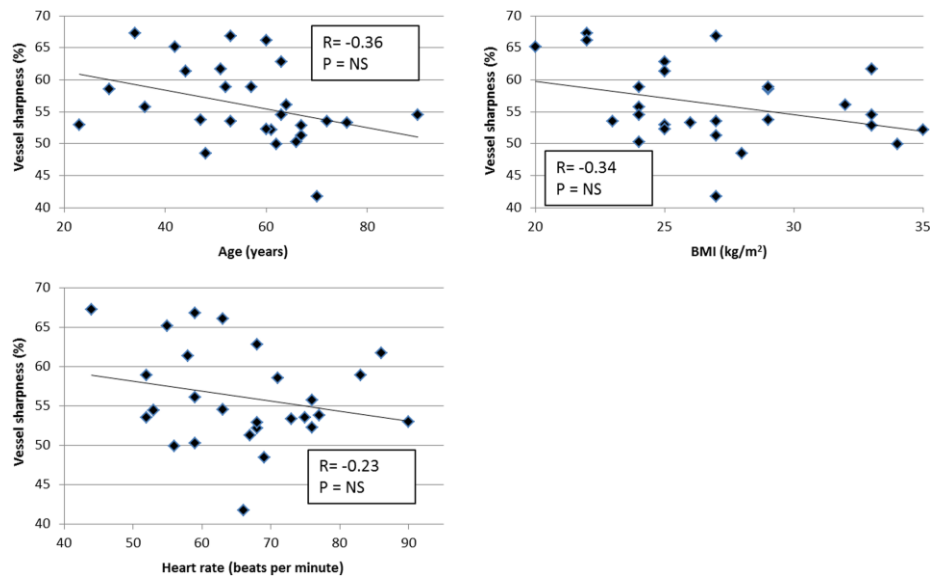


Figure 21

Scatter plots of coronary vessel well sharpness (VWS) versus age, body mass index (BMI), and heart rate. No statistically significant results were found for any of the correlations. NS, not significant.

3.2.3.2. CMRA DIAGNOSTIC PERFORMANCE

Seven patients (24%) were found to have significant CAD based on the invasive X-ray coronary angiography. This included 8 diseased proximal segments, four middle segments and three distal segments. The 2D iNAV CMRA receiver-operator characteristics (ROC) curves for detection of significant CAD per patient, vessel and segment are shown in

Figure 22. The per-patient, vessel and segment area under the curve was 91% (95% CI: 79% to 100%), 93% (95% CI: 81% to 100%) and 92% (95% CI: 84% to 99%), respectively. CMRA was able to detect significant CAD in 6 out of 7 patients (86%), 8 out of 10 vessels (80%), and 11 out of 15 segments (73%). The sensitivity, specificity, positive predictive value and negative predictive value for the-per patient, vessel and segmental analysis are summarised in Table 8. Illustrative reformatted CMRA images from three patients with significant CAD, where the diagnostic findings of the CMRA were confirmed by the invasive X-ray coronary angiography, are shown in Figure 23.

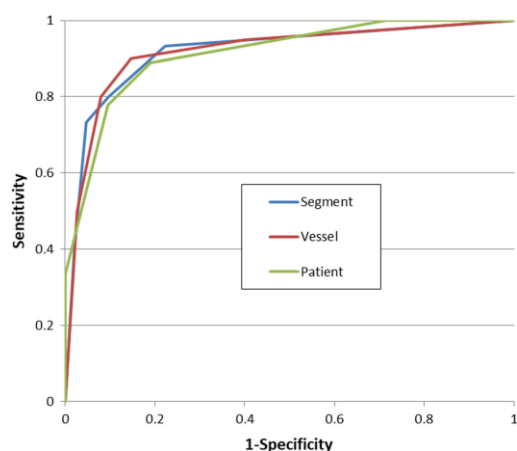


Figure 22

Receiver operator characteristic (ROC) curves of the 2D iNAV CMRA for detecting significant coronary artery stenosis.

	Patient	Vessel	Segment
Sensitivity	86% (6/7) [42–99]	80% (8/10) [44–97]	73% (11/15) [45–92]
Specificity	83% (21/24) [62–95]	92% (68/72) [83–97]	95% (227/238) [92–98]
PPV	60% (6/10) [37–79]	57% (8/14) [34–75]	50% (11/22) [34–66]
NPV	95% (20/21) [76–99]	97% (68/70) [91–99]	98% (227/231) [96–99]

Table 8

Diagnostic performance of the 2D iNAV CMRA for the detection of significant coronary artery disease (CAD). Data are shown as % (raw data) [95% confidence interval]. PPV, positive predictive value. NPV, negative predictive value.



Figure 23

Images from three patients with significant coronary artery disease, diagnosed using the 2D iNAV CMRA (top row) and confirmed with invasive X-ray coronary angiography (bottom row).

3.2.4. DISCUSSION

In this work we have evaluated the performance of CMRA to rule out significant CAD using the 2D iNAV approach investigated in Study 1, comparing its results with those obtained with invasive X-ray coronary angiography. As previously described, this image-based navigator with inline correction permits real-time reconstruction of the CMRA datasets at the scanner console. This allows quick visualisation of the coronary arteries to aid diagnosis without interrupting the clinical imaging workflow.

In our study, we have obtained diagnostic image quality in the majority of the coronary artery segments (241 of 253; 95%). The high negative predictive value (95-98% per patient, vessel and segment) suggests that the proposed 2D iNAV CMRA approach is a robust and reliable tool to rule out significant CAD, which has a clear additive clinical value.

There is scant data available reporting the diagnostic performance of CMRA with conventional respiratory motion compensation in patients with CAD. In a multicentre trial Kato and co-workers (Kato et al., 2010) compared the diagnostic performance of SSFP whole-heart CMRA with conventional 1D NAV at 1.5 Tesla to invasive X-ray coronary angiography in 138 adult patients with suspected CAD. The reported per-patient sensitivity and specificity were 88% and 72%, respectively. As in our study, they used conventional Cartesian k-space sampling and a similar spatial resolution. In another comparative study, Yang and collaborators (Yang, Q, et al., 2009) evaluated the diagnostic accuracy of CMRA

with a conventional diaphragmatic navigator at 3 Tesla in 69 adult patients with suspected CAD. Instead of the SSFP sequence, they used a GRE acquisition (less prone to imaging artefacts due to magnetic field inhomogeneity and radio-frequency distortion, frequent at 3 Tesla) following a slow infusion of a high relaxivity contrast agent; they reported a sensitivity of 94% and specificity of 82%. While the diagnostic performance in these studies was comparable to our 2D iNAV CMRA, the acquisition duration was approximately 2 minutes longer, with a large distribution of values reflecting the unpredictability of scan times using the conventional navigator approach. Furthermore, the reported failure rate in these studies was 8–10%, while the completion rate of the 2D iNAV CMRA was 100%.

The use of advanced respiratory motion compensation strategies has also been evaluated in patients with CAD. Piccini *et al.* (Piccini et al., 2014) compared the diagnostic performance of a respiratory self-navigated post-contrast SSFP CMRA to invasive X-ray coronary angiography in 78 adult patients with suspected CAD. Instead of a Cartesian k-space sampling adopted in our study, they used a radial k-space sampling with translational correction and a fixed 100% gating efficiency, and obtained a per-patient sensitivity and specificity of 71% and 62%, respectively. In comparison to our 2D iNAV approach, they have reported a much lower per-patient sensitivity and specificity. The 1D projection navigator used by Piccini *et al.* to detect cardiac motion might explain these differences as its use can result in cardiac motion under-estimation due to “contamination” with signal from the static surrounding tissue. Our 2D iNAV avoids this problem, allowing for accurate cardiac motion estimation even with only a few phase encoding steps (Henningsson et al., 2012). In addition, we implemented a constant 50% gating efficiency for the 2D iNAV CMRA, effectively discarding most of the motion data that may have been corrupted by large translations and non-rigid cardiac motion. Despite the scan time penalty introduced by the respiratory gating, because we also used a parallel imaging factor of 2.5, the average scan duration in our study (7.21 minutes) was shorter than the one reported by Piccini *et al.* (7.50 minutes). These results also highlight the trade-off between a clinically feasible acquisition duration and obtaining an adequate spatial resolution for diagnostic assessment.

He Y and co-workers (He et al., 2016) also assessed the diagnostic performance of a self-navigated SSFP CMRA in 60 adults patients using invasive X-ray coronary angiography as the reference gold standard. They used a 3D radial k-space sampling with a fixed 100%

respiratory gating efficiency and retrospective 3D affine motion correction. Their per-patient sensitivity and specificity was 96% and 69%, respectively. Despite the technical differences in strategies for respiratory motion correction, the use of higher field strength [3 Tesla, which increases both signal- and contrast-to-noise ratio, and conveniently improves the use of parallel imaging (Rajiah and Bolen, 2014)] and higher isotropic spatial resolution (voxel size of 1mm³), He *et al.* applied a stricter exclusion criteria excluding patients with arrhythmia. In contrast, such criterion was not used in our study, which could have affected the 2D iNAV CMRA diagnostic performance. Indeed, the majority (75%) of non-diagnostic segments in our study were found in two patients with significant arrhythmia during the acquisition. An important advantage of the 2D iNAV CMRA compared to the approach developed by He Y *et al.* is that it does not require offline, retrospective post-processing thus permitting a real-time assessment of the coronary image quality. This enables the cardiac imager to decide whether it is necessary to repeat the acquisition as well as to use the 3D CMRA for adequate planning other sequences (e.g. flow through small and tortuous vessels).

A robust CMRA sequence such as the one presented, with short and predictable scan time, would allow its integration into routine clinical CMR protocols (with stress perfusion and tissue characterisation), with a number of advantages in comparison with invasive X-ray coronary angiography or cardiac computed tomography angiography (CCTA): it is non-invasive, ionising-radiation free, not limited by the presence of coronary calcifications, and uses well tolerated and not nephrotoxic contrast agents. The high negative predictive value of CMRA (similar to CCTA studies) may increase the future use of CMR as a first line tool to screen patients with low to intermediate pre-test probability of significant CAD (i.e. CMR as a gate-keeper for invasive X-ray coronary angiography).

3.2.5 LIMITATIONS

We acknowledge some limitations to this study. Firstly, the study population had relatively low prevalence of CAD (24%). This resulted in a wide 95% confidence interval, which may impact the statistical significance of the study findings. Secondly, from a technical perspective, the sequence is currently incompatible with the conventional arrhythmia rejection algorithm, which renders it unsuitable for patients with frequent arrhythmias.

If compared to current high-end computed tomography (CT) scanners the spatial resolution of the proposed CMRA sequence may be insufficient for accurate quantification of a coronary stenosis, we have demonstrated that it could accurately rule out significant CAD (i.e. > 50% coronary stenosis) and complement the clinical CMR protocol (i.e. stress and rest perfusion acquisition, followed by CMRA and LGE imaging). Furthermore, if coronary calcifications are best demonstrated on CT, they can also result in blooming and partial volume artefacts leading to an overestimation of the true luminal narrowing (Kruk et al., 2014). Conversely, on CMRA calcification may be appreciated as areas of low signal intensity and but does not impair analysis (Wang et al., 2018).

3.2.6. CONCLUSIONS

Following our encouraging experience with the 2D iNAV CMRA sequence in Study 1, we tested this approach in patients with suspected CAD. Compared to the gold standard invasive X-ray coronary angiography, the proposed methodology showed high sensitivity and specificity (per patient, per vessel and per segment) to rule out obstructive CAD. It was demonstrated that the 2D iNAV is a robust approach for mitigating CMRA motion artefacts in patients with suspected CAD, and due to its short and predictable acquisitions times, it could add clinical value as a part of a comprehensive ischaemic heart disease CMR protocol (Henningsson et al., 2017).

3.3. STUDY 3: 2D iNAV CMRA IN PAEDIATRIC PATIENTS WITH CONGENITAL HEART DISEASE

3.3.1. BACKGROUND

Following the feasibility study and the evaluation of the diagnostic accuracy of the recently developed 2D iNAV CMRA sequence for the assessment of CAD, we proposed to further optimise it and test its performance in paediatric patients with CHD. This was the group of patients that we were interested to study coronary microcirculation adaptations using CFD. The computational task for this research required the acquisition of high quality anatomic data so that the coronary arteries could be accurately segmented using our customised software package CRIMSON.

As in adults, paediatric CMRA is usually acquired during free breathing using a VCG-triggered SSFP readout, with T2 preparation pulses to generate contrast between blood and myocardium, and are frequently combined with a fat suppression technique to eliminate the signal from epicardial and mediastinal fat. However, compared to their adults counterparts, CMRA imaging in paediatric patients has a few further challenges: (1) the smaller diameter of the coronary arteries often results in images with lower spatial resolution and signal-to-noise ratio (SNR), thus reducing the diagnostic accuracy; (2) the higher HR determines shorter rest periods (shorter diastasis, where cardiac motion is minimal and acquisition window is ideal for coronary imaging) and longer acquisitions that are then prone to respiratory and cardiac motion artefacts; (3) irregular breathing (thus low respiratory tracking efficiency) and usually lower cooperation with apnoea, particularly with long acquisitions, which frequently results in the need for scanning under general anaesthesia/sedation; and (4) overall small contrast doses that limit the optimal peak vascular enhancement window. Not surprisingly, despite being an ideal modality to image infants and young children with suspected coronary anomalies, paediatric CMRA remains challenging and the experience is mostly limited to high volume expertise centres (Taylor et al., 2005; Tangcharoen et al., 2011; Valsangiacomo Buechel et al., 2015).

One option to further increases the SNR (and the contrast-to-noise ratio, CNR) and thus improve image quality of CMRA sequences, is the administration of a gadolinium-based contrast agent. The rationale behind this study was that in many cases a contrast agent is given to assess myocardial perfusion and viability/fibrosis (e.g. in Kawasaki disease), and so a specific sequence design could exploit their paramagnetic effects to further improve CMRA imaging.

Furthermore, improved CNR could be achieved by replacing the T2 preparation pulses with an inversion-recovery (IR) pre-pulse. This introduces heavy T1-weighting and thus is beneficial with the administration of a T1-shortening gadolinium-based contrast agent. Such design could also suppress signal from fluid within the pericardium and pericardial recesses due to its long T1 (and typically bright on T2-prepared CMRA), which, in some subjects, can obscure the proximal coronary arteries (Stuber et al., 1999a; Makowski et al., 2011).

All contrast agents used clinically are gadolinium (Gd) based. The main difference between the several contrast agents used resides in the chelator required to encase the highly toxic Gd^{3+} ion, which determines its uptake and elimination. Gd has paramagnetic properties as it catalytically relaxes water hydrogen atoms (protons) in the tissue resulting in enhanced signal on T1-weighted images and, together with appropriate sequence parameters, an improved image contrast (Reiter et al., 2012). Among the different contrast agents available, those with longer plasma half-life and thus longer period of peak vascular enhancement, render higher intravascular signal facilitating CMRA.

Gadobenate dimeglumine (Gd-BOPTA, MultiHance®; Bracco Imaging, Milan, Italy) is a second-generation Gd-based contrast agent. It has been classified as a high-relaxivity contrast agent, and in fact has the highest longitudinal proton relaxation rate at all field strengths (Pintaske et al., 2006). Compared to the first-generation contrast agents, that randomly distribute in the intravascular and interstitial extracellular fluid spaces and are eliminated rapidly in their unchanged forms (so called extracellular gadolinium-based contrast agents, EC-GBCA), Gd-BOPA reversibly binds to blood albumin. This slows its total blood clearance and thus increases its plasma half-life. The resulting effect is a higher and prolonged intravascular signal. This is well suited for high resolution CMRA, where the usually long acquisitions are not ideal for the short time window available for optimal vascular signal with EC-GBCA. In fact, the use of Gd-BOPA has been shown to improve coronary imaging in adult patients as it provides high homogenous signal not limited to the first-pass arterial-phase as EC-GBCA (Nassenstein et al., 2009; Yang, Q, et al., 2009; Hu et al., 2011).

Gd-BOPA offers an additional advantage compared to other available high-relaxivity contrast agents (so called blood pool agents as they are typically confined to the intravascular space): it can diffuse into the interstitial extracellular space due to its weak and reversible interaction with serum albumin and smaller molecules. This diffusion is slow, compared with EC-GBCA (Ni, 2011), but tissue characterisation has been shown to be feasible with Gd-BOPA (Klein et al., 2008). If the advantages of Gd-BOPA kinetics in CMRA have been demonstrated in adult patients, to the date of this research there was no data available in paediatric patients.

In this study, we have compared the use of Gd-BOPTA in combination with a specific CMRA sequence design that exploits its high relaxivity (IR replacing the T2 pre-pulse), to the conventional T2-prepared 3D SSFP CMRA in paediatric CHD patients, both sequences using the 2D iNAV approach developed for Studies 1 and 2.

3.3.2. MATERIAL AND METHODS

3.3.2.1. STUDY POPULATION

Consecutive children (age >2 years) with CHD undergoing a clinical CMR study under general anaesthesia were enrolled. Exclusion criteria included any contra-indications to CMR (e.g. pacemakers), known allergy to CMR contrast-agents and impaired renal function (estimated renal clearance < 30 millilitres/minute/1.73 m²).

3.3.2.2. CMR IMAGING PROTOCOL

All scans were performed on a 1.5 Tesla clinical CMR scanner (Achieva, Philips Healthcare, Best, The Netherlands) using a 5-channel phased-array cardiac surface coil under general anaesthesia, following the local institutional practice for infants and small children. In our institution, general anaesthesia during CMR is offered after careful weighting the benefits of a diagnostic examination, the developmental maturity and prior patient's experience, parents' insights of their child's capacity to cooperate with the study and the anticipated length of the imaging protocol, rather than a rigid age limit.

The study was approved by the local institutional research ethics committee (South East London Research Ethic Committee, 10/H0802/65). Informed consent was obtained from all participants' parents/guardians prior to scanning.

The CMRA consisted of a VCG-triggered 3D SSFP sequence acquired in coronal orientation, a readout in the FH direction, a phase encoding in LR direction and slice encoding in AP direction. The following imaging parameters were used: isotropic spatial resolution with an acquired voxel size of $1.3 \times 1.3 \times 1.3\text{mm}^3$ (0.65 x 0.65 x 0.65 mm reconstructed voxel size); a TR/TE = 4.5/2.2 ms; flip angle=70°; and parallel imaging acceleration factor (SENSE) = 2 (in-plane phase encoding direction). Data acquisition was synchronised with the VCG to coincide with the longest quiescent cardiac phase. The optimal

trigger delay time and acquisition window were set for each patient and single-phase studies were acquired.

The conventional pre-contrast CMRA sequence used T2 and fat-suppression pre-pulses to suppress signal from the myocardium and thus improve the blood-to-myocardium contrast (sequence A). Subsequently, contrast (Gd-BOPTA) was administered as a bolus by hand injection followed by 10 to 20 ml of a saline bolus (Hu et al., 2011). The post-contrast CMRA scan (sequence B) was performed approximately 5-8 minutes after the injection of Gd-BOPTA (0.2 ml/kg), following previous experience (Cavagna et al., 1997; Gurney et al., 2007) and after a pre-study validation of the technique in five patients. This allowed the circulating contrast material to stabilise in the blood-pool and thereby avoid significant changes in the inversion-time (TI) during the post-contrast acquisition. For the post-contrast CMRA scan, an IR-approach was used to null signal from the myocardium. The optimal TI for nulling the myocardium was determined using a Look-Locker sequence prior to the post-contrast CMRA.

For respiratory motion compensation, both sequence A and B used the 2D iNAV evaluated in Studies 1 and 2. As explained before, the start-up echoes of the SSFP sequence were used to generate a low-resolution 2D projection image of the heart, with the same geometric properties as the whole-heart CMRA. The 2D iNAV was then used to directly track and correct the respiratory motion of the heart in the FH and LR directions. Additionally, respiratory gating using the CRUISE algorithm with a constant efficiency of 50% was used to limit data acquisition to end-expiration (Henningsson et al., 2018).

The rest of the CMR protocol was dictated by the clinical indication and imaging findings, including conventional cine acquisitions in short and long-axis, phase-contrast CMR (PC-CMR) flows and a time-resolved contrast-enhanced angiography with keyhole (4D-TRAK).

3.3.2.3. DATA ANALYSIS

Quantitative Analysis

Coronary reformatting and quantitative analysis of vessel length, diameter and wall sharpness was performed using dedicated software ("Soap-Bubble", Philips Medical

Systems, Best, The Netherlands), as previously described (Etienne et al., 2002; Makowski et al., 2011).

Acquisition of a noise image required for global SNR and CNR calculations with parallel imaging was not considered practical due to time constraints (Yu et al., 2011). Nevertheless, by ensuring that imaging parameters such as the patient position, FoV, matrix-size, flip-angle, phase-encoding direction and acceleration factor were unchanged between sequence A and B, and by selecting identical ROIs in both sets of images, a local SNR (SNR_l) and local CNR (CNR_l) were calculated as detailed:

$$SNR_l = \frac{I_B}{SD(L)}$$

Equation 7

$$CNR_l = \frac{I_B - I_M}{SD(L)}$$

Equation 8

where I_B and I_M refers to the mean signal-intensity of an ROI in the blood-pool (proximal ascending aorta) and myocardium (mid ventricular septum) respectively, and $SD(L)$ refers to the standard deviation of an ROI in the air of the lungs (chosen to contain a minimum of 100 pixels while avoiding any visible vascular structures). These ROIs were specifically drawn in similar locations in both sequence A and B by one expert reader using patient-specific landmarks.

Qualitative Image Analysis

Coronary image quality was determined on the basis of a five point grading system (Table 9) as described by Makowski and co-workers (Makowski et al., 2011). This seemed a more appropriate qualitative score than the one used in Study 2 as it had been previously applied to CMRA studies involving children with CHD (Greil et al., 2002; Makowski et al., 2011). Analysis was performed by two independent experienced readers blinded to the study results or details of the sequences used to report the findings. Grading involved careful visual inspection of the image quality of the proximal to distal segments of the coronary arteries of each patient dataset, according to the standardised American Heart Association (AHA)

coronary segmentation model adapted for CCTA (Abbara et al., 2009). Prior to the study analysis, agreement was assessed on illustrative coronary imaging cases not part of the study sample (Figure 24). In case of significant disagreement between the two readers, a consensus score was given.

Qualitative Score	
1 - Poor-quality 2 - Marked blurring	Non-diagnostic
3 - Moderate blurring 4 - Minimal blurring 5 - Sharply defined borders	Diagnostic

Table 9
Image quality grading system.

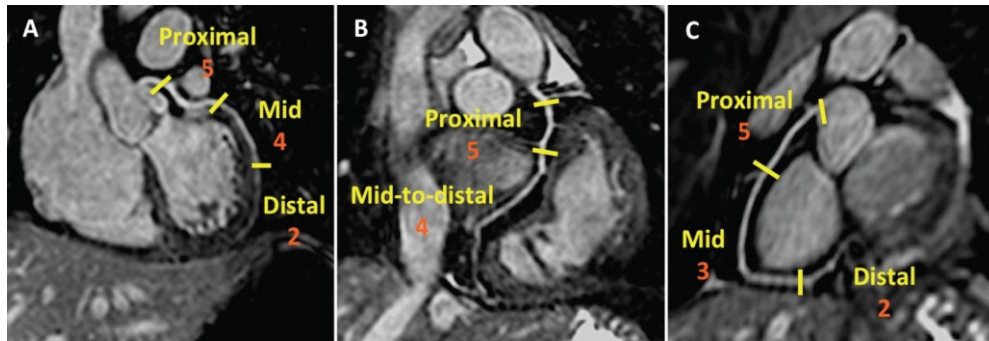


Figure 24

Examples of consensual image quality scores given by the two independent readers to the different coronary segments of the LAD (panel A), LCx (panel B) and RCA (panel C).

3.3.2.4. STATISTICAL ANALYSIS

A sample size calculation was performed prior to the study to plan recruitment. Using a standard deviation of 10% taken from previous VWS measurements in congenital CMRA (Uribe et al., 2011), a power level of 80%, and a significance level of 0.05 to detect a clinically significant change of 10% in VWS, 36 patients were estimated to be needed for a bivariate analysis. Continuous quantitative variables are expressed as mean \pm standard deviation. As we compared CMRA pre and post contrast in the same study subjects (i.e. paired observations), differences in measures such as image quality, vessel length and diameter, and VWS were evaluated with a paired *t*-test for parametric variables and the Wilcoxon signed rank test for nonparametric variables, as appropriately. One-way ANOVA

and Tukey HSD *post hoc* test were used to test for any difference in mean VWS values per coronary artery territory imaged with both pre and post-contrast sequences.

Intra and inter-observer variability for the qualitative scores given to each coronary segments imaged with sequences A and B were evaluated using the 95% limits of agreement approach proposed by Bland and Altman (Bland and Altman, 1986) and the Cohen's kappa coefficient. This was performed for the 40 subjects enrolled. For the intra-observer variability, the two readers independently scored each coronary segment twice in different days to reduce any potential bias. For the inter-observer variability, the average qualitative score given to each coronary segment by one of the readers was compared to the results obtained by the other reader. The Cohen's kappa coefficient of agreement was graded as follows: 0 to 0.2 = poor to slight; 0.21 to 0.4 = fair; 0.41 to 0.6 = moderate; 0.61 to 0.8 substantial; and 0.81 to 1.0 = nearly perfect (Landis and Koch, 1977).

Bivariate analyses were performed to assess any correlation between imaging parameters (VWS and qualitative score) and age, body surface area (BSA) and HR. Additionally, a multivariate linear regression model was built to explore whether any of the patient's variables (age, BSA, and HR) was associated with the coronary imaging results. Differences were considered statistically significant for a p value < 0.05 (two-tailed). All statistical analyses were performed using SPSS version 22.0 (IBM SPSS Statistics, IBM Corporation, Armonk, New York).

3.3.3. RESULTS

Consecutive patients (N=40; mean age 6 ± 2.8 years; 73% males) were prospectively recruited. This constituted a very heterogeneous population in terms of clinical indications for the CMR study (Table 10), that span from simple cardiac defects (e.g. atrial septal defects) to more complex CHD (e.g. single ventricle physiology defects), representative of real-world referrals to a congenital CMR centre.

CMRA was successfully acquired in all patients, with diagnostic image quality. No adverse events or any contrast reaction occurred during this study.

Some examples of the coronary imaging results achieved with the two sequences are provided in Figure 25.

Clinical characteristics (N = 40)		
Age (years)	6 ± 2.8 [2;12]	
Gender	29 male (73%); 11 female (27%)	
BSA (Kg/m ²)	0.75 ± 0.31	
Indication	Aortic coarctation/interrupted arch	7
	Tetralogy of Fallot/Pulmonary atresia	6
	ASD/VSD	3
	HLHS	3
	Pulmonary atresia	3
	TGA	2
	PAPVR	2
	Ebstein's anomaly	1
	Common arterial trunk	1
	Coronary fistula	1
	Marfan's syndrome	1
	Complex CHD ¹	10

Table 10

Characteristics of the study population. ASD, atrial septal defect. CHD, congenital heart disease. HLHS, hypoplastic left heart syndrome. PAPVR, partial anomalous pulmonary venous return. TGA, transposition of the great arteries. VSD, ventricular septal defect. ¹Multiple congenital heart defects.

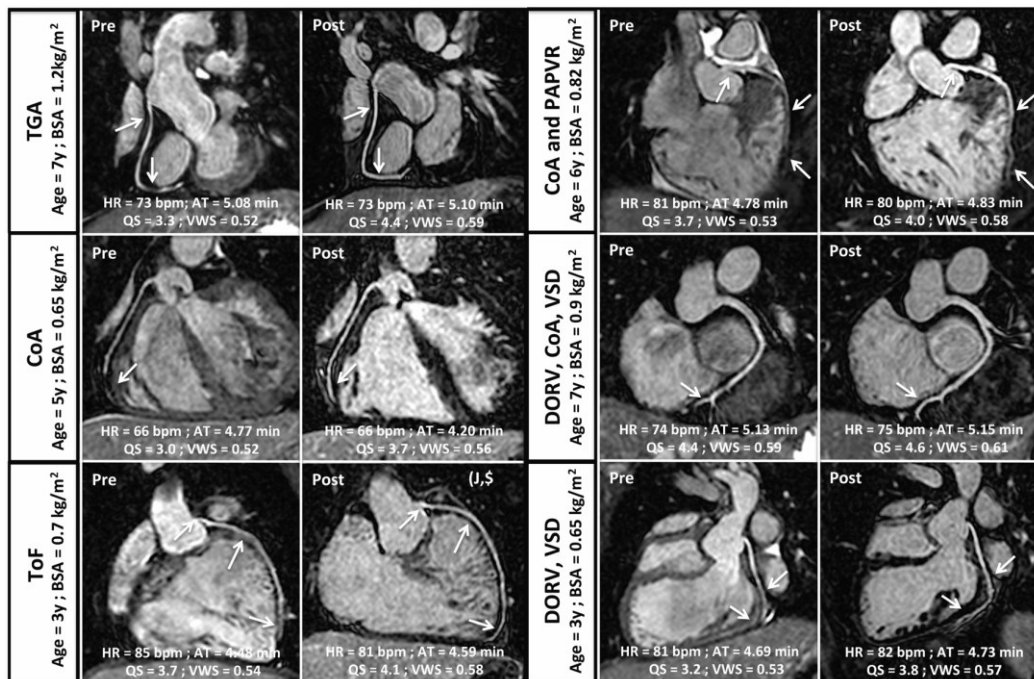


Figure 25

CMRA reformatted images from six randomly selected patients with their demographic details, average heart rate (HR), acquisition duration and image quality parameters depicting areas of improved visualization. **Left-hand panels** - sequence A (pre-contrast). **Right-hand panels** - sequence B (post-contrast). Arrows point to coronary segments with improved visualisation after contrast. DORV, double outlet right ventricle; CoA, aortic coarctation; PAPVR, partial anomalous venous return; TGA, transposition of the great arteries; ToF, tetralogy of Fallot; VSD, ventricular septal defect.

A summary of the coronary imaging parameters and attributes of the two sequences is provided in Table 11. Both sequence A (pre-contrast) and sequence B (post-contrast) had similar acquisition durations (A = 5.3 ± 1.8 versus B = 5.2 ± 1.5 minutes; $p = 0.532$). Furthermore, there was no significant difference in the HR during both sequence acquisitions, with a mean HR of 78 ± 14.7 bpm for sequence A versus 78 ± 14.5 bpm for sequence B ($p = 0.443$). The average TI of sequence B was 234 ± 14.6 ms [210 – 260 ms]. The mean vessel length was 5.2 ± 1.8 (A) versus 6.4 ± 2.0 cm (B) ($p < 0.001$) for a similar average vessel diameter of 2.2 ± 0.2 (A) versus 2.2 ± 0.2 mm (B) ($p = 0.922$).

	Sequence A (pre)	Sequence B (post)	<i>p</i>	95% CI of the Difference
Acquisition duration (minutes)	5.3 ± 1.8	5.2 ± 1.5	0.532	[-0.218, 0.415]
Heart rate (bpm)	78 ± 14.7 [56-109]	78 ± 14.5 [54-114]	0.443	[-0.644, 1.444]
Mean vessel length (cm)	5.2 ± 1.8	6.4 ± 2.0	<0.001	[- 1.670, - 0.772]
Average vessel diameter (mm)	2.2 ± 0.2	2.2 ± 0.2	0.922	[- 0.055, 0.061]
Signal-to-noise ratio	12.6 ± 4.4	31.1 ± 7.4	<0.001	[-188.478, -128.625]
Contrast-to-noise ratio	9.0 ± 1.8	13.5 ± 3.7	<0.001	[- 7.244, -4.306]
Coronary arteries VWS	0.53 ± 0.07	0.56 ± 0.07	0.001	[- 0.045, - 0.012]

Table 11

Pre and post-contrast CMRA sequence parameters. CI, confidence interval. VWS, vessel wall sharpness.

Five patients had coronary anomalies (Table 12). Table 13 depicts the average qualitative score given by the two readers. There were narrow limits of agreement for the qualitative coronary scores given by the two independent readers (Figure 26 and Figure 27), indicative of consistency of the results. In fact, the mean differences for both intra-observer (reader 1: sequence A, $k = 0.545$, $p < 0.001$ and sequence B, $k = 0.782$, $p < 0.001$; reader 2: sequence A, $k = 0.654$, $p < 0.001$ and sequence B, $k = 0.743$, $p < 0.001$) and inter-observer agreement (sequence A, $k = 0.75$, $p < 0.001$; sequence B, $k = 0.717$, $p < 0.001$) were close to zero.

Main clinical diagnosis	Coronary anomaly
Single outlet right ventricle	Single coronary
Transposition of the great arteries	Anomalous origin of the RCA from the LAD
Tetralogy of Fallot	Dual LAD supply
Tricuspid stenosis	Single coronary
Coronary-cameral fistula	RCA fistula to left atrium

Table 12
Coronary arteries anomalies identified in the study population.

		Sequence A		Sequence B		<i>p</i>	
		Score	Non-diagnostic	Score	Non-diagnostic	Score	Non-diagnostic
All	Coronaries	3.8 ± 0.59	42 (13.1%)	4.1 ± 0.53	33 (10.3%)	<0.001	0.002
LAD	All LAD	3.9 ± 0.98	9 (7.5%)	4.2 ± 0.96	8 (6.7%)	0.009	0.566
	Proximal	4.5 ± 0.72	0	4.8 ± 0.45	0	0.002	>0.999
	Mid	4.2 ± 0.83	2	4.2 ± 0.79	1	0.670	0.323
	Distal	3.2 ± 0.91	7	3.6 ± 1.08	7	0.01	>0.999
LCx	All LCx	3.6 ± 1.11	20 (25%)	4.0 ± 1.11	14 (17.5%)	0.005	0.019
	Proximal	4.2 ± 0.87	3	4.7 ± 0.48	0	0.002	0.083
	Mid and distal	3.3 ± 1.10	17	3.7 ± 1.19	14	0.002	0.002
RCA	All RCA	3.9 ± 1.03	13 (10.8%)	4.1 ± 1.09	11 (9.2%)	0.037	0.033
	Proximal	4.5 ± 0.60	0	4.7 ± 0.55	0	0.088	0.323
	Mid	3.6 ± 1.02	3	3.8 ± 1.14	3	0.042	0.160
	Distal	3.2 ± 1.06	10	3.4 ± 1.15	8	0.192	0.183

Table 13
Coronary arteries average qualitative score and non-diagnostic segments.

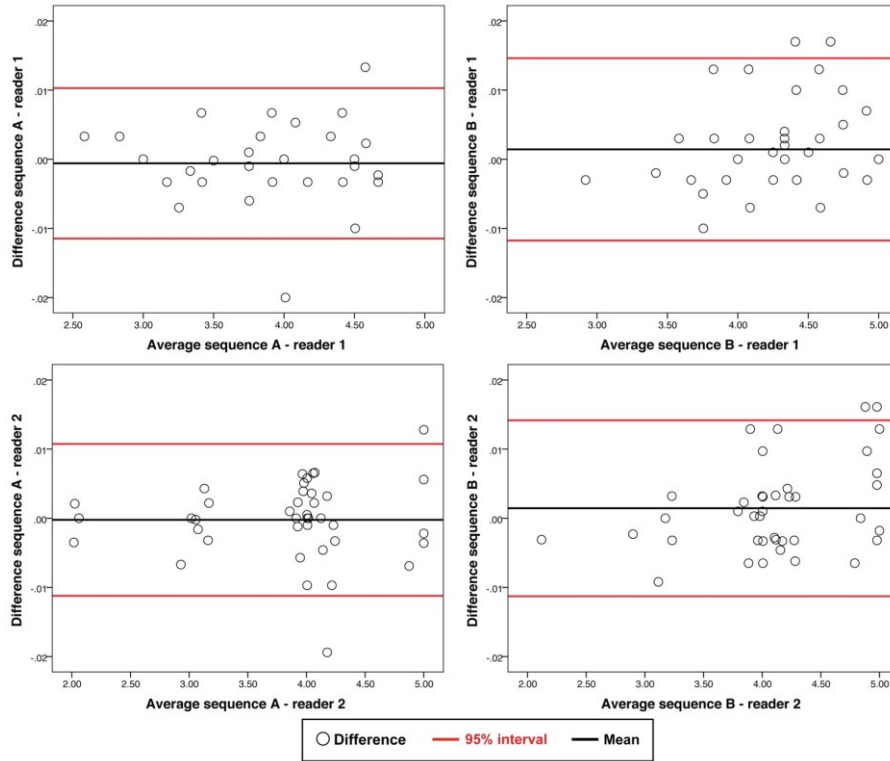


Figure 26

Bland-Altman plots showing the intra-observer agreement for the qualitative coronary scores of sequences A and B. In the scatter plots the Y axis is the difference between the two paired measurements for sequences A and B, taken in by each reader in the study cohort. The X axis represents the average of these measures. For both readers, 95% of the attributed scores for sequences A and B lie within ± 1.96 standard deviation of the mean difference, which according to Bland and Altman confirms good agreement.

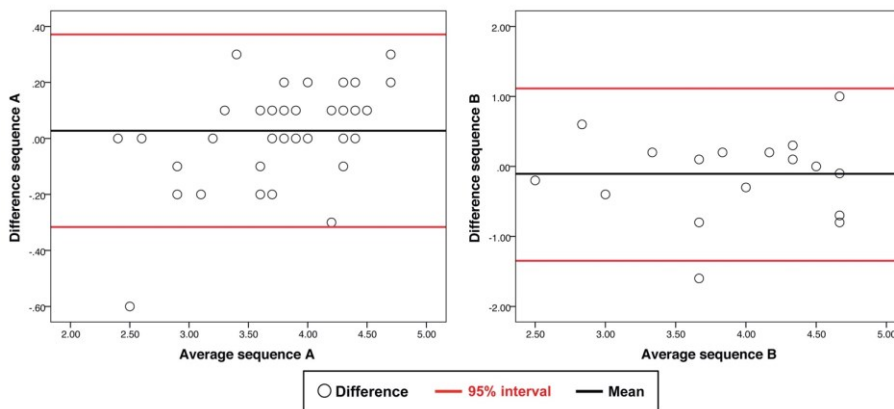


Figure 27

Bland-Altman plots depicting the inter-observer agreement for the coronary scoring system used for qualitative assessment of both sequence A and B. The mean difference and 95% limits of agreement (± 1.96 SD) are presented. There was good inter-observer agreement for the scores attributed.

CMRA after Gd-BOPTA administration and acquired with the 2D iNAV IR SSFP sequence (B) resulted in significantly higher SNR ($A = 12.6 \pm 4.4$ versus $B = 31.1 \pm 7.4$; $p < 0.001$) and CNR ($A = 9.0 \pm 1.8$ versus $B = 13.5 \pm 3.7$; $p < 0.001$), compared to the pre-contrast T2-prepared SSFP sequence (A).

Overall, higher coronary VWS values ($A = 0.53 \pm 0.07$ versus $B = 0.56 \pm 0.07$; $p = 0.001$) and qualitative scores ($A = 3.8 \pm 0.59$ versus $B = 4.1 \pm 0.53$; $p < 0.001$) were achieved with sequence B as depicted in Figure 28. Except for the LCx VWS values, this improvement was statistically significant in all coronary territories (Table 13 and Figure 29). The number of non-diagnostic coronary segments (score 1 and 2) was significantly lower for sequence B [$A = 42$ (13.1%) versus $B = 33$ (10.3%); $p = 0.002$]. Furthermore, while there were three non-diagnostic proximal segments with sequence A (0.9%), all involving the LCx, there were none in the post-contrast sequence. In fact, it was in the LCx territory that both sequences had lower VWS values and qualitative scores (Table 13 and Figure 29). However, when analysing by coronary artery segment imaged, there were no statistically significant differences in the mean pre-contrast as well as in the mean post-contrast VWS as determined by one-way ANOVA (sequence A: $F(2, 117) = 0.651$, $p = 0.524$; sequence B: $F(2, 117) = 1.83$, $p = 0.164$).

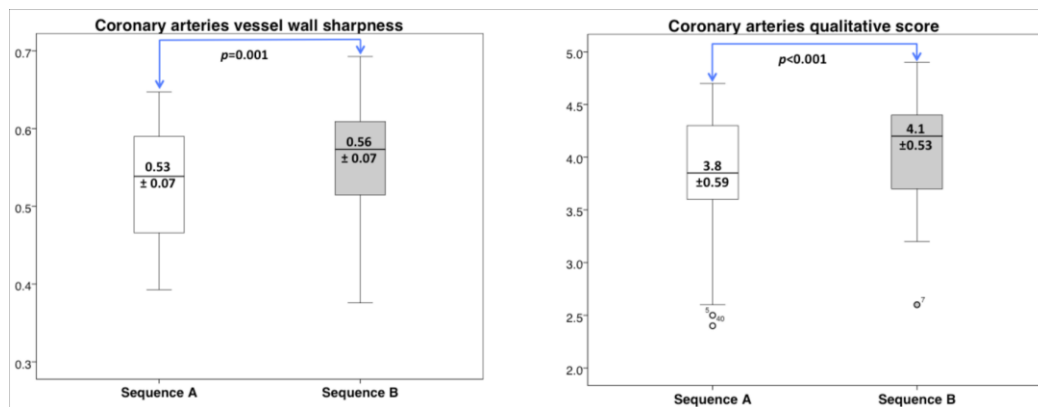


Figure 28

Vessel wall sharpness (VWS) and qualitative score results for both the pre-contrast (A) and post-contrast sequences (B) for all coronary arteries.

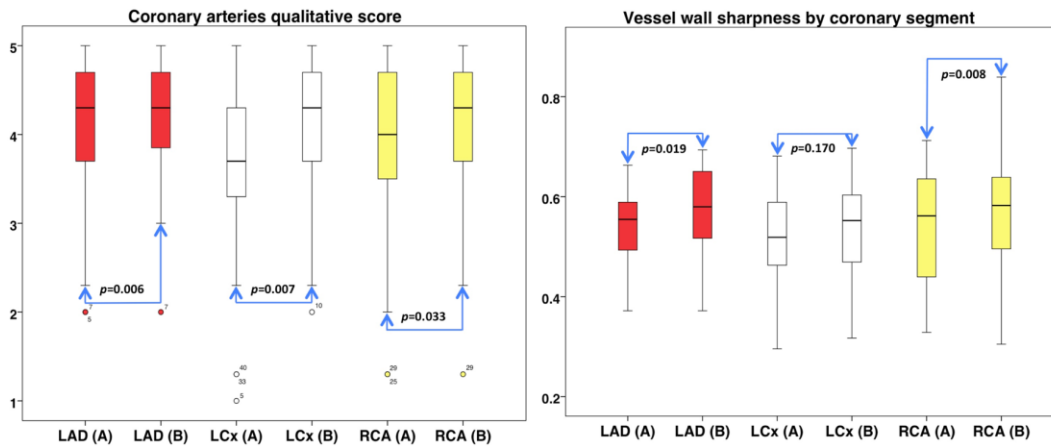


Figure 29

Vessel wall sharpness (VWS) and qualitative score results for both the pre-contrast (A) and post-contrast sequences (B), for each coronary artery.

In our study, the same trigger delay was used in both sequences A and B, and ranged from 180 to 290 ms for systolic-triggered scans and 430 to 759 ms for diastolic acquisitions. Two thirds of the acquisitions (N = 29; 72.5%) were synchronised with the diastolic phase. On bivariate analysis, there was no correlation between the resting trigger delay selected and the coronary VWS values for both sequence A ($R = 0.071$, $p = 0.663$) and B ($R = 0.173$, $p = 0.285$).

Finally, there was no correlation between patients' variables such as age, BSA or HR and coronary VWS results as summarised in the scatterplots of Figure 30. None of these patient's variables were shown to predict the coronary VWS values on the multiple linear regression analysis ($R^2 = 0.108$, $p = 0.242$ for sequence A; $R^2 = 0.033$, $p = 0.744$ for sequence B).

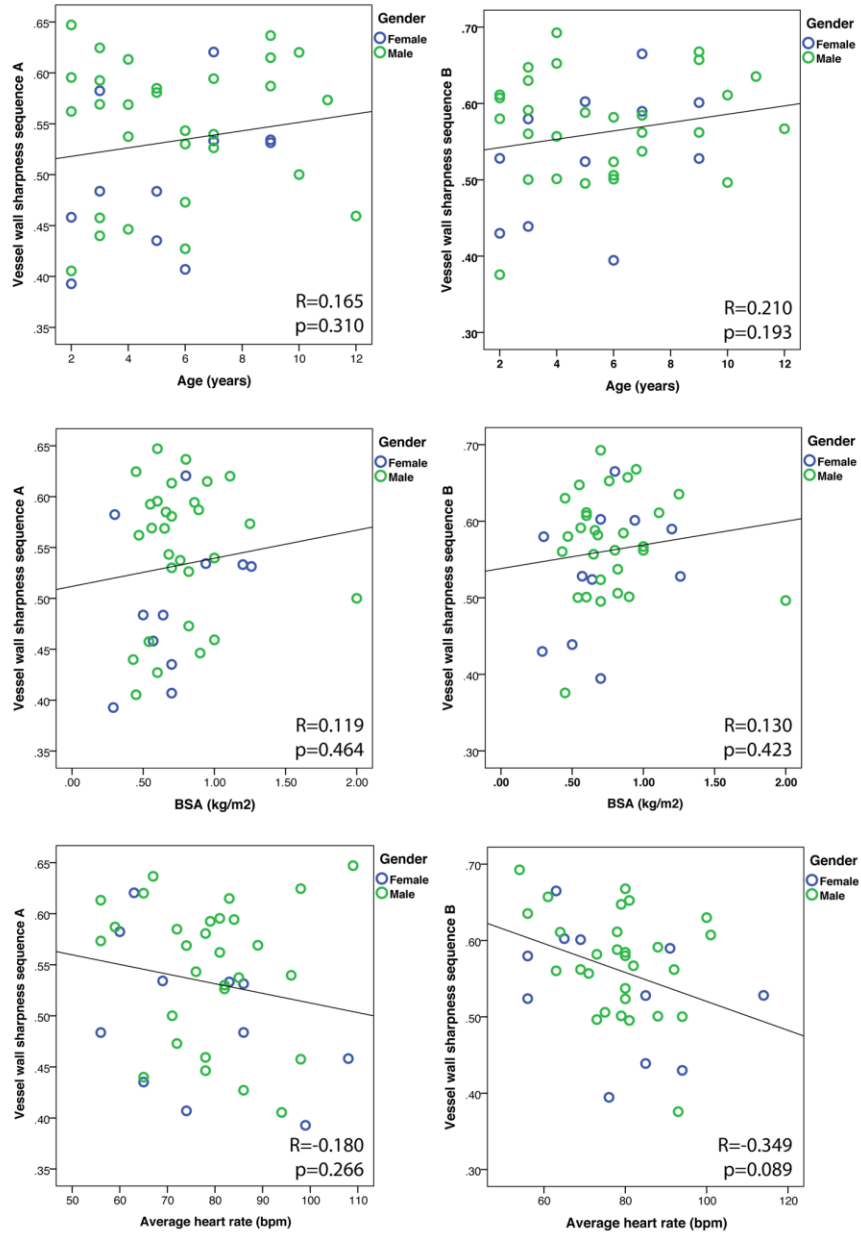


Figure 30

Scatter plots showing no correlation between vessel wall sharpness (VWS) and potential image detrimental factors such as age, body surface area (BSA) and heart rate.

3.3.4. DISCUSSION

In this prospective crossover trial, we have imaged consecutive infants and young children with CHD referred to our centre using two image-navigated SSFP sequences (A and B), following the work developed in Studies 1 and 2. The goal was to assess whether the use of a high-relaxivity contrast agent together with an IR approach (sequence B) could offer

further improvement in the coronary imaging quality of infants and young children compared to a non-contrasted CMRA (sequence A).

In both sequences A and B we have used the novel image-based navigation approach validated in adults with CHD (Study 1) and in adults with suspected CAD [Study 2] (Henningsson et al., 2016, 2017). As in the 2D iNAV used in Study 2 of this thesis, we applied a fixed respiratory gating efficiency of 50% with only the best 50% of the collected data used for image reconstruction (acquired data with large translations and non-rigid cardiac motion were discarded). In contrast to Studies 1 and 2, all patients were scanned under general anaesthesia as per protocol in our centre for infants and young children with CHD, with no change in the anaesthetic procedure throughout the CMR scan (average time interval between both sequences was of 18.05 ± 4.0 minutes). Therefore, the only difference between the two sequences investigated was the magnetisation preparation scheme and the use of contrast. Sequence B used an IR instead of a T2 pre-pulse and was acquired 5-8 minutes after administration of Gd-BOPTA, so a head-to-head comparison between the two CMRA acquisitions was possible. We showed that there was a statistically significant improvement in objective image quality measures (e.g. ~59% improvement in SNR and ~5% in VWS).

Different magnetisation preparation techniques have been employed to improve coronary visualisation in 3D SSFP CMRA sequences. In SSFP imaging, fat has a steady-state signal close to that of blood because of their similar T2/T1 ratios. So, with a fat suppression technique, signal from epicardial fat where the coronary arteries are embedded can be suppressed thus improving contrast with signal from the coronary blood pool. In addition, signal from subcutaneous and mediastinal fat can be also suppressed, helping to reduce artefacts in the CMRA. The addition of a T2-prepared magnetisation scheme that employs a 90° radiofrequency pulse to flip the longitudinal magnetization (M_z) vector into the M_{xy} plane is also beneficial. These magnetisation pre-pulses were originally proposed by Brittain and co-workers (Brittain et al., 1995) and are based on the fact that the T2 of myocardium (approximately 50 ms) is considerably less than that of arterial blood. They have been employed in 3D SSFP sequences to suppress signal from tissues with a short T2 relaxation time, such as the myocardium, the epicardial fat and veins with deoxygenated blood and thus improve coronary visualisation (Botnar et al., 1999). However, the addition

of a T2 pre-pulse has a negative influence on SNR and can decrease the signal from the coronary artery wall (Botnar et al., 1999; Bogaert et al., 2012). If in adults this might be negligible, adequate SNR is vital for visualisation of the small coronary arteries in paediatric CHD.

Improved coronary blood SNR can also be achieved with the use of a T1-shortening contrast agent, enabling increased spatial resolution without significantly increasing the imaging time. This in turn can reduce potential cardiac and respiratory motion artefacts during a long acquisition. In this regard, equilibrium free-breathing contrast-enhanced 3D SSPF CMRA would benefit from the use of “intravascular” or “blood-pool” contrast agents that have a long plasmatic half-life, while extracellular agents would be more adequate for first-pass breath-hold approaches (Stuber et al., 1999; Huber et al., 2003). The contrast between the coronary blood pool and the myocardium could be further improved using a IR pre-pulse as shown by Tandon and co-workers (Tandon et al., 2016). This is a conventional spin echo sequence preceded by a 180° inverting pulse, whose function is to flip the initial longitudinal magnetization (M_z) of all tissues in the imaged slice or volume in the opposite direction of the main magnetic field (B_0). During a predefined TI interval, these tissues undergo T1 relaxation as they variably seek to re-establish their magnetisation along the z-direction. Notably, after contrast injection, the magnetisation of the coronary blood returns more rapidly to the equilibrium than for the myocardium and this results in improved contrast between both.

Gd-BOPTA is a second-generation gadolinium-based contrast-agent, with a more lipophilic structure compared with conventional EC-GBCAs, which results in a weak and reversible interaction with serum albumin. In turn, this slows its extravasation out of the vascular space and increases its relaxivity compared to other agents, thus rendering a higher intravascular signal. Likewise, this effect has been shown to improve the diagnostic performance of CMRA (Hu et al., 2011; Yun et al., 2014; Shen et al., 2015).

Sequence B was designed to benefit from the T1 shortening effects and prolonged intravascular half-life of Gd-BOPTA by introducing an IR approach to null signal from the myocardium and thus increase the blood-to-background tissue contrast. In our study, the use of Gd-BOPTA resulted in a higher and stable intravascular signal (higher SNR and CNR), allowing isotropic high-spatial resolution coronary imaging to be performed within a

clinically feasible scan time of about five minutes, while also permitting dynamic vascular imaging with a single contrast injection (i.e. time-resolved angiography).

Adding the contrast to the proposed sequence design resulted in a significant improvement in coronary visualisation independent of age, BSA and HR, known to have detrimental effects on image quality. This improvement was noted in all coronary segments and was independent of the vessel imaged or the resting cardiac phase chosen.

Likely associated with the higher vascular signal obtained with Gd-BOPA, which allowed a better delineation of the coronary wall (as demonstrated by the higher VWS values obtained), the mean vessel length obtained with sequence B was significantly higher than that of sequence A. Surprisingly, the mean vessel diameter was similar for both sequences, a finding counterintuitive given the normal angiographic tapering of the coronary arteries. However, because the vessel wall was less clearly visualised before contrast injection, we hypothesise that signal loss due to partial volume effect and noise artefacts resulted in underestimation of the true lumen in sequence A despite having the same spatial resolution as sequence B (Hazirolan et al., 2005).

In addition to the high, homogenous and prolonged intravascular signal not limited to the first-pass arterial-phase, Gd-BOPTA can diffuse into the interstitial extracellular space due to its weak and reversible interaction with serum albumin and due to its smaller molecules. Compared to EC-GBCAs, this diffusion is slow, (Bogaert et al., 2012), and so after setting the appropriate TI, we noticed that the myocardial signal remained nulled even after the 3D coronary imaging acquisition. Therefore, we hypothesise that the proposed sequence optimised for Gd-BOPTA may also enable tissue characterisation with the same patient preparation as with EC-GBCAs and a single contrast bolus, with no need for dedicated or cumbersome mixed double contrast protocols (e.g. EC-GBCAs for perfusion/delayed enhancement followed by an intravascular agent for vascular imaging), a known limitation of “blood-pool” contrast agents (BP-CAs) imaging (Klein et al., 2008). Importantly, no heavy venous enhancement was seen with sequence B, which has been described to complicate interpretation of coronary imaging with BP-CAs (Stillman et al., 1996).

3.3.5. CLINICAL SIGNIFICANCE

CMRA has become an important alternative to echocardiography and angiography (CT or invasive) in the evaluation of paediatric patients with suspected congenital or acquired coronary anomalies (Kellenberger et al., 2007; Valsangiacomo Buechel et al., 2015). This is a diverse group of disorders (ranging from variation of the coronary artery origin from the aorta, to fistulae and abnormalities in the calibre such as seen post-Kawasaki), and a cause of myocardial ischaemia and sudden cardiac death (Basso et al., 2005; Shiwani et al., 2018; Finocchiaro et al., 2019). Although it is estimated that the prevalence of congenital coronary anomalies in the general population is low (~ 1-2%), they are commonly seen in CHDs (Davis et al., 2001; Angelini Paolo, 2007). Therefore, it is crucial that high quality, non-invasive and radiation-free coronary imaging is attainable in paediatric CHD patients.

In Studies 1 and 2 of this thesis we have demonstrated that the proposed image-navigation approach, directly tracking and compensating for the bulk cardiac motion, improved coronary imaging compared to the “conventional” 1D diaphragmatic respiratory-navigated (1D NAV) CMRA sequence, in both adults with CHD (Study 1) and those at risk of CAD to the point that it could be used to screen for a significant stenosis (Study 2). In addition, the image acquisition was faster thus enabling its inclusion in a clinical CMR protocol. Compared to adults, CMRA is even more challenging in children due to their smaller size and thus small contrast bolus, relatively higher cardiac output, and the potential for image degradation due to limited patient cooperation during the critical time window for image acquisition with EC-GBCAs. In this study, we showed the 2D iNAV, together with a high-relaxivity agent with prolonged intravascular transit (Gd-BOPTA) and an IR-recovery magnetisation scheme, managed to achieve a further improvement in the blood-background tissue differentiation (i.e. higher CNR and SNR), even sharper images (small but statistically significant differences in VWS, a semi-automated quantitative method to compare images with no subjective bias) thus facilitating visualisation of even the small distal coronary arteries. This improvement was obtained against a state-of-the-art navigation method (both sequence A and B were obtained with the same 2D iNAV approach), whose higher performance, compared to the conventional 1D NAV, was demonstrated in Studies 1 and 2.

CMRA studies in the paediatric population are limited. To the best of our knowledge this is the largest published paediatric CHD cohort and the first study testing Gd-BOPTA and

the proposed imaging scheme. Tandon *et al.* (Tandon et al., 2016) compared a T2prep “conventional” 1D NAV CMRA to an IR 1D NAV CMRA post gadofosveset trisodium (a high relaxivity blood pool agent) at 1.5 Tesla in a paediatric cohort (n=35; median age of 10.7 years; 18 under general anaesthesia or sedation). Comparatively, our images had higher spatial resolution (1.3cm³ versus 1.2-1.6cm³), achieved higher visual scores and more importantly, at shorter acquisition times (5.2 ± 1.5 versus 7:57 ± 4:06 minutes). Vasanaawala *et al.* (Vasanaawala et al., 2011) also evaluated a 1D NAV CMRA sequence post gadofosveset trisodium in a paediatric cohort (n=23; mean age of 4.5 years) under general anaesthesia/sedation support: the reported scan time was lower (4.4 minutes) but at the cost of lower spatial resolution (slice thickness 1–2.2 mm) and poor intra- and inter-observer correlations for the coronary arteries (no quantitative scoring was performed).

Gd-BOPTA has been shown to improve diagnostic coronary CMRA in adults, and its efficacy and safety profile makes it an appealing choice for coronary imaging in paediatrics. Moreover, the use of Gd-BOPTA and the described sequence design is an attractive alternative to streamline CMR studies by enabling, in a single examination, detailed functional (ischemia/viability) and anatomical (coronary) assessment. The incremental diagnostic value of combined CA imaging, myocardial perfusion and LGE assessment using a versatile agent such as Gd-BOPTA has already been shown in adults (Klein et al., 2008).

3.3.6. LIMITATIONS

Some limitations need to be acknowledged. First, although powered to identify any statistical significant difference between the two tested sequences, this was a single-centre study performed in a referral imaging department. Also, all scans were performed under general anaesthesia following the institutional practice and in the setting of a careful multidisciplinary clinical planning. Local practices vary, and this access to specialised personnel and equipment resources is not widely available. Nevertheless, general anaesthesia ensured prolonged cooperation, reliable breathing pattern as well as less HR fluctuations. If on the one hand, this might affect the transferability and comparability of these results with other studies performed in non-anaesthetised paediatric patients, on the other hand this allowed an objective head-to-head comparison of two similarly defined sequences, whilst assessing for potential confounding factors such as HR changes/gating efficiency during the

two different acquisitions (no differences in HR and acquisitions lengths were noted). As we have demonstrated that the gating approach used improves coronary imaging in awake adult patients with CHD and CAD of this thesis (Studies 1 and 2, respectively), we assume that such improvement is likely to occur in awake paediatric scans. Notably, this protocol could also be adapted to other CMR vendors and help to streamline the imaging service delivery.

In this study we have not formally assessed the diagnostic accuracy of the proposed sequence to screen for coronary stenosis/anomalies. On the one hand, this was not a predefined study end-point. On the other hand, there were not enough coronary anomalies in this study population to report on the accuracy of each sequence to be able to detect them. This would require a larger sample and, ideally, validation with invasive data, which without clinical justification, was deemed unethical in a cohort of paediatric patients. However, we expect that the increase in spatial resolution attained with this high-relaxivity contrast agent and sequence design would help to reduce flow-induced signal voids, partial volume artefacts and/or velocity-shear effects. This could allow a more accurate diagnosis and estimation of the severity of a coronary stenosis, particularly in the proximal segments, as demonstrated previously (Schneider et al., 2007; Yang, Q, et al., 2009).

Finally, we have not tested the proposed protocol at a higher field strength, which also has been shown to result in higher spatial resolution, SNR and CNR values between blood and myocardium. However unreliable VCG-triggering due to amplified magneto-hydrodynamic effects, frequent susceptibility artefacts, and increased T1 radiofrequency field distortions are known drawbacks.

3.3.7. CONCLUSIONS

In this work we have implemented the validated image-navigation approach and evaluated a novel sequence designed to maximise Gd-BOPTA properties (high-relaxivity and prolonged intravascular) and improve CMRA in paediatric patients with CHD. A direct comparison was performed between two image-navigated 3D SSFP CMRA sequences, one using a conventional T2 pre-pulse (pre-contrast), and one employing a different magnetisation scheme, with an IR pre-pulse and contrast-enhanced. Both sequences were acquired in the same patient during general anaesthesia, thus controlling for HR and breathing variations. Via this approach, we were able to make a direct comparison between

the two sequences and evaluate the benefits of introducing heavy T1-weighting in the post-contrast sequence. We had assumed that this would be beneficial to increase the signal from the coronary blood pool compared to the pre-contrast CMRA.

We have demonstrated that our proposed CMRA sequence resulted in improved visualisation of the coronary tree in small infants and young children regardless of the HR or body size and within a clinically acceptable scan time. This highly resolved 3D SSFP CMRA sequence could be easily implemented in a clinical protocol for paediatric CHD. We can therefore speculate that the use of this CMRA sequence design may allow to replace invasive cardiac catheterisation for diagnostic coronary imaging and preoperative planning in paediatrics, thus reducing the risks associated with such procedures.

4

CMR IMAGING

BIOMARKERS

This chapter presents two CMR imaging studies complementary to Study 6 (Chapter 5). In Study 4, we showed how the evaluation of left atrial function using CMR-feature tracking in hypertrophic cardiomyopathy patients could be useful for disease staging. This tracking tool was then used in Study 6 (Chapter 5) to parametrise the left atrium in the 0D heart LPN of the patient-specific computational model. In Study 5, we developed and tested a software for automated aortic centreline extraction and pulse wave velocity calculation using different CMR sequences. This automated tool was then also used in Study 6 for parametrisation of the 3D computational domains stiffness (aortic and pulmonary).

4.1. OVERVIEW

With each heartbeat, the ventricles pump oxygenated blood into the systemic/pulmonary arterial vasculature to be distributed to different organs and tissues and meet the body's metabolic demands. This interaction between the atria, the ventricles and the arterial vasculature upstream [i.e. atrial-ventricular-arterial coupling] (Miyoshi et al., 2011) is an important determinant of cardiovascular function (Chirinos, 2013). Coupling concerns two critical actions: that of the heart as a pump connected to an hydraulic system with a certain (after)load and the perfusion of the heart itself.

Studying cardiac performance is important, in both acquired and CHD, to assess underlying pathophysiology, provide prognosis and tailor therapy, and requires investigation of the properties of ventricle itself, but also of the modulating role of the arterial system on LV/RV function (i.e. ventriculo-arterial coupling).

Analysis of the P-V loops has been used to study ventricular-arterial coupling. The slope of the end-systolic P-V loop (E_{es}) has been shown to be a load-independent metric of the contractile function, of ventricular elastance at end-systole, and of the heart's interaction with the upstream vasculature (Borlaug and Kass, 2011; Davidson and Giraud, 2012). Making a number of simplified assumptions, Sunagawa *et al.* (Sunagawa et al., 1983, 1985) has related this slope to the arterial properties and proposed that it could be used as a lumped parameter of the impedance that the arterial tree offers to the stroke volume (effective arterial elastance). However, E_{es} determination conventionally requires invasively measured ventricular pressure and volumes recorded over a range of cardiac loading conditions, which has hampered its broader clinical application.

Key to understanding (atrial)ventricular-arterial interactions is the notion that the wall of the large arteries, and in particular of the aorta, is a complex 3D structure (the “fifth chamber of the heart”) that has two critical roles: it is both a conduit and a reservoir. As a conduit, it provides delivery of blood at adequate pressure to the peripheral organs and tissues (including the heart) to meet the demands of the body's metabolism. As a reservoir, it buffers each ventricular contraction and avoids sudden drops of arterial pressure during diastole (Cavalcante et al., 2011). The spatially variable histological structure of the aorta reflects this dual function: the media (the key element controlling the stress imposed on the wall) of the proximal aorta is rich in elastin fibres to support each ventricular systole and

accommodate the stroke volume, whereas the more distal aorta and branches become progressively stiffer, given the predominance of collagen fibres (Lee and Kamm, 1994).

With aging, the elastic fibres of the media of the proximal aorta are progressively replaced with more rigid collagen fibres. The genetics of this vascular remodelling is area of active research (Hayward et al., 2018). A simplified schematic of important concepts required to understand age-related vascular remodelling is provided in Figure 31 (right panel), which also depicts the linear and non-linear behaviour in elastic and biologic materials (left panel).

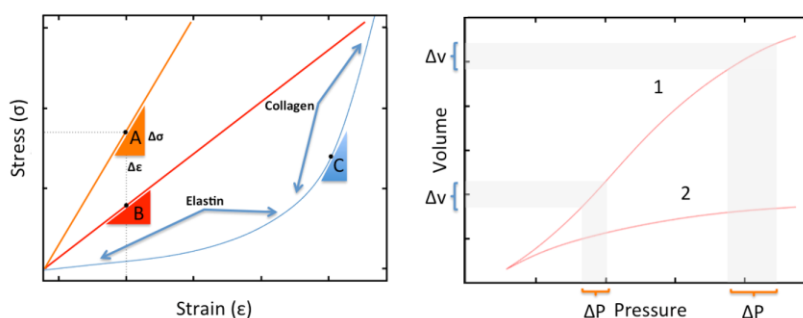


Figure 31

Left panel. The linear stiffness curves of two different materials (material A and material B). In an elastic material, stress (σ) is linearly proportional to strain (ϵ) and the relationship between stress and strain (stiffness, E) can be expressed by $E = \sigma/\epsilon$. In the graphs, material A has a steeper curve (stiffer material), indicating that for the same deformation (strain) higher degrees of stress are required. Curve C represents the typical stress-strain relationship in biological tissues such as blood vessels and heart. The curve is non-linear with a typical J-shape. The initial part of the curve is dominated by elastin fibres. The ascending limb of the curve represents the collagen-dominated response that occurs in these tissues at higher stresses. In other words, at higher stresses (pressure), the aorta has a stiffer behaviour, with smaller deformations for incrementing stresses. **Right panel.** Pressure to volume curve ($\Delta V/\Delta P$) representing the typical compliance of arterial tissue in young (curve 1) and in elderly individuals (curve 2). Compliance (C) is defined as a change in volume (ΔV) for a given change in pressure (ΔP), i.e. $C = \Delta V/\Delta P$. The compliance curve shows a non-linear relationship between volume and pressure. This means that when the tissue is exposed to higher pressures, it experiences smaller changes in volume for a given change in pressure. As apparent by both graphs in the above figure, arterial stiffness and compliance are inversely proportional to each other. V , volume. P , pressure.

The two studies we proceed to describe concern the biomechanical pathophysiology concepts aforementioned (i.e. atrial function, arterial wall properties, atrial-ventriculo-arterial coupling) and imaging tools and that were important in the conceptualisation and design of the PSCM model of Study 6 (Chapter 5). In Study 4 we describe how LA function assessment using CMR-feature tracking could prove useful for hypertrophic cardiomyopathy (HCM) staging – this tool was also used in Study 6 for parametrisation of the LA (volumes and elastance) in the 0D heart LPN of the PSCM. In Study 5, we present a novel tool for automated segmentation of aortic centrelines and PWV calculation from different CMR

sequences – this tool was used in Study 6 for defining the area change of the aorta and pulmonary arteries during the cardiac cycle and calculation of the corresponding vascular stiffness, which was then prescribed to the 3D domains of the PSCM.

4.2. STUDY 4: LEFT ATRIAL PERFORMANCE IN THE COURSE OF HYPERTROPHIC CARDIOMYOPATHY

4.2.1. BACKGROUND

HCM is an autosomal-dominant disorder of the myocardium caused, in the majority of cases (60 to 70%) by mutations in one of several sarcomere genes that encode components of the contractile apparatus (Ingles et al., 2015). The defining phenotypic feature of HCM is LV hypertrophy (LVH) [increased mass and wall thickness], not explained by abnormal loading conditions. Phenocopies of sarcomeric HCM, with similar patterns and extent of LVH, have been described in diseases associated with mutations in non-sarcomeric genes and with different patterns of inheritance (Lim et al., 2001; Sankaranarayanan and Fleming, 2013). With a prevalence of ~1:500 in the general population, it is the most common heritable cardiovascular disorder and an important cause of sudden cardiac death in young individuals and athletes (Veselka et al., 2017).

HCM has a heterogeneous clinical expression, with a highly age-dependent and incomplete penetrance of LVH (Ho, 2009). Most HCM patients are asymptomatic or have minor symptoms [e.g. fatigue, dyspnoea, chest pain on exertion] (Maron et al., 1999). Therefore, affected individuals are often diagnosed as a result of a detection of a murmur during routine examination, the identification of an abnormal ECG or during family screening.

The histological hallmarks of HCM are myocyte disarray with myocyte hypertrophy and replacement fibrosis (Maron and Maron, 2013; Chan et al., 2014). From an early age, HCM patients present an enlarged and disorganised architecture of the matrix collagen (part of the structural skeletal framework of the myocardium) when compared to their counterparts without evidence of cardiovascular disease or those with LVH secondary to systemic hypertension. The trigger for the increased collagen compartment remains unclear, but it has been attributed both to premature myocyte death caused by “stresses” imposed directly by

sarcomere mutations and neurohormonal pathways, and to later pathologic changes, including intracavitary obstruction, small-vessel disease and ischaemia (Ho et al., 2010). The intramural coronary arterioles have been shown to be structurally abnormal with decreased luminal cross-sectional area and impaired vasodilatory capacity resulting in blunted myocardial blood flow during stress (i.e., "small vessel ischemia"). Over time, repetitive bouts of small vessel ischaemia lead to myocyte cell death and ultimately repair in the form of replacement fibrosis (Shirani et al., 2000).

One of the most important challenges in HCM management is the identification of therapeutic biomarkers that could be useful for early stratification of patients that are at high risk of evolution from a "stable" disease towards LV dysfunction and heart failure or that are at increased risk of ventricular arrhythmias and sudden cardiac death.

In HCM, LV systolic impairment is usually an end-stage disease finding, while almost all patients have some degree of diastolic dysfunction (Nagueh et al., 2003). Because the presence of subtle changes in LV filling and relaxation could identify patients with preclinical disease (without LVH), there has been an extensive search for accurate, non-invasive methods for quantifying LV diastolic dysfunction severity.

Doppler-echocardiography provides the most practical routine clinical approach for evaluating LV diastolic function, with a large clinical and experimental evidence supporting its use (Nagueh et al., 2016). However, as systolic function, assessment of LV diastole is loading and operator dependent, and differentiation between normal and abnormal profiles can be complicated by an overlap of Doppler indices between healthy individuals and HCM patients. Not surprising, the utility of most Doppler-derived diastolic parameters for predicting clinically meaningful outcome measures in HCM remains to be clarified (Rakowski and Carasso, 2007).

Over the last two decades, CMR has emerged as an important imaging technique in the diagnosis and management of HCM. Besides being the gold standard for the assessment of ventricular volumes and function with a high degree of reproducibility (Grothues et al., 2002), CMR can provide a detailed characterisation of the different HCM phenotypes through accurate identification and quantification of both LVH and fibrosis using LGE techniques (Maron, 2012). Quantitative LV LGE has materialised into an important parameter to grade the severity of HCM, providing predictive information regarding sudden

cardiac death as well as adverse LV remodelling resulting in systolic dysfunction (Bruder et al., 2010; O’Hanlon et al., 2010; Chan et al., 2014). Furthermore, CMR can provide an accurate assessment of the left atrial (LA) remodelling, difficult in 2D echocardiography in part because of the LA’s complex geometry, intricate fibre orientation and the variable contributions of its appendage and pulmonary veins.

LA enlargement mirrors LV diastolic dysfunction in HCM and is an established marker of disease severity and predictor of adverse cardiovascular events (Yang, Q, et al., 2009; Hoit, 2014; Farhad et al., 2017). Currently, LA remodelling is considered a time-dependent response of atrial myocytes to varying “stressors” - electrical, mechanical, and metabolic (Thomas and Abhayaratna, 2017).

Recently, sophisticated, non-invasive indexes of LA function assessing its different functional components (the reservoir function for pulmonary venous return during ventricular systole, the conduit function for pulmonary venous return during early ventricular diastole, and a booster pump function that augments ventricular filling during late ventricular diastole) have been shown to provide prognostic information beyond LA size and volume (Habibi et al., 2014; Farhad et al., 2017). However, available data on LA functional abnormalities in HCM is inconsistent. While some researchers have described increases in LA contractile booster pump function together with impaired reservoir and conduit functions (Anwar et al., 2007, 2008; Kowallick et al., 2014), others have reported impairment of all LA functional components – reservoir, conduit and contractile (Paraskevidis et al., 2009; Eshoo et al., 2010).

LVH seems to be the major independent factor altering LA-LV mechanics (Urbano-Moral et al., 2014). However, the determinants and the degree of LA dysfunction in different HCM phenotypes are not fully understood. We assume that LVH and fibrosis, both representing substrates of LV diastolic dysfunction, are associated with LA dysfunction in HCM. To try to clarify this, in this study we have characterised LA mechanics in HCM using fractional volume changes as well as CMR feature-tracking derived strain and strain rate based on conventional 2D cine images (Kowallick et al., 2014), and explored their relationship with LVH and fibrosis.

4.2.2. MATERIAL AND METHODS

4.2.2.1. STUDY POPULATION

Consecutive patients with suspected HCM referred for CMR evaluation in our Department were recruited. Inclusion criterion was CMR demonstration of a hypertrophied and non-dilated LV (wall thickness $\geq 15\text{mm}$; or $\geq 13\text{mm}$ in case of a first-degree relative with HCM) in the absence of another systemic or cardiac disease that could justify LVH. Exclusion criteria were: (1) history of atrial fibrillation or atrial fibrillation by the time of CMR; (2) history of myocardial infarction or myocarditis; (3) history of septal myectomy or alcoholic septal ablation; (4) severe claustrophobia, impaired renal function or metallic implants including pacemaker and defibrillator devices. An age- and gender-matched control group of healthy subjects was included. The study was conducted in accordance with the standards set by the Local Institutional Ethics Committee and informed consent was obtained from all patients.

4.2.2.2. CMR IMAGING PROTOCOL

CMR was performed in 1.5 and 3 Tesla scanners (Philips, Best, the Netherlands) using standard VCG-gated SSFP cines in 3 long-axis planes and sequential short-axis planes covering the LV from the atrio-ventricular ring to the apex. LGE images were acquired 10 to 20 minutes after intravenous administration of 0.2 ml/kg (gadobutrol, Gadovist®, Bayer AG, Leverkusen, Germany) using a segmented 2D IR or phase-sensitive IR sequence in identical planes as for cine imaging. The appropriate inversion time (TI) was set using a Look-Locker sequence (Look and Locker, 1970).

4.2.2.3. DATA ANALYSIS

LV volumes, mass and ejection fraction (EF) were measured using standard volumetric techniques using a commercially available software (cvi⁴²®, Circle Cardiovascular Inc. Calgary Canada version 5.2.2). LV endocardial and epicardial contours were drawn in the LV short-axis cine images excluding the papillary muscles. Maximum LV wall thickness was defined as the greatest dimension at any site within the LV myocardium, at end-diastole.

LV long- and short-axis LGE images were first visually assessed for the presence of LGE by two experienced observers. Quantification of LGE was then performed by one observer on all LGE-positive studies, by manually adjusting a grey-scale threshold to define areas of LGE in the short-axis planes using a commercially available software (cvi⁴²®, Circle Cardiovascular Inc. Calgary Canada version 5.2.2), as previously described (Chan et al., 2014). The “normal” remote myocardium was first defined and then the software automatically identified the LGE areas based on the signal intensity (mean plus five standard deviation), which were then inspected and corrected in all slices. The identified areas were summed to generate a total volume of LGE, expressed as a proportion of total LV myocardial mass. According to the proportion of LGE, the study group was divided into four subgroups (Chan et al., 2014): (1) non-LGE; (2) mild LGE $\leq 10\%LV$; (3) intermediate LGE 11-19%LV; (4) severe LGE $\geq 20\%LV$.

LA phasic volumes were quantified by semi-automated tracking of the LA area and length in the two and four chamber views excluding pulmonary veins and the LA appendage, as previously described (Dodson et al., 2014; Kowallick et al., 2015). LA volumes were calculated according to the biplane area-length method (Hudsmith et al., 2007; Dodson et al., 2014),

$$LA \text{ volume indexed} = \frac{0.85 \times LA4C \times LA2C}{L \times BSA}$$

Equation 9

where LA4C and LA2C are the maximal planimetered LA area in four and two chamber views, and L is the LA long-axis shortest length determined as the perpendicular distance from the middle of the plane of the mitral annulus to the superior aspect of the LA, measured in both the four and two chamber views. LA volumes were assessed at LV end-systole (LAV_{max}), at LV diastole prior to LA contraction (LAV_{pac}) and at late LV diastole after LA contraction [LAV_{min}] (Dodson et al., 2014; Pellicori et al., 2015). Total LA emptying fraction (LAEF Total, corresponding to the LA reservoir), passive LA emptying fraction (LAEF Passive, corresponding to the LA conduit function) and active LA emptying fraction

(LAEF Booster, corresponding to the LA contractile booster pump function) were defined as fractional volume changes according to the following equations:

$$LAEF_{Total} = \frac{(LAV_{max} - LAV_{min}) * 100}{LAV_{max}}$$

Equation 10

$$LAEF_{Passive} = \frac{(LAV_{max} - LAV_{pac}) * 100}{LAV_{max}}$$

Equation 11

$$LAEF_{Booster} = \frac{(LAV_{pac} - LAV_{min}) * 100}{LAV_{pac}}$$

Equation 12

LA strain and SR were analysed using commercially available CMR feature-tracking software (TomTec Imaging Systems, Unterschleissheim, Germany) as previously described (Kowallick et al., 2014). This is a post-processing optical-flow based method that tracks certain features (e.g. LA wall, myocardium) in successive cine images in order to measure their displacement, and thus requires no additional image acquisition (Schuster et al., 2016). LA endocardial borders were tracked in the two- and four-chamber cine views (see Figure 32). Three aspects of LA strain were analysed: passive strain (ϵ_e , corresponding to the atrial conduit function), active strain (ϵ_a , corresponding to the atrial contractile booster pump function) and total strain, the sum of passive and active strain (ϵ_s , corresponding to the atrial reservoir function). Accordingly, three strain rate parameters were evaluated: peak positive strain rate (SRs, corresponding to the atrial reservoir function), peak early negative strain rate (SR_e, corresponding to the atrial conduit function) and peak late negative strain rate [SR_a, corresponding to the atrial contractile booster pump function] (Hoit, 2014; Kowallick et al., 2015).

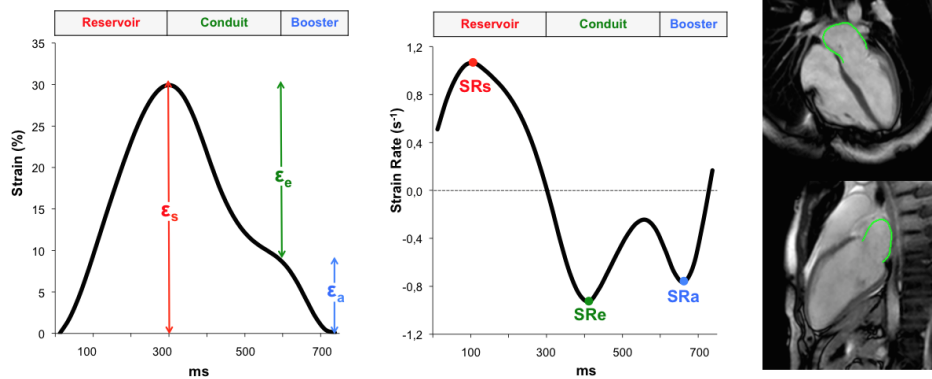


Figure 32

LA strain (left) and strain rate (middle) profiles and corresponding 2D SSFP cine images tracking (right). Three aspects of LA strain are displayed: passive strain (ϵ_e , corresponding to the atrial conduit function), active strain (ϵ_a , corresponding to the atrial contractile booster pump function) and total strain, the sum of passive and active strain (ϵ_s , corresponding to the atrial reservoir function). Strain rate profiles resulted in peak positive strain rate (SRs, corresponding to the atrial reservoir function), peak early negative strain rate (SRe, corresponding to the atrial conduit function) and peak late negative strain rate (SRa, corresponding to the atrial contractile booster pump function).

4.2.2.4. STATISTICAL ANALYSIS

Continuous variables were tested for normal distribution using the Shapiro-Wilk test and are presented as mean \pm standard deviation. Categorical variables are presented as frequencies (percentages).

Differences between HCM and controls were evaluated with the Student's *t* test or Mann-Whitney U test, as appropriate for continuous variables or using the Chi-square test for categorical variables. Differences between the HCM groups regarding the extent of LV LGE (non-LGE [n=15], percentage of LGE $\leq 10\%$ [n=34], 11-19% [n=17] and $\geq 20\%$ [n=7]) were evaluated with a one-way ANOVA and Bonferroni *post hoc* correction or with the Kruskal-Wallis test and the Mann-Whitney-U test for *post hoc* testing, as appropriate.

A multivariable linear regression was conducted using the maximum LV wall thickness, the indexed LV mass, and %LGE as the dependent variable and each LA parameter as an independent variable. To avoid collinearity, correlations between continuous variables were tested using Spearman correlation coefficients and variables with $r > 0.50$ were not included in the same multivariable model. The models were adjusted for (1) indexed LV mass, %LGE and presence of mitral regurgitation; (2) LV maximum wall thickness, %LGE and presence of mitral regurgitation; (3) LV maximum wall thickness, indexed LV mass and presence of mitral regurgitation. Pearson correlation coefficients between LV LGE and LA

parameters were calculated. Intra- and inter-observer reproducibility for LA parameters and volumes (20 randomly selected subjects) and LV LGE quantification (10 randomly selected subjects) were assessed by intraclass correlation coefficients. All statistical tests with p values < 0.05 were considered statistically significant. Statistical analysis was performed using IBM SPSS Statistics version 22.0 for Macintosh (IBM Corp, Armonk, NY).

4.2.3. RESULTS

A total of 90 patients met the inclusion criteria for the study. Of note, seven had a history of paroxysmal atrial fibrillation and further five patients were in atrial fibrillation at the time of the CMR exam. In three patients, the LGE images were considered of poor quality to allow LGE quantification. Additionally, in two patients, the image quality of the cine images was not sufficient to allow good tracking of the LA wall displacements using CMR feature-tracking. These patients were excluded from the analysis and the final cohort was composed of 73 HCM patients (55 men, 75%) with an average age of 59 ± 13 years [25–85]. Concomitantly, 23 healthy age and gender matched controls were enrolled (17 men [74%], with an average age of 55 ± 11 years [33–71]).

Table 14 summarises the baseline demographic, clinical and CMR data collected in both the HCM patients and controls. Differences between these two groups were evaluated with the appropriate statistics, as previously described, and the results are presented in the first three columns. Differences between these same variables within HCM subgroups, categorised according to the extent of LV fibrosis, in turn quantified with LGE, are shown in the other columns. It is noteworthy that HCM patients with $\geq 20\%$ LGE had also more severe heart failure symptoms and higher LV mass.

4.2.3.1. LGE QUALITATIVE AND QUANTITATIVE ANALYSIS

Visual inspection detected LGE in 58 HCM patients (79%). In turn, quantitative LGE analysis showed that 34 patients had mild LGE ($\leq 10\%$), 17 patients had intermediate LGE (11-19%) and 7 patients showed severe LGE ($\geq 20\%$).

There were no significant differences in LV volumes and function between the defined HCM LGE-subgroups.

			<i>P</i>	All HCM (n=73)				<i>P</i> *
	HCM (N=73)	Controls (N=23)		Non-LGE (N=15)	≤10% (N=34)	11-19% (N=17)	≥20% (N=7)	
Age, y	59±13	55±11	0.27	62±10	56±16	61±12	61±9	0.44
Male, n (%)	55 (75)	17 (74)	0.55	10 (67)	27 (79)	12 (71)	6 (86)	0.69
Weight, kg	89±22	82±24	0.14	88±17	88±25	86±16	99±32	0.68
Height, m	1.7±0.2	1.7±0.1	0.98	1.7±0.1	1.7±0.2	1.7±0.1	1.7±0.3	0.22
BSA, m²	2.0±0.2	1.9±0.2	0.09	2.0±0.3	2.0±0.3	2.0±0.2	2.1±0.2	0.74
Heart Rate, bpm	69±11	65±7	0.07	73±11	69±12	70±6	63±14	0.25
NYHA Class, n (%)								
Mean	1.7±0.8	---	---	1.6±0.6	1.4±0.7 [†]	1.9±0.7	2.7±0.5 [‡]	<0.001
I	36 (49)	---	---	7 (47)	24 (70) [§]	5 (29)	---	0.001
II	23 (32)	---	---	7 (47)	6 (18) [§]	8 (47)	2 (29)	0.004
III/IV	14 (19)	---	---	1 (6)	4 (12)	4 (24)	5 (71) [‡]	0.002
CMR variables								
LVEDV, ml/m ²	74±20	75±15	0.86	72±22	76±16	67±13	89±37	0.20
LVESV, ml/m ²	26±16	28±8	0.09	25±13	26±13	20±7	41±35	0.82
LVSV, ml/m ²	48±11	47±9	0.56	47±10	50±11	47±12	48±16	0.71
CO, l/min/m ²	3.3±0.9	2.9±0.8	0.06	3.4±0.9	3.3±1.0	3.3±0.8	3.3±0.9	0.99
EF, %	66±11	64±5	0.034	66±8	66±11	70±9	59±19	0.38
Max. wall thickness, mm	18±3	8±1	<0.001	15±1	17±2 [†]	20±4	18±3	<0.001
LV mass, g/m ²	87±32	47±14	<0.001	68±19	84±26	88±34	134±33 [‡]	<0.001
MR on SSFP, n (%)	30 (41)	---	---	4 (27)	12 (35)	9 (53)	5 (71)	0.14
LVOT, n (%)	17 (23)	---	---	2 (13)	7 (21)	6 (35)	2 (29)	0.49
LGE, %	9±9	---	---	---	5±3	15±3	29±9	<0.001[¶]
SCD risk factors (0-4), n (%)								
Mean	0.5±0.7	---	---	0.3±0.5	0.4±0.7	0.8±1.0	0.3±0.5	0.19
Family History of SCD	14 (19)	---	---	2 (13)	5 (15)	5 (29)	2 (29)	0.51
Unexplained Syncope	11 (15)	---	---	2 (13)	4 (12)	5 (29)	---	0.23
NSVT on Holter*	7 (10)	---	---	---	4 (12)	3 (18)	---	0.47
Max. LVH ≥ 30 mm	1 (1)	---	---	---	---	1 (6)	---	---
Locations of LGE, n (%)								
Septum	45 (62)	---	---	---	23 (68)	15 (88)	7 (100)	<0.001[¶]
LV free wall	40 (55)	---	---	---	18 (53)	15 (88)	7 (100)	<0.001[¶]
Apex	20 (27)	---	---	---	10 (29)	5 (29)	5 (71) [‡]	0.006
Only at RV insertion	4 (6)	---	---	---	4 (12)	---	---	---
Pattern of LVH, n (%)								
Septal asymmetrical	55 (75)	---	---	11 (73)	25 (74)	13 (77)	6 (86)	0.92
Symmetrical (concentric)	2 (3)	---	---	1 (7)	---	1 (6)	---	0.45
Apical	13 (18)	---	---	2 (13)	8 (24)	2 (12)	1 (14)	0.69
Lateral asymmetrical	3 (4)	---	---	1 (7)	1 (3)	1 (6)	---	0.85
Drugs, n (%)								
β-Blockers	40 (55)	---	---	7 (47)	18 (53)	11 (65)	4 (57)	0.77
CAC	18 (25)	---	---	3 (20)	6 (18)	5 (29)	4 (57)	0.15
Diuretics	9 (12)	---	---	1 (7)	4 (12)	2 (12)	2 (29)	0.54

Table 14

A comparison for the different demographic data, clinical and CMR variables between HCM patients and controls is shown in the first three columns. In the other columns, a comparison between the different HCM subgroups (according to the extent of LGE) is presented, for these same variables, using the appropriate statistics as described in text. Bold values indicate statistical significance.

*Comparison between HCM subgroups according to LGE extent: † ≤10% versus 11-19%; ‡ ≥20% versus all other groups; § ≤10% versus all other groups; || non-LGE versus all other groups; ¶ each group versus all other groups.

#Holter was performed in 50 of 73 study patients.

BSA, body surface area; CCA, calcium channel antagonists; CMR, cardiovascular magnetic resonance; CO, cardiac output; EF, ejection fraction; HCM, hypertrophic cardiomyopathy; LGE, late gadolinium enhancement; LV, left ventricular; LVH, left ventricular hypertrophy; LVEDV, left ventricular end-diastolic volume; LVESV, left ventricular end-systolic volume; LVSV, left ventricular stroke volume; NYHA, New York Heart

Association Functional Class; SCD, sudden cardiac death; SSFP, steady-state free precession images; VT, ventricular tachycardia.

4.2.3.2. LA FUNCTION IN HCM AND CONTROLS

A comparison between of the LA volumes and dynamics quantified by fractional volume changes and deformation indexes (strain, SR) in the HCM and healthy control group is presented in Table 15.

LA volumes (maximum, minimum and prior to atrial contraction) were higher in the HCM patients. LA reservoir and conduit functions as assessed by both techniques showed significantly lower values in HCM when compared to the healthy controls. In contrast, there was no significant difference between the two groups in relation to LA contractile booster pump function quantified by both methods.

	All HCM (n=73)							p value
	HCM (N=73)	Controls (N=23)	p value*	Non-LGE (N=15)	≤10% (N=34)	11-19% (N=17)	≥20% (N=7)	
LA Reservoir function								
LAEF Total, %	51±12	59±6	0.001	57±10	55±8	47±9‡	31±9§	<0.001
εs, %	23±7	30±7	<0.001	27±7	25±6	20±5‡	12±5§	<0.001
SRs, s ⁻¹	0.9±0.3	1.2±0.3	0.001	1.1±0.2	1.0±0.3	0.9±0.2	0.6±0.3§	0.001
LA Conduit function								
LAEF Conduit, %	22±10	32±7	<0.001	26±14¶	25±8#	16±6	14±4	<0.001
εe, %	10±5	16±5	<0.001	12±6¶	11±4#	8±3	6±2	0.001
SRe, s ⁻¹	-0.6±0.2	-0.9±0.4	<0.001	-0.6±0.2¶	-0.6±0.2#	-0.4±0.2	-0.4±0.1	<0.001
LA Booster pump function								
LAEF Booster, %	38±10	40±8	0.634	42±7	39±8	37±9	20±10§	<0.001
εa, %	13±5	13±4	0.301	14±5	13±5	12±4	6±5§	0.001
SRa, s ⁻¹	-1.1±0.4	-1.3±0.4	0.201	-1.3±0.3	-1.2±0.4	-1.1±0.4	-0.6±0.4§	0.001
LA volume								
LAVmax, ml/m ²	52±17	38±7	<0.001	45±16	48±12	57±17	72±20§	0.001
LAVmin, ml/m ²	26±13	16±4	<0.001	20±9¶	22±8	31±12	50±16§	<0.001
LAVpac, ml/m ²	41±15	26±6	<0.001	34±15¶	36±11	48±14	62±15§	<0.001

Table 15

Left atrial dynamics in patients with HCM and controls groups as well as within the different HCM subgroups defined according to the extent of LGE. LA, left atrial; LAEF Booster, LA contractile emptying fraction; LAEF Conduit, LA conduit emptying fraction; LAEF Total, LA total emptying fraction; LAVmax, maximum LA volume; LAVmin, LA minimum volume; LAVpac, LA volume prior to atrial contraction; εs, LA total strain; εe, LA conduit strain; εa, LA contractile strain; SRa, LA contractile strain rate; SRe, LA conduit strain rate; SRs, LA total strain rate. Bold values indicate statistical significance.

‡ 11-19% versus all other groups; § ≥20% versus all other groups; || non-LGE versus all other groups; ¶ non-LGE versus 11-19% and ≥20%; # ≤10% versus 11-19% and ≥20%.

* Comparison between HCM (n=73) and Controls (n=23).

** Comparison between HCM subgroups according to LGE extent.

4.2.3.3. ASSOCIATION OF LA FUNCTION WITH LV MAXIMUM WALL THICKNESS, LV MASS AND LV FIBROSIS

The results of the multivariable regression performed to evaluate the presence of any association between LV parameters (maximum wall thickness, indexed LV mass and fibrosis) and the LA functional components and volumes are summarised in Table 16.

We found no association between LV maximum wall thickness and LA functional components or volumes. Notably, LA volumes (maximum, minimum and prior to LA contraction) were associated with indexed LV mass, whilst there was no association with LA functional components. Finally, all LA functional components and volumes showed an association with LV LGE.

When analysing LA functional components and volumes in the different HCM subgroups stratified according to the extent of LV fibrosis, we found that LA reservoir and contractile function were significantly lower in patients with severe LGE ($\geq 20\%$) than in those with intermediate LGE (11-19%). This difference in LA functional components was paralleled by higher LA volumes. Notably, there were no differences in conduit function between the intermediate and severe fibrosis HCM subgroups. Furthermore, we found no significant differences in LA conduit and contractile functions or LA volumes in the non-LGE and LGE $\leq 10\%$ HCM subgroups. However, there was a significant difference in SR-derived LA reservoir function (SRs) between these two subgroups.

In comparison with healthy controls, LA conduit function was impaired in non-LGE HCM patients and in those with mild LV LGE (Figure 33). In contrast, LA contractile booster pump function was impaired only in HCM patients with severe LV LGE.

	LVMWT ⁽¹⁾		LV mass ⁽²⁾		%LGE ⁽³⁾	
	β	p	β	p	β	p
LA Reservoir function						
LAEF Total, %	-0.305	0.125	-0.065	0.726	-0.716	<0.001
ϵ_s , %	-0.191	0.246	-0.123	0.414	-0.525	<0.001
SRs, s ⁻¹	-0.127	0.404	-0.186	0.162	-0.378	0.005
LA Conduit function						
LAEF Conduit, %	-0.268	0.108	0.007	0.964	-0.528	<0.001
ϵ_c , %	-0.077	0.633	-0.182	0.202	-0.434	0.001
SRe, s ⁻¹	0.216	0.170	0.191	0.181	0.347	0.017
LA Booster pump function						
LAEF Booster, %	-0.113	0.490	-0.073	0.625	-0.536	<0.001
ϵ_a , %	-0.128	0.363	-0.017	0.898	-0.353	0.004
SRa, s ⁻¹	0.153	0.259	0.079	0.526	0.270	0.033
LA volume						
LAVmax, ml/m ²	0.001	0.991	0.330	0.012	0.350	0.014
LAVmin, ml/m ²	0.109	0.557	0.325	0.042	0.626	<0.001
LAVpac, ml/m ²	0.097	0.578	0.366	0.012	0.515	<0.001

Table 16

Association of left atrial mechanics and volumes with (1) LV maximum wall thickness, (2) indexed LV mass and (3) %LGE in patients with HCM. The table illustrates multivariable regression analyses of the association of left atrial (LA) functional parameters with left ventricular (LV) hypertrophy and fibrosis. Each row represents a separate multivariable model with (1) *LV maximum wall thickness (LVMWT)*; (2) *Indexed LV mass*; and (3) *%LGE* as the dependent variable and the LA parameter as the independent variable, respectively. Bold values indicate statistical significance.

(1) adjusted for age, gender, indexed LV mass, %LGE and presence of mitral regurgitation.

(2) adjusted for age, gender, LV maximum wall thickness, %LGE and presence of mitral regurgitation.

(3) adjusted for age, gender, LV maximum wall thickness, indexed LV mass and presence of mitral regurgitation.

Abbreviations as in previous tables.

A comparison between the LA strain and SR profiles in two selected HCM cases with mild (A) and severe (B) LV LGE is shown in Figure 34.

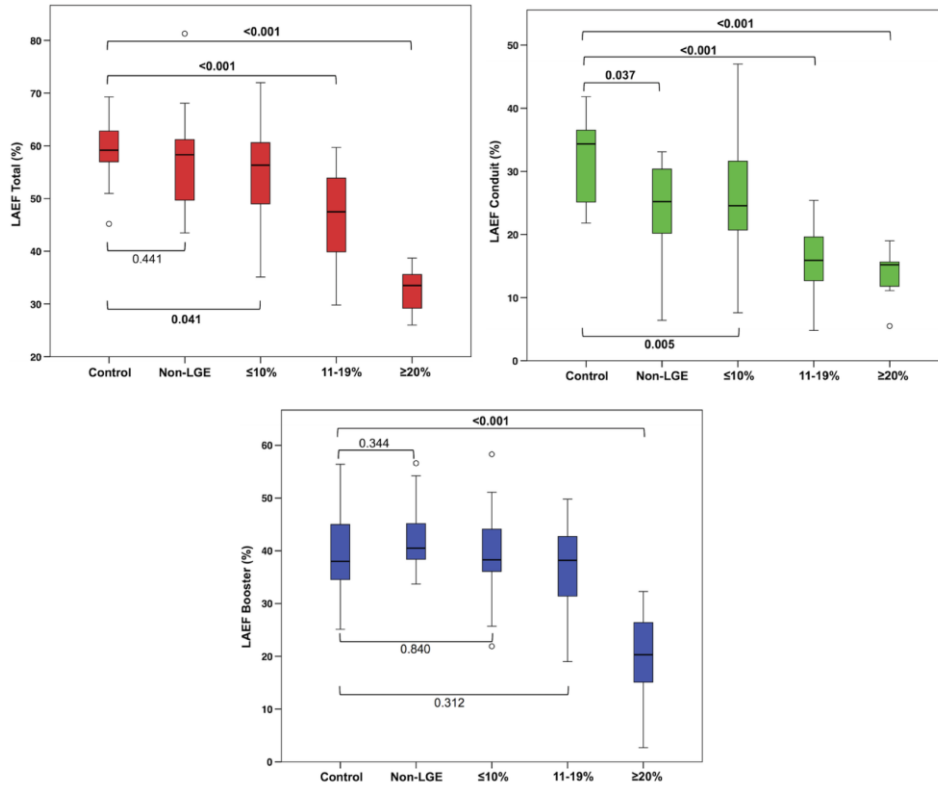


Figure 33

Box plots comparing LA reservoir (upper left panel), LA conduit (upper right panel) and LA contractile booster pump functions (bottom panel) quantified by LA emptying fractions (LAEF) in healthy controls and HCM patients, according to the extent LV fibrosis (LGE).

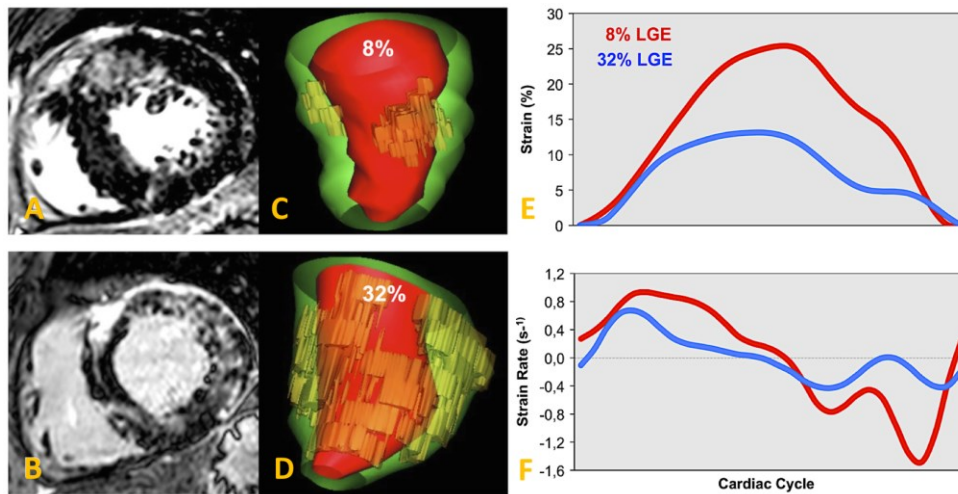


Figure 34

Panels A and B show the basal short-axis LGE images from two selected HCM patients with mild (A) and severe (B) fibrosis (8% versus 32%, respectively). **Panels C and D** present the 3D LV “scar” models generated after segmenting the whole short-axis LGE stack (red: endocardium; green: epicardium; yellow: areas of LGE). **Panels E and F** show the corresponding LA strain and LA strain rate profiles. Impaired LA deformation is evident from the strain and strain rate curves of the HCM patient with severe LGE.

The scatter plots in Figure 35 display the association between LA dynamics/volumes and LV LGE. Overall, more extensive LV fibrosis was associated with more impaired LA reservoir, conduit and booster pump functions. The highest correlation was found between LAEF Total and %LGE ($r = -0.76, p < 0.001$). LV fibrosis was also associated with increased LA volumes. Correlations followed the same patterns in HCM patients with and without mitral regurgitation and LV outflow tract obstruction (LVOTO).

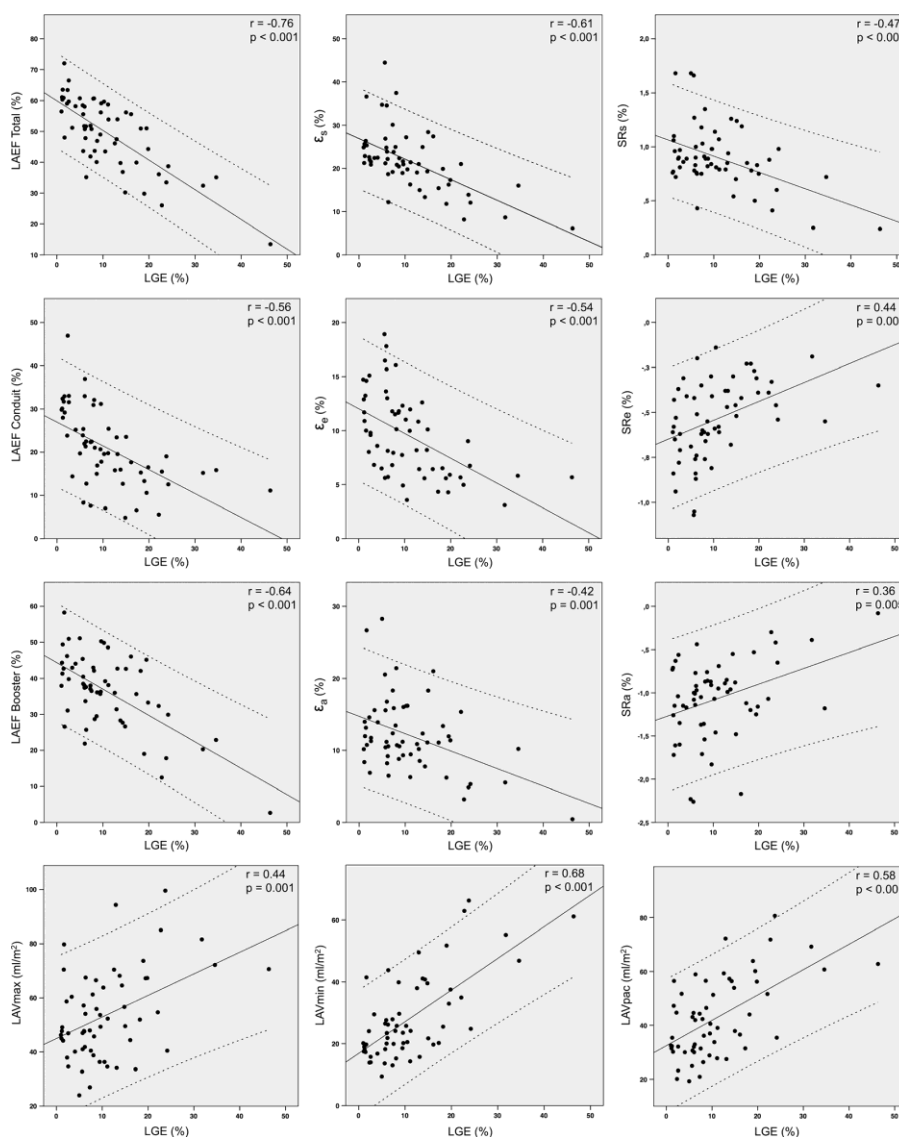


Figure 35

Scatter plots showing the Pearson correlations of LA parameters and %LGE. All LA functional parameters and volumes showed a significant correlation with the extent of LV LGE, with LAEF Total showing the highest ($r = -0.76, p < 0.001$) and SRa showing the weakest correlation ($r = 0.36, p = 0.005$). Constant line: line of best-fit; dashed lines: 95% confidence interval. Abbreviations as in previous tables.

4.2.3.4. REPRODUCIBILITY

Overall, there was excellent intra and inter-observer reproducibility for the LA functional components as derived from fractional volume changes, strain and SR as well as for LA volumes and for the LV LGE quantification, as summarised in Table 17. The intra- and inter-observer intraclass correlation coefficients ranged between 0.84 and 0.99 for all LA functional components or volumes, whereas they were 0.99 and 0.98 for intra- and inter-observer variability in the quantification of LV LGE, respectively.

	Intra-observer		Inter-observer	
	ICC	CI	ICC	CI
LA Reservoir function				
LAEF Total	0.98	0.95-0.99	0.96	0.91-0.99
ϵ_s	0.99	0.98-1.00	0.98	0.96-1.00
SRs	0.95	0.88-0.98	0.88	0.69-0.95
LA Conduit function				
LAEF Conduit	0.94	0.85-0.98	0.92	0.81-0.97
ϵ_c	0.98	0.95-0.99	0.98	0.95-0.99
SRe	0.98	0.94-0.99	0.96	0.89-0.98
LA Booster pump function				
LAEF Booster	0.95	0.88-0.98	0.86	0.63-0.94
ϵ_a	0.97	0.91-0.99	0.97	0.92-0.99
SRa	0.98	0.95-0.99	0.98	0.94-0.99
LA volume				
LAVmax	0.99	0.98-1.00	0.84	0.61-0.94
LAVmin	0.99	0.98-1.00	0.90	0.75-0.96
LAVpac	0.99	0.98-1.00	0.93	0.81-0.97

Table 17

Reproducibility of left atrial dynamics and volumes in 20 randomly selected subjects. Abbreviations as in previous tables.

4.2.4. DISCUSSION

It was the aim of this work to examine LA mechanics in HCM. In light of the pathophysiological relation between LA and LV mechanics (i.e. atrial-ventricular coupling), we have assumed that the extent of LVH and fibrosis was related to LA remodelling (i.e. enlargement and dysfunction) frequently described in HCM patients.

In recent years, there has been a resurgence of interest in the assessment of LA size and function as it provides a mirror into the LV diastolic function, known to be impaired in the early stages of HCM. Despite being a simpler metric compared to other diastolic imaging parameters, specific monitoring of LA remodelling has not been incorporated into clinical

decision-making (Hoit, 2014). Inconsistencies in LA functional abnormalities reported in previous studies have likely contributed to this.

In our work, we have quantified LA dynamics from standard two and four chamber CMR cine images using fractional volume changes as well as CMR feature-tracking derived strain and SR parameters. The results provide several insights into LA function in HCM in our cohort: (1) LA enlargement was associated with both the extent of LVH and LV fibrosis; (2) LA functional abnormalities were related to the extent of LV fibrosis but not to LVH; (3) LA conduit function was impaired in the early stages of HCM characterised by absent or mild LV fibrosis; (4) LA contractile booster pump function was preserved in HCM with absent to intermediate LV fibrosis but was impaired in HCM patients with severe LV fibrosis.

4.2.4.1. LA MECHANICS IN HCM

LA functional abnormalities have been previously described in HCM using echocardiography-based deformation imaging (Paraskevaïdis et al., 2009). More recently, these findings have been confirmed using sophisticated, less operator dependent and highly reproducible CMR feature-tracking (Kowallick et al., 2014). The results of the current work suggest that the discrepancies in LA dysfunction reported in previous studies most likely resulted from including patients in different stages of the disease. In fact, our data suggests that LA reservoir function progressively deteriorates during the course of the disease. In contrast, impaired LA conduit function appears to be present in the early stages of the disease characterised by absent or mild LV fibrosis. Our results also suggest a trend toward increased LA contractile booster pump function in HCM with absent LV fibrosis. However, this difference was not statistically significant. Furthermore, LA booster pump function remained preserved in patients with mild and intermediate LV fibrosis, and was only impaired in those with severe LV fibrosis. Notably, HCM patients with severe LV fibrosis were more often in NYHA class III/IV, although there was no statistically significant difference in LV volumes or function between the different HCM subgroups stratified according to the extent of LV LGE.

In light of these findings, we speculate that preserved LA booster pump function represents a possible compensatory mechanism to maintain LV filling and stroke volume as the disease progresses, and its deterioration could contribute to heart failure symptoms in

HCM. Research in heart failure suggests that LA contractile booster pump function is important for preserving cardiac output (Hoit and Gabel, 2000), modulating PAWP (Rahimtoola et al., 1975) as well as in arrhythmogenesis (Negishi et al., 2016), and its impairment with exercise contributes to the development of acute dyspnoea (Melenovsky et al., 2007). Whether or not similar mechanisms apply to HCM remains to be demonstrated.

4.2.4.2. ASSOCIATION OF LA MECHANICS WITH LVH AND FIBROSIS

LA structural and/or functional remodelling is a complex multifactorial process that is poorly understood and whose magnitude varies: it is thought to be dependent on the type, severity, and duration of exposure to varying external “stressors” (Thomas and Abhayaratna, 2017). In HCM, there is a strong correlation between the severity of LV diastolic dysfunction and LA remodelling (Yang et al., 2005; Ho et al., 2009; Maron et al., 2014; Farhad et al., 2017; Debonnaire et al., 2017). The morphological substrates of LV diastolic dysfunction in HCM are mainly represented by LVH and replacement fibrosis (Rakowski and Carasso, 2007). Accordingly, the results of our study showed an association between LVH and LA enlargement, whereas LV fibrosis assessed by LGE was associated with both LA enlargement and functional abnormalities. This finding is consistent with the fact that the presence of fibrosis represents a more severe spectrum of the disease, regardless of the degree of LVH. Thus, we assume that at an early stage of the disease, the occurrence of LV diastolic dysfunction is predominantly reflected in the LA as an increase in size. With disease progression, increased LV wall thickness due to myocyte hypertrophy and an expanded extracellular matrix (resulting in interstitial and replacement fibrosis) results in raised LV filling pressures and further relaxation impairment. This in turn leads to additional LA enlargement paralleled by LA dysfunction. As LA remodelling signals the presence of subtle changes in LV filling, it may prove to be an important metric to identify patients with preclinical disease as well as a marker of disease progression.

Previous research has demonstrated that LA dysfunction is more common in patients with HCM than in subjects with LVH secondary to hypertension (Eshoo et al., 2010) or physical training (Gabielli et al., 2012), despite all having a similar LV mass. Corroborating our findings, neither the grade of mitral regurgitation (Eshoo et al., 2010) nor the presence

of LVOTO (Paraskevaïdis et al., 2009), frequently observed in HCM patients, have been shown to be sufficient predictors of abnormal LA function in HCM.

In our study, LA mechanics were evaluated by fractional volume changes as well as by CMR feature-tracking derived strain and SR. LAEF showed a closer correlation with LV fibrosis than LA strain and SR parameters. However, CMR feature-tracking derived reservoir SR (SRs) was the only parameter to show significant differences between HCM subgroups with absent or with mild LV LGE. As CMR feature-tracking is a relatively novel technique for the quantification of atrial dynamics (Kowallick et al., 2014; Habibi et al., 2014, 2015), its prognostic role in HCM will need to be addressed in future work.

We also found that the minimum LA volumes showed a closer association with LV fibrosis than the maximum volumes. Measurement of LA volumes is important as they reflect the burden and chronicity of elevated LV filling. If evaluation of maximum (or LV end-systole) LA volumes is currently recommended (Lang et al., 2016) as it is a strong predictor of outcomes in HCM as well as in other cardiovascular diseases (Yang, W.I., et al., 2009), measurement of minimum LA volumes is not routinely performed. However, minimum LA volume might be a more sensitive marker of LV diastolic dysfunction in HCM thus providing incremental prognostic information since it is measured at ventricular end-diastole, after the LA is exposed to the increased LV diastolic pressure (Hoit, 2014). Future investigations should try to assess its role in combination with LA functional components.

4.2.5. CLINICAL SIGNIFICANCE

The mechanical function of the LA plays an important role in the overall cardiovascular performance (in normal subjects it contributes to nearly 30% of LV stroke volume). Furthermore, impaired LA function is a well-established early marker of cardiac dysfunction and predictor of adverse cardiac events in many conditions including in HCM (Hoit, 2014). Historically, compared to LV morphology (i.e. degree of LVH) and function (i.e. EF), the assessment of LA mechanics in HCM has been largely underutilised. In our study, we showed that CMR-derived markers of LA performance can be sensitive to subclinical disease and early LV diastolic impairment (LA conduit function was already impaired in those patients with normal EF and no fibrosis, regardless of the presence of LVH) and be marker of HCM progression (while LA reservoir function decreased in later stages of

the disease, LA contractile boost pump increased likely to compensate for raised LV filling pressures). To the best of our knowledge, this is the largest well-phenotyped HCM cohort showing the clinical relevance LA function assessment (Maron et al., 2014; Farhad et al., 2017). In those patients with subclinical disease (no LVH or identifiable fibrosis), LA function is a simpler, not preload dependent metric, and a window into LV diastolic impairment. We envisage that these parameters could be integrated into a risk stratification tool to identify those patients at higher risk of tachyarrhythmias or progressive heart failure, thus contributing to the clinical decision-making process.

4.2.6. LIMITATIONS

There are some potential limitations to this research findings. The main objective of this study was to examine whether there is any association between LA functional abnormalities and LVH/LV fibrosis in HCM using CMR. We accept that there is limited access to this imaging technique despite current recommendations to include CMR in the evaluation and sudden cardiac death risk stratification of HCM patients (Gersh et al., 2011). Also, all HCM diagnoses in our study cohort were based on clinical and imaging findings as recommended by major medical societies. Because information about the presence of a disease-causing mutation was available for a minority of patients and due to the substantial genetic heterogeneity in HCM, we decided to not include this variable in the analysis.

In this study, LV fibrosis was quantified by the percentage of enhanced LV mass in a conventional LGE technique, using a validated methodology (Chan et al., 2014). LV LGE is an independent predictor of sudden death and its presence is a structural nidus for the generation of potentially lethal reentry ventricular tachyarrhythmias and for LV adverse remodelling (O'Hanlon et al., 2010; Bruder et al., 2010; Gersh et al., 2011; Chan et al., 2014). However, we have not used novel CMR tissue characterisation techniques such as T1 mapping (Hinojar et al., 2015; Swoboda et al., 2016), LA LGE (Benito et al., 2017) or 3D whole-heart phase sensitive inversion recovery (Ginami et al., 2017) to better characterise atrial and myocardial interstitial disease.

T1 parametric mapping is a novel CMR tool histologically validated to measure the diffuse interstitial expansion occurring with fibrosis (Messroghli et al., 2017). This is an advantage relative to LGE techniques that depend on the spatial heterogeneity of signal and

a reference “normal” tissue to detect fibrosis, and therefore, may not be sensitive to diffuse changes (Moon et al., 2013). In addition, nearly 40% of HCM patients are LGE negative (Gersh et al., 2011). Early data (Brouwer et al., 2014; Hinojar et al., 2015) suggests that T1 mapping can provide means of phenotyping structural myocardial remodelling in HCM carriers (i.e. genotype positive, phenotype negative subjects) and is a strong predictor of clinical outcomes (Messroghli et al., 2017). However, at the time of this study, we were faced with a number of technical challenges related to the accuracy and precision in the image acquisition and post-processing methods (Moon et al., 2013; Messroghli et al., 2017), and so we exclude T1 mapping from the research protocol.

In this study we have not measured atrial LGE. For long has atrial fibrosis been recognised in autopsied hearts from patients with atrial fibrillation (Bailey et al., 1968) as well as in those with dilated cardiomyopathy and “burned out” HCM [i.e. advanced disease with features mimicking dilated cardiomyopathy] (Ohtani et al., 1995). More recently, there has been a resurgence in interest in the identification of atrial fibrosis by means of CMR LGE techniques, with early data in atrial fibrillation suggesting that the extent of LA LGE is associated with increased risk of cerebrovascular events (King et al., 2017). At the time of this research, atrial LGE remains a controversial topic due to the heterogeneity and lack of reproducibility of the proposed methods (Benito et al., 2017). Furthermore, it has not been systematically studied in HCM.

Finally, the association between LA mechanics in HCM and clinical endpoints (e.g. heart failure, sudden cardiac death, atrial fibrillation) was beyond the scope of this study.

4.2.7. CONCLUSIONS

In this work we have demonstrated how LA mechanics derived from standard CMR cine imaging can provide sensitive markers for HCM staging as well as for earlier detection of disease progression. LA functional abnormalities were associated with LV fibrosis quantified by LGE CMR techniques, but not with LVH. We postulate that the increase in LV fibrosis is paralleled by a continuous deterioration of the LA reservoir function, while the LA conduit function might be already impaired at an early stage of the disease, where LV fibrosis is either absent or mild. In contrast, LA contractile booster pump function appears to be

preserved in patients with absent, mild, or intermediate LV fibrosis and is impaired in those with severe LV fibrosis (Kowallick et al., 2017).

4.3. STUDY 5: AORTIC LENGTH MEASUREMENTS FOR PULSE WAVE VELOCITY CALCULATION: MANUAL 2D VERSUS AUTOMATED 3D CENTRELINE EXTRACTION

4.3.1. BACKGROUND

Ageing is associated with histologic changes in the walls of the systemic arteries that occur independently of alterations attributed to atherosclerosis (Cecelja and Chowienczyk, 2009; Cecelja et al., 2011). The main age-related changes in the arterial wall occur in the intima and in the load-bearing media: on the one hand, the intima undergoes hyperplasia; on the other hand, the elastic fibres and laminae of the media display thinning and fragmentation. In addition there is an age-related increase in the collagen content of the arterial wall, which is much stiffer (at least 500 times) than elastin (Nichols, 2005). These alterations in the elastic properties of the arterial wall cause profound changes in the timing and amplitude of pressure waves reflected at the peripheral tree. Currently, there is an established body of evidence confirming that increased arterial stiffness is a marker of subclinical organ damage and an early predictor of cardiovascular risk that can be used to individualise risk assessment and risk-reduction strategies (Laurent et al., 2006).

Non-invasive surrogate measures of arterial stiffness include pulse pressure, distensibility, and PWV (Adji et al., 2011). Of those, PWV is regarded as the gold standard method to non-invasively quantify central aortic stiffness. PWV is the velocity of the blood pressure wave generated by each cardiac systole as it travels a known distance between two anatomic sites within the arterial system. The age-related stiffening of the walls of the central arteries, which is accelerated by a number of diseases such as hypertension (Harvey et al., 2015), increases PWV as the reflected wave from the periphery occurs with a greater amplitude and earlier [in systole] (McEniery et al., 2005). Such modification in wave reflection characteristics causes a decrease in cardiac output and a corresponding decline in coronary artery perfusion pressure (Weber et al., 2004; Nichols, 2005). Not surprisingly,

aortic PWV has also been shown to be an independent predictor of cardiovascular events and all-cause mortality (Vlachopoulos et al., 2010).

Conventionally, aortic PWV has been assessed transcutaneously by determining the transit time (Δt) between the feet of two pressure or flow waveforms measured at the common carotid and femoral arteries (i.e. “carotid-femoral” PWV using the foot-to-foot methodology), recorded sequentially with a short time apart. This is then divided by an approximation of the travelled distance (D), usually the surface distance between the two recording sites (Laurent et al., 2006). PWV measured as such (Equation 13) provides a regional measurement of arterial stiffness.

$$PWV = \frac{D \text{ (meters)}}{\Delta t \text{ (seconds)}}$$

Equation 13

Most large epidemiological, pathophysiological and pharmacological studies have used ultrasound-based regional carotid-femoral PWV measurements as a surrogate of aortic stiffness (Laurent et al., 2006). The aorta is a major vessel of interest as it has the largest contribution to the arterial buffering function (Nichols et al., 2005; Laurent et al., 2006), it is strongly correlated with age and blood pressure (Cecelja and Chowienczyk, 2009), and its structural changes are an independent predictor of outcome in a variety of populations (Laurent et al., 2006; Vlachopoulos et al., 2010). However, all arterial sites have potential interest and measurement of local stiffness may also provide important prognostic information.

Local arterial stiffness of superficial arteries can be determined using ultrasound methods. However, the deep arteries like the thoracic and abdominal aorta are usually not easily assessable using such methodologies. Conversely, CMR provides adequate visualisation of the aorta and has been used to assess local aortic PWV, at a discrete number of anatomical segments (Mohiaddin et al., 1993). The conventional approach in CMR-based PWV studies has been to calculate the transit time (Δt) between two or more arterial locations (Figure 36) from the arrival time of a flow wave measured using 2D time-resolved phase-contrast CMR [PC-CMR] flow (Wentland et al., 2014).

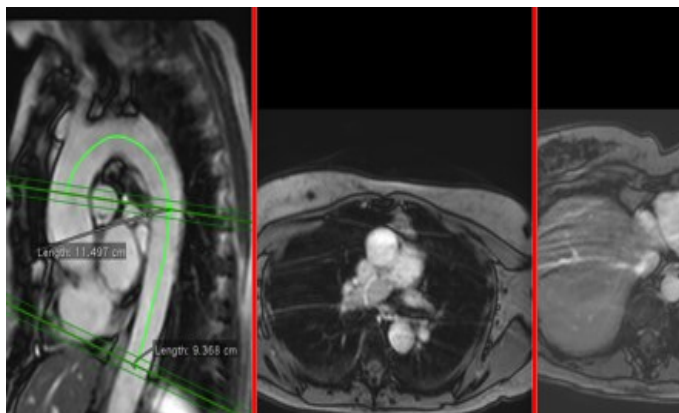


Figure 36

Calculation of the wave distance by identifying the 2D PC-CMR flow acquisition planes (proximal ascending aorta and aorta at the diaphragm level in the middle and right panels, respectively) in a reformatted aorta image. PC-CMR, phase-contrast cardiovascular magnetic resonance flow.

Previous studies have investigated different methods to obtain the transit time between two flow waveforms for CMR-based aortic PWV calculation (Dogui et al., 2011; Gaddum et al., 2013; Vardoulis et al., 2013). Accurate estimation of the travel distance between the waveform locations is, at least, equally important (Boutouyrie et al., 2009). This is commonly estimated from 2D sagittal views of the aorta, either by directly obtaining these using cine images (Voges et al., 2012; Devos et al., 2015; Abbas et al., 2015) or by using a reformatted oblique plane from a 3D volumetric acquisition (Wentland et al., 2013). Measuring the 3D vessel lengths may be more accurate due to the effects of out-of-plane curvature. However, longer 3D volumetric acquisitions are required. Wentland *et al.* have shown differences in the PWV calculated from 2D PC-CMR and 4D flow CMR, for which a 3D centreline was obtained (Wentland et al., 2013). However, their work focused on the effect on the transit time of using different temporal resolutions in the PC-CMR and did not analyse the critical contribution of differences in vessel length measurements.

Another concern relates to the fact that manual annotation of 3D centrelines can be challenging and time-consuming due to the need to inspect the pathline adequacy in three orthogonal planes. Automated/semi-automated centreline tracking tools have been developed for both CT (Shin et al., 2001; Wörz et al., 2010; Krissian et al., 2014) and CMR (Johnson et al., 2010; Babin et al., 2014). The methods usually involve an initial semi-automated lumen segmentation from which the centreline is extracted (Shin et al., 2001; Johnson et al., 2010) or a direct extraction of the centreline from the image data, either by image intensity in

combination with an aortic model (Krissian et al., 2014) or by interactive circle-fitting along the artery (Craiem et al., 2012). Nevertheless, the segmentation process described in these works is still time-consuming and potentially error-prone (Boskamp et al., 2004).

Some authors have also developed sophisticated filters which, when applied to a 2D or 3D image, enhance the vascular structures of interest while reducing background signal (Frangi et al., 1998). This filter is based on the Hessian matrix of the image (a second order partial derivative function that permits to calculate the local shape of an image) and has been used for automated analysis of a large variety of vessels (Lesage et al., 2009). Krissian *et al.* (Krissian et al., 2014) used a vesselness filter to identify a set of potential centrelines in multi-detector CCTA from chronic aortic dissection patients and then manually selected the most adequate one. An intrinsic problem of automatic algorithms is that their performance is optimised for certain image data (CMR versus CT) and often needs to be modified for different contrast settings. Nevertheless, automated 3D centreline extraction methods could increase reproducibility and streamline PWV analysis.

In this research work we have investigated different methodologies for aortic centreline measurements for PWV analysis. Firstly, we have evaluated a novel 3D centreline tracking algorithm on three commonly used CMR sequences. Secondly, we have applied this algorithm to a larger dataset and assessed the differences between 2D and 3D aortic centreline length measurements and its impact on PWV calculations. For this research we have recruited two different cohorts of patients: a healthy middle-aged twins group and a group of patients post-coarctation repair, with altered aortic geometries.

4.3.2. MATERIAL AND METHODS

4.3.2.1. STUDY POPULATION

A schematic overview of the study subjects data, acquired CMR sequences, and performed centreline segmentations is provided in Figure 37.

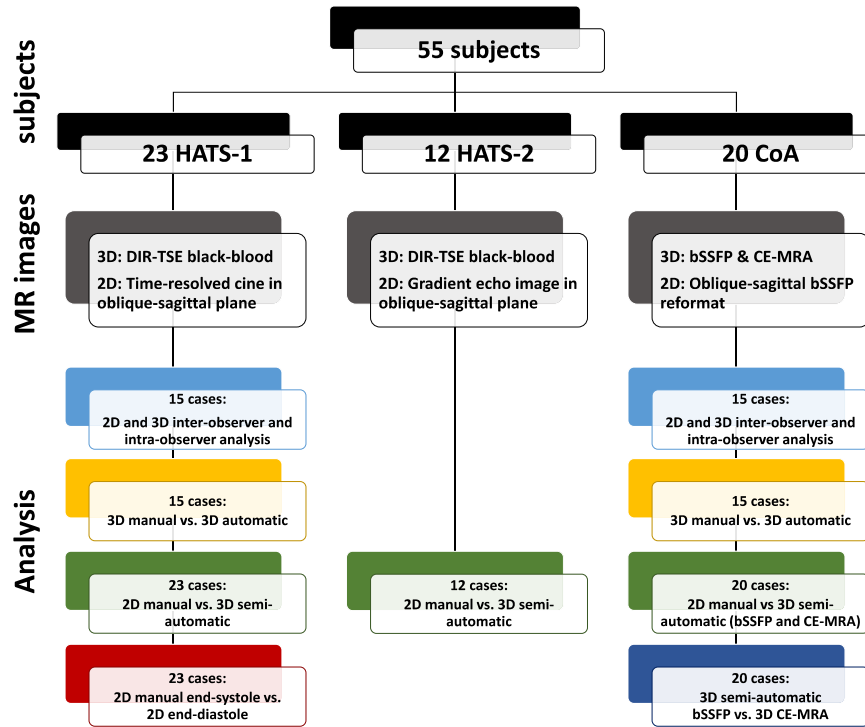


Figure 37

Patient selection flowchart showing the acquired set of images and the performed analyses. HATS, Healthy Ageing Twin Study. CoA, Coarctation study. DIR-TSE, double inversion recovery turbo spin echo. bSSFP, balanced steady-state free precession. CE-MRA, contrast-enhanced magnetic resonance angiography.

Centrelines were obtained from both 2D cine and 3D volumetric CMR images. By definition, a centreline is a series of interconnected points that are located at the centre of a 3D space. Here, we will also use the term centreline to refer to the points located on the centroid of a vessel on a 2D image, from a 2D cine, a reformatted projection of a 3D balanced steady-state free precession (bSSFP) contrast enhanced magnetic resonance angiography (CE-MRA) or multi-slice 2D double inversion recovery turbo spin echo (DIR-TSE) black-blood images.

Data from the 55 subjects were included in our work: (1) 35 subjects from the Healthy Ageing Twin Study (HATS) part of the TwinsUK Registry (all female, mean age of 69 ± 7 years) that were scanned with different CMR sequences; and (2) 20 patients with non-stented, surgically repaired aortic coarctation (CoA; 13 male, mean age of 27 ± 8 years) referred for a clinical CMR scan.

4.3.2.2. CMR IMAGING PROTOCOL

CMR images were acquired on a 1.5 Tesla Philips Ingenia (HATS-1 and CoA) or Achieva (HATS-2) scanner (both Philips Healthcare, Best, the Netherlands). Sequence details are provided in Table 18. The different sequences used in this study were acquired as part of a longer clinical/research imaging protocol, with a total imaging time of about one hour.

Imaging Parameters	PC-CMR	2D cine	2D GRE	DIR-TSE	DIR-TSE	3D bSSFP	CE-MRA
	All	HATS-1	HATS-2	HATS-1	HATS-2	CoA	CoA
TE (ms)	2.7 ± 0.2	1.8 ± 0.3	1.3	13.4 ± 0.5	5.0	1.5 ± 0.2	1.1 ± 0.1
TR (ms)	4.5 ± 0.4	3.7 ± 0.6	4	1684 ± 242	1330 ± 466	3.6 ± 0.2	3.8 ± 0.1
Acquisition	Oblique-sagittal, single-slice	Oblique-sagittal, single-slice	Oblique-sagittal, single-slice	Axial, multi-slice	Axial, multi-slice	Coronal, 3D volumetric acquisition	Coronal, 3D volumetric acquisition
Acquired resolution (mm)	2.2 ± 0.1	1.4 ± 0.4	2.0	1.5 × 1.9 ± 0.1	1.0	1.4 ± 0.2	1.8
Reconstructed in-plane voxel size (mm)	1.1 ± 0.1	0.9 ± 0.3	1.8	1.1 ± 0.04	0.3	0.8 ± 0.2	1.2 ± 0.01
Slice thickness (mm)	8-10	8-10	15	5	5	1.6 ± 0.7	1.8
Temporal resolution (ms)	8.4 ± 5.5	24.5 ± 4.7	-	-	-	-	-
FA (°)	15-20	45-60	30	90	90	70	30
SENSE factor	1	1	1	1	1	1.2 ± 0.3	1.5

Table 18

CMR scan protocol. bSSFP, balanced steady-state free precession. CE-MRA, contrast-enhanced magnetic resonance angiography. CoA, Coarctation study. DIR-TSE, double inversion recovery turbo spin echo. FA, flip angle. HATS, Healthy Ageing Twin Study. TE, echo time. TR, repetition time.

In all patients, free-breathing high-temporal resolution 2D through-plane velocity-encoded PC-CMR were acquired in the ascending (ASC), descending (DESC) and diaphragmatic (DIAPH) aorta.

The 3D centreline tracking method was evaluated in different CMR sequences, exploiting the fact the image data was obtained from two different studies: (1) multi-slice 2D DIR-TSE black-blood images for the HATS cohort; and (2) 3D bSSFP and 3D CE-MRA (0.2mmol/Kg of Gadovist®; Bayer Schering Pharma; Berlin, Germany) for the CoA patients.

The 2D lengths in the HATS cohort were obtained using two different imaging sequences: (1) an oblique-sagittal 2D cine of the aorta for 23 of the HATS subjects (called HATS-1 hereafter); and (2) a single-slice oblique-sagittal gradient recalled echo or gradient

echo (GRE) image with transverse saturation slabs for the remaining 12 subjects (HATS-2). In the CoA patients, the 2D lengths were obtained from an oblique-sagittal plane by reformatting the 3D bSSFP images.

4.3.2.3. DATA ANALYSIS

4.3.2.3.1. MANUAL CENTRELINE ANNOTATIONS

Manual annotations of the thoracic aortic path were made on 3D images (for comparison with the automated centreline tracking algorithm) and on 2D images (to compare 2D and 3D-derived lengths).

The 3D centrelines were generated in 30 randomly selected subjects, 15 from HATS-1 and 15 from the CoA cohort, on both bSSFP and CE-MRA images using a custom-made tool developed in MeVisLab platform (Medical Visualization Laboratory V2.6.1). This image tool, allows careful annotation with simultaneous inspection of the centrelines in three orthogonal planes (Figure 38). The manual centrelines were cut at the point closest to the centre of the cross-sectional lumen of the ASC, DESC and DIAPH aorta, using the 2D PC-CMR planes as landmarks.

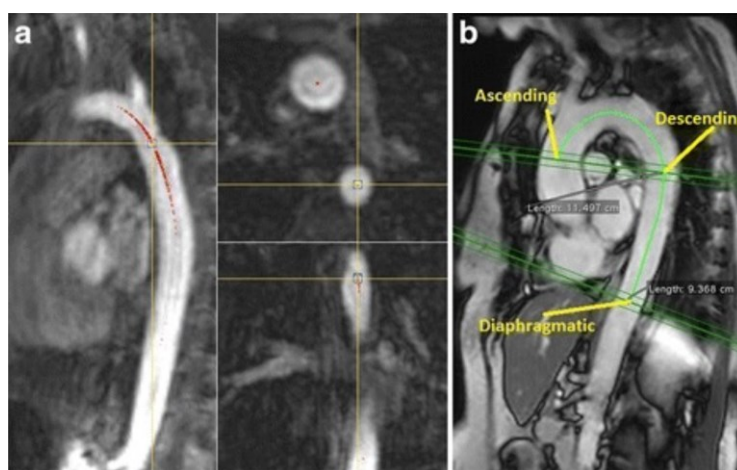


Figure 38

Example of the manual annotation in 3D dataset using a custom-made tool developed in MeVisLab V2.6.1 (panels A and B) and using Osirix Medical Imaging software 2D viewer (panel C).

The 2D centrelines for the thoracic aorta were manually obtained on all datasets using Osirix Medical Imaging software V.7.5 (Geneva, Switzerland; www.osirix-viewer.com). The start and end points of the manual annotations were defined by projecting in the aorta the 2D

PC-CMR flow planes (Figure 36). In all HATS-1 subjects, the distances were obtained at end-systole (ES) and end-diastole (ED).

4.3.2.3.2. AUTOMATED CENTRELINE ANNOTATIONS

The automated algorithm described in this work was developed to be used with different volumetric input images, whether multi-slice 2D or “true” 3D acquisitions, regardless of the orientation. In order to compute the centrelines, three steps were required: (1) a vesselness filter (Frangi et al., 1998); (2) fast marching (Wink et al., 2000) and (3) a centreline refinement.

The vesselness filter applied has been used for vascular image processing as it enhances vessel-like structures visualisation (Wink et al., 2000; Krissian et al., 2014). In brief, this filter combines the eigenvalues of the Hessian matrix to get a maximum response for vascular structures. The Hessian matrix is computed at several scales, depending on the size of the vessel of interest, and the maximum response over the different scales is then taken at each voxel (Frangi et al., 1998). In this work, we compared several scale settings for the Hessian matrix, based on the expected aortic diameters: using 4 scales, ranging from 4 to 7 mm, and using 2 scales being either 4 and 6 mm, or 6 and 8 mm. Bi-directional fast marching (Wink et al., 2000; Florkow et al., 2016) was performed to find the most ideal path between a start and end point. Here, a “wavefront” propagates from both ends using a speed map based on the vesselness. The start and end points for centreline tracking were defined by taking the centre of the ascending and diaphragmatic aorta on the first phase of the 2D PC-CMR images. To account for inadvertent patient movement between the 2D PC-CMR acquisition and the sequence used for the centreline tracking, an ellipse was fitted in the aorta in the 3D data (Wink et al., 2000; Merx et al., 2012) to re-centre the start and end points. Finally, the pathlines were centred and smoothed by an open active contour (Lobregt and Viergever, 1995). The active contour makes use of two equally weighted forces: an internal force to minimise the curvature and an external force to centre the contour.

This algorithm was implemented in a PWV prototype on the Philips IntelliSpace Discovery (Philips, Best, the Netherlands), an advanced visualisation and analysis solution, working similarly to the Vessel Explorer tool (Bescós et al., 2009). Manual adjustment of the obtained centreline was also possible in this prototype.

The automated centreline tracking tool was evaluated in the 30 randomly selected patients for which manual annotations were also made. To compare 3D and 2D distances, manual adjustment of the obtained 3D centrelines was performed to reposition control points in the centre of the vessel in cases where the algorithm produced inaccurate results. This tracking, followed by manual correction, was performed in all subjects for the comparison between 2D and 3D centrelines. In this work, we refer to automated centrelines to those where only manual selection of the artery of interest on the 2D PC-CMR was performed, without further user interaction, and centrelines that have subsequently been adjusted as semi-automated.

Pulse Wave Velocity Calculations

Volumetric flow waveforms were obtained with the centreline tracking tool from the 2D PC-CMR at the ASC, DESC and DIAPH aorta, by fitting a circle to the vessel edge along a number of ray casts and propagating the segmentation to all phases. The transit time (Δt), describing the delay between the arrival of the pulse wave at two locations, was subsequently automatically computed using the foot-to-foot method as described by Gaddum and co-workers (Gaddum et al., 2013). The foot of each flow curve was determined based on the intersection of a line tangent to the average maximum gradient during systole and a horizontal line through the local minimum. PWV was then calculated by dividing the centreline length between two locations by the transit time between those locations (Equation 13). For each subject, PWV calculations were performed for the segments ASC-DESC, DESC-DIAPH and for the entire thoracic aorta.

4.3.2.4. STATISTICAL ANALYSIS

Reproducibility and repeatability of the 2D and 3D manual annotations were determined by assessing the inter- and intra-observer variation in centreline length, respectively.

Intra- and inter-observer variability were assessed for both 3D and 2D manual annotations of the 30 subjects that were also randomly selected to evaluate the automated centreline tracking tool. For the HATS-1 cohort, the intra- and inter-observer variability were assessed at end-diastole. For the CoA cohort, the reformatting of a 2D oblique-sagittal plane

was repeated for each annotation, and was also part of the intra- and inter-observer analysis. Subsequently, the centreline with median length obtained following three annotations, was taken as the reference centreline for further analysis.

For evaluation of the automated centreline tracking in the 30 randomly selected subjects, the following steps were taken. First the number of failed tracings, defined as the centreline tracings leaving the lumen, was counted. Then, the following parameters were obtained for non-failed cases: centreline length, the distance between manual and automatic centrelines, and PWV. All centrelines were resampled to a spacing of 0.1mm. Subsequently, the centrelines were split at the level of the DESC aorta in the 2D PC-CMR flow to obtain the ASC-DESC and DESC-DIAPH lengths separately. The minimal distance between manual and automatic centrelines was then calculated for each point along the resampled centrelines.

We also compared the 2D and 3D aortic length, and the corresponding PWV values. This analysis was performed for each individual dataset (HATS-1, HATS-2, CoA bSSFP and CoA CE-MRA). The results, separated for the different aortic segments, were assessed using the Bland-Altman test (Bland and Altman, 1986).

Furthermore, for the 2D cine images in the HATS-1 subset, the difference between the end-diastolic and end-systolic length and resulting PWV was assessed. For the CoA cohort the difference between centrelines obtained from bSSFP and CE-MRA images was analysed. As the DIR-TSE BB images were triggered at end-systole, the end-systolic 2D measurements were taken for comparisons in the HATS-1 cohort.

We tested all results (length differences, PWV differences, centreline distances) for normality using a Kolmogorov-Smirnov test. Since the majority of results was not normally distributed, they are presented with their median and interquartile range (IQR), and comparisons were made using a paired Wilcoxon signed rank test. Differences were considered statistically significant for a p value < 0.05 (two-tailed).

Finally, we also timed the manual annotations for one experienced user in different datasets: (1) the 2D centrelines on 5 HATS-1 and 5 CoA subjects; and (2) the 3D centrelines on 5 HATS-1, 5 CoA bSSFP and 5 CoA CE-MRA subjects.

4.3.3. RESULTS

4.3.3.1. MANUAL CENTRELINE ANNOTATIONS

The results for the inter- and intra-reader differences in the manual centreline lengths obtained for both 2D and 3D are provided in Table 19. Overall, centreline length annotation was more consistent for the HATS cohort than for the CoA patients. The intra- and inter-reader variability was higher for the 2D measurement across all cohorts. However, absolute differences generally stayed well below 1 cm or 5% of total centreline length. Those differences were mostly due to discrepancies in the aortic arch (ASC-DESC).

		Absolute length difference (mm, %)					
		ASC-DESC		DESC-DIAPH		TOTAL	
HATS-1 2D (ED)	IAO	2.3 [1.0–3.3], 1.8 [0.8–2.7]%	1.1 [0.4–1.6], 1.0 [0.3–1.5]%	2.6 [1.5–4.5], 1.1 [0.6–1.9]%			
	IEO	5.2 [3.4–7.9], 4.1 [2.7–5.8]%	0.7 [0.4–2.0], 0.7 [0.4–1.8]%	5.8 [3.1–8.0], 2.5 [1.5–3.5]%			
CoA 2D	IAO	2.7 [1.2–4.8], 2.4 [0.9–4.4]%	1.1 [0.5–1.7], 1.1 [0.4–1.7]%	2.8 [1.7–3.9], 1.2 [0.7–1.9]%			
	IEO	5.6 [3.7–7.7], 5.2 [3.4–6.9]%	2.1 [0.8–4.1], 1.6 [0.7–3.1]%	4.8 [2.8–6.9], 2.1 [1.2–3.2]%			
HATS-1 3D	IAO	0.9 [0.4–1.5], 0.8 [0.3–1.2]%	0.2 [0.1–0.4], 0.2 [0.1–0.3]%	0.9 [0.5–1.5], 0.4 [0.2–0.7]%			
	IEO	0.8 [0.4–2.1], 0.7 [0.3–1.7]%	0.4 [0.2–0.5], 0.4 [0.2–0.5]%	1.3 [0.5–2.5], 0.6 [0.2–1.2]%			
bSSFP CoA 3D	IAO	1.2 [0.5–2.1], 1.0 [0.5–1.7]%	0.2 [0.1–0.5], 0.2 [0.1–0.4]%	1.3 [0.6–2.5], 0.6 [0.3–1.0]%			
	IEO	2.3 [1.5–3.9], 2.0 [1.3–3.2]%	0.7 [0.3–0.9], 0.7 [0.2–1.1]%	2.8 [1.6–4.7], 1.4 [0.7–1.8]%			
CE-MRA CoA 3D	IAO	0.9 [0.3–1.7], 0.8 [0.3–1.8]%	0.3 [0.1–0.7], 0.3 [0.1–0.6]%	1.0 [0.5–1.9], 0.4 [0.2–0.7]%			
	IEO	2.9 [1.7–5.6], 2.5 [1.5–4.6]%	0.8 [0.3–1.5], 0.6 [0.2–1.2]%	3.0 [0.8–6.5], 1.4 [0.4–2.8]%			

Table 19

Intra- (IAO) and inter-reader (IEO) variation in centreline length annotation (mm and %, provided as median [IQR]). ASC, ascending aorta. bSSFP, balanced steady-state free precession. CE-MRA, contrast enhanced magnetic resonance angiography. CoA, aortic coarctation. DESC, descending aorta. DIAPH, diaphragmatic aorta. ED, end-diastole. HATS, Healthy Ageing Twin Study.

Manual annotation duration in 2D sequences did not differ much between HATS-1 and CoA subjects, with a total average of 49.3s [42.6–58.1], including: an average of 21.1s for setting the start and end points; an average of 15.3s for tracking ASC-DESC path; and an average of 12.9s for tracking DESC-DIAPH segment. An additional 22.3s [13.2–31.4] were required for reformatting the 3D bSSFP images of the CoA patients.

Manual annotation of the 3D centrelines took on average for the 1.12 minutes for the HATS-1 black-blood DIR TSE, 2.11 minutes for the CoA CE-MRA and 2.24 minutes for the CoA 3D bSSFP sequences.

4.3.3.2. AUTOMATED CENTRELINE TRACKING

The results of the automatic centreline tracking using different scale settings are shown in Table 20. Selected examples of obtained centrelines are shown in Figure 39.

	Failed tracings	Absolute length difference (mm)	Average centreline distance (mm)	Absolute PWV difference (m/s+ %)
HATS-1				
Scales: 4, 5, 6, 7 mm	-	4.0 [1.9 5.0]	1.3 [0.9 2.0]	0.13 [0.08 0.21], 1.9 [0.9 2.0]%
Scales: 4, 6 mm	-	2.4 [1.8 4.3]	1.3 [0.8 1.9]	0.08 [0.06 0.19], 1.1 [0.8 1.8]%
Scales: 6, 8 mm	-	5.4 [3.7 8.0]	1.5 [1.0 2.3]	0.22 [0.16 0.28], 2.4 [1.7 3.3]%
CoA bSSFP^a				
Scales: 4, 5, 6, 7 mm	5	7.3 [5.6 8.2]	1.6 [1.0 2.7]	0.15 [0.11 0.20], 2.9 [2.5 3.2]%
Scales: 4, 6 mm	3	6.4 [4.7 8.9]	1.5 [0.9 2.7]	0.15 [0.09 0.21], 2.8 [2.0 4.7]%
Scales: 6, 8 mm	5	8.0 [7.1 9.9]	2.0 [1.2 4.1]	0.16 [0.12 0.21], 3.1 [2.6 4.0]%
CoA CE-MRA				
Scales: 4, 5, 6, 7 mm	-	3.9 [2.7 6.3]	1.2 [0.8 1.9]	0.09 [0.05 0.13], 1.5 [1.2 2.8]%
Scales: 4, 6 mm	-	2.9 [1.9 4.9]	1.2 [0.7 1.9]	0.07 [0.03 0.12], 1.5 [0.8 2.6]%
Scales: 6, 8 mm	-	5.0 [3.5 8.1]	1.4 [0.9 2.3]	0.11 [0.08 0.18], 2.3 [1.5 3.6]%

Table 20

Automated centreline tracking versus manual annotation: length differences, point-based distances and corresponding PWV measurements accuracy, all provided as median [IQR]. ^aResults for bSSFP are presented after excluding failed centrelines. Abbreviations as in the previous tables.

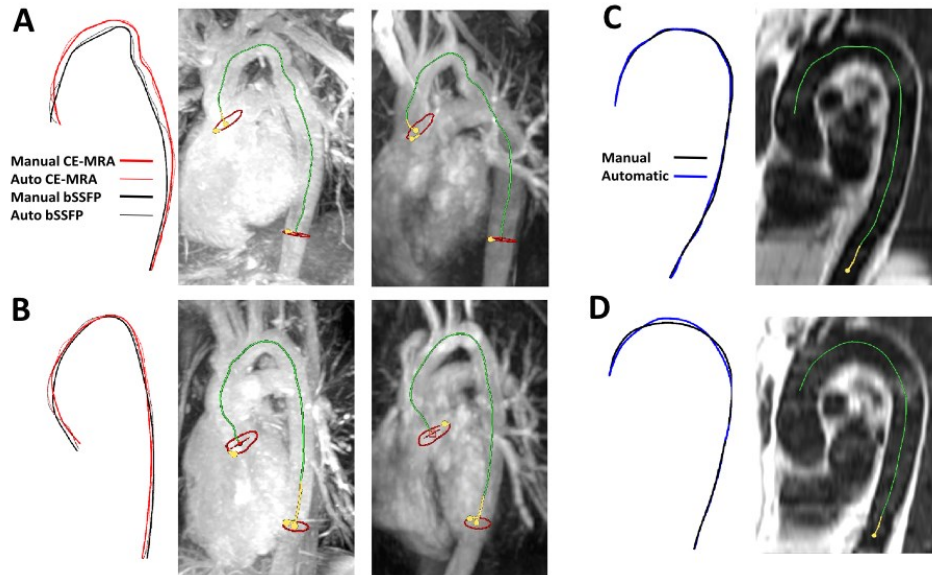


Figure 39

Selected examples of the automated centreline tracking results. **Panels A and B.** Results for maximum intensity projection (MIP) images generated from a volumetric 3D bSSFP (left) and a CE-MRA (right) belonging to two different CoA patients. **Panels C and D.** Results for HATS patients with the obtained centreline projected on a sagittal plane. Abbreviations as in the previous tables.

Overall, the automated tracking tool generated valid aortic centrelines in all images types, only failing in a small fraction of the bSSFP images (N=13, 12% of the total attempts). Of the three scale settings evaluated for calculating the Hessian matrix, using 2 scales (4 and 6 mm) provided the best results. With these optimal scale settings, only three failed tracings occurred. In one case, this was due to a small deviation of the centreline outside the aortic lumen, easily adjustable by moving manually the control points. In the other two cases, the automated centreline failed to accurately track the aortic arch and went wrongly to the pulmonary artery or the heart.

Compared to the manual annotations, the automated method resulted in smaller differences in aortic lengths (< 1 cm) and PWV calculations (< 0.5 m/s), both below 5%. The highest rate of failure of the automated algorithm was observed in the bSSFP images (3/15). The largest differences between automated and manual centreline lengths was also seen in the bSSFP images. A more detailed analysis of the results for automated tracking using the optimised settings in the ASC-DESC and DESC-DIAPH segments is given in Table 21. In turn, differences in length and PWV were larger for the ASC-DESC segment (which includes the aortic arch) than for the DESC-DIAPH segment.

	Absolute length difference (mm)		Average centreline distance (mm)		Absolute PWV difference (m/s and %)	
	Arch	DESC	Arch	DESC	Arch	DESC
HATS-1	2.7 [1.4 4.3]	0.2 [0.1 0.5]	1.7 [1.1 2.6]	1.1 [0.7 1.4]	0.21 [0.11 0.35], 2.6 [1.8 3.6]%	0.02 [0.01 0.05], 0.2 [0.1 0.4]%
CoA bSSFP^a	4.8 [3.6 7.4]	1.5 [0.6 2.4]	2.0 [1.2 3.4]	1.3 [0.8 2.3]	0.26 [0.15 0.31], 4.2 [3.2 5.9]%	0.06 [0.02 0.09], 1.3 [0.4 1.9]%
CoA CE-MRA	2.4 [0.9 4.3]	0.5 [0.4 1.3]	1.3 [0.8 2.1]	1.2 [0.7 1.7]	0.12 [0.04 0.18], 2.3 [0.9 3.7]%	0.03 [0.01 0.05], 0.7 [0.3 1.0]%

Table 21

Results for best chosen automated centreline algorithm (scale 4–6mm), split between the arch (ASC-DESC) and descending aorta (DESC-DIAPH). Results for bSSFP are after excluding failed centrelines. Abbreviations as in the previous tables and figures.

4.3.3.3. DIFFERENCES BETWEEN 2D VERSUS 3D APPROACHES

The comparison between the aortic centreline length measurements (ASC-DIAPH) obtained using the 2D and 3D datasets is provided in Table 22. The difference in PWV, specified per aortic segment, is depicted in the Bland-Altman plots of Figure 40, with corresponding limits of agreement provided in Table 23.

	Difference length (mm)	Difference PWV (mean, %)	Absolute Difference PWV (mean, %)
2D–3D			
<i>HATS-1</i>**	7.4 [2.4 11.6]	0.26 [0.08 0.48], 3.0 [1.1 4.9]%	0.28 [0.17 0.50], 3.3 [2.3 4.9]%
<i>HATS-2</i>*	-6.9 [-8.8 0.3]	-0.26 [-0.35 0.02], -2.7 [-4.1 0.2]%	0.26 [0.16 0.35], 3.2 [1.8 4.1]%
<i>CoA bSSFP</i>**	-6.3 [-10.8 -2.1]	-0.13 [-0.22 -0.04], -3.1 [-4.5 -1.0]%	0.13 [0.05 0.22], 3.1 [1.1 4.5]%
<i>CoA CE-MRA</i>	-4.0 [-13.5 6.5]	-0.07 [-0.24 0.11], -1.6 [-4.9 2.6]%	0.18 [0.11 0.38], 3.7 [2.5 7.5]%
ED-ES**	-1.5 [-3.2 -1.3]	-0.08 [-0.10 -0.04], -0.6 [-1.4 -0.5]%	0.08 [0.04 0.10], 0.6 [0.5 1.4]%
bSSFP-CE-MRA	7.8 [-8.1 14.4]	0.14 [-0.13 0.25], 2.9 [-3.6 5.4]%	0.22 [0.13 0.30], 4.2 [3.4 6.7]%

Table 22

Comparison between different methods for measuring aortic centreline length and the resulting PWV calculations. 2D-3D, 2D manual minus 3D semi-automatic length. ED-ES, end-diastolic (ED) minus end-systolic (ES) length. bSSFP-CE-MRA, bSSFP minus CE-MRA length (* = $p \leq 0.05$, ** = $p \leq 0.01$, calculated for the PWV difference). ‘Difference length’ and ‘Difference PWV’ indicate whether a bias is present, whereas ‘absolute difference PWV’ indicates the average difference between the methods, disregarding a bias between the two. All results are provided as median [IQR]. Abbreviations as in the previous tables and figures.

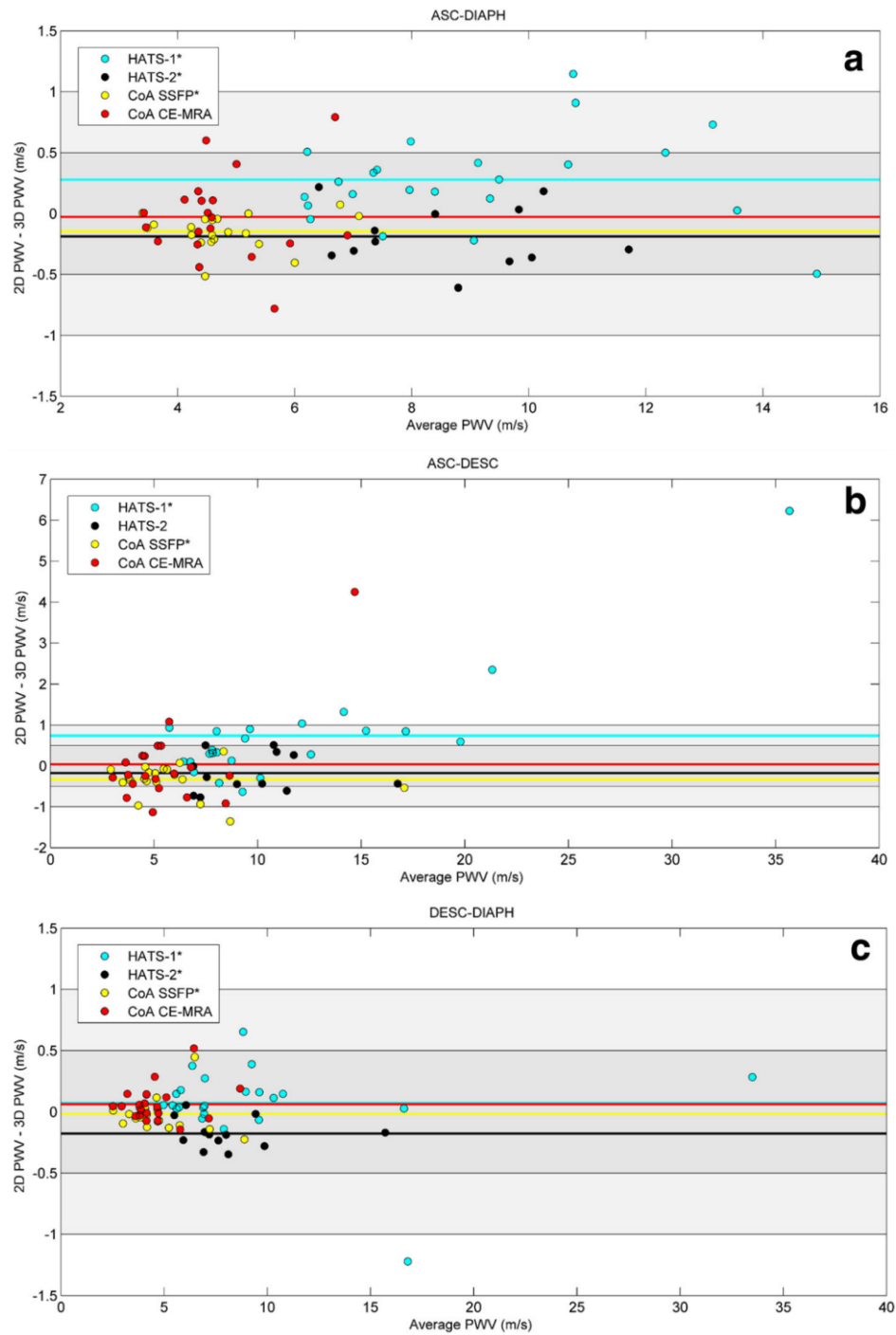


Figure 40

Bland-Altman plots depicting 2D versus 3D PWV, for (a) ASC-DIAPH, (b) ASC-DESC and (c) the DESC-DIAPH segment. Shaded areas indicate the difference < 0.5 m/s and 1 m/s. Different cohorts are shown with different colours. The average difference for each cohort is indicated by the corresponding coloured line. For clarity of the figure the 95% confidence intervals are not shown. Abbreviations as in the previous tables and figures.

	ASC-DIAPH	ASC-DESC	DESC-DIAPH
ATS-1	0.28 [-0.44 1.00]	0.74 [-1.91 3.40]	0.07 [-0.58 0.72]
HATS-2	-0.19 [-0.68 0.30]	-0.17 [-1.11 0.76]	-0.18 [-0.42 0.07]
CoA bSSFP	-0.15 [-0.42 0.13]	-0.33 [-1.09 0.43]	-0.02 [-0.29 0.26]
CoA CE-MRA	-0.03 [-0.72 0.67]	0.04 [-2.16 2.24]	0.06 [-0.23 0.35]

Table 23

Average and limits of agreement for the PWV data presented in Figure 40. Abbreviations as in the previous tables and figures.

The analysis of the data showed significant differences in the aortic centreline length for HATS-1 (2D > 3D), HATS-2 (3D > 2D) and the CoA bSSFP images (3D > 2D). In turn, the absolute difference between PWV derived from a 2D or a 3D centreline was above 0.5 m/s in 15% of the cases (37% for the ASC-DESC segment), and greater than 1 m/s in one case (1%). The smallest limits of agreement were seen in the CoA bSSFP images.

A sub-analysis showed that the significant differences in the absolute length measured in the 2D versus the 3D datasets in the three studied cohorts were mainly in the ASC-DESC segment. In ASC-DESC segment, the overall absolute difference in PWV for all studied subjects was 0.38 [0.24–0.76] m/s (5.2 [3.1–9.9] %), while in the DESC-DIAPH it was 0.09 [0.04–0.18] m/s (1.6 [0.7–2.8] %). Moreover, for the aortic arch segment, in 37% of cases the absolute difference in PWV was larger than 0.5 m/s and in 11% larger than 1 m/s. There were two outliers with a PWV of 4.2 and 6.2 m/s owing to both a very short transit time (4–5 ms) and a large length difference (2.3 and 2.6 cm). For the descending aorta segment, a difference larger than 0.5 m/s was observed in only 4% of cases, while a difference greater than 1 m/s was found in only 1% of all cases.

The difference between end-diastolic and end-systolic length measurements was -1.5 [-3.2 to -1.3] mm (ES > ED, $p < 0.01$). This discrepancy resulted in a calculated PWV difference of 0.08 [0.04–0.10] m/s. Additionally, although the difference between the 3D centrelines measured on the bSSFP and CE-MRA images in the CoA cohort was not significant, the absolute differences in PWV were relatively large (4.2 [3.4–6.7]%, ranging up to 0.8 m/s).

4.3.4. DISCUSSION

In this work, we have developed and tested a customised tracking tool for aortic centreline annotation that can be implemented in a clinical and/or research protocol in order to streamline PWV measurements. We have demonstrated that aortic centrelines can be extracted accurately from 3D CMR images with minimal user interaction. Furthermore, we have shown that centrelines obtained manually from 2D and 3D datasets can result in significant differences in length, and therefore in PWV calculations.

4.3.4.1. AUTOMATED EXTRACTION TOOL

Our proposed centreline tracking algorithm was successfully applied to volumetric data acquired as a 2D multi-slice or “true” 3D, regardless of the orientation. Overall, a relatively small number of tracking failures (N=13, 12% of total tracings) occurred when using the automated tracking algorithm, all on the bSSFP datasets of the CoA cohort. With the optimal scale settings, only three failed tracings occurred, all in the aortic arch and associated with signal loss in this segment. Besides manual adjustment of the centrelines, these errors could also be avoided by adding further control points to the aortic lumen. The excellent performance of the automated tracking tool with different imaging protocols highlights its robustness and supports its integration in a practical clinical and/or research workflow.

4.3.4.2. CENTRELINE ANNOTATIONS AND CMR SEQUENCE

There was a direct correlation between successful annotation of the aorta centrelines and the CMR imaging sequence used. On the one hand, the manual tracking performance was more prone to intra- and inter-reader variability when using 2D datasets. Inaccuracies often resulted from suboptimal planning during the image acquisition or tortuosity of the aorta preventing adequate capture of its curvature in a 2D plane. In addition, the start and end points of the 2D images were user defined, while the annotated 3D centrelines were post-processed to start and end automatically at predefined points (the projection of the 2D PC-CMR flow onto the aorta). On the other hand, the most accurate centrelines were obtained using black-blood and contrast-enhanced images, while bSSFP images were more prone to failed tracings and showed larger intra- and inter-reader differences in length.

A number of reasons might explain the poorer performance of the centreline tracking tool in the bSSFP data: (1) all the bSSFP data was from the CoA cohort who presented more anatomical variations in the aortic geometry; (2) the 3D bSSFP sequences are known to be highly sensitive to local magnetic field inhomogeneities, particularly when using long TRs necessary for high resolution images (Bangerter et al., 2004); and (3) signal loss can occur in bSSFP sequences with highly turbulent or rapid flow jets across stenotic lesions (as it was the case in these CoA patients) despite intrinsic flow-compensation in all three directions (Scheffler and Lehnhardt, 2003; Bieri and Scheffler, 2005; Ferreira et al., 2013).

4.3.4.3. 2D VERSUS 3D CENTRELINE LENGTHS DIFFERENCES

As expected, the aortic centrelines obtained from the 2D images (i.e. 2D projections obtained from reformatted 3D datasets in the CoA cohort or 2D cines of the aorta in the HATS-2 cohort) were shorter than with a 3D method. Notably, such difference between 2D and 3D aortic centreline length was larger in the arch than in the descending aorta segment. This likely relates to out of plane curvature of the aorta at the level of the arch not well captured in a 2D projection.

The different image sequences used in the HATS and CoA cohorts hinders direct interpretation of the 2D versus 3D centreline length variability. Nevertheless, intra- and inter-reader variation for both 2D and 3D approaches was slightly larger in the CoA cohort, likely associated with more anatomical variations in the aortic centrelines in these patients.

Surprisingly, we found that for the HATS-1 cohort, the aortic 3D centreline distances were shorter than those obtained with 2D datasets. From a mathematical perspective, the projection of a 3D line onto a 2D plane cannot produce a longer length. After inspecting the cases with differences larger than 1 cm, we attributed this pattern to either patient motion or a suboptimal planning of the oblique-sagittal plane at the time of the scan acquisition, which forced the observers to estimate the course of the aortic arch.

4.3.4.4. SYSTOLIC VERSUS DIASTOLIC AORTIC DISTANCES

The difference between aortic distances measured in 2D cines at end-systole versus end-diastole aortic lengths was small (-1.5 [-3.2 to -1.3] mm), but significant. Cardiac pulsation as well as respiratory motion is known to cause displacement and deformation of

the aorta between end-diastole and end-systole (Suh et al., 2014). As a result of geometric changes with the cardiac cycle, the aortic centreline may appear slightly higher in the axial direction, along the arch, and result in the longer distances measured. Although we did not have the data to confirm this finding using 3D images, given that the differences were so small we argue that the effect of measuring PWV using lengths obtained at end-systole or at end-diastole may be negligible.

4.3.4.5. IMPACT ON PWV MEASUREMENTS

Using aortic centreline lengths measured manually in 2D versus 3D datasets resulted in a small (< 0.5 m/s) but significant difference in the calculated PWV in the majority of cases. Conversely, using the automated tracking tool with the optimised algorithm for aortic centreline measurement resulted in smaller differences in PWV calculations compared to the manual method. Notably, higher variability using the automated approach was seen in the CoA cohort, particularly at the arch. This was probably a result of the more tortuous aortic centrelines at the level of the arch as explained before. Also, in stiffer vascular segments with shorter transit time of the flow/pulse waveform, larger differences in centreline length will have a greater effect on PWV calculation (Equation 13).

4.3.5. CLINICAL SIGNIFICANCE

High-fidelity determination of PWV is important in the study of arterial viscoelastic properties, wave reflections, and ventricular-arterial interactions. Furthermore, PWV is a well-established biomarker of arterial stiffness and early atherosclerotic disease burden (Laurent et al., 2006). A systemic overestimation of the travel distance has been shown to occur with ultrasound-derived PWV, considered the gold standard non-invasive method (Boutouyrie et al., 2009). Conversely, CMR permits a careful pathway measurement but most research so far has focused on the impact in PWV calculation of correct measurement of the travel time between two flow waveforms. In this study we have shown that manual aortic centreline measurement from 2D images introduced small but significant differences in PWV, a concern reduced by automating aortic segmentation from different sets of 3D CMR images. The need for computerised methods to consistently measure PWV from different medical images has long been reported (Chiu et al., 1991). However, to the best of our

knowledge this is the first study to report this finding using state-of-the art CMR images. This could have methodological implications in future longitudinal studies designs using CMR-PWV and underscores the potential low reproducibility of ultrasound-derived PWV. Finally, the prototype tool can streamline PWV calculation so that it is included in the clinical CMR workflow, hence enriching the information extracted from the scan.

4.3.6. LIMITATIONS

The design of this study resulted in a heterogenous sample recruited from three cohorts, imaged with different 2D and 3D CMR sequences. However, this set-up allowed us to test the proposed automated centreline tracking tool, as well as the effect of 2D versus 3D length measurements, in different CMR sequences in a “real world” clinical setting.

In this study, we have not employed novel time-resolved 3D PC-CMR flow techniques with large 3D volumetric coverage and flow-encoding in all three spatial directions (so-called “4D” PC-CMR flow) as they were not available for clinical use at the time of the image acquisition for this research. Among the many advantages, this technology offers the possibility of acquiring isotropic high spatially resolved flow data, retrospective flow interrogation in any plane of the acquired volume, and it generates simultaneous phase-contrast angiograms for aortic distance calculation without the need for additional anatomic sequences. Initially hampered by poor temporal and spatial resolution, and unfeasible long acquisition times, recent developments have overcome much of these limitations. This has made it possible to accurately assess PWV using 4D PC-CMR flow. Nevertheless, the temporal resolution is still about one quarter of the 2D PC-CMR flow sequence used in this research. Further research comparing the two approaches to the gold standard ultrasound-based PWV is needed to understand the impact of this lower temporal resolution in the accurate estimation of the transit time.

4D PC-CMR flow can also help to quantify 3D displacement of the aortic arch during the cardiac cycle and respiration, and its impact in PWV measurements. This is a challenging problem because of the need to establish and register two different images in the end-diastolic and end-systolic phases, and the geometric complexity of the aortic arch in some patients (e.g. CoA).

Despite these limitations, we have shown that accurate centreline extraction is a critical step and the use of automated tools such as the one described provides a more accurate and user-independent method of determining the centre of the vessel, compared to manual annotations.

4.3.7. CONCLUSIONS

The primary aim of this study was to test a novel tool for obtaining accurate aortic 3D centrelines from routine clinical CMR datasets with minimal user interaction. We wanted to evaluate the robustness of the automated tracking prototype in different CMR sequences so that it could be integrated into a practical clinical-research protocol for the assessment of PWV. We have maintained the ability of the user to introduce manual adjustment of the obtained centreline in order to produce the most accurate lengths measurements.

We have demonstrated that the presented algorithm was able to extract accurately the aortic centrelines in different CMR sequences with a small number of tracking failures. We found that the algorithm performance was worst in bSSFP images and, in particular, in the aortic arch segment. These sequences are more prone to banding artefact and signal loss but a “class-effect” could also explain the poorer tracing in arch as all bSSFP images were from CoA patients, some with abnormal aortic geometries.

As a second aim, we wanted to assess whether there were significant differences in PWV values calculated using centreline lengths obtained from a 2D or a 3D method. Previous research has focused in the importance of accurate assessment of the transit time for PWV calculation and has shown that the foot-to-foot methodology provides the most reproducible measurements (Dogui et al., 2011; Gaddum et al., 2013; Wentland et al., 2014). Also critical for CMR-based PWV calculation is accurate assessment of the distance travelled by the flow waveform. Using a high temporally resolved 2D PC-CMR flow sequence, we have isolated the effect of different aortic distances in PWV calculations. Our research has revealed small but significant differences in PWV (between 0.5 and 1 m/s) calculated using centreline lengths obtained from 2D or 3D datasets. Although these differences might not be of clinical relevance for diagnostic purposes, they might be important for follow-up assessment and for reproducibility of measurements. These differences were particularly large in short and tortuous segments such as the aortic arch. Therefore, whenever feasible, we recommend

measuring aortic centrelines lengths in 3D datasets; optionally, this could be done in 2D datasets, where the aortic geometry enables the acquisition of a well-planned oblique-sagittal cine.

Finally, inadvertent patient movement between the anatomic and flow images can result in inaccuracies in the measured travelled distance. Thus, the images used to measure the transit time (e.g. 2D PC-CMR flows) and vessel length should be acquired consecutively, minimising the chance and impact of sudden patient movement and/or haemodynamic changes in the accuracy of PWV calculation (van Engelen et al., 2017).

5

PATIENT-SPECIFIC

COMPUTATIONAL MODELLING

This chapter presents the main research study of this PhD thesis concerning the application of a novel image-based computational modelling framework to study coronary haemodynamics in an ALGS child and enhance current cardiovascular risk assessment prior to liver transplantation. This will in turn motivate the suggested future work described in Chapter 6.

5.1. STUDY 6: PATIENT-SPECIFIC MODELLING OF RIGHT CORONARY CIRCULATION VULNERABILITY POST-LIVER TRANSPLANT IN ALAGILLE'S SYNDROME

5.1.1. BACKGROUND

As discussed in Chapter 2, ALGS is a rare polymalformative disorder whose clinical picture is dominated by hepatic failure symptoms. Early in infancy, around 20-30% require liver transplantation mostly due to refractory and debilitating cholestasis symptoms (e.g. pruritus, xanthomas) and cirrhotic complications. During orthotopic liver transplantation, ALGS patients are at high risk of RHF (Tzakis et al., 1993; Emerick et al., 1999; Razavi et al., 2001; Kamath and Loomes, 2018) and haemodynamic instability due to the presence of concomitant CHD (in particular PPS). These changes are aggravated in those patients with low cardiac reserve (i.e. RV dilation and systolic impairment secondary to PPS). Chronically elevated RV pressures in ALGS patients with PPS and secondary maladaptive RV hypertrophy (RVH) has been shown to hamper the heart's ability to respond to the marked pre-load changes during surgery (Png et al., 1999). When the inferior vena cava is clamped and intraoperative fluid requirements are increased, RV pressure/volume overload and pump failure can occur, which in turn can lead to hepatic congestion and decreased hepatic perfusion (Kamath and Loomes, 2018). Furthermore, the unclamping of the inferior vena cava and reperfusion of the new liver is associated with an additional and abrupt increase in preload, raised pulmonary pressures, and followed by a decrease in systemic vascular resistance and blood pressure due to the release of vasoactive factors into the circulation (Steadman, 2004). Aggarwal and co-workers (Aggarwal et al., 1987) have described a syndrome whose hallmark is systemic hypotension occurring within the first 5 minutes after reperfusion of the liver graft (PRS, post-reperfusion syndrome), a key determinant of the immediate surgical outcome. Data from adult patients suggests that nearly 50% of patients undergoing liver transplantation suffer from profound systemic hypotension or PRS (Chui et al., 2000; Hilmi et al., 2008; Paugam-Burtz et al., 2009). Although information in children, including those with ALGS, is scarce (Zhang et al., 2018), we speculate that a similar scenario may occur.

Since the risk of transplant complications (i.e. both graft and patient survival), particularly during the critical period of liver reperfusion, has been shown to be higher in ALGS than in other causes of childhood liver transplantation (Arnon et al., 2010; Kamath and Loomes, 2018), a thorough pre-operative assessment has been recommended. Some centres perform a dynamic test (dobutamine stress CMR, DSCMR) with concomitant right heart catheterisation to predict the patients' ability to increase the cardiac output in the immediate post-transplant period to meet the demands of systemic hypotension that occurs with liver reperfusion (Razavi et al., 2001; Squires et al., 2014). An increase in cardiac output of less than 40% has been reported to identify those patients at high risk of RHF during liver transplantation. Razavi *et al.* also proposed that those patients with suitable anatomy could benefit from pre-operative PPS percutaneous/surgical treatment (Razavi et al., 2001). While those ALGS patients with impaired RV systolic function at rest or inappropriate response to DSCMR are certainly at high risk of complications, a 40% increase in cardiac output might not guarantee adequate RCA perfusion during PRS and ultimately lead to RV ischaemia and systolic functional impairment/RHF. Hereof, studying *in silico* the mechanisms of coronary pressure and flow autoregulation in ALGS, including during a virtual liver transplantation setup, might provide further insight into the likelihood of cardiac complications.

5.1.1.1. CORONARY AUTOREGULATION IN ALAGILLE'S SYNDROME

Under resting physiologic conditions, CBF occurs predominantly during diastole, when intra-myocardial tissue pressure, particularly in the ischaemia-prone endocardium, falls below the aortic root pressure (Hoffman and Spaan, 1990; Tune, 2014). Notably, normalised resting CBF to the RV, which is significantly lower than that to the LV due to its lower MVO₂, is not significantly affected by its contraction. Due to lower RV systolic extravascular compressive forces, flow in the RCA occurs throughout the cardiac cycle (Lowensohn et al., 1976; Tune, 2014). In contrast, flow in the LCA is predominantly diastolic.

As described in Chapter 2, a complex network of highly integrated pathways not fully understood (metabolic, myogenic and endothelial-dependent), modulates the coronary microcirculation vasomotor tone, exerting a delicate control of the myocardial perfusion so that there is a close match between oxygen delivery and changes in MVO₂ (Tune et al., 2004; Arthurs et al., 2016). Given the heart's limited anaerobic capacity and oxygen extraction

reserve, notably reduced in RV pressure overload states such as in ALGS, the ability of the coronary microvasculature to dilate in response to inadequate myocardial oxygen delivery is critical to ensure adequate transmural delivery of oxygen and substrates to the heart, thus mitigating ischaemic injury (Wong et al., 2011; Tune, 2014). Despite a high degree of coronary microcirculation autoregulation (i.e. in hearts with effective autoregulatory responses, CBF remains constant as the coronary artery pressure is reduced below aortic pressure, over a wide range, if the determinants of myocardial oxygen consumption are kept constant) there is a threshold below which a further fall in the aortic perfusion pressure (e.g. during PRS) cannot be compensated by an additional decrease in coronary resistance (Dankelman et al., 1999; Tune, 2014). In other words, when the coronary arteries are maximally dilated and the perfusion pressure falls to the lower limit of autoregulation, flow becomes pressure-dependent, resulting in the onset of subendocardial ischemia. Moreover, the coronary vasodilator reserve appears to be lower in the RCA territory (Zong et al., 2005).

During physiological autoregulation, CBF changes in response to a decrease in mean arterial pressure (MAP), such as that occurring during PRS, are the result of both a reduced coronary perfusion pressure and a reduced MVO_2 , consequence of a lower LV afterload. In other words, any disturbance in the heart and/or peripheral circulation is ultimately reflected in the CBF via alterations in cardiac workload (Duncker and Bache, 2008; Tune, 2014). This strong coupling between CBF and MVO_2 makes it difficult to study *in vivo* complex coronary pressure-flow autoregulation mechanisms and isolate their individual contributions, and makes computational modelling an appealing alternative (Tune, 2014).

As previously described, some form of pulmonary vasculopathy is present in ALGS, with PPS reported in over two third of cases of ALGS patients (Alagille et al., 1987; Emerick et al., 1999; Kamath et al., 2018). PPS directly increases the workload burden of the RV. Two other consequences of PPS have been reported. On the one hand, PPS reduces the perfusion to the affected lung segments and can impaired downstream vessel growth if normal pulmonary haemodynamics are not restore in a timely fashion (Yang et al., 2018). On the other hand, as reported in patients with Tetralogy of Fallot, PPS induces progressive structural remodelling (stiffening) of the walls of the pulmonary arteries, (Bédard et al., 2009; Inuzuka et al., 2013). Furthermore, some researchers have observed that in the presence of hypoplastic proximal pulmonary arteries or relatively underdeveloped and stiff pulmonary

circulation, percutaneous/surgical repair prior to liver transplantation might not improve the pulmonary pressure and relative lung perfusion in ALGS, resulting in a chronic increase in RV afterload (Agnoletti et al., 2004; Razavi et al., 2013; Monge et al., 2013; Yang et al., 2018).

Sustained RV hypertension triggers structural changes (e.g. changes in myosin isoform expression) and neurohormonal activation that ultimately results in RVH. These mechanisms aim to maintain pulmonary blood flow and left atrial filling without a further increase in RV wall stress (Murali et al., 1993). They allow for an adaptive (or compensated) RVH state, characterised by a cardiac output that is still sufficient to meet the metabolic demands of the body (Williams and Frenneaux, 2006; Frump et al., 2018). However, the RV adaptation to a chronic increased afterload is limited (Szabó et al., 2006). As such, once the RV's compensatory mechanisms are exhausted, a transition from adaptive to maladaptive (or decompensated) RVH occurs: the RV becomes hypocontractile, with decreased cardiac output. The precise mechanisms involved in the transition from adaptive RVH to maladaptive remodelling and failure are not completely understood (Rich, 2012; Razavi et al., 2013; Frump et al., 2018). Furthermore, there is heterogeneity in RVH responses in terms of its effects on cardiac output and the likelihood of progression to RHF, not simply explained by differences in RV mass or RV pressure overload. In other words, despite similar elevations in RV pressure and RVH, some ALGS patients may have maladaptive forms of RVH and rapidly decompensate during liver transplantation, which further complicates pre-transplant assessment (Ryan and Archer, 2014).

The RV macro and microvasculature have recently emerged as critical modulators of RV adaptation in the setting of pressure overload and of progression to maladaptive RVH (Frump et al., 2018). Raised RV afterload commonly seen ALGS patients results in increased RV wall tension and can decrease the coronary perfusion gradient between the aorta and RCA bed (extravascular compressive resistance). Although robust in ALGS evidence is lacking, their poorer liver transplantation survival compared to other children is likely related to the underlying pulmonary vasculopathy and its effects in the RV and coronary macro and microvasculature (Kamath and Loomes, 2018).

van Wolferen *et al.* observed that in adults with PAH, RCA flow was markedly decreased and became predominantly diastolic, with systolic RCA flow impeding

proportional to the raised RV pressures and increased mass (van Wolferen et al., 2008). RCA flow impairment in ALGS with RV hypertension could predispose to RV ischemia (Gomez et al., 2001; van Wolferen et al., 2008), a phenomenon likely exacerbated by any additional increased myocardial oxygen demand, such as that due to an additional increase in RV afterload during liver transplantation. Although to our knowledge no data is available in ALGS children, we hypothesise that a similar scenario to that describe in PAH may occur, with increasing RV wall tension and consequently RVMVO₂ resulting in a progressive shift of RCA flow to diastole, rendering it more LCA-like and CBF diastolic dependent.

In addition there is also evidence that the RV microvasculature in patients with chronic raised afterload and compensatory RVH is dysfunctional and rarefied, rendering it unable to meet the increased oxygen/substrate demand of the hypertrophied myocardium (Gomez et al., 2001). Indeed, reduced RV capillary density and ensuing microvascular ischemia in sections of PAH models associated with RHF has been identified as a critical mediator of the transition from adaptive to maladaptive RVH (Partovian et al., 1998; Voelkel et al., 2006; Bogaard et al., 2009; Piao et al., 2013; Vonk Noordegraaf et al., 2017; Frump et al., 2018). In ALGS children with near-systemic RV pressures and compensatory RVH, it is plausible that this also occurs. Furthermore, the additional increase in RV afterload following inferior vena cava unclamping not only increases the myocardial metabolic demand but also can result in compression of the intramyocardial vessels which, together with the systemic hypoperfusion of the post-reperfusion period, can reduce the coronary perfusion pressure gradient. In such scenario, CBF impairment could occur even before the vasodilator reserve is exhausted (Zong et al., 2002; van Wolferen et al., 2008; Hsu et al., 2016), resulting in RV ischaemia and contractile dysfunction (i.e. RHF). This could trigger a rapidly progressive downward spiral to haemodynamic collapse, with hepatic ischaemic congestion and graft failure, LV underfilling and further systemic hypotension (Png et al., 1999; Greyson, 2010; Kamath and Loomes, 2018). In theory, progressive RV adverse remodelling secondary to persistent RV hypertension could alter the threshold at which the downward spiral of haemodynamic collapse begins and could explain why some ALGS patients with apparently stable pulmonary haemodynamics can abruptly decompensate (Greyson, 2008, 2010; Kamath and Loomes, 2018).

We submit that the DSCMR study (Razavi et al., 2001; Squires et al., 2014), currently

used to predict the patient's ability to increase the cardiac output in the immediate post-transplant period to meet the demands of systemic hypotension that occurs with liver reperfusion, does not account for all key hemodynamic events during liver transplantation. While the test might reproduce the increase in HR and myocardial metabolic demand, it fails to account for the systemic hypotension and corresponding coronary perfusion pressure drop during transplantation (Bruinsma et al., 1988). Furthermore, as previously mentioned, the general guideline of 40% increase in cardiac output during DSCMR might not guarantee adequate RCA perfusion during PRS and the test might fail identify those ALGS children that are at high risk RHF.

In this study, we propose to use computational modelling in combination with image-based and catheterisation data from an ALGS subject undergoing cardiovascular risk assessment, to shed some light into the coronary haemodynamics during PRS and the pathophysiology of RHF. Using two subject-specific haemodynamic stages (rest and stress) of the pre-operative XMR, we have simulated three different conditions:

- 1) Rest condition, in which a computational model of RV, LV, RCA, LCA, aorta, and pulmonary arteries is calibrated to reproduce baseline haemodynamic data for the patient.
- 2) Stress condition, in which the computational model above is adjusted to reproduce the haemodynamic conditions during DSCMR for the same patient.
- 3) Post-reperfusion (PRS) condition, entirely computational, in which the Stress condition is further modified to account for the systemic pressure drop during PRS.

In the next section we describe in detail how we have progressed from the image data (i.e. XMR) to the construction of a closed-loop coupled multidomain 0D-3D computational model of an ALGS child to predict whether the coronary autoregulation would be effective during a PRS state, and whether this could place the patient at risk of RHF during liver transplantation.

5.1.2. MATERIAL AND METHODS

5.1.2.1. PATIENT DETAILS

A 6-year-old female subject with a confirmed diagnosis of ALGS and under consideration for liver transplantation due to progressive hepatic disease and growth retardation was referred to our Department for pre-surgical workup. The patient had undergone percutaneous treatment of PPS and, despite raised RV afterload at baseline (Rest Condition), had no residual proximal stenosis as shown in the black blood CMR images of Figure 41, suggesting some degree of pulmonary vascular remodelling.

The patient was admitted 24h prior to the study for standard pre-anaesthesia evaluation.

5.1.2.2. HYBRID XMR STUDY

The patient underwent a XMR study to quantify PVR by use of simultaneous invasive pressure monitoring and 2D PC-CMR flow, following the Department standard procedure (Muthurangu et al., 2004; Tzifa et al., 2012; Pushparajah et al., 2015). The study also included a dobutamine pharmacological CMR stress test to unmask abnormal cardiac responses and predict early heart failure post-transplant.

The study was performed in a specifically designed catheterisation laboratory (Figure 41) located in the Paediatric Cardiology Department at the Evelina London Children's Hospital, which is equipped with a Philips BV Pulsera cardiac X-ray unit and a 1.5 Testa CMR scanner (Achieva, Philips, Best, The Netherlands). The table-top design of the CMR scanner enabled the patient to be quickly and safely moved from one modality to the other with minimal repositioning. In addition, the table position was stored within the CMR/angiographic console system allowing image fusion for reference planning. The suite also includes in-room controls and monitor display of the acquired CMR images and haemodynamic pressure traces as well as CMR-conditional equipment for patient monitoring and anaesthesia support. All the fluoroscopy procedures were performed outside the 5-gauss line marked in the CMR floor. Standard safety-checks were conducted throughout the study to confirm the use of CMR-conditional equipment, and all ferromagnetic objects used during the fluoroscopy-guided catheterisation were outside the 5-gauss line.

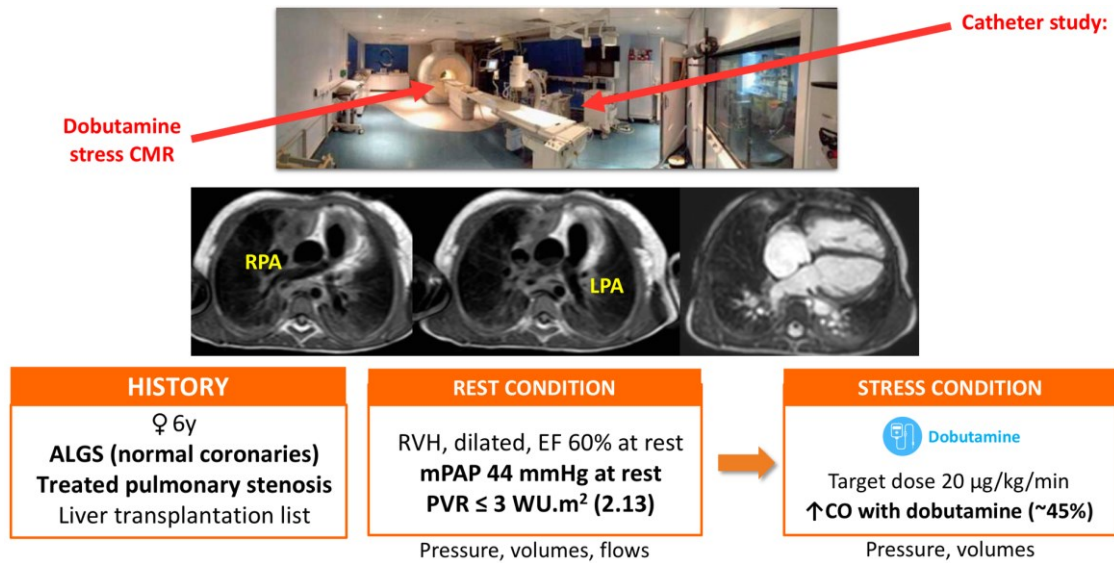


Figure 41

Image of the hybrid X-ray/MR suite where a 6-year old ALGS underwent the dobutamine stress CMR and a right heart catheter study. Schematic summarising some of the clinical data used to inform the patient-specific computational model. ALGS, Alagille's syndrome. CO, cardiac output. EF, ejection fraction. LPA, left pulmonary artery. mPAP, mean arterial pulmonary pressure. PVR, pulmonary vascular resistance. RPA, right pulmonary artery. RVH, right ventricular hypertrophy.

The patient was anaesthetised in a dedicated area adjacent to the imaging suite. Sevoflurane and intravenous remifentanyl were used for anaesthesia induction and maintenance. The patient was then wheeled into the XMR room on a CMR-conditional trolley, quickly transferred to the specially designed CMR table in the non-magnetic area and connected to the CMR-conditional respiratory ventilator system. Standard ECG leads were placed outside the radiographic FoV and attached to the anaesthetic CMR-conditional system for cardiac monitoring during the fluoroscopy. Before the patient was moved into the scanner bore, they were replaced by a three-lead CMR-conditional VCG for triggering and gating. CMR-conditional pulse oximeter and non-invasive blood pressure monitoring equipment were also attached. Flexible phased array radiofrequency coils were placed. Because they are relatively radiolucent, they were used for both fluoroscopic and CMR imaging. An aseptic technique was maintained throughout the procedure.

For pressure monitoring, the commercially available haemodynamic monitoring system EP Tracer 102 (CardioTek B.V, Maastricht, The Netherlands) was used. Non-invasive measurement of the partial pressure of carbon dioxide (CO₂) in the exhaled breath (capnography) was used throughout the procedure to retrieve instantaneous information about ventilation (the efficiency of CO₂ elimination by the pulmonary system), perfusion (the

efficiency of CO₂ transport through the vascular system), and metabolism (CO₂ production by cellular metabolism). All the haemodynamic data was sent from the CMR-conditional monitoring equipment via an optical network to a console in the control room, where the Cardiac Physiologist was stationed.

The XMR catheterisation procedure started by obtaining femoral vascular access in the non-magnetic field area of the XMR room with a 4 French (F) BRITE TIP® Interventional Sheath introducer (Cordis, NJ, USA). A heparin bolus of 750 units (50 units/kilogram) was given with activated clotting time monitoring once vascular access was obtained (total of 1250 units). Continuous invasive arterial pressure monitoring was available throughout the procedure via a femoral arterial cannula. A Thruway™ Short Taper Guidewire (0.018") was used to navigate the vessels of interest and support a 4F CMR-conditional angiographic balloon catheter (Balloon Wedge-Pressure catheter, Arrow, Reading, PA, USA). The balloon was filled with 1 millilitre (ml) of CO₂ to create negative contrast (signal void) and facilitate CMR passive tracking. To minimise ionising radiation exposure and improve real-time anatomical visualisation of the cardiovascular structures, catheter advancement and positioning in the appropriate vessels/chambers was carried out under CMR-guidance. Initial reference CMR scans were acquired and included an interactive sequence with landmark plans for catheter guidance. Manipulation within the heart and great vessel was performed using a specific designed 2D SSFP sequence (TE 1.45ms, TR 2.9ms, matrix 128×128) with a temporal resolution of 10–14 frames per second. Fluoroscopy was reserved for difficult catheter manipulation. Once the right heart catheterisation was completed, the catheter was left in place in the main pulmonary artery for continuous haemodynamic pressure monitoring. This enabled acquisition of simultaneous CMR and invasive pressure data that was later used to parameterise the computational model.

5.1.2.3. CMR IMAGING PROTOCOL

The parameters of the sequences acquired and used to parametrise the PSCM are shown in Table 24. A number of different CMR datasets were acquired for the patient under two different conditions:

- 1) Rest Condition, corresponding to the baseline measurements. It included a short-axis cine stack and three long-axis cines for LV/RV functional assessment, 2D PC-

CMR flow images acquired perpendicular to the long-axis of the vessel of interest (the proximal main pulmonary artery, the proximal right and left pulmonary arteries, the aortic root and the descending aorta at the diaphragm level); in addition a dual-phase 3D SSFP CMRA sequence was acquired using the design tested in Study 3 of this thesis;

2) Stress Condition, corresponding to the haemodynamic measurements during peak dobutamine infusion. The protocol included a two-stage dobutamine infusion with concentrations of 10 $\mu\text{g}/\text{kg}/\text{min}$ and 20 $\mu\text{g}/\text{kg}/\text{min}$, respectively. At each stage, a short-axis cine stack was acquired for functional assessment (i.e. measurement of cardiac output response to dobutamine). This staged approach allowed to assess the response to increasing doses and therefore prevent complications. Razavi *et al.* (Razavi et al., 2001) described that a significant decrease in the systemic vascular resistance was only observed with the higher dose of 20 $\mu\text{g}/\text{kg}/\text{min}$ and thus this has been established as the target dose for a diagnostic test as well as the concentration defining the “peak dobutamine stress” in this work (i.e the simulated Stress Condition).

	Short-axis cine	Flows	3D morphology
Sequence type	2D SSFP	2D PC-CMR	3D SSFP (dual-phase)
Number of phases	30	30	-
Slice Thickness (mm)	7	6	1.8
TR (ms)	2.7	4.3	4.5
TE (ms)	1.4	2.7	2.3
In-plane pixel size (mm)	1.7x1.6	2.0x1.6	1.3x1.3
Flip angle	60	15	90
Signal average	1	3	1
Respiratory Motion Compensation	None (breath-hold)	Respiratory gating	2D iNAV

Table 24

Parameters of the different CMR sequences acquired and used to parametrise the PSCM. iNAV, image-based navigation. TE, echo time. TR, repetition time. PC-CMR, phase-contrast CMR flow. SSFP, steady-state free precession.

A novel modelling framework that integrates this image data and the detailed invasive/non-invasive measurements was used to obtain a faithful computational representation of the patient's physiology.

5.1.2.4. PSCM MODELLING OF HAEMODYNAMICS

Our image-based computational modelling workflow followed the paradigm for blood flow numerical simulations discussed in Chapter 2 (Vignon-Clementel et al., 2006; Taylor and Figueroa, 2009). It involved three key steps: (1) creating a geometrical 3D mesh; (2) choosing adequate boundary conditions to solve the Navier-Stokes equations of conservation of mass and momentum; and (3) the numerical computation of the solution (Arbia et al., 2014). In this workflow we integrated tools that were developed/validated in Studies 1-5 (Figure 42), which were important to ensure the simulation results matched the clinical data: the 2D iNAV IR-CMRA sequence developed and tested in Studies 1-3 enabled the acquisition of high quality 3D images of the coronary tree as well as the extracardiac vascular structures of the patient; Studies 4 and 5 provided tools for parametrisation of the 0D heart LPN and aortic/pulmonary stiffness of the 3D domain, respectively.

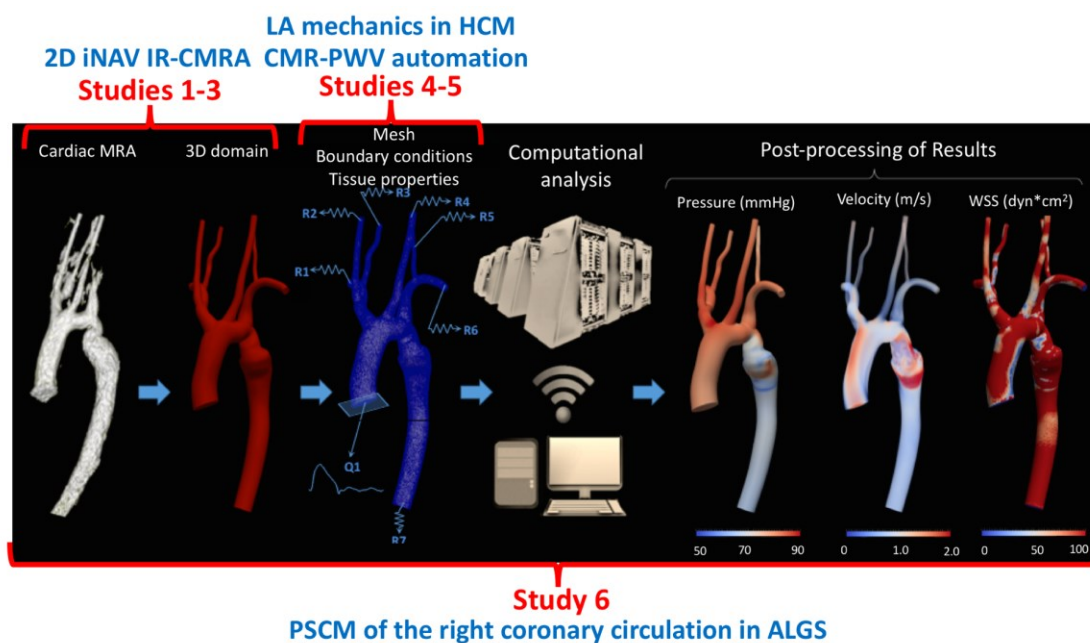


Figure 42

Schematic of how Studies 1-5 were intertwined with the typical image-based computational modelling workflow discussed in Chapter 2 and used in the study of the right coronary circulation autoregulation of an ALGS child. 2D iNAV IR-CMRA, 2D image-navigated inversion-recovery coronary magnetic resonance

angiography. CMR-PWV, cardiovascular magnetic resonance derived pulse wave velocity. HCM, hypertrophic cardiomyopathy. LA, left atrium/atrial. PSCM, patient-specific computational model.

After defining the physics of the 3D and reduced-order models, we used two main computational methods to solve the coupled systems:

(1) the coupled multidimensional method (Vignon-Clementel et al., 2006) to couple the 3D parts of the PSCM (i.e. the aorta and central pulmonary arteries) segmented from the 2D iNAV IR-CMRA sequence developed in Studies 1-3, with the reduced order models of the heart, vessels outside the FoV of the CMRA, and the microcirculation;

(2) the coronary autoregulation control method (Arthurs et al., 2016) that adjusted the coronary LPN resistances to increase CBF and match the cardiac metabolic demand.

We proceed to describe the PSCM design, starting with the segmentation of the 3D geometric models of the aorta and pulmonary arteries.

5.1.2.4.1. FLUID-SOLID INTERACTION 3D MODELS OF THE AORTA AND PULMONARY ARTERIES

The CRIMSON custom software (CardiovasculaR Integrated Modeling and SimulatiON; <http://www.crimson.software/>) was used to segment the aorta and main branches, including the coronaries, and the central pulmonary arteries, from the diastolic phase of the 2D iNAV IR-CMRA sequence, to produce an analytical representation of the vessels (Figure 43). CRIMSON is an open source package that provides a complete pipeline from medical image data to 3D model construction, meshing, and blood flow simulation. It is based on Medical Imaging Interaction Toolkit (MITK) research platform. It not only allows to interact and visualise medical imaging, construct the 3D geometric model, generate and edit volumetric flow waveforms from 2D PC-CMR data, but it also incorporates a 1D and 3D flow solver for blood flow numerical analysis.

A 2D segmentation approach, originally introduced by Wang *et al.* (Wang et al., 1999a), was used to create the geometric model. First, paths were delineated through the centreline of the vessels (Figure 43) that were included in the model (i.e. aorta and major branches, coronaries and the proximal pulmonary arteries). This was followed by a 2D manual or semi-automatic segmentation of the vessel wall along the created paths and perpendicular to it, at a discrete number of locations. Finally, an automatic lofting operation

using these contours and a NURBS algorithm was performed (Figure 44). The use of smoothing options based on Fourier transforms reduced the generation of sharp edges in the 3D model.

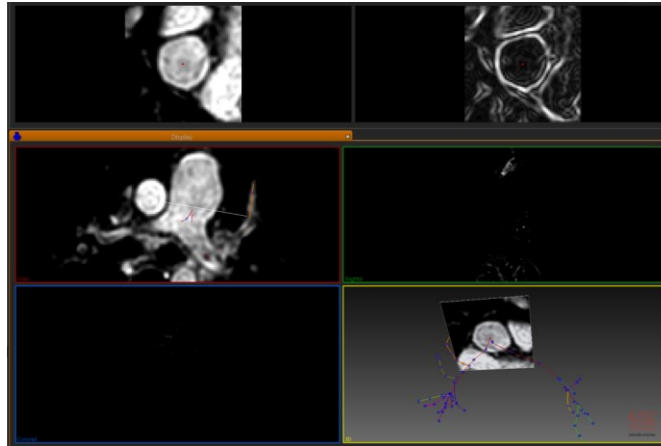


Figure 43

Graphic user interface from CRIMSON showing the 2D segmentation process. In the initial step, centreline paths through the middle of the vessel of interest were delineated. Resliced images are displayed in the top panels perpendicular to the created path lines.

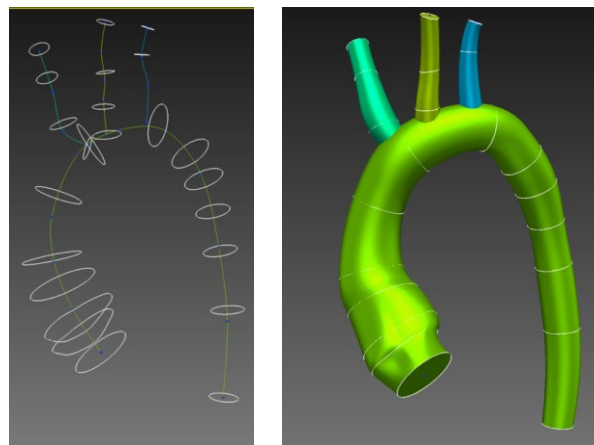


Figure 44

Example of path lines created during the segmentation of the aorta (left panel) and the result after a loft operation has been performed (right panel). A smoothing algorithm for the intersections was applied during the 3D geometric model segmentation, with different fillet sizes to avoid the generation of sharp edges. The described process was repeated for each vessel to produce a 3D analytically smooth solid model that was then meshed.

The 3D geometry was then discretised into a volumetric finite element mesh (Figure 45) consisting of 1,687,949 tetrahedral elements (characteristic dimension of 0.8mm) and 325,463 nodes, with curvature-based refinement.

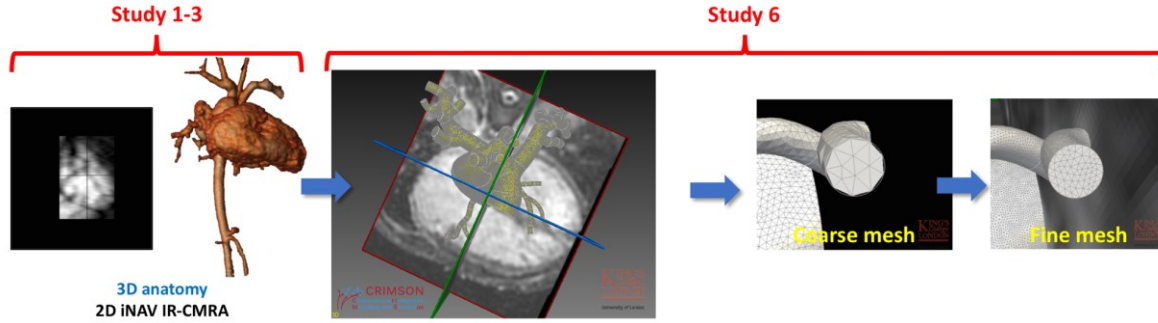


Figure 45

The 3D geometric models of the aorta (including the coronaries) and pulmonary arteries were built by segmenting the 2D iNAV IR CMRA, which was validated in Studies 1-3, using an open-source software CRIMSON® that was developed by our team. The 3D geometric model was then discretised into a 3D mesh, which was iteratively refined to best match the simulation and the clinical data (i.e. we increased the mesh density using a smaller element size). 2D iNAV IR-CMRA, 2D image-navigated inversion-recovery coronary magnetic resonance angiography.

Blood was modelled as an incompressible Newtonian fluid (density $\rho=0.00106$ g/mm³ and viscosity $\mu=0.004$ g/mm·s). Blood vessels were modelled using the Coupled Momentum Method, whereby an incompressible linear elastic membrane with spatially-varying structural stiffness is monolithically-coupled to the fluid domain (Xiao et al., 2013). The linearised stiffness (E) of the aorta, its branches and the central pulmonary arteries (Figure 46, right hand panel) were prescribed according to the equation:

$$E = \frac{P_{syst} - P_{diast}}{D_{syst} - D_{diast}} \times D_{diast}$$

Equation 14

where P_{syst} and P_{diast} represent the catheter-derived systolic and diastolic pressures, respectively, and D_{syst} and D_{diast} the systolic and diastolic diameters at the level of the aortic and pulmonary artery roots, respectively, measured using the CMR-PWV tracking tool validated in Study 5 (Figure 46, left hand panel). Wall thickness was prescribed to be 1 mm throughout. This produced a linearised stiffness of 2.26×10^5 g/mm·s² for the systemic and 1.30×10^5 g/mm·s² for the pulmonary arteries.

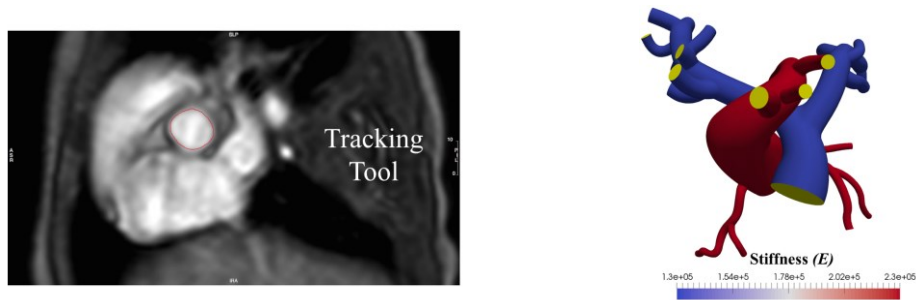


Figure 46

Tracking of the vessel wall during an entire cardiac cycle was done using the 2D PC-CMR aortic/pulmonary flow magnitude images (left hand panel). The tracking tool, which was developed and validated in Study 5 to automated PWV calculation, provided the systolic and diastolic aortic/pulmonary artery roots diameters used to calculate the linearised aorta/pulmonary stiffness prescribed to the 3D domains of the computational model (right hand panel). PC-CMR flow, phase-contrast cardiovascular magnetic resonance flow. PWV, pulse wave velocity.

5.1.2.4.2. CLOSED-LOOP COUPLED MULTIDOMAIN MODEL

Due to the limits of the 2D iNAV IR-CMRA resolution and computational resources, it was impossible to include all the vessels in the cardiovascular system in a 3D Navier-Stokes simulation (Marsden and Esmaily-Moghadam, 2015). Therefore, expanding on previous developments by our research group (Lau and Figueroa, 2015), we have designed a closed-loop coupled multidomain (0D-3D) model consisting of LPN (0D) models of the heart chambers, arterial and venous distal circulations, and image-based (3D) portions of the pulmonary and systemic circulations, where image data was available (Figure 47).

As the local flow dynamics are known to be greatly influenced by conditions upstream and downstream of the 3D models, adequate selection of boundary conditions was of paramount importance (Vignon-Clementel et al., 2006; Marsden and Esmaily-Moghadam, 2015). In order to facilitate adequate parametrisation of the PSCM model, the following strategy was followed. First, a family of simplifications of the complete model was determined, to allow parameters to be identified in the simplest setting, without confounding complexity. Within more complex models, fine-tuning of the LPN parameters was performed to perfect the agreement between the simulation and the patient data. The hierarchy of simplifications was as follows, from most simplified to most complete:

(1) Pure-0D open-loop model, in which the 3D domains were entirely replaced by a simple resistor-capacitor network – the 3D domain replacement (3DDR). Only the Windkessel, coronary and heart boundary LPNs were included (i.e. the circulatory loop was open). Parameters adjusted using this simplified model were: Windkessel resistance and

compliance, ventriculo-arterial valve resistance and inertance.

(2) Pure-0D closed-loop network, which added the downstream LPNs to the model above (i.e. pulmonary and systemic vascular beds). Parameters adjusted were: venous resistance and compliance, atrio-ventricular valve resistance and inertance, and atrial volume and compliance.

(3) Final 0D-3D closed-loop deformable model, in which the 3DDR was replaced with deformable 3D image-based models of the pulmonary and aortic domains. Parameters adjusted were: Windkessel compliance and resistance. Each 3D domain inflow was extracted from the 0D heart model ordinary differential equation solution, thus incorporating the responses of the heart and global physiology to altered flow conditions (e.g. PRS Condition).

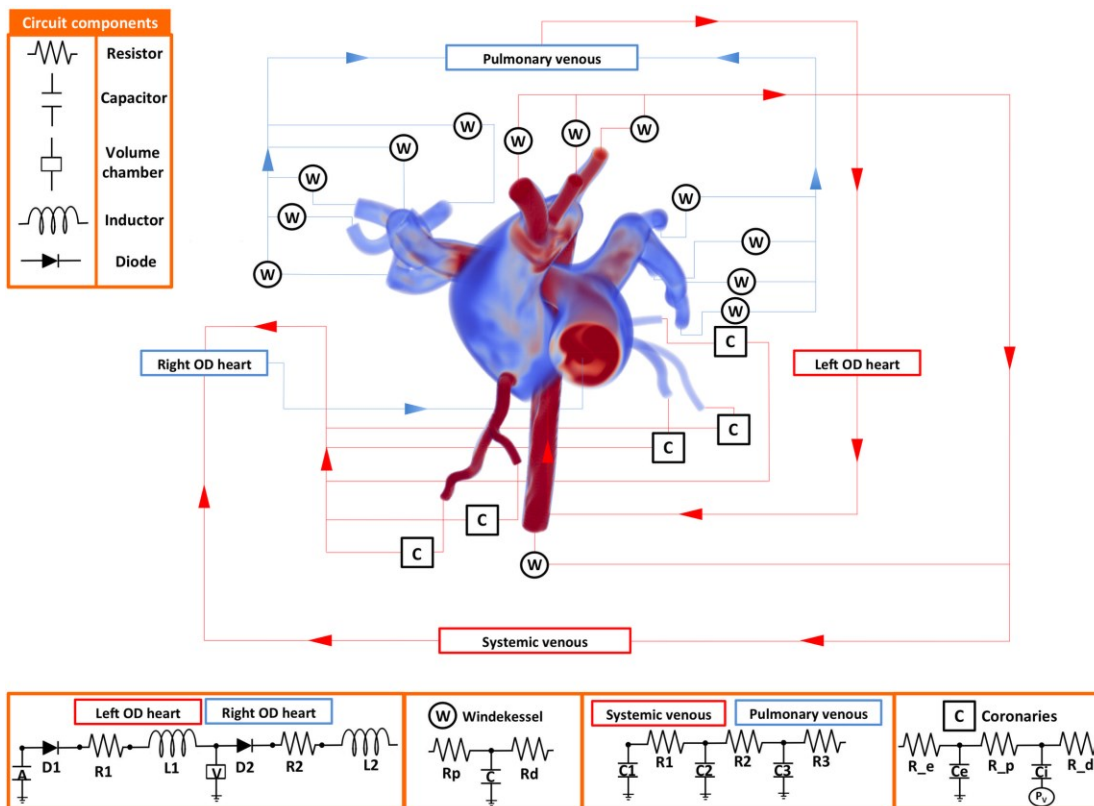


Figure 47

Patient-specific closed-loop model used to simulate pulsatile haemodynamics, coupling lumped parameter networks (LPN, 0D) and image-based (3D) vascular models. The model includes: LV (0D), aorta, coronary arteries and major branches (3D), medium and small systemic arteries (0D), arterioles (0D), venules (0D), veins (0D), right atrium (0D), RV (0D), pulmonary arteries up to second generation branching (3D), small pulmonary arteries (0D), arterioles (0D), venules (0D), veins (0D) and left atrium (0D). P_v represents the node where the broadcasted intraventricular pressure was transmitted as described by Arthurs *et al.* (Arthurs *et al.*, 2016).

LPN Heart Model

We used a 0D LPN model to represent the left and right atrial and ventricular chambers and the delimiting valves (Figure 47). A time-varying ventricular elastance function (E_{Ve}), defined as the ratio of the patient-specific ventricular pressure (P_{Ve}) and volume (V_{Ve}) was obtained for the Rest and Stress conditions according to:

$$E_{Ve}(t) = \frac{P_{Ve}(t)}{V_{Ve}(t)}$$

Equation 15

These elastance functions (Figure 48), describing cyclic ventricular volume and intraventricular pressures changes, were derived from ventricular CMR cines and catheterisation data. $V_{Ve}(t)$ was obtained by manually contouring the endocardial borders of all cardiac phases of the short-axis cine stack using the cvi⁴²® software (Circle Cardiovascular Inc. Calgary Canada version 5.2.2), with delineation of the papillary muscles. $P_{Ve}(t)$ was available from ventricular pressure catheterisation data. Given that CMR pulses were triggered by the occurrence of an R-wave in the console vectorcardiogram, $V_{Ve}(t)$ and $P_{Ve}(t)$ were temporally aligned by matching the initial point of the volumetric curve with the corresponding R-wave in the invasive pressure recordings. Ventricular volumetric parameters derived from the CMR dataset for the Rest and Stress conditions and used to define their corresponding elastance functions are listed in Table 25.

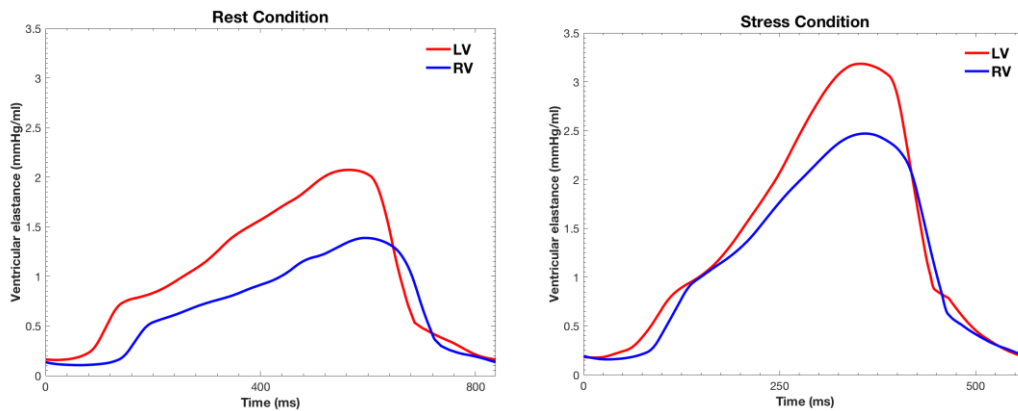


Figure 48

Time-varying left and right ventricular elastance (E) functions were calculated for the Rest and Stress Conditions using the XMR derived ventricular volume (V) and pressure (P) data [$E(t) = P(t) / V(t)$]. These were then prescribed to the 0D heart LPN heart. LV, left ventricle. RV, right ventricle.

Condition	Heart Rate (bpm)	Mass index		EDV ^a		ESV ^b		EF ^c	
		(g/m ²)		(ml/m ²)		(ml/m ²)		(%)	
		LV	RV	LV	RV	LV	RV	LV	RV
Rest	73			81	90	35	44	60	51
		54.2	59.8						
Stress	106			80	95	23	37	71	61

Table 25

RV and LV volumetric parameters for Rest and Stress conditions measured from the CMR scan. ^aEDV, end-diastolic volume. ^bESV, end-systolic volume. ^cEF, ejection fraction.

The atrio-ventricular and the aortic valves were competent, and so modelled via diodes permitting only forward flow as described before (Lau and Figueroa, 2015). The pulmonary valve was incompetent, therefore it was modelled as a two-state resistor, having a low resistance to forward flow, and a high but finite resistance to backward flow. The pulmonary valve resistance when the valve was closed ($PV_{R,C}$) was determined from the patient data by:

$$PV_{R,C} = \frac{P_{PA,C} - P_{RV,C}}{Q_{PV,C}}$$

Equation 16

where $P_{PA,C}$ and $P_{RV,C}$ are the mean pressures in the pulmonary artery and the RV respectively, during the period when the valve was closed; $Q_{PV,C}$ is the mean flow through the pulmonary valve during the same period. The resistance of the valve in the open state, $PV_{R,O}$, was set to $3.00 \times 10^{-3} \text{ g}/(\text{mm}^4 \cdot \text{s})$.

Valvular inertance (L) was calculated according to the equation (Broomé et al., 2013):

$$L = \frac{\rho l}{A}$$

Equation 17

where ρ is blood density; and l and A the length and area of the valve respectively. These were measured from cine images and 2D PC-CMR through-plane flow data at the valve level. Values are presented in Table 26.

	VAV inertance $\text{g}\cdot\text{mm}^{-4}$	AVV inertance $\text{g}\cdot\text{mm}^{-4}$	VAV resistance $\text{g}/(\text{mm}^4\cdot\text{s})$		AVV resistance $\text{g}/(\text{mm}^4\cdot\text{s})$	
			Open	Closed	Open	Closed
LV	2.61×10^{-5}	3.69×10^{-5}	2.00×10^{-3}	∞	1.00×10^{-3}	∞
RV	6.90×10^{-6}	8.90×10^{-6}	3.00×10^{-3}	1.80×10^{-2}	6.00×10^{-3}	∞

Table 26

Parameters for all heart valves. VAV, ventriculo-arterial valves. AVV, atrioventricular valves.

Both the left and right atria were modelled as passive compartments with a constant elastance (E_{LA} and E_{RA}) calculated using the available invasive pressure data and atrial volumes (biplane method) as detailed in Table 27.

Heart chamber	Elastance	Volume
	Pa/mm^3	mm^3
Right atrium	3.52×10^{-2}	4.00×10^4
Left atrium	1.40×10^{-1}	2.25×10^4

Table 27

Elastance parameters and volumes for the atria

5.1.2.4.4. LPN MODEL OF THE PERIPHERAL SYSTEMIC AND PULMONARY VASCULATURE

At each outlet of the 3D domain of the aorta and pulmonary arteries a 3-element Windkessel was coupled to represent the downstream vasculature (Figure 47). The parameters for the proximal and distal resistor and compliance at outlet i ($R_{p,i}$ and $R_{d,i}$, and C_i respectively) were computed using the available patient data and 1D non-linear theory considerations described by Xiao *et al.* (Xiao *et al.*, 2013), and assuming minimisation of wave-reflections at the outlet faces.

For the systemic and pulmonary circulations, the respective total peripheral resistance $R_{T,S}$ and $R_{T,P}$ were computed using

$$R_{T,j} = \frac{P_{mean,j}}{Q_{mean}}$$

Equation 18

where $P_{mean,j}$ is the mean pressure in the aortic ($j=S$) or pulmonary ($j=P$) root, and Q_{mean} the mean aortic or pulmonary flow as derived from the 2D PC-CMR through-plane flow. We then apportion the total resistance to the individual outlets using

$$R_i = R_{T,j} \frac{Q_{mean}}{Q_i}$$

Equation 19

where j was selected according to whether the i -th outlet is on the pulmonary or systemic side.

The proximal resistance $R_{p,i}$, the distal resistance $R_{d,i}$, and the diastolic wave speed C_{diast}^i at outlet i , were determined using

$$C_{diast}^i = \frac{a_2}{(2R_{diast}^i)^{b_2}}$$

Equation 20

$$R_{p,i} = \frac{\rho C_{diast}^i}{A_{diast}^i}$$

Equation 21

$$R_i = R_{p,i} + R_{d,i}$$

Equation 22

where A_{diast}^i and R_{diast}^i are the diastolic area and radius of outlet i respectively, measured using the diastolic phase of the 2D iNAV IR-CMRA. The remaining terms are constants: $a_2=13.3$, $b_2=0.3$, and the blood density $\rho=0.00106 \text{ g}\cdot\text{mm}^{-3}$.

Windkessel compliances were calculated by writing

$$C_{T,j} = C_{C,j} + C_{P,j}$$

Equation 23

with $C_{T,j}$ the total compliance of the systemic ($j=S$) or pulmonary ($j=P$) circulation, and $C_{P,j}$ and $C_{C,j}$ the total peripheral (LPN) and 3D domain compliances on each side, respectively.

$C_{T,j}$ was computed from data using

$$C_{T,j} = \frac{Q_{max,j} - Q_{min,j}}{P_{syst,j} - P_{diast,j}} \Delta t_{Q_{min,j}}^{Q_{max}}$$

Equation 24

where $Q_{max,j}$ and $Q_{min,j}$ are the maximum and minimal flow into domain j , measured from the 2D PC-CMR flow, $\Delta t_{Q_{min,j}}^{Q_{max}}$ the time interval between $Q_{max,j}$ and $Q_{min,j}$, and $P_{syst,j}$ and $P_{diast,j}$ the systolic and diastolic root pressures on side j , respectively.

The compliance of vessel branch i of the 3D domain ($C_{C,j}$) was computed from

$$C_c^i = \frac{A_{diast}^i L^i}{\rho (C_{diast}^i)^2}$$

Equation 25

where L^i was the segment length calculated from the 2D iNAV IR-CMRA anatomical data, from the point where it branches from its parent vessel to the outlet (for the aorta, from the root to the aortic outlet at the diaphragmatic level).

$C_{C,j}$ is then the sum of C_c^i over all branches i belonging to circulation j (pulmonary or systemic).

The peripheral compliance at outlet i (C_p^i) was computed as

$$C_p^i = C_{P,j} \frac{Q_i}{Q_{mean}} \left(\frac{R_{p,i} + R_{d,i}}{R_{d,i}} \right)$$

Equation 26

where outlet i is part of circulation j , Q_{mean} is the mean cardiac output per unit time, and Q_i is the mean expected flow through outlet i per unit time.

To close the circulatory loop, the distal resistor of each 3-element Windkessel was coupled to a downstream LPN circuit representing the arterioles, venules and veins, with the final venous compartment connected to the right and left atrium, respectively (see Figure 47 and Figure 49). The initial parameters for this circuit were derived from previous work from Lau *et al.* (Lau and Figueroa, 2015) and iteratively adjusted in order to match the available patient haemodynamic data at rest and stress (Table 28 and Table 29).

Parameters		Arterioles	Venules	Veins
Resistance g/(mm ⁴ ·s)	Systemic vascular bed	8.89 x 10 ⁻² (R1)	3.56 x 10 ⁻³ (R2)	2.97 x 10 ⁻³ (R3)
	Pulmonary vascular bed	1.40 x 10 ⁻⁴ (R1)	5.54 x 10 ⁻⁷ (R2)	9.9 x 10 ⁻⁸ (R3)
Compliance mm ⁴ ·s ² /g	Systemic vascular bed	8.9 x 10 ⁻³ (C1)	3.60 x 10 ⁻⁴ (C2)	2.97 x 10 ⁻⁴ (C3)
	Pulmonary vascular bed	1.40 x 10 ⁻⁷ (C1)	2.97 x 10 ⁻⁴ (C2)	9.0 x 10 ⁻⁸ (C3)

Table 28
Systemic and pulmonary vascular bed compartment LPN parameters.

Windekessel (W)		Proximal resistor (Rp) g/(mm ⁴ ·s)	Capacitor (C) mm ⁴ ·s ² /g	Distal resistor (Rd) g/(mm ⁴ ·s)	
Rest	Systemic	BCT	4.00 x 10 ⁻⁴	1.29	4.31 x 10 ⁻²
		LCC	9.80 x 10 ⁻⁴	6.17 x 10 ⁻¹	9.06 x 10 ⁻²
		LSA	9.90 x 10 ⁻⁴	6.14 x 10 ⁻¹	9.09 x 10 ⁻²
		Aorta ¹	2.50 x 10 ⁻⁴	1.78	2.88 x 10 ⁻²
		R1	1.64 x 10 ⁻¹	2.34 x 10 ⁻¹	2.08 x 10 ⁻¹
		R2	1.94 x 10 ⁻¹	2.00 x 10 ⁻¹	2.47 x 10 ⁻¹
		R3	3.77 x 10 ⁻¹	1.03 x 10 ⁻¹	4.80 x 10 ⁻¹
		R4	1.59 x 10 ⁻¹	2.44 x 10 ⁻¹	2.02 x 10 ⁻¹
	Pulmonary	R5	1.97 x 10 ⁻¹	1.97 x 10 ⁻¹	2.50 x 10 ⁻¹
		R6	2.47 x 10 ⁻¹	1.57 x 10 ⁻¹	3.14 x 10 ⁻¹
		R7	2.72 x 10 ⁻¹	1.42 x 10 ⁻¹	3.46 x 10 ⁻¹
		R8	1.58 x 10 ⁻¹	2.45 x 10 ⁻¹	2.01 x 10 ⁻¹
		L1	2.72 x 10 ⁻¹	1.42 x 10 ⁻¹	3.46 x 10 ⁻¹
		L2	2.54 x 10 ⁻¹	1.52 x 10 ⁻¹	3.23 x 10 ⁻¹
		L3	4.82 x 10 ⁻¹	8.00 x 10 ⁻²	6.13 x 10 ⁻¹
		L4	2.80 x 10 ⁻¹	1.38 x 10 ⁻¹	3.57 x 10 ⁻¹
Stress	Systemic	L5	4.82 x 10 ⁻¹	8.00 x 10 ⁻²	6.14 x 10 ⁻¹
		L6	4.20 x 10 ⁻¹	9.20 x 10 ⁻²	5.35 x 10 ⁻¹
		BCT	6.15 x 10 ⁻⁷	2.13 x 10 ⁻¹	5.18 x 10 ⁻⁴
		LCC	1.01 x 10 ⁻⁶	1.55 x 10 ⁻¹	7.75 x 10 ⁻⁴
		LSA	2.46 x 10 ⁻⁶	7.40 x 10 ⁻²	1.63 x 10 ⁻³
		Aorta ¹	2.48 x 10 ⁻⁶	7.37 x 10 ⁻²	1.64 x 10 ⁻³
		R1	2.46 x 10 ⁻¹	8.19 x 10 ⁻³	3.43 x 10 ⁻¹
		R2	2.91 x 10 ⁻¹	7.00 x 10 ⁻³	4.08 x 10 ⁻¹
	Pulmonary	R3	5.66 x 10 ⁻¹	3.61 x 10 ⁻³	7.92 x 10 ⁻¹
		R4	2.39 x 10 ⁻¹	8.54 x 10 ⁻³	3.33 x 10 ⁻¹
		R5	2.96 x 10 ⁻¹	6.90 x 10 ⁻³	4.13 x 10 ⁻¹
		R6	3.71 x 10 ⁻¹	5.50 x 10 ⁻³	5.18 x 10 ⁻¹
		R7	4.08 x 10 ⁻¹	4.97 x 10 ⁻³	5.71 x 10 ⁻¹
		R8	2.37 x 10 ⁻¹	8.58 x 10 ⁻³	3.32 x 10 ⁻¹
		L1	4.08 x 10 ⁻¹	4.97 x 10 ⁻³	5.71 x 10 ⁻¹
		L2	3.81 x 10 ⁻¹	5.32 x 10 ⁻³	5.33 x 10 ⁻¹
L3	7.23 x 10 ⁻¹	2.80 x 10 ⁻³	1.01		
L4	4.20 x 10 ⁻¹	4.83 x 10 ⁻³	5.89 x 10 ⁻¹		
L5	7.23 x 10 ⁻¹	2.80 x 10 ⁻³	1.01		
L6	6.30 x 10 ⁻¹	3.22 x 10 ⁻³	8.83 x 10 ⁻¹		

Table 29

Windekessel parameters for all outlets. The components referred to are shown in Figure 47, and the outlet labels are shown in Figure 49. R, right pulmonary branches. L, left pulmonary branches. ¹At diaphragm level.

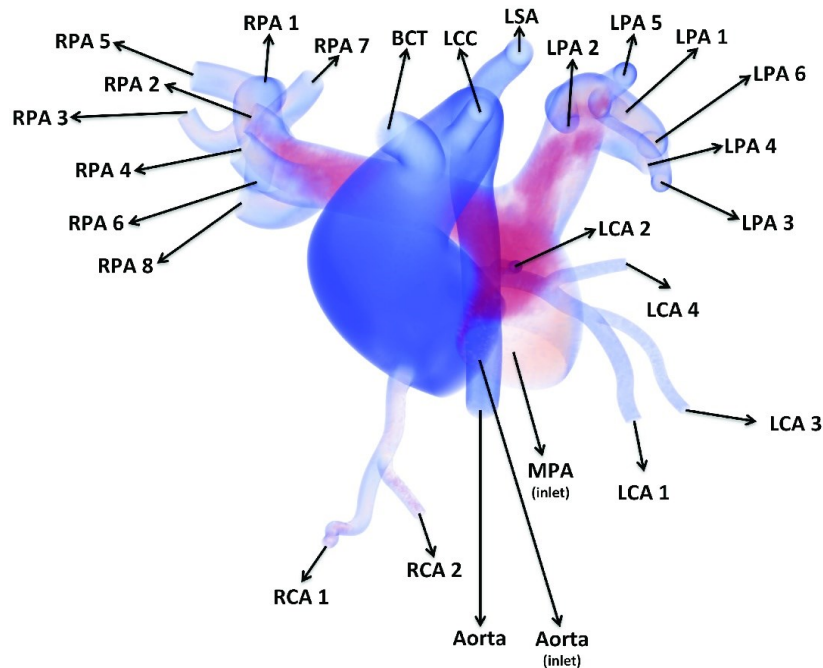


Figure 49

The segmented 3D solid representing the imaged central systemic and pulmonary arteries, with the outlet names specified. BCT, brachiocephalic trunk. LCA, left coronary artery. LCC, left common carotid artery. LPA, left pulmonary artery. LSA, left subclavian artery. MPA, main pulmonary artery. RPA, right pulmonary artery.

5.1.2.4.5. LPN CORONARY MODEL WITH CONTROLLED MICROVASCULAR RESISTANCE

A coronary LPN (see Figure 10, Chapter 2) was attached to each of the coronary outlets of the 3D aortic domain. It “lumped” the distal LCA and RCA epicardial branches not adequately visible in the 2D iNAV IR-CMRA to be accurately segmented, as well as the coronary intramyocardial microvascular circulation (Figure 50). The initial coronary LPN parameters, such as resistance and capacitance, were calculated using the available patient data and the 1D non-linear theory considerations described by Xiao *et al.* (Xiao *et al.*, 2013): the proximal epicardial vessel cross-sectional area was measured from the 2D iNAV IR-CMRA; the coronary perfusion pressure was the XMR aortic root diastolic pressure minus the left/right ventricular diastolic pressure; we assumed that 5% of the cardiac output (Deussen *et al.*, 2012), calculated from the product of the LV stroke volume measured with the CMR and the heart rate, was delivered to the coronary circulation; we scaled the CBF to the myocardial mass of the left and right ventricles as measured with the CMR scan (Choy and Kassab, 2008), to compute how the flow was distributed to the LCA and RCA. The magnitude of resistance assigned to the epicardial and intramyocardial LPN resistors followed that described by Arthurs *et al.* (Arthurs *et al.*, 2016). The CMCM model then

adjusted the distal resistor in the coronary 0D LPN to increase CBF and match any increase in metabolic demand.

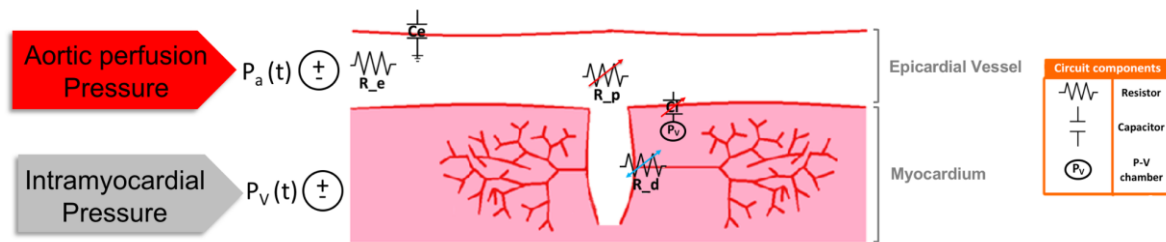


Figure 50

Schematic depicting the location in the coronary circulation of the different components of the coronary LPN described in Figure 10 (Chapter 2). C_e , epicardial capacitor. C_i , intramyocardial capacitor. P_a , aortic perfusion pressure. P_v , pressure-volume chamber (i.e. the left and right ventricles). R_e , epicardial resistor. R_d , distal resistor. R_p , proximal resistor

The resistance of the coronary circulation LPN was controlled by a coronary microvasculature control model (CMCM), which integrates the aggregate behaviour of the neural, local metabolic, myogenic, and shear stress control mechanisms acting in the coronary circulation to match the myocardial oxygen demand with the supply, assuming a constant level of coronary oxygen extraction.

This model has been previously tested against invasive patient data and is capable of reproducing invasive patient data during changes in cardiac workload (Arthurs et al., 2016). The ability to predict CBF adaptations in response to changes in the myocardial oxygen demand and the coronary perfusion pressure gradient permits simulation of the coronary responses to a generalised vasodilation state as that occurring post-transplant reperfusion, and enables specific probing of the complex coronary microcirculatory responses.

As described in the Chapter 2, the CMCM model is based on a hypothetical concept of myocardial “hunger” (oxygen supply error signal due to the mismatch between myocardial oxygen demand and supply) and a control system that acts to counter any of such imbalance. The myocardial oxygen demand per heartbeat was computed from the cardiac workload, in turn determined by the 0D heart model, after integrating the area of the left and right ventricular P-V curves and the ventricular elastance function. The alpha-vasoconstriction that dominates in vessels of diameters $>100 \mu\text{m}$ was represented R_p , and the dominant feedforward beta-vasodilation and feedback metabolic control, predominantly affecting vessels $<100 \mu\text{m}$, was modelled by adjustment of R_d (Chilian et al., 1989). The model

dynamically computed the time derivative of the inverse of the coronary resistance to be applied to the distal resistor (R_d), in order to increase CBF and eliminate any myocardial demand-supply mismatch or hunger (Figure 51). The cycle-mean values of these parameters, once periodicity was achieved, are presented in Table 30.

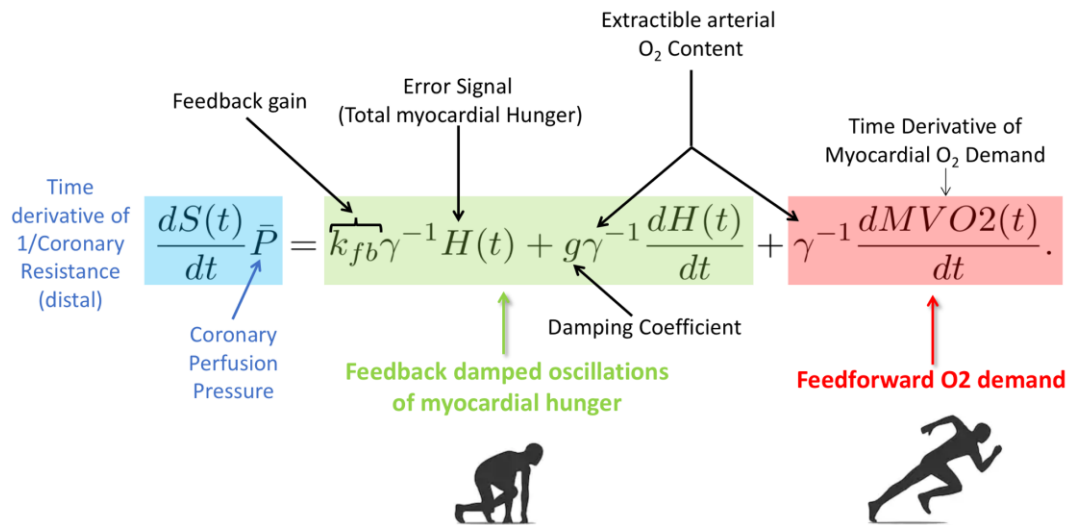


Figure 51

The coronary microvasculature control model (CMCM) computed the time derivative of the inverse of the coronary resistance by accounting the time derivative of the myocardial oxygen demand at the onset of a stressor (feedforward loop - red) and the myocardial hunger or oxygen deficit (feedback loop - green). This resistance was then passed to the distal resistor (R_d) in the 0D coronary LPN (see Figures 10 and 50), which was attached to each coronary outlet of the 3D geometric model shown in Figure 47. By adjusting this resistor, the CMCM can increase/decrease the coronary blood flow to match the myocardial metabolic demand. For further description please see text in Chapter 2 - “Dynamic Coronary Flow Control Model For Computational Simulations”.

In our study, the extravascular systolic compression experienced by the intramyocardial coronary vasculature was modelled by passing the instantaneous left or right ventricular pressure (P_v in Figure 50) to the corresponding intramyocardial vessels capacitor (C_I). This replicated CBF out of phase with the aortic flow and the clinically observed diastolic coronary flow peak (Marsden and Esmaily-Moghadam, 2015).

Coronary		R _d g/(mm ⁴ ·s)	R _i g/(mm ⁴ ·s)	R _e g/(mm ⁴ ·s)	C _i mm ⁴ ·s ² /g	C _e mm ⁴ ·s ² /g
Rest	R1	8.84	1.07	1.82	3.34 x 10 ⁻³	3.92 x 10 ⁻⁴
	R2	9.75	1.18	2.01	3.08 x 10 ⁻³	3.61 x 10 ⁻⁴
	L1	1.28 x 10 ¹	1.74	2.96	2.04 x 10 ⁻³	2.39 x 10 ⁻⁴
	L2	2.56 x 10 ¹	3.47	5.88	1.05 x 10 ⁻³	1.23 x 10 ⁻⁴
	L3	2.18 x 10 ¹	1.75	4.32	1.43 x 10 ⁻³	1.68 x 10 ⁻⁴
	L4	2.05 x 10 ¹	2.82	4.78	1.29 x 10 ⁻³	1.51 x 10 ⁻⁴
Stress	R1	7.32	5.92 x 10 ⁻¹	1.82	4.38 x 10 ⁻²	5.13 x 10 ⁻³
	R2	8.19	6.53 x 10 ⁻¹	2.01	2.23 x 10 ⁻²	2.23 x 10 ⁻²
	L1	1.21x 10 ¹	9.63 x 10 ⁻¹	2.96	3.03 x 10 ⁻²	3.55 x 10 ⁻³
	L2	2.43 x 10 ¹	1.91	5.88	2.73 x 10 ⁻²	3.20 x 10 ⁻³
	L3	1.76 x 10 ¹	1.40	4.31	7.91 x 10 ⁻²	9.28 x 10 ⁻³
	L4	1.93 x 10 ¹	1.55	4.78	7.21 x 10 ⁻²	8.45 x 10 ⁻³
PRS	R1	1.36	5.92 x 10 ⁻¹	1.82	4.38 x 10 ⁻²	5.13 x 10 ⁻³
	R2	1.49	6.53 x 10 ⁻¹	2.01	2.23 x 10 ⁻²	2.23 x 10 ⁻²
	L1	3.77	9.63 x 10 ⁻¹	2.96	3.03 x 10 ⁻²	3.55 x 10 ⁻³
	L2	7.86	1,91	5.88	2.73 x 10 ⁻²	3.20 x 10 ⁻³
	L3	5.55	1.40	4.31	7.91 x 10 ⁻²	9.28 x 10 ⁻³
	L4	5.99	1.55	4.78	7.21 x 10 ⁻²	8.45 x 10 ⁻³

Table 30

Coronary LPN resistors and capacitors parameters. R_d, distal intramyocardial resistor. R_i, intramyocardial resistor. R_e, epicardial resistor. C_i, intramyocardial vessel capacitor. C_e, epicardial vessel capacitor. R, right coronary artery branches. L, left coronary artery branches.

5.1.2.4.6. ADDITIONAL SPECIFICATIONS FOR THE EXPERIMENTAL CONDITIONS

At peak DSCMR, the clinical data showed that cardiac output increased by approximately 45% from baseline. No regional wall motion abnormalities were noted. In addition, the CMRA showed a normal coronary anatomy with no luminal stenosis. The normalised LV-to-RV mass ratio calculated from the CMR data was 0.91:1 indicative of RVH.

In the PSCM, tissue stiffness was kept constant through all three experimental conditions. The PRS condition was defined by imposing a 31% drop in the MAP relative to the Stress condition, following Hilmi *et al.* (Hilmi et al., 2008) definition of significant PRS.

5.1.2.4.7. MODELLING ASSUMPTIONS

A number of modelling assumptions were made:

(1) Dependent upon the condition being simulated, constant oxygen extraction per unit of blood volume delivered in both the left and right coronary circulation was assumed, resulting in the myocardial oxygen delivery being solely dependent on CBF changes. Prior research has shown that under resting physiological conditions, the LV oxygen extraction is

nearly at its maximum (~80%), so the LV myocardial oxygen supply increases are predominantly provided by increasing CBF. Conversely, RV oxygen extraction at rest is lower (~40%), so RV oxygen supply can be increased either by increasing CBF or by increasing oxygen extraction (Zong et al., 2005; Tune, 2014; Arthurs et al., 2016). Therefore, for the Rest condition, we assumed an oxygen extraction of 40% for the RCA and 80% for the LCA, whereas for the Stress and PRS conditions, we assumed 100% extraction for both coronary circulations. This approach favours sensitivity over specificity for detecting RV hunger. Physiologically, the relative contributions of RCA CBF and oxygen extraction to balance increased RV oxygen demand in the face of PVD remain uncertain, but it appears the former mechanism is more pronounced (Zong et al., 2005).

(2) The myocardial oxygen demand was computed from the cardiac workload, determined from the 0D heart model. As proposed by Suga H (Suga, 2003) this is a good approximation as oxygen consumption per heartbeat reflects the ventricular work as represented by the ventricular P-V loops area, integrating wall tension, shortening and contractility (Suga, 1990, 2003). This computed oxygen demand was used as input to the CMCM.

(3) It was assumed that the RCA supplies the entire RV myocardium, without any contribution to the LV. This RCA perfusion territory might not perfectly represent the reality, but this simplified assumption was considered sufficient for our purposes.

(4) As previously mentioned, the extravascular compression experienced by the intramyocardial vessels was modelled by imposing the instantaneous LV/RV pressures upon the corresponding coronary LPN. This allows reproduction of the coronary systolic flow impediment in a manner directly dependent upon the ventricular pressure.

5.1.2.4.8. COMPUTATIONAL SIMULATIONS

Analyses were performed using a time-step size of 0.0005 seconds (s) on 128 cores of a 640 core SGI Altix UV HPC for a total simulation time of 150 hours per case. Convergence to a cycle-to-cycle periodic state was achieved after 100,000 time steps (i.e., 50s of physical time). Three different conditions were simulated Figure 52.

Simulated conditions


- **REST** – baseline measurements during XMR
 - **STRESS** – peak dobutamine stress CMR measurements
 - **PRS** – entirely simulated (virtual transplant)
- ↓ 31% MAP from STRESS condition
- 

Figure 52

Three different conditions were simulated: Rest and Stress Conditions reproducing the measurements of the clinical XMR study during baseline and at peak dobutamine stress; a PRS Condition, entirely simulated as no clinical data was available, using the fine-tuned Stress Condition computational model and adjusting the resistance in the 3-element Windkessels of the systemic arterial bed until a 31% drop in MAP was achieved (following Hilmi *et al.* definition for significant PRS), thus reproducing the systemic vasodilation during the liver graft reperfusion. CMR, cardiovascular magnetic resonance. MAP, mean arterial pressure. PRS, post-reperfusion syndrome. XMR, hybrid X-ray magnetic resonance study.

Manual mesh refinement was performed for each condition, and a global combined continuity and momentum residual of less than 1×10^{-3} was considered. As detailed previously, we used a strategy for gradually increasing the complexity of the final coupled multidomain model starting with a pure-0D open-loop model and then moving to a closed-loop coupled 0D-3D model, iteratively adjusting parameters such as Windkessel resistance and compliance, among others, and finally increasing mesh density to best match simulation and the patient data.

The computational simulations outputs (Figure 53) such as atrial/ventricular pressure and volume, aortic/pulmonary pressure, resistance and flows repartition to different branches were post-processed and visualised using an open source software (Paraview®) at selected locations (e.g. aortic and pulmonary root). This allowed us to detect discrepancies with the clinical XMR data (e.g. comparing the distensibility of the aortic/pulmonary root in the 3D model versus the clinical 2D PC-CMR flow) and introduce further refinements to the PSCM. Other quantities of interest that were computed (not directly measured in the clinical data) included wall shear stress; cardiac workload, coronary pressure, flows and resistance; LV and RV instantaneous MVO_2 ; and the total myocardial hunger (i.e. myocardial metabolic demand-supply mismatch). Once we found that with subsequent mesh refinements there was no change in the computational results (e.g. differences in the computed mean and pulse

pressure in the aorta and pulmonary systems, mean pulmonary and aortic pressure, ventricular volumes and pressure were approximately less than 5% between iterations), we assumed that convergence was attained. This entailed using a final mesh with around 5 times as many elements as used initially (from ~ 300,000 elements initially to ~ 1,700,000 elements in the final simulation mesh).

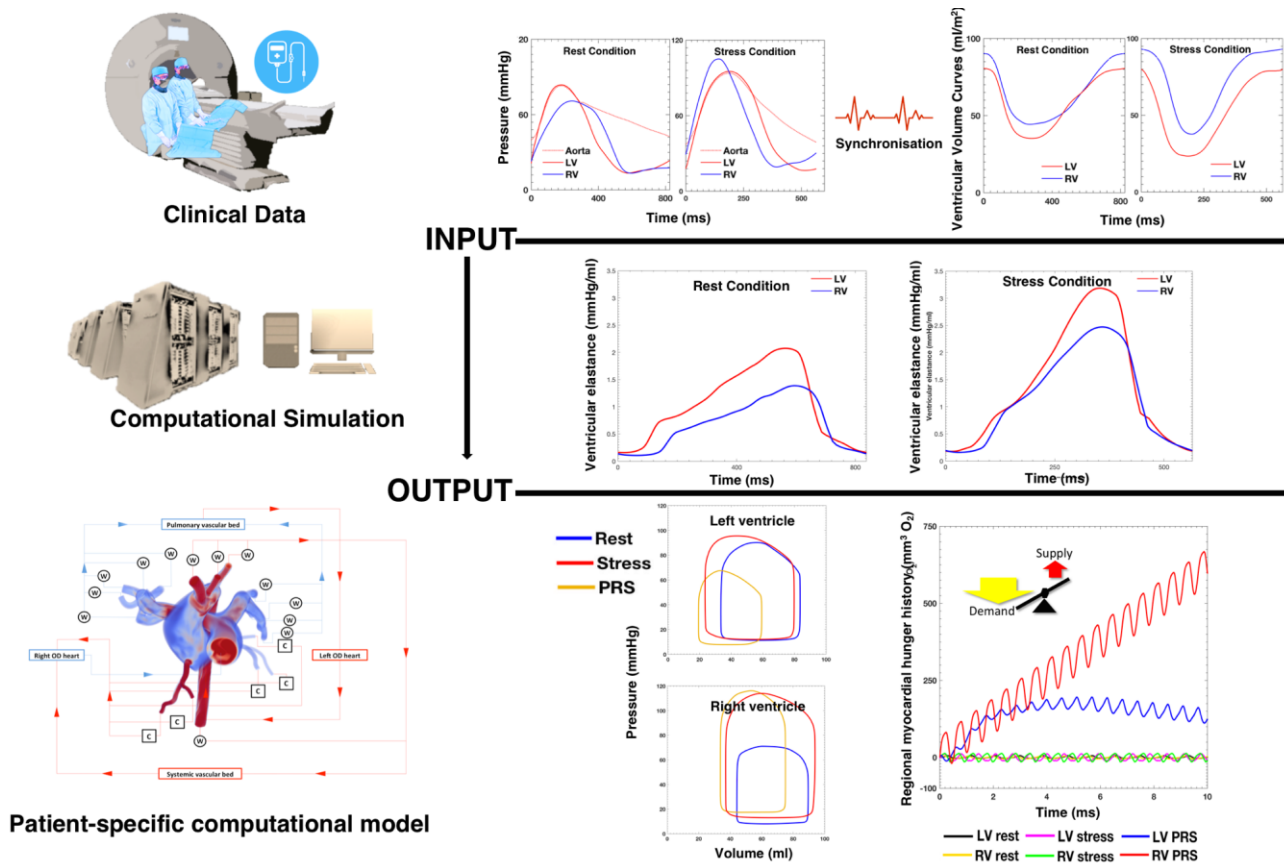


Figure 53

With a discrete number of input variables obtained from the clinical XMR such as ventricular pressure/volume and aortic pressure (upper panel), we informed the patient-specific computational model (e.g. parameterised the boundary conditions such as the OD heart LPN with a time-varying elastance function as shown in the middle panel) and obtained detailed metrics such as pressure-volume loops, cardiac workload and the MVO₂ demand-supply match (lower panel).

Some initial numerical instabilities, mainly at the OD-3D heart valve interfaces, required the inclusion of an influx coefficient with a factor beta of 0.2. The stabilisation was attained as detailed by Bazilevs Y *et al.* (Bazilevs et al., 2009), with the coefficient beta as described by Esmaily Moghadam *et al.* (Esmaily Moghadam et al., 2011). The value of beta was empirically found to provide numerical stability.

5.1.3. RESULTS

5.1.3.1. PSCM SOLUTION VERSUS PATIENT DATA

The step-wise calibration of the different components of the PSCM was performed using a discrete number of clinical parameters obtained during the clinical XMR study, such as ventricular volumes, aortic and pulmonary pressures/resistances and flows. After iterative fine-tuning of the PSCM parameters, we were able to successfully reproduced the patient's haemodynamic data obtained with the clinical XMR study, at rest and stress. A comparison between the computed (blue) and measured (red) pressure, flow, volume and resistance indices, at different locations of the aorto-pulmonary circulation and cardiac chambers, is shown in Figure 54.

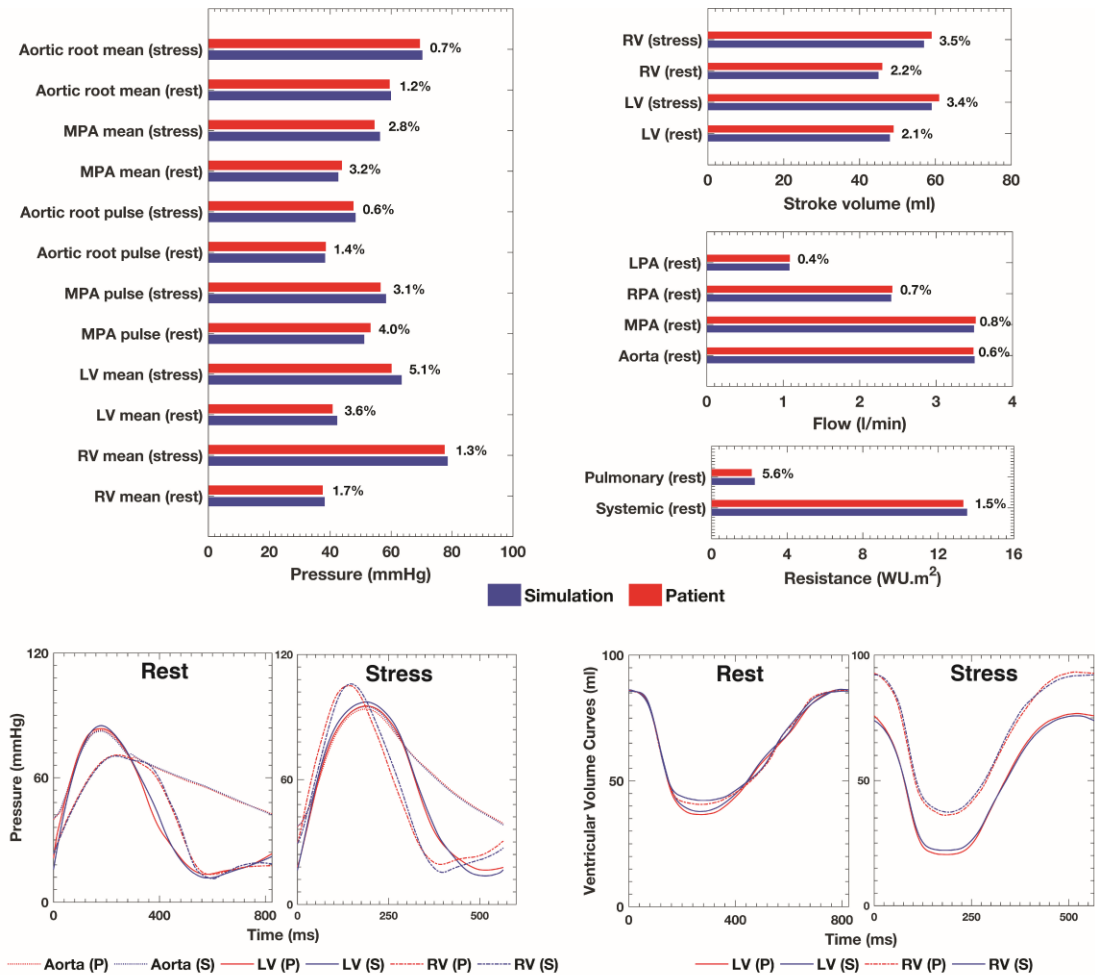


Figure 54

Relative error between patient (red) and simulation (blue) data given as a percentage. Bar plots comparing the clinical pressure and flow at relevant anatomic landmarks, and ventricular stroke volume and systemic and

pulmonary vascular resistance data at Rest and Stress, and corresponding 0D-3D coupled multidomain computational model simulation results. Selected pressures and ventricular volumes transient waveforms corresponding to the cycle-to-cycle equilibrium for the Rest and Stress Conditions (patient clinical versus simulation data) are also show. P, patient clinical data. S, simulation results.

Overall, there was a good agreement (< 6% discrepancy) between the simulated and the clinical haemodynamic data for the Rest and Stress Condition. This was key to assure reliability of the simulation results.

5.1.3.2. PSCM OF CORONARY HAEMODYNAMICS DURING REST, STRESS AND PRS

Relevant haemodynamic simulation results are presented in Table 31 and Table 32. Patient-specific LV/RV P-V loops were computed for the Rest and Stress Conditions using the left and right ventricular pressure and volume data obtained during the XMR study. The P-V loops area (Figure 55) was used to calculate the cardiac workload and MVO_2 shown in Table 31. The CMC then adjusted the coronary resistance (i.e. reduced the distal resistor in the coronary 0D LPN) to increased CBF and matched the MVO_2 . The PRS condition was a modification of the calibrated PSCM for the Stress Condition, where we imposed a 31% drop in MAP and thus simulated the haemodynamics of liver transplantation, as no clinical data was available for the patient. Here, the autoregulation acted to meet the myocardial metabolic demand while trying to forestall a decrease in coronary perfusion pressure

Condition	Cardiac workload		MVO ₂	
	(Joules)		(ml/min)	
	LV	RV	LV	RV
Rest	4.6 x 10 ⁻¹	3.5 x 10 ⁻¹	5.42	5.10
Stress	5.2 x 10 ⁻¹	7.2 x 10 ⁻¹	6.97	7.93
PRS	2.7 x 10 ⁻¹	4.9 x 10 ⁻¹	4.39	8.91

Table 31

Cardiac workload and MVO_2 results obtained from the 0D-3D coupled multidomain computational model, after calibrating the Rest and Stress Conditions simulations against the clinical XMR data. LV/RV, left/right ventricle. MVO_2 , myocardial oxygen consumption. WSS, wall shear stress. PRS, post-reperfusion syndrome.

At Rest Condition, reflecting high RV afterload, $LVMVO_2$ was just 6% higher than $RVMVO_2$. However, during the Stress Condition $RVMVO_2$ was 12 % higher than $LVMVO_2$ as a result of the increased RV afterload during dobutamine infusion and supra-systemic

intraventricular pressures.

CBF results are reported at the stable periodic (patho)physiological states attained after perturbation of the circulatory system (e.g. dobutamine infusion for the Stress Condition). Coronary indices such as CBF, coronary resistance and WSS, as well as the diastolic-to-systolic flow ratio computed from the simulation are shown in Table 32. Using the calibrated PSCM, a 40% increase in CBF was predicted to occur during the Stress Condition (i.e. coronary flow reserve or CFR of ~1.4, calculated from ratio between coronary blood flow at maximal hyperemia, obtained during the Stress Condition, and at the baseline or the Rest Condition). In a virtual PRS scenario, the CMCM predicted that there would be a 46% decrease in CBF.

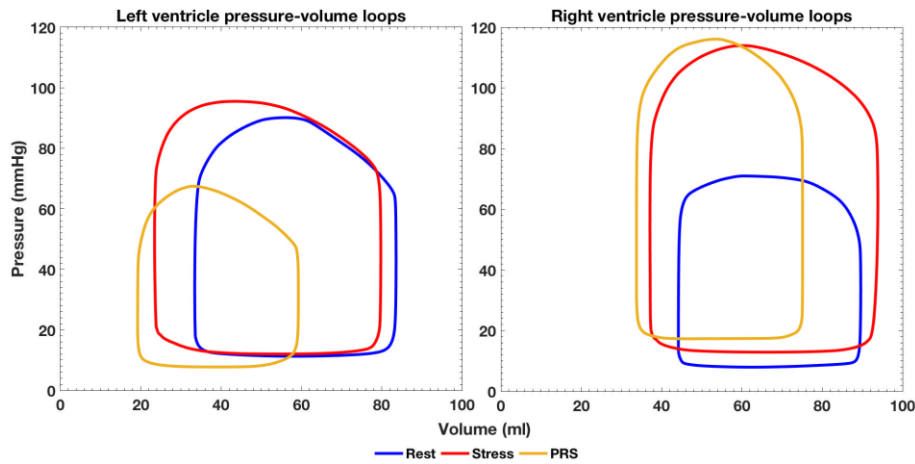


Figure 55

Left and right ventricle pressure-volume loops. All curves presented were derived from the 0D-3D coupled multidomain computational model simulation. The Rest and Stress Conditions pressure-volume curves matched those obtained directly from the clinical XMR after careful adjustment of the different parameters in the model, as explained in text. As no patient data was available during transplantation, the PRS Condition curves represent the ventricular haemodynamics during a simulated liver transplantation. PRS, post-reperfusion syndrome.

Condition	Coronary blood flow (ml/min/g)		Diastolic/systolic flow ratio		Coronary Resistance (WU.m ²)		Coronary WSS (dyn.cm ²)		
	LCA	RCA	LCA	RCA	LCA +	RCA	RCA	LCA	RCA
Rest	66.2	67.6	1.8:1 (36.8:29.4)	1.9:1 (35.6:32.0)	1.07 x 10 ²		1.05 x 10 ²	2.82	5.20
Stress	88.3	93.4	2.5:1 (53.0:35.3)	2.7:1 (58.8:34.6)	6.50 x 10 ¹		5.83 x 10 ¹	5.33	24.18
PRS	51.5	44.6	0.7:1 (15.4:36.1)	2.1:1 (23.4:21.2)	2.36 x 10 ¹		1.42 x 10 ¹	3.34	15.61

Table 32

Coronary haemodynamics measures including average coronary blood flow, coronary resistance and WSS, obtained from the 0D-3D coupled multidomain computational model Rest, Stress and PRS simulations. Dyn, dynes. LCA/RCA, left/right coronary artery. WSS, wall shear stress. WU, Woods units (mmHg.min⁻¹). PRS, post-reperfusion syndrome.

In all three conditions, the coronary perfusion in both the left and right coronaries occurred mostly during diastole. RCA flow was pathologically diastolic dominant due to high RV afterload. This RCA biphasic profile became more prominent during Stress and PRS conditions, with a dominant diastolic phase, marked systolic flow reversal, and higher peak diastolic-to-systolic flow ratios. Figure 56 illustrates the interplay between LV/RV pressures and coronary waveforms.

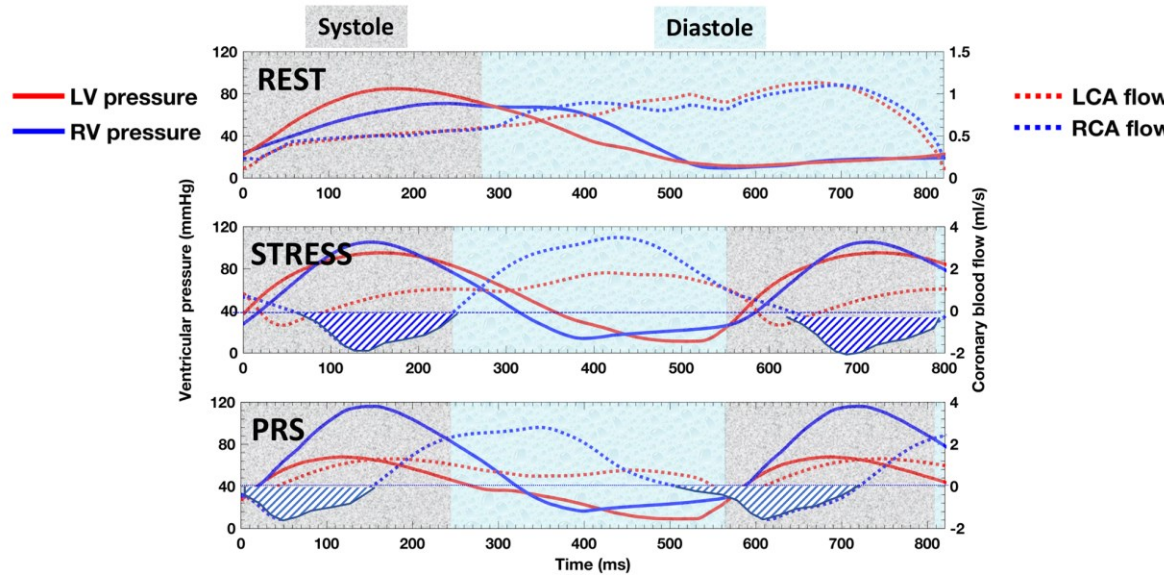


Figure 56

Simulated left and right coronary blood flow waveforms plotted against the simulated ventricular pressure, for all three conditions. The coronary blood flow profiles were obtained from the 0D-3D coupled multidomain computational model simulations. Different y-axis scales were used in the Rest and Stress/PRS Conditions to best convey the waveforms pulsatility. LCA, left coronary artery. LV, left ventricle. PRS, post-reperfusion syndrome. RCA, right coronary artery. RV, right ventricle.

Time-averaged 3D maps of pressure, velocity and WSS (central panel) and waveforms of aortic and ventricular pressure, as well as right and left coronary flows and pressures are shown in Figure 57 (left and right panels). In all three conditions, RCA mean velocity and WSS maps displayed higher values than in the LCA.

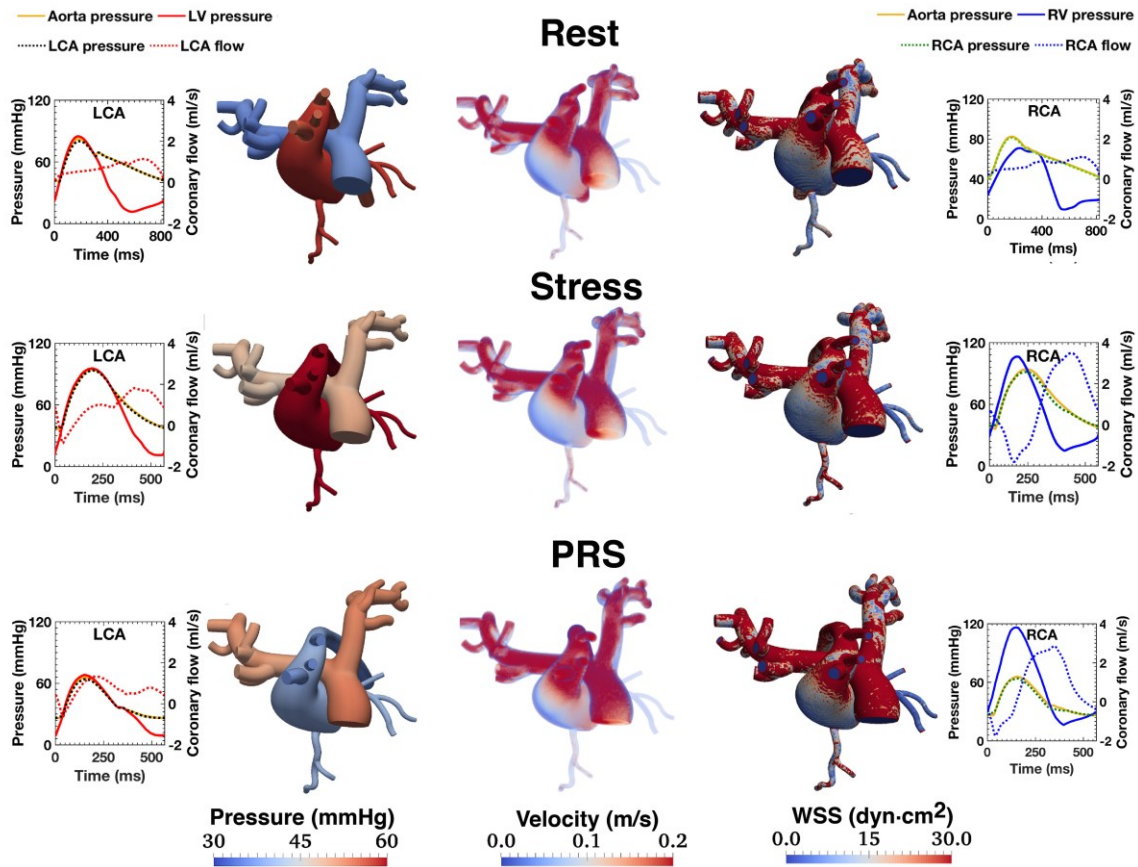


Figure 57

Time averaged maps of pressure, velocity and wall shear stress (WSS) [central panel] and selected flow and pressure waveforms (right and left panels) obtained from the 0D-3D coupled multidomain computational model Stress, Rest and PRS simulations. Notably, mean velocities and WSS in the RCA were higher than in the LCA. LCA/RCA, left/right coronary artery. PRS, post-reperfusion syndrome.

Figure 58 shows the myocardial hunger history in the 0D-3D coupled multidomain computational model (panel A) and after replacing the 3D computational models of the aorta and pulmonary circulation with a simple resistor-capacitor network - the 3D domain replacement (3DDR) - in order to achieve a more temporally resolved solution (panel B). At Rest, coronary resistance was higher in the LCA than in the RCA by just 2% (Table 32), with a perfect match between the MVO_2 demand and supply. During Stress, the 39% and 44% drop in LCA and RCA resistance (Table 32), respectively, was sufficient to match the MVO_2 demands. However, despite a dramatic vasodilatory response in the RCA during PRS condition, with a 76% reduction in resistance (Table 32), the CCM predicted insufficient myocardium oxygen delivery (i.e. myocardial hunger). In turn, the LCA autoregulation

predicted a 64% fall in resistance, which was sufficient to counter the demand-supply mismatch after a brief period of ischaemia.

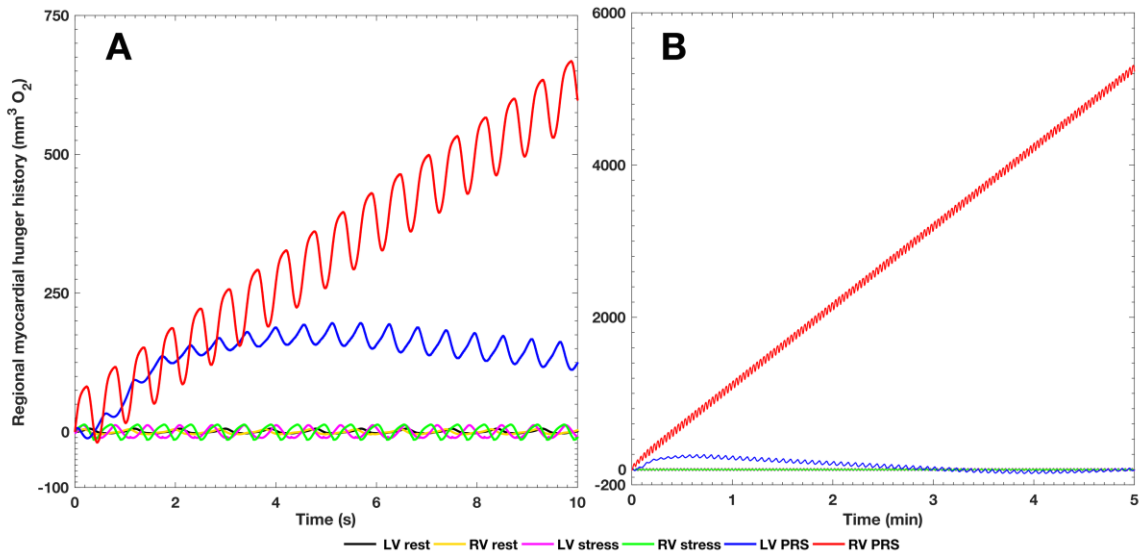


Figure 58

Myocardial oxygen demand-supply mismatch (myocardial hunger) computed from the simulations for all three conditions. **Panel A.** Ten seconds of high-resolution results obtained with the 0D-3D coupled multidomain computational model. **Panel B.** A longer simulation time (five minutes) obtained with a reduced-order (0D) model reveals an ever increasing RV myocardial hunger and normalisation of LV hunger in the long term. LV/RV, left/right ventricle. PRS, post-reperfusion syndrome.

5.1.4. DISCUSSION

5.1.4.1. THE VALUE OF IMAGE-BASED COMPUTATIONAL MODELLING

In this study, we have used image-based computational modelling to investigate coronary haemodynamics and MVO_2 changes during PRS. We wanted to assess whether in our ALGS patient, PRS could result in a state of coronary hypoperfusion hampering the ability of the RV coronary circulation autoregulation to maintain the metabolic demand-supply balance. Current pre-operative cardiovascular risk assessment using DSCMR might reproduce increases in HR and thus myocardial metabolic demand, but fails to replicate this systemic hypotension and associated coronary perfusion pressure drop, and so it might not be able to predict RV performance during liver transplantation (Bruinsma et al., 1988). We hypothesised that impaired RV coronary microvascular function could lead to adverse clinical outcomes, as shown in both animal and human PAH studies, by predisposing this patient to RV ischaemia (Greyson, 2010; Ryan and Archer, 2014; Frump et al., 2018). RV ischemia would cause a reduction in contractile function, compromising the RV's capacity

to handle the peri-operative elevated RV afterload and systemic hypoperfusion, which would further reduce cardiac output and cause a rapidly and progressive downward spiral to RHF and haemodynamic collapse during transplantation (Greyson, 2008, 2010).

At the outset, instead of directly assessing RHF, a significant cause of mortality/morbidity in ALGS undergoing liver transplantation (Png et al., 1999; Emerick et al., 1999; Razavi et al., 2001; Kamath and Loomes, 2018), we probed for myocardial demand-supply imbalance during a virtual PRS. The rationale was that the CMCM computed the myocardial demand-supply imbalance at every time-point of the simulation, and this precedes RV pump (diastolic/systolic) failure in the myocardial ischaemic cascade (Nesto and Kowalchuk, 1987; Maznyczka et al., 2015; Zelt et al., 2019).

The second point to highlight relates to the complexity of *in vivo* assessment of coronary autoregulation, which requires invasive methodologies that are generally unsuitable for use in patients, particularly in paediatrics. Furthermore, the interplay of highly coordinated control mechanisms acting in the coronary microvasculature makes computational modelling an appealing prospect for assessing transient events following liver transplantation, such as PRS, a serious intraoperative haemodynamic complication associated with significant morbidity and mortality.

Combining image-based and catheterisation data at Rest and Stress Conditions from an ALGS patient undergoing cardiovascular risk assessment prior to liver transplantation, we designed a closed-loop 0D-3D deformable multidomain computational model able to replicate these two haemodynamic states.

5.1.4.2 INNOVATIVE ASPECTS OF THE PATIENT-SPECIFIC COMPUTATIONAL MODEL

The rich clinical information available enabled us to couple in parallel two highly parametrised arterial circulations (systemic and pulmonary) to a heart model. We used the multidomain approach with a close-loop configuration because this methodology has been shown to provide an accurate description of the cardiovascular haemodynamics (Vignon-Clementel et al., 2006, 2010; Arbia et al., 2014; Marsden and Esmaily-Moghadam, 2015). This approach opens the possibility of incorporating patient-specific clinical data into the different types of boundary conditions and capture the interaction between the 3D domains and the global circulation (the reduced order models), thus increasing the reliability of the

flow/pressure solution. Furthermore, in this closed-loop configuration, blood flow in the large systemic and pulmonary arteries is highly dependent not only on the tissue properties assigned but also on the outflow boundary conditions imposed to represent the vascular bed downstream of the 3D domains (Vignon-Clementel et al., 2006). For instance, wall deformation in the 3D domains of the PSCM depended directly on the wall stiffness (prescribed using the XMR data) as well as on the pressure level in the vessel, which in turn was largely determined by the resistance in arterioles and capillaries (i.e. the arterial bed LPNs). The same vascular resistance was also responsible for regulating the distribution of blood flow to different regions of the body, the ventricular afterload and preload (Marsden and Esmaily-Moghadam, 2015). As the effects from the global circulation were fully coupled to influence the overall simulated physiology, we could better select and adjust the parameters of the reduced order models, for which we had no direct measurement, and match the clinical data.

Another advantage of the coupled multidomain approach was that it enabled the incorporation of detailed 3D models of the aorta, coronaries and proximal pulmonary arteries, so we could capture certain 3D haemodynamic phenomena that occur in large vessels, such as flow and pressure waves damping, dispersion and reflection at branching points or due to vessel calibre changes, a feature not attainable with simpler models.

A key innovative aspect of the PSCM was the inclusion of a control system of the coronary microvasculature (CMCM), fully coupled with the systemic and pulmonary circulations. The CMCM adjusted the coronary LPN resistors to match the instantaneous myocardial oxygen demand-supply of both the LV and RV as computed from the area of the Rest and Stress XMR-derived P-V loops. Hence, as we had no invasively obtained coronary pressure/flow data, we did not rely on assumed coronary pressure/flow waveforms for the Rest and Stress Conditions. In addition, the CMCM also “sensed” the instantaneous intramyocardial pressure thus reproducing physiologic coronary waveforms (e.g. diastolic coronary flow peak).

We then imposed a 31% drop in systemic arterial pressure to simulate a severe PRS, as defined by Hilmi *et al.* (Hilmi et al., 2008) and evaluate whether the CMCM model could maintain the balance between myocardial oxygen demand and supply. This systemic hypotension was achieved by manually reducing the resistance in the 3-element

Windekessels representing the medium and small systemic arteries outside the 2D iNAV CMRA image data (see Figure 47).

5.1.4.3. STUDY FINDINGS

Coronary autoregulation and microvascular function

To our knowledge, few studies have studied coronary microvascular function in children (Muzik et al., 1996; Giulia Gagliardi et al., 2001; Cicala et al., 2008) and none has explored coronary haemodynamics or myocardial metabolic demand-supply balance in ALGS, which precludes direct comparison of our results. Nevertheless, it is worth mentioning the work by Muzik *et al.* (Muzik et al., 1996) in children post-Kawasaki disease (a common childhood vasculitis) exploring coronary flow reserve (CFR), an index that expresses the capacity of the coronary circulation to respond to a physiological increase in oxygen demands with a corresponding increase in CBF (Gould et al., 1974; Gould and Johnson, 2018). In a small study (20 patients; mean age of 12 ± 3 years) using positron emission tomography (considered the gold standard for quantification of myocardial perfusion) and adenosine stress perfusion, Muzik and co-workers reported that CFR was impaired in children post-Kawasaki disease with no detectable coronary abnormalities compared to healthy volunteers (CFR of 3.2 ± 0.7 versus 4.6 ± 0.9 , respectively) due to microvascular dysfunction. Although the distinctive methodological approaches make direct comparison to our results difficult, we observed a much smaller hyperaemic response to pharmacological stress (CFR ~ 1.4), notwithstanding an adequate increase in cardiac output elicited by DSCMR, suggestive of coronary microvascular dysfunction. An important difference lies in the fact that we measured the CBF response to a different pharmacological stressor: dobutamine, a sympathomimetic amine acting on alfa/beta-adrenoceptors, induces both a positive chronotropic/inotropic response and increases CBF through a metabolic-mediated vasodilation. Whilst the use of an A₂A receptor agonist such as adenosine is the gold standard for inducing hyperaemia, dobutamine assesses the cardiac output response, enabling a more physiological approach for studying demand ischaemia. Moreover, adenosine can have vasodilatory effects in the pulmonary vascular bed, affecting RV afterload and consequently RVMVO₂ and CBF (Fullerton et al., 1996).

Myocardial metabolic demand-supply balance during Rest and Stress

At the Rest Condition, we found that LVMVO₂ was just slightly higher (6%) than RVMVO₂ (Table 32). This pattern was reversed during the Stress Condition (LVMVO₂ was 12% lower than RVMVO₂), observed after prescribing a 31% increase in HR. These observations reflect high RV afterload (at the Stress Condition, the systolic RV/ aortic pressure ratio was 1.14:1, well above normal ratio of <0.5) and are highly pathological (Figure 59). Significantly, there was no residual PPS in this patient and thus the raised afterload was likely related to a stiff pulmonary circulation. To the best of our knowledge there are no reported ranges of pulmonary vascular stiffness in ALGS children for comparison (and scant data in paediatrics in general). The closest analogy are children with PAH. Compared to the results from Ploegstra *et al.* (Ploegstra *et al.*, 2018), pulmonary compliance in children with PAH (mean age 2.1 years [0.6–6.4]) was 0.18 mm²/mmHg (0.08–0.43), measured using intravascular ultrasound to simultaneous record the pulmonary pressure and luminal area, while in our patient it was 0.271 mm²/mmHg. The different methodologies and patients' characteristics might explain the small differences, but the order of magnitude is similar and does suggest the presence of a stiff pulmonary circulation.

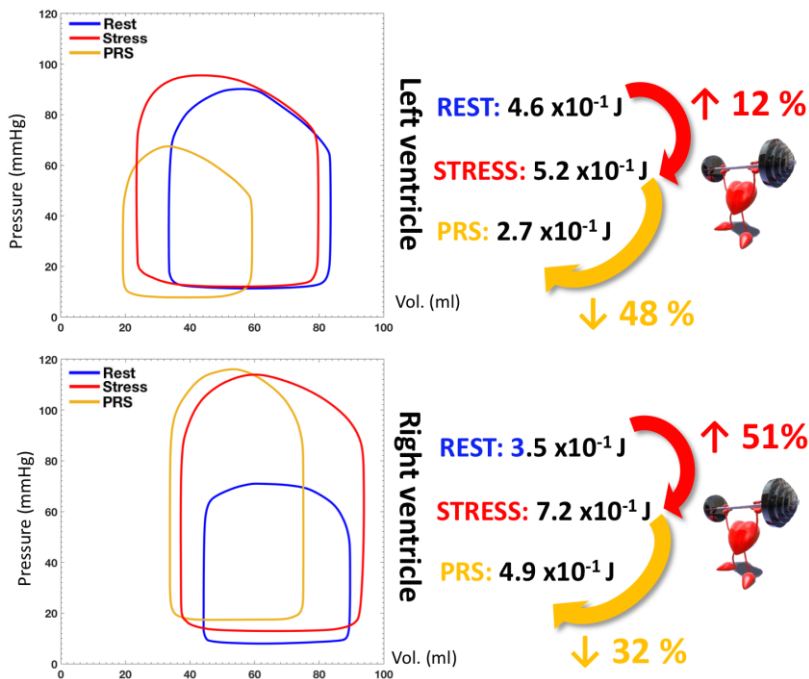


Figure 59

Schematic summarising the changes in the left and right ventricles workload between the Rest and Stress Conditions, computed from the 0D-3D coupled multidomain computational model simulation, in turn, fine-

tuned to match the clinical XMR data. The changes between the Stress and PRS Conditions are also displayed, which were obtained after manually adjusting the systemic arterial bed resistors to virtually simulate the mean arterial pressure drop often observed during liver reperfusion. J, Joules. PSCM, patient-specific computational model. PRS, post-reperfusion syndrome. XMR, hybrid X-ray/ magnetic resonance guided study.

During the Stress Condition, a further increase in RV afterload was observed resulting in supra-systemic RV pressures (Figure 59). Despite the increase in cardiac workload (51%), through a significant reduction in RCA resistance and corresponding increase in CBF, there was a perfect match between the cardiac metabolic demand and supply (Figure 58). In line with this supra-systemic RV pressure and higher MVO_2 , the computed vasodilatory response during the Stress Condition was more prominent in the RCA than in the LCA (44% versus 39% decrease in coronary resistance, respectively).

Myocardial metabolic demand-supply balance during PRS

In this study we adopted the concept of myocardial hunger as described by Arthurs *et al.* (Arthurs et al., 2016) to investigate myocardial demand-supply perfusion mismatch during liver transplantation (i.e. ischaemia). By assuming a fixed 100% oxygen extraction, the metabolic demand during Stress and PRS was entirely dependent on the CMCM adjustments of the microvascular resistances and CBF was pressure-dependent, thus favouring sensitivity over specificity for detecting RV hunger. Since there is a minimum physiologically achievable microvascular tone, based on limited available data in children (Muzik et al., 1996), we set achievable values for microvasculature resistance that are likely below the physiological minima. This means that if we see hunger in the model, we would expect that the myocardial oxygen supply would be insufficient clinically. However, the converse is not necessarily true.

In our simulations, we observed that the RCA vasodilatory response in the Stress Condition was sufficient to avoid myocardial hunger. However, in the PRS Condition, due to a significant drop in the MAP (31%) and resulting reduction in the coronary driving pressure, the vasodilatory reserve was exhausted (there was a 76% decrease in RCA resistance) and the PSCM predicted inadequate post-transplant myocardial perfusion (i.e. ischaemia), the precursor of RHF. This result was not anticipated by the adequate increase in cardiac output with the clinical DSCMR.

High temporally resolved 0D simulation

Given the high computational costs of the coupled 0D-3D multidomain model, we wanted to confirm our findings in a more temporally resolved solution. Hence, by replacing the 3D computational models of the aorta and pulmonary circulation with a simple resistor-capacitor network – the 3D domain replacement (3DDR), we computed the MVO₂ and coronary haemodynamics for several minutes of physical time. We observed that in the PRS Condition the RV myocardial hunger was ever increasing (Figure 58). This computed exponential hunger curve is unlikely to be entirely physiologic as our model did not account for the progressive decline of contractility during ischaemia, which would further increment the myocardial O₂ demand-supply mismatch (Allen and Orchard, 1987). However, it helps to support the 0D-3D simulation observations and our initial hypothesis that due to abnormal ventriculo-arterial-coronary coupling, RCA flow impairment in this ALGS patient may limit the RV's ability to adapt to the haemodynamic changes during liver reperfusion. This could then trigger a downward spiral leading to RHF and haemodynamic collapse. To the best of our knowledge, there is no specific research addressing this issue in ALGS children.

Coronary blood flow profiles

Besides the events in coronary microvasculature previously described, we also explored those occurring in the coronary “macrovasculature” (i.e. the epicardial coronary arteries). During the Rest Condition the RCA exhibit an abnormal flow profile (diastolic dominant). This profile became even more pathological during the Stress Condition, with a RCA diastolic/systolic CBF ratio (2.7:1) higher than that of the LCA (2.5:1) and systolic flow reversal, reflecting RV supra-systemic intraventricular pressures with systolic compression of the microvasculature (see Figure 56). van Wolferen *et al.* have also previously reported the presence of such pathological biphasic RCA profile (akin to that of the LCA) in adults with PAH using CMR (Figure 60). This is the first time it is reported in an ALGS child.

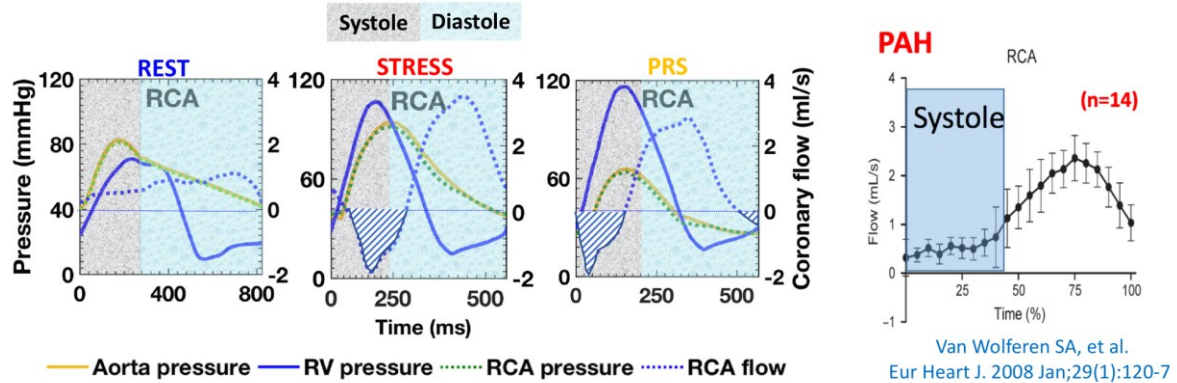


Figure 60

RCA abnormal flow profile obtained from the 0D-3D coupled multidomain computational model. The RCA displayed a diastolic dominant curve, secondary to high RV afterload, in the three simulated conditions (more marked in the Stress and PRS Conditions) and similar to what has been reported by van Wolferen *et al.* in 14 adults with PAH using CMR. PAH, pulmonary arterial hypertension. PRS, post-reperfusion syndrome. RCA, right coronary artery. RV, right ventricle.

5.1.5. CLINICAL SIGNIFICANCE

Although several modelling assumptions and simplifications were needed, this study provides a detailed snapshot of how RV coronary autoregulation impairment in ALGS patients may restrict their ability to adapt to the dramatic peri-operative loading changes of liver transplantation. The proposed methodology has the advantage of using real patient data to recreate some of the haemodynamics of liver transplantation and understand why the coronary circulation may fail to adapt to the marked preload and afterload changes and result in RHF. This may be an unrecognised factor determining the immediate and long-term post-transplant outcomes.

Our model emulated coupled ventricular-vascular maladaptations occurring in ALGS (increased RV afterload resulting in supra-systemic intra-ventricular pressures) that not only increase RVMVO₂ but also impose an additional burden on the coronary microcirculation autoregulation at the time of surgery (extravascular compression resistance). We hypothesise that by detecting RV metabolic demand-supply mismatch impairment (or hunger) we could identify a subgroup of patients that are at higher risk of developing RHF during liver transplantation, despite adequate cardiac output increase with dobutamine stress. This subgroup of patients could benefit from meticulous optimisation of the pre-transplant care (e.g. early diagnosis and endovascular treatment of PPS before irreversible pulmonary vascular and RV remodelling occurs; periodic assessment of RV function and size with a

CMR study; limiting ischaemia–reperfusion injury during organ harvesting) and post-transplant care (e.g. strict haemodynamic monitoring, tailored management of pharmacologic interventions such as vasoactive drugs administration and volume therapy to avoid hypovolaemia, as well as excessive cardiac filling resulting in pulmonary oedema and deterioration of gas exchange).

Despite the wealth of evidence from experimental animal studies, there is limited patient data available on coronary microvascular pathophysiology and abnormal ventriculo-arterial-coronary coupling. Furthermore, because of technical challenges and limitations of *in vivo* human studies, the role of coronary microvasculature reserve exhaustion in the evolution of diseases that course with chronic increased RV afterload and eventually progress to RHF is unclear (Voelkel et al., 2006). In patients with PAH, a far common disease, research suggests that increased RV pressure afterload impairs RCA flow and thus myocardial perfusion (Akasaka et al., 1996; van Wolferen et al., 2008), increasing the risk of RHF (Hsu et al., 2016). The ultimate validation of our work would require acquisition of CBF data in ALGS children undergoing liver transplantation, which is ethically and clinically unfeasible. However, the use of a patient-specific framework as the one presented, adequately parameterised at baseline and during dobutamine stress to replicate the patient's haemodynamics, has enabled us to simulate and explore the pathophysiological events in the coronary microcirculation during liver transplantation, for which it is nearly impossible to obtain data.

There are new techniques being developed to measure non-invasively CBF such as time-resolved 3D PC-CMR (or 4D flow) and coronary ultrafast Doppler angiography [CUDA] (Deng et al., 2014; Maresca et al., 2018), that could complement our computational modelling framework. If the findings of our PSCM study were replicated in other ALGS patients, we could explore whether abnormal RCA CBF profiles can be used as a non-invasive method to screen patients at high risk of RHF during transplantation.

This innovative framework could also be used to study other more frequent conditions, such as PAH in children with CHD, where the pathophysiology of RHF, the main cause of death (Tonelli et al., 2013; Vonk-Noordegraaf et al., 2013), is still poorly understood.

5.1.6. LIMITATIONS

Despite the merits of the proposed methodology highlighted in the previous section, there are some limitations to be acknowledged. Firstly, the expertise required and the computational cost of the proposed image-based computational modelling hinders its widespread clinical adoption. As a direct consequence of the computational costs, we had to resort to a simpler 0D model of the aorta and pulmonary arteries to achieve a more temporally resolved solution and confirm the findings of the complex 0D-3D PSCM. If on the one hand, this has enabled us to simulate, nearly in real time, the haemodynamics of the first critical five minutes following the reperfusion of the liver graft, on the other hand, the time-varying values of pressure and flow obtained did not contain spatial variables to capture complex haemodynamics. Furthermore, some of the events in the failing heart may have not been adequately represented. For instance, our PSCM did not account for the downregulation of the ventricular contractile function that is known to occur at the onset of ischaemia and contributes to a downward spiral leading to haemodynamic collapse (He and Downey, 1998).

The ultimate goal of this research was to demonstrate the application of an image-based methodology to an ALGS patient in order to study potential pathophysiologic responses following PRS, a problem for which it is difficult to acquire *in vivo* data. As such, this work was focused on the methodology and the hypothesis generation, based in the concept of “predictive personalised medicine”, and not on obtaining statistical metrics on a larger patient cohort. Therefore, at the moment we do not know whether these findings occur in all ALGS patients with RV hypertension or there other factors, such as intrinsic genetic or epigenetic differences in susceptibility to decompensation (Ryan and Archer, 2014).

The results of our work have been calibrated for the Rest and Stress Conditions. Except for the CBF, we had direct measurements of aortic/pulmonary pressure, flow, resistance and cardiac volumes at different anatomic locations to inform our PSMC. However, the lack of data for the PRS Condition makes validation difficult. Therefore, we had to rely on arbitrary estimates of the physiologic limit of the coronary microcirculation vasodilatory response and maximal oxygen extraction.

The fluid-structure interaction model utilised in this work relies on a small deformation assumption. While this simplification reduces the computational cost, the deformations of the pulmonary tree and the aorta are such that alternative formulations for

large structural displacements might be needed.

The PSCM also did not include other physical phenomena that occur at other (smaller) scales and that have been documented in patients with PVD, such as: impaired O₂ extraction [in our simulations the matching of myocardial metabolic demand and supply was fully dependent on CMCM adjustments of the coronary LPN resistors since the O₂ extraction capacity was fixed in both Stress and PRS Conditions (Wong et al., 2011; Tune, 2014)]; impaired blood rheology that may theoretically increase the flow resistance and may be of haemodynamic significance (Yaylali et al., 2019).

Interventricular dependence has been noted to be important in PAH patients, with increased RV afterload potentially limiting LV filling (Naeije and Badagliacca, 2017). Because the RV and LV are nested within the pericardium, share the septum and are encircled with common myocardial fibres, RV pressure overload commonly seen in ALGS patients can affect the LV function. Indeed, the RV dilation and systemic-like pressures in our case resulted in a leftward shift of the ventricular septum and modification of the LV geometry that was seen in the CMR 2D cine images, particularly during peak dobutamine stress. This is an additional factor increasing the risk of liver graft ischaemic insult as well as the host morbidity and mortality. Our heart model did not include any specific boundary condition specification for this interventricular dependence and thus there was no pressure feedback between ventricles. However, we assumed that the results of the virtual PRS Condition are realistic because the computational model was fine-tuned to replicate the patient's clinical data at Rest and Stress Conditions, for which we had detailed data (i.e. the P-V loops likely reflected such ventricular interaction). This interdependence element could be included in future designs of the LPN heart model in a similar fashion to that described by Arthurs *et al.* for the CMCM. There, the changes in cardiac workload and metabolic demands estimated from the P-V loops were “broadcasted” to the LPN coronary resistors so that a mathematical model therein could attempt to enforce matching of oxygen demand and supply. A potential model that could be used here would be to impose a threshold in the right intraventricular pressure above which this would modify the left heart elastance function to cause LV underfilling. This would likely further reduce the coronary perfusion during PRS.

5.1.7. CONCLUSION

To the best of our knowledge this is the first computational effort to examine altered haemodynamics in ALGS patients. We have built an image-based closed-loop 0D-3D multidomain computational model coupling the systemic and pulmonary circulations, and tuned it to replicate the pressure and flow data of an ALGS patient. This data was obtained during a XMR study with dobutamine stress performed for cardiovascular risk assessment prior to liver transplantation. We then used this image-based computational methodology to simulate the haemodynamic conditions during a virtual PRS and probe into the possible pathophysiological events in the coronary microcirculation during liver transplantation.

Our model showed how impaired RCA autoregulation, not anticipated by the DSCMR, may restrict adaptive responses in face of reduced aortic perfusion pressure such as that occurring immediately post-transplant. This is likely to result in significant RV myocardial oxygen demand-supply imbalance resulting in RHF, and could be related to worsened ALGS survival post-transplant described in the literature (Arnon et al., 2010). This novel patient-specific computational model could be used to gain insight into the impaired vasoregulatory mechanisms in ALGS, as well as other pulmonary vasculopathies, and aid pre-hepatic transplant cardiac risk stratification.

6

FUTURE WORK

This chapter will suggest new exploratory lines of research as well as new imaging and computational tools, expanding on the different studies conducted, with the ultimate aim of that adding further insight into the coronary microcirculation of ALGS children as well as those with pulmonary vasculopathies.

6.1. CORONARY MAGNETIC RESONANCE ANGIOGRAPHY

In the three prospective CMRA studies conducted, we have implemented and evaluated the diagnostic ability of a new image-based navigation approach for 3D whole-heart SSFP CMRA, both in adults (with acquired and CHD) and children with CHD. In single-phase studies, the 2D iNAV directly enabled measurement and respiratory motion correction of the heart itself rather than the diaphragm, in real-time (i.e. with no extra post-processing). In all studies, a significant reduction in acquisition time and improvement in the coronary image quality was attained.

A number of future developments could be introduced to further improve 2D iNAV IR-CMRA. The sequence was optimised for single-phase studies. However, Uribe *et al.* (Uribe et al., 2011) have shown that the optimal timing for coronary artery visualisation (i.e. the selection of a systolic versus diastolic rest period) is patient dependent and different for each coronary artery segment, thus favouring a dual-phase CMRA sequence. Also, Hussain *et al.* (Hussain et al., 2012) have shown that images obtained during the systolic rest period offer better clarity for many cardiac segments in patients with CHD. A theoretical concern of dual-phase imaging is the possible reduction of SNR because of the acquisition of two cardiac phases during a single cardiac cycle when compared with a single-phase CMRA sequence. More recently, Moyé *et al.* (Moyé et al., 2018) have successfully tested the 2D iNAV in a dual-phase CMRA acquisition (isotropic resolution of 1.5mm^3) in a small sample of healthy volunteers (seven subjects; mean age of 33.1 ± 8.4 years) and awake paediatric patients with CHD (30 subjects; mean age 16.7 ± 5.1 years). The coronary imaging results were then compared to those obtained with a conventional 1D diaphragmatic navigator. These initial results are encouraging, with the 2D iNAV significantly reducing scan time ($6:41 \pm 2:17$ and $9:57 \pm 3:29$ minutes, respectively) for a similar coronary image quality in both systolic and diastolic acquisitions. Further work is required to understand whether compared to single-phase 2D iNAV studies, the diagnostic performance of the dual-phase 2D iNAV (for instance for detection of coronary stenosis) is not compromised, so these findings can be translated into clinical practice.

Currently, the 2D iNAV implementation is incompatible with arrhythmia rejection algorithms. Integrating an arrhythmia would entail enabling the labelling of the measured k-space data as accepted or rejected so that data previously sent for image reconstruction could

be remeasured in real-time. This would further increase the clinical applicability of the sequence.

6.2. IMAGING BIOMARKERS

6.2.1. STUDY 4: LEFT ATRIAL PERFORMANCE IN THE COURSE OF HYPERTROPHIC CARDIOMYOPATHY

We have studied LA function in HCM using novel CMR-derived biomarkers. As we have discussed, HCM is a genetically determined heart muscle disease inherited in an autosomal dominant pattern, with variable expressivity and age-related penetrance. If for the majority of patients, HCM is characterised by a relatively benign prognosis, the phenotypic expression and clinical course diversity are a challenge for disease staging.

Diastolic function is often impaired early in the course of the disease, so simple and reproducible parameters of diastolic impairment could be helpful in the evaluation of symptoms and disease staging (Shah, 2003). Doppler echocardiography, the most practical clinical approach for LV diastolic impairment evaluation in HCM (Afonso et al., 2008) has a number of pitfalls (e.g. its metrics are influenced by loading conditions, HR, age, and are cumbersome), and its utility in predicting clinically meaningful outcome measures has not yet been clarified (Elliott et al., 2014). Conversely, Doppler echocardiography-derived parameters of LA dynamics, often impaired in the early stages of HCM secondary to LV diastolic dysfunction, have been shown to provide simple and reproducible metrics with prognostic information (Hoit, 2014; Thomas and Abhayaratna, 2017). More recently CMR has also been used to assess LA dynamics (Kowallick et al., 2014), with many advantages over echocardiography: (1) it can reliably assess LA morphology for volumetric and functional assessment; (2) it can calculate atrial and ventricular volumes precisely independent of geometric assumptions; (3) it can provide reproducible atrial and ventricular deformation parameters for assessment of LA-LV coupling; (4) it can provide information on myocardial as well as atrial tissue composition.

In our work, we have used a recently developed CMR tool (CMR-feature tracking) to study LA functional mechanics in HCM and correlate these parameters with the presence of LV fibrosis. In future research work, it would be interesting to use a validated atrial LGE

protocol to cross-link functional and structural remodelling of the LA in HCM patients. In addition, we could apply CMR-feature tracking to evaluate intrinsic regional and global myocardial deformation parameters and correlate them with the results from advanced tissue characterisation techniques (e.g. LV LGE quantification and T1 mapping). Better understanding of impaired LV-LA coupling mechanics could provide means of phenotyping structural myocardial/atrial remodelling in phenotypically sub-expressed HCM gene carriers. However, an association with clinical endpoints is deemed necessary to prove the usefulness of such biomarkers and likely requires a multicentre (registry) design.

6.2.2. STUDY 5: AORTIC LENGTH MEASUREMENTS FOR PWV CALCULATION: MANUAL 2D VERSUS AUTOMATED 3D CENTRELINE EXTRACTION

The primary aim of this study was to demonstrate the robustness of our methodology for accurate aortic centreline extraction using different CMR sequences to streamline PWV calculation. However our research also revealed small but significant differences in PWV calculations derived from 2D versus 3D datasets. To establish the transit time using the foot-to-foot methodology, we have acquired free-breathing high temporally resolved 2D PC-CMR flows at the aortic root, distal arch and thoracic aorta at the level of the diaphragm (this has allowed us to assess PWV in different thoracic segments). The distance travelled by the flow waveform was measured in acquired sets of 2D or 3D images of the aorta. The 2D PC-CMR flow plane was then used to define the start and end points of the aortic centreline. Although this methodology has been previously established as a reliable technique (Grotenhuis et al., 2009), novel time-resolved 3D (so-called “4D”) PC-CMR techniques allow simultaneous volumetric coverage and velocity encoding in all three spatial directions. 4D PC-CMR flow is an attractive approach for full volumetric assessment of aortic PWV as it offers simultaneous acquisition of anatomic data for distance measurement and isotropic high spatial resolution flow for transit time estimation. Additionally, 4D PC-CMR flow may offer several advantages: (1) it permits investigation of the internal consistency of the flow data assessing for “conservation of mass”; (2) it enables retrospective placement of analysis planes at any location across the acquired 3D volume to calculate local/regional PWV; (3)

simplifies scan prescription since it requires positioning of a single acquisition volume compared to the need to accurately locate and plan the 2D acquisitions (particularly advantageous in complex geometries such as CoA patients); (4) since it can measure velocity in three spatial directions with a superior spatial coverage it can better capture the peak velocity of a stenotic jet; (5) can visualise and measure complex flow fields (intra-vascular and intra-cardiac) without any restrictions to a predefined imaging plane.

4D PC-CMR flow has been recently used to calculate PWV in healthy subjects and acute stroke patients. It showed high accuracy even in patients with complex aortic geometries compared to 2D-based CMR approaches (Markl et al., 2010, 2012; Wentland et al., 2014). In addition, reference values have been recently established in a population-based study (Harloff et al., 2018).

At the time of image acquisition for this research, none of the major MR systems manufacturers routinely provided 4D PC-CMR flow sequences or packages to researchers or clinical users, and there was still no consensus regarding the best sequence protocol (Dyverfeldt et al., 2015). These sequences were also hampered by a relatively low temporal/spatial resolution and long acquisition times. However, 4D PC-CMR sequences with improved design and commercial software for post-processing analysis have since been approved for clinical use. With current technological advances in acceleration methods, 4D PC-CMR flow can be acquired in a clinically feasible time of less than 10 minutes, with a reasonable spatial and temporal resolution (Crandon et al., 2017).

As the most reproducible manual and automated centreline annotations in our study were obtained using 3D datasets, these novel 4D PC-CMR sequences with higher temporal and spatial resolution could allow for further improvement in PWV accuracy. Moreover, such 4D flow-based PWV measurements could be less prone to errors resulting from inadvertent movement of the patient inside the scanner gantry or sudden haemodynamic changes compared to 2D approaches. It would be interesting to investigate in a large, preferably multicentre study, with optimised and consensual protocols, the comparability between 2D and 4D PC-CMR-based PWV measurements, as well as the ideal spatial and temporal resolution required for this application.

6.3. PATIENT-SPECIFIC COMPUTATIONAL MODELLING

The goal of the different intertwined studies presented in this thesis was to develop and demonstrate the application of an image-based methodology to an ALGS patient and study potential pathophysiologic coronary responses during liver transplantation (a proof-of-concept). As part of future work, we intend to expand the proposed PSCM, with additional sophistications (see below), and use it to explore the occurrence of RV microvascular function impairment in other ALGS patients and understand its importance in the outcome of those undergoing liver transplantation. As our institution is a referral centre for the pre-operative cardiovascular risk assessment of ALGS patients (Subramaniam et al., 2011), pending on ethical approval, we could retrospectively replicate the methodology used in this thesis using data from patients that have undergone the standard assessment and liver transplantation, while concealing the surgical outcome to the computational data analysis. This could be followed by a multicentre prospective design to derive metrics for risk estimation that could be extracted from simple CMR scans (e.g. CBF profiles, diastolic/systolic RCA/LCA flow ratio) for those proposed for liver transplantation. Moreover, in those ALGS patients with PPS being considered for percutaneous/surgical treatment prior to liver transplantation, we could use our PSCM workflow to produce post-operative simulation-derived haemodynamics not just on pulmonary flow distribution as in the study by Yang *et al.* (Yang et al., 2018), but also on coronary haemodynamics. This could prove useful for surgical or transcatheter planning (e.g. selecting those patients that could benefit from PPS treatment prior to liver transplantation). This work could serve as a stepping stone to ultimately develop a robust risk stratification tool that could be applicable to all ALGS and also a broader spectrum of more complex CHDs

In children/adults with PAH associated with CHD or primary PAH, maladaptive RVH is thought to predispose to RV ischaemia, RV systolic dysfunction and eventually RHF (Zong et al., 2005; Guarracino et al., 2005; Ryan and Archer, 2014). Although RV function is recognised as a key predictor of outcome in PAH as well as in many cardiovascular disease states, there are no clinically approved therapies that directly or selectively improve RV function. Hereof, we could use our methodology to model abnormal RV loading conditions of PAH patients, during different setups (e.g. following a stressor – exercise or

pharmacological), and investigate the effects of advanced pulmonary vasodilator therapy in the coronary circulation haemodynamics and RV function.

In addition, there are several refinements that could be implemented in the current methodology (some already being used by our research group) that could increase the reliability of the solution. Examples include: the introduction of a patient-specific inflow profile instead of the idealised profiles we have used based on the patient's 2D PC-CMR flow waveform (Youssefi et al., 2017); the use of non-linear stiffness and wall thickness (Cuomo et al., 2017); the use of a Kalman-filter based methodology for estimation of the parameters of the outflow boundary conditions and efficient model calibration instead of the iterative manual approach used in this research (DeVault et al., 2008). Nevertheless, it is important to consider the algorithmic complexity required to represent all relevant domains and scales in one physical model, which may lead to an extremely large set of unknowns, the additional insight into the biomechanics gained and the added computational cost.

ABBREVIATIONS

Abbreviation	Meaning
0, 1, 2 or 3D	Zero, one, two or three-dimensional
3DDR	3D domain replacement
µm	Microns
ALGS	Alagille's syndrome
ASC	Ascending thoracic aorta
AP direction	Antero-posterior direction
APD	Average Perpendicular Distance
ATP	Adenosine triphosphate
BA	Biliary atresia
BMI	Body mass index
bpm	Beats per minute
BP-CAs	Blood-pool contrast agents
BSA	Body surface area
C index	Conformity index
CAD	Coronary artery disease
CBF	Coronary blood flow
CE-MRA	Contrast-enhanced magnetic resonance angiography
CFD	Computational fluid dynamics
CFR	Coronary flow reserve
CFCM	Coronary flow control model
CHD	Congenital heart disease
CI	Confidence interval
cm	Centimetres
CMCM	Coronary microvasculature control system
CMR	Cardiovascular magnetic resonance
CMRA	Coronary magnetic resonance angiography
CNR	Contrast-to-noise ratio

CoA	Aortic coarctation
CO ₂	Carbon dioxide
CR	Cinematic Rendering
CRF	Cardiovascular risk factors
CRFs	Conditional random fields
CRIMSON	CardiovasculaR Integrated Modeling and SimulatiON
CRUISE	Constant respiratory efficiency using single end-expiratory threshold
CCTA	Cardiac computed tomography angiography
CT	Computed tomography
DESC	Descending thoracic aorta
DI	Dice Index
DIAPH	Diaphragmatic aorta
DIR-TSE	Double inversion recovery turbo spin echo
DS	Dual-source
DSCMR	Dobutamine stress CMR
DZ	Dizygotic
EC-GBCAs	Extracellular gadolinium-based contrast agents
ECV	Extracellular volume
ED	End-diastole
EF	Ejection fraction
ES	End-systole
EVC	Extravascular compression
FCNN	Fully Convolutional Neural Networks
FH direction	Foot-to-head direction
FoV	Field-of-view
Gd	Gadolinium
Gd-BOPTA	Gadobenate dimeglumine
GRE	Gradient recalled echo or gradient echo
<i>H</i>	Myocardial hunger
HATS	Healthy Ageing Twin Study
HCM	Hypertrophic cardiomyopathy
HP	High-pitch
HPC	High performance computing
HPS	Hepato-pulmonary syndrome
HR	Heart rate
IMT	Intima-media thickening
iNAV	Image-based navigator
IQR	Interquartile range
IR	Inversion recovery

LA	Left atrium/atrial
LCA	Left coronary artery
LCX	Left circumflex artery
LGE	Late gadolinium enhancement
LM artery	Left main artery
LPN	Lumped parameter network
LR direction	Left-right direction
LV	Left ventricle
LVOTO	LV outflow tract obstruction
LVH	Left ventricular hypertrophy
m	Meters
ml	Millilitre
mm	Millimetres
ms	Milliseconds
MAP	Mean arterial pressure
MVO ₂	Myocardial oxygen consumption
MZ	Monozygotic
RCA	Right coronary artery
RHF	Right heart failure
ROI	Region of interest
RV	Right ventricle
PAH	Pulmonary arterial hypertension
PAP	Pulmonary arterial pressure
PAWP	Pulmonary artery wedge pressure
PC-CMR flow	Phase-contrast CMR flow
POPH	Porto-pulmonary hypertension
PPS	Peripheral pulmonary stenosis
PRS	Post-reperfusion syndrome
PSCM	Patient-specific computational modelling
PSPD	Peak systolic to peak diastolic
P-V loops	Pressure-volume loops
PVD	Pulmonary vascular disease
PVR	Pulmonary vascular resistance
PWV	Pulse wave velocity
ROC curve	Receiver-operator characteristics curve
RVH	Right ventricular hypertrophy
s	Seconds
SF	Semantic flow
(b)SSFP	(balanced) Steady-state free precession

SNR	Signal-to-noise ratio
SR	Strain rate
T-FCNN	Temporal Convolution Neural Network
TE	Echo time
TI	Inversion time
TR	Repetition time
VCG	Vectorcardiogram
VR	Volume rendering
VWS	Vessel wall sharpness
WSS	Wall shear stress
XMR study	Hybrid X-ray/ magnetic resonance guided study

CO-AUTHOR PUBLICATIONS

Contributions

	Study	Study	Study	Study	Study
	1	2	4	5	6
Devised the project/the main conceptual ideas		x	x	x	x
Designed the study		x	x	x	x
Sample recruitment	x	x	x	x	x
Designed and performed the experiments, (i.e. questionnaires, imaging acquisitions, clinical measurements)		x	x	x	x
Processed and analysed the experimental data the data (performed the segmentations, calculations, statistical analysis)	x	x	x	x	x
Verification of the analytical methods	x	x	x	x	x
Contributed to the interpretation of the results	x	x	x	x	x
Provided critical feedback and helped shape the research, analysis and manuscript writing	x	x	x	x	x
Worked on the manuscript writing	x	x	x	x	x
Reviewed the final manuscript	x	x	x	x	x

REFERENCES

- Abbara, S., Arbab-Zadeh, A., Callister, T.Q., et al. (2009) SCCT guidelines for performance of coronary computed tomographic angiography: A report of the Society of Cardiovascular Computed Tomography Guidelines Committee. *J Cardiovasc Comput Tomogr*, 3 (3): 190–204. doi:10.1016/j.jcct.2009.03.004.
- Abbas, A., Cecelja, M., Hussain, T., et al. (2015) Thoracic but not abdominal phase contrast magnetic resonance-derived aortic pulse wave velocity is elevated in patients with abdominal aortic aneurysm. *J Hypertens*, 33 (5): 1032–1038. doi:10.1097/HJH.0000000000000516.
- Adji, A., O'Rourke, M.F. and Namasivayam, M. (2011) Arterial stiffness, its assessment, prognostic value, and implications for treatment. *American Journal of Hypertension*. doi:10.1038/ajh.2010.192.
- Afonso, L.C., Bernal, J., Bax, J.J., et al. (2008) Echocardiography in Hypertrophic Cardiomyopathy. *JACC Cardiovasc Imaging*, 1 (6): 787–800. doi:10.1016/j.jcmg.2008.09.002.
- Aggarwal, S., Kang, Y., Freeman, J.A., et al. (1987) Postreperfusion syndrome: cardiovascular collapse following hepatic reperfusion during liver transplantation. *Transplant Proc*, 19 (4 Suppl 3): 54–55.
- Agnoletti, G., Boudjemline, Y., Bonnet, D., et al. (2004) Surgical reconstruction of occluded pulmonary arteries in patients with congenital heart disease: effects on pulmonary artery growth. *Circulation*, 109 (19): 2314–2318. doi:10.1161/01.CIR.0000129273.50975.F4.
- Aitken, A.P., Henningson, M., Botnar, R.M., et al. (2015) 100% Efficient three-dimensional coronary MR angiography with two-dimensional beat-to-beat translational and bin-to-bin affine motion correction. *Magn Reson Med*, 74 (3): 756–764. doi:10.1002/mrm.25460.
- Akasaka, T., Yoshikawa, J., Yoshida, K., et al. (1996) Comparison of relation of systolic flow of the right coronary artery to pulmonary artery pressure in patients with and without pulmonary hypertension. *Am J Cardiol*, 78 (2): 240–244. doi:10.1016/S0002-9149(96)90407-5.

Alagille, D., Borde, J., Habib, E.C., et al. (1969) Surgical attempts in atresia of the intrahepatic bile ducts with permeable extrahepatic bile duct. Study of 14 cases in children. *Arch Fr Pediatr*, 26 (1): 51–71.

Alagille, D., Estrada, A., Hadchouel, M., et al. (1987) Syndromic paucity of interlobular bile ducts (Alagille syndrome or arteriohepatic dysplasia): review of 80 cases. *J Pediatr*, 110 (2): 195–200.

Allen, D.G. and Orchard, C.H. (1987) Myocardial contractile function during ischemia and hypoxia. *Circulation Research*, 60 (2): 153–168. doi:10.1161/01.res.60.2.153.

Angelini Paolo (2007) Coronary Artery Anomalies. *Circulation*, 115 (10): 1296–1305. doi:10.1161/CIRCULATIONAHA.106.618082.

Anwar, A.M., Soliman, O.I.I., Geleijnse, M.L., et al. (2007) Assessment of left atrial ejection force in hypertrophic cardiomyopathy using real-time three-dimensional echocardiography. *J Am Soc Echocardiogr*, 20 (6): 744–748. doi:10.1016/j.echo.2006.11.017.

Anwar, A.M., Soliman, O.I.I., Nemes, A., et al. (2008) An integrated approach to determine left atrial volume, mass and function in hypertrophic cardiomyopathy by two-dimensional echocardiography. *Int J Cardiovasc Imaging*, 24 (1): 45–52. doi:10.1007/s10554-007-9224-x.

Arbia, G., Corsini, C., Esmaily Moghadam, M., et al. (2014) Numerical blood flow simulation in surgical corrections: what do we need for an accurate analysis? *Journal of Surgical Research*, 186 (1): 44–55. doi:10.1016/j.jss.2013.07.037.

Arciero, J.C., Carlson, B.E. and Secomb, T.W. (2008) Theoretical model of metabolic blood flow regulation: roles of ATP release by red blood cells and conducted responses. *Am J Physiol Heart Circ Physiol*, 295 (4): H1562–H1571. doi:10.1152/ajpheart.00261.2008.

Ardehali, A. and Ports, T.A. (1990) Myocardial Oxygen Supply and Demand. *Chest*, 98 (3): 699–705. doi:10.1378/chest.98.3.699.

Arnon, R., Annunziato, R., Miloh, T., et al. (2010) Orthotopic liver transplantation for children with Alagille syndrome. *Pediatr Transplant*, 14 (5): 622–628. doi:10.1111/j.1399-3046.2009.01286.x.

Arthurs, C.J., Lau, K.D., Asrress, K.N., et al. (2016) A mathematical model of coronary blood flow control: simulation of patient-specific three-dimensional hemodynamics during exercise. *Am J Physiol Heart Circ Physiol*, 310 (9): H1242–H1258. doi:10.1152/ajpheart.00517.2015.

Assomull, R.G., Shakespeare, C., Kalra, P.R., et al. (2011) Role of Cardiovascular Magnetic Resonance as a Gatekeeper to Invasive Coronary Angiography in Patients Presenting With Heart Failure of Unknown Etiology. *Circulation*, 124 (12): 1351–1360. doi:10.1161/CIRCULATIONAHA.110.011346.

- Babin, D., Devos, D., Pižurica, A., et al. (2014) Robust segmentation methods with an application to aortic pulse wave velocity calculation. *Comput Med Imaging Graph*, 38 (3): 179–189. doi:10.1016/j.compmedimag.2013.12.001.
- Bailey, G.W., Braniff, B.A., Hancock, E.W., et al. (1968) Relation of left atrial pathology to atrial fibrillation in mitral valvular disease. *Ann Intern Med*, 69 (1): 13–20.
- Bangerter, N.K., Hargreaves, B.A., Vasanawala, S.S., et al. (2004) Analysis of multiple-acquisition SSFP. *Magn Reson Med*, 51 (5): 1038–1047. doi:10.1002/mrm.20052.
- Basso, D.C., Associate Professor and Director, Institute of Pathologic Anatomy, University of Padua Medical School, Thiene, G., et al. (2005) Congenital Coronary Artery Anomalies at Risk of Myocardial Ischaemia and Sudden Death. *European Cardiology Review*, 1 (1): 1. doi:10.15420/ECR.2005.1i.
- Baumgartner, H., Bonhoeffer, P., De Groot, N.M.S., et al. (2010) ESC Guidelines for the management of grown-up congenital heart disease (new version 2010). *Eur Heart J*, 31 (23): 2915–57. doi:10.1093/eurheartj/ehq249.
- Bazilevs, Y., Gohean, J.R., Hughes, T.J.R., et al. (2009) Patient-specific isogeometric fluid-structure interaction analysis of thoracic aortic blood flow due to implantation of the Jarvik 2000 left ventricular assist device. *Comput Methods Appl Mech Eng*, 198 (45–46): 3534–3550. doi:10.1016/j.cma.2009.04.015.
- Bédard, E., McCarthy, K.P., Dimopoulos, K., et al. (2009) Structural Abnormalities of the Pulmonary Trunk in Tetralogy of Fallot and Potential Clinical Implications. *J Am Coll Cardiol*, 54 (20): 1883–1890. doi:10.1016/j.jacc.2009.06.040.
- Bell, J.R. and Fox, A.C. (1974) Pathogenesis of subendocardial ischemia: *Am J Med Sci*, 268 (1): 2–13. doi:10.1097/00000441-197407000-00001.
- Benito, E.M., Carlosena-Remirez, A., Guasch, E., et al. (2017) Left atrial fibrosis quantification by late gadolinium-enhanced magnetic resonance: a new method to standardize the thresholds for reproducibility. *Europace*, 19 (8): 1272–1279. doi:10.1093/europace/euw219.
- Bescós, J.O., Sonnemans, J., Habets, R., et al. (2009) Vessel Explorer: a tool for quantitative measurements in CT and MR angiography. *Medicamundi*, 53 (3).
- Bi, X., Deshpande, V., Carr, J., et al. (2006) Coronary artery magnetic resonance angiography (MRA): a comparison between the whole-heart and volume-targeted methods using a T2-prepared SSFP sequence. *Journal of Cardiovascular Magnetic Resonance: Official Journal of the Society for Cardiovascular Magnetic Resonance*, 8 (5): 703–707. doi:10.1080/10976640600723706.
- Bieri, O. and Scheffler, K. (2005) Flow compensation in balanced SSFP sequences. *Magn Reson Med*, 54 (4): 901–907. doi:10.1002/mrm.20619.

- Bland, J.M. and Altman, D.G. (1986) Statistical methods for assessing agreement between two methods of clinical measurement. *Lancet*, 1 (8476): 307–310.
- Bogaard, H.J., Natarajan, R., Henderson, S.C., et al. (2009) Chronic pulmonary artery pressure elevation is insufficient to explain right heart failure. *Circulation*, 120 (20): 1951–1960. doi:10.1161/CIRCULATIONAHA.109.883843.
- Bogaert, J., Dymarkowski, S., Taylor, A.M., et al. (eds.) (2012) *In Clinical Cardiac MRI*. Medical Radiology. 2nd ed. Berlin, Heidelberg: Springer Berlin Heidelberg. pp. 31–51. doi:10.1007/978-3-642-23035-6.
- Borlaug, B.A. and Kass, D.A. (2011) Ventricular-vascular interaction in heart failure. *Cardiol Clin*, 29 (3): 447–459. doi:10.1016/j.ccl.2011.06.004.
- Boskamp, T., Rinck, D., Link, F., et al. (2004) New Vessel Analysis Tool for Morphometric Quantification and Visualization of Vessels in CT and MR Imaging Data Sets. *RadioGraphics*, 24 (1): 287–297. doi:10.1148/rg.241035073.
- Botnar, R.M., Stuber, M., Danias, P.G., et al. (1999) Improved coronary artery definition with T2-weighted, free-breathing, three-dimensional coronary MRA. *Circulation*, 99 (24): 3139–3148.
- Boutouyrie, P., Briet, M., Collin, C., et al. (2009) Assessment of pulse wave velocity. *Artery Res*, 3 (1): 3–8. doi:10.1016/j.artres.2008.11.002.
- Braunwald, E. (1971) Control of myocardial oxygen consumption. *Am J Cardiol*, 27 (4): 416–432. doi:10.1016/0002-9149(71)90439-5.
- Brittain, J.H., Hu, B.S., Wright, G.A., et al. (1995) Coronary angiography with magnetization-prepared T2 contrast. *Magn Reson Med*, 33 (5): 689–696.
- Broomé, M., Maksuti, E., Bjällmark, A., et al. (2013) Closed-loop real-time simulation model of hemodynamics and oxygen transport in the cardiovascular system. *Biomed Eng Online*, 12 (1): 69. doi:10.1186/1475-925X-12-69.
- Brouwer, W.P., Baars, E.N., Germans, T., et al. (2014) In-vivo T1 cardiovascular magnetic resonance study of diffuse myocardial fibrosis in hypertrophic cardiomyopathy. *J Cardiovasc Magn Reson*, 16 (1): 28. doi:10.1186/1532-429X-16-28.
- Bruder, O., Wagner, A., Jensen, C.J., et al. (2010) Myocardial Scar Visualized by Cardiovascular Magnetic Resonance Imaging Predicts Major Adverse Events in Patients With Hypertrophic Cardiomyopathy. *J Am Coll Cardiol*, 56 (11): 875–887. doi:10.1016/j.jacc.2010.05.007.
- Bruinsma, P., Arts, T., Dankelman, J., et al. (1988) Model of the coronary circulation based on pressure dependence of coronary resistance and compliance. *Basic Res Cardiol*. doi:10.1007/BF01906680.

Buffington, C.W. and Feigl, E.O. (1983) Effect of coronary artery pressure on transmural distribution of adrenergic coronary vasoconstriction in the dog. *Circ Res*, 53 (5): 613–621.

Bunce, N.H., Lorenz, C.H., Keegan, J., et al. (2003) Coronary artery anomalies: assessment with free-breathing three-dimensional coronary MR angiography. *Radiology*, 227 (1): 201–208. doi:10.1148/radiol.2271020316.

Canty, J.M. and Klocke, F.J. (1985) Reduced regional myocardial perfusion in the presence of pharmacologic vasodilator reserve. *Circulation*, 71 (2): 370–377.

Cavagna, F.M., Maggioni, F., Castelli, P.M., et al. (1997) Gadolinium chelates with weak binding to serum proteins. A new class of high-efficiency, general purpose contrast agents for magnetic resonance imaging. *Invest Radiol*, 32 (12): 780–796.

Cavalcante, J.L., Lima, J.A., Redheuil, A., et al. (2011) Aortic stiffness: current understanding and future directions. *J Am Coll Cardiol*, 57 (14): 1511–1522. doi:10.1016/j.jacc.2010.12.017.

Cecelja, M. and Chowienczyk, P. (2009) Dissociation of aortic pulse wave velocity with risk factors for cardiovascular disease other than hypertension: A systematic review. *Hypertension*, 54 (6): 1328–36. doi:10.1161/HYPERTENSIONAHA.109.137653.

Cecelja, M., Jiang, B., Bevan, L., et al. (2011) Arterial Stiffening Relates to Arterial Calcification But Not to Noncalcified Atheroma in Women. *J Am Coll Cardiol*, 57 (13): 1480–1486. doi:10.1016/j.jacc.2010.09.079.

Champion, H.C., Michelakis, E.D. and Hassoun, P.M. (2009) *Comprehensive invasive and noninvasive approach to the right ventricle-pulmonary circulation unit state of the art and clinical and research implications*. doi:10.1161/CIRCULATIONAHA.106.674028.

Chan, R.H., Maron, B.J., Olivetto, I., et al. (2014) Prognostic Value of Quantitative Contrast-Enhanced Cardiovascular Magnetic Resonance for the Evaluation of Sudden Death Risk in Patients With Hypertrophic Cardiomyopathy. *Circulation*, 130 (6): 484–495. doi:10.1161/CIRCULATIONAHA.113.007094.

Chilian, W.M. and Ackell, P.H. (1988) Transmural differences in sympathetic coronary constriction during exercise in the presence of coronary stenosis. *Circ Res*, 62 (2): 216–225.

Chilian, W.M., Layne, S.M., Eastham, C.L., et al. (1989) Heterogeneous microvascular coronary alpha-adrenergic vasoconstriction. *Circ Res*, 64 (2): 376–388.

Chirinos, J.A. (2013) Ventricular–arterial coupling: Invasive and non-invasive assessment. *Artery Res*, 7 (1): 2–14. doi:10.1016/j.artres.2012.12.002.

Chiu, Y.C., Arand, P.W., Shroff, S.G., et al. (1991) Determination of pulse wave velocities with computerized algorithms. *American Heart Journal*, 121 (5): 1460–1470. doi:10.1016/0002-8703(91)90153-9.

Choy, J.S. and Kassab, G.S. (2008) Scaling of myocardial mass to flow and morphometry of coronary arteries. *Journal of Applied Physiology*, 104 (5): 1281–1286. doi:10.1152/jappphysiol.01261.2007.

Chui, A.K., Shi, L., Tanaka, K., et al. (2000) Postreperfusion syndrome in orthotopic liver transplantation. *Transplant Proc*, 32 (7): 2116–2117.

Cicala, S., Galderisi, M., Grieco, M., et al. (2008) Transthoracic Echo-Doppler Assessment of Coronary Microvascular Function Late after Kawasaki Disease. *Pediatric Cardiology*, 29 (2): 321–327. doi:10.1007/s00246-007-9030-1.

Condino, A.A., Ivy, D.D., O'Connor, J.A., et al. (2005) Portopulmonary hypertension in pediatric patients. *The Journal of Pediatrics*, 147 (1): 20–26. doi:10.1016/j.jpeds.2005.02.019.

Cornelissen, A.J.M., Dankelman, J., VanBavel, E., et al. (2002) Balance between myogenic, flow-dependent, and metabolic flow control in coronary arterial tree: a model study. *Am J Physiol Heart Circ Physiol*, 282 (6): H2224–2237. doi:10.1152/ajpheart.00491.2001.

Craiem, D., Chironi, G., Redheuil, A., et al. (2012) Aging Impact on Thoracic Aorta 3D Morphometry in Intermediate-Risk Subjects: Looking Beyond Coronary Arteries with Non-Contrast Cardiac CT. *Ann Biomed Eng*, 40 (5): 1028–1038. doi:10.1007/s10439-011-0487-y.

Crandon, S., Elbaz, M.S.M., Westenberg, J.J.M., et al. (2017) Clinical applications of intracardiac four-dimensional flow cardiovascular magnetic resonance: A systematic review. *Int J Cardiol*, 249: 486–493. doi:10.1016/j.ijcard.2017.07.023.

Crea, F., Lanza, G.A. and Camici, P.G. (2014) *Coronary Microvascular Dysfunction*. Milano: Springer.

Cruz, G., Atkinson, D., Henningson, M., et al. (2017) Highly efficient nonrigid motion-corrected 3D whole-heart coronary vessel wall imaging: Highly Efficient Motion-Compensated 3D Coronary Vessel Wall. *Magn Reson Med*, 77 (5): 1894–1908. doi:10.1002/mrm.26274.

Cuomo, F., Roccabianca, S., Dillon-Murphy, D., et al. (2017) Effects of age-associated regional changes in aortic stiffness on human hemodynamics revealed by computational modeling. *PLOS ONE*, 12 (3): e0173177. doi:10.1371/journal.pone.0173177.

Danias, P.G., McConnell, M.V., Khasgiwala, V.C., et al. (1997) Prospective navigator correction of image position for coronary MR angiography. *Radiology*, 203 (3): 733–736. doi:10.1148/radiology.203.3.9169696.

Danias, P.G., Stuber, M., Botnar, R.M., et al. (1999) Relationship between motion of coronary arteries and diaphragm during free breathing: lessons from real-time MR imaging. *AJR. American journal of roentgenology*, 172 (4): 1061–1065. doi:10.2214/ajr.172.4.10587147.

Danias, P.G., Roussakis, A. and Ioannidis, J.P.A. (2004) Diagnostic performance of coronary magnetic resonance angiography as compared against conventional X-ray angiography: a meta-analysis. *J Am Coll Cardiol*, 44 (9): 1867–1876. doi:10.1016/j.jacc.2004.07.051.

Dankelman, J., Spaan, J.A., Stassen, H.G., et al. (1989) Dynamics of coronary adjustment to a change in heart rate in the anaesthetized goat. *J Physiol*, 408: 295–312.

Dankelman, J., Stassen, H.G. and Spaan, J.A. (1990) System analysis of the dynamic response of the coronary circulation to a sudden change in heart rate. *Med Biol Eng Comput*, 28 (2): 139–148.

Dankelman, J., Vergroesen, I., Han, Y., et al. (1992) Dynamic response of coronary regulation to heart rate and perfusion changes in dogs. *Am J Physiol*, 263 (2): H447–H452. doi:10.1152/ajpheart.1992.263.2.H447.

Dankelman, J., Stassen, H.G. and Spaan, J.A.E. (1999) Interaction between Gregg's phenomenon and coronary flow control: a model study. *Medical & Biological Engineering & Computing*, 37 (6): 742–749. doi:10.1007/BF02513377.

Davidson, B.P. and Giraud, G.D. (2012) Left ventricular function and the systemic arterial vasculature: remembering what we have learned. *J Am Soc Echocardiogr*, 25 (8): 891–894. doi:10.1016/j.echo.2012.06.020.

Davis, J.A., Cecchin, F., Jones, T.K., et al. (2001) Major coronary artery anomalies in a pediatric population: incidence and clinical importance. *Journal of the American College of Cardiology*, 37 (2): 593–597. doi:10.1016/s0735-1097(00)01136-0.

Debonnaire, P., Joyce, E., Hiemstra, Y., et al. (2017) Left Atrial Size and Function in Hypertrophic Cardiomyopathy Patients and Risk of New-Onset Atrial Fibrillation. *Circ Arrhythm Electrophysiol*, 10 (2). doi:10.1161/CIRCEP.116.004052.

DeCampli, W.M., Argueta-Morales, I.R., Divo, E., et al. (2012) Computational fluid dynamics in congenital heart disease. *Cardiology in the Young*, 22 (6): 800–808. doi:10.1017/S1047951112002028.

Deng, Z., Fan, Z., Xie, G., et al. (2014) Pressure gradient measurement in the coronary artery using 4D PC-MRI: towards noninvasive quantification of fractional flow reserve. *Journal of Cardiovascular Magnetic Resonance*, 16 (S1): O55. doi:10.1186/1532-429X-16-S1-O55.

Deriche, R. (1990) Fast algorithms for low-level vision. *IEEE Trans Pattern Anal Mach Intell*, 12 (1): 78–87. doi:10.1109/34.41386.

Desai, M.S., Zainuer, S., Kennedy, C., et al. (2011) Cardiac structural and functional alterations in infants and children with biliary atresia, listed for liver transplantation. *Gastroenterology*. doi:10.1053/j.gastro.2011.06.082.

Deussen, A., Ohanyan, V., Jannasch, A., et al. (2012) Mechanisms of metabolic coronary flow regulation. *Journal of Molecular and Cellular Cardiology*, 52 (4): 794–801. doi:10.1016/j.yjmcc.2011.10.001.

DeVault, K., Gremaud, P.A., Novak, V., et al. (2008) Blood Flow in the Circle of Willis: Modeling and Calibration. *Multiscale Model Simul*, 7 (2): 888–909. doi:10.1137/07070231X.

Devos, D.G.H., Rietzschel, E., Heyse, C., et al. (2015) MR pulse wave velocity increases with age faster in the thoracic aorta than in the abdominal aorta. *J Magn Reson Imaging*. doi:10.1002/jmri.24592.

Dhorne-Pollet, S., Deleuze, J.F., Hadchouel, M., et al. (1994) Segregation analysis of Alagille syndrome. *J Med Genet*. doi:10.1136/jmg.31.6.453.

Diller, G.P. and Gatzoulis, M.A. (2007) Pulmonary vascular disease in adults with congenital heart disease. *Circulation*, 115 (8): 1039–1050. doi:10.1161/CIRCULATIONAHA.105.592386.

Dillon-Murphy, D., Noorani, A., Nordsletten, D., et al. (2016) Multi-modality image-based computational analysis of haemodynamics in aortic dissection. *Biomech Model Mechanobiol*, 15 (4): 857–876. doi:10.1007/s10237-015-0729-2.

Dodson, J.A., Neilan, T.G., Shah, R.V., et al. (2014) Left Atrial Passive Emptying Function Determined by Cardiac Magnetic Resonance Predicts Atrial Fibrillation Recurrence After Pulmonary Vein Isolation. *Circ Cardiovasc Imaging*, 7 (4): 586–592. doi:10.1161/CIRCIMAGING.113.001472.

Dogui, A., Redheuil, A., Lefort, M., et al. (2011) Measurement of aortic arch pulse wave velocity in cardiovascular MR: Comparison of transit time estimators and description of a new approach. *J Magn Reson Imaging*, 33 (6): 1321–1329. doi:10.1002/jmri.22570.

Downey, J.M. and Kirk, E.S. (1975) Inhibition of coronary blood flow by a vascular waterfall mechanism. *Circ Res*, 36 (6): 753–760.

Duerinckx, A.J. and Urman, M.K. (1994) Two-dimensional coronary MR angiography: analysis of initial clinical results. *Radiology*, 193 (3): 731–738. doi:10.1148/radiology.193.3.7972815.

Duncker, D.J. and Bache, R.J. (2008) Regulation of Coronary Blood Flow During Exercise. *Physiol Rev*, 88 (3): 1009–1086. doi:10.1152/physrev.00045.2006.

Dyverfeldt, P., Bissell, M., Barker, A.J., et al. (2015) 4D flow cardiovascular magnetic resonance consensus statement. *J Cardiovasc Magn Reson*, 17 (1). doi:10.1186/s12968-015-0174-5.

Edelman, R.R., Manning, W.J., Burstein, D., et al. (1991) Coronary arteries: breath-hold MR angiography. *Radiology*, 181 (3): 641–643. doi:10.1148/radiology.181.3.1947074.

Ehman, R.L. and Felmlee, J.P. (1989) Adaptive technique for high-definition MR imaging of moving structures. *Radiology*, 173 (1): 255–263. doi:10.1148/radiology.173.1.2781017.

Elliott, P.M., Anastasakis, A., Borger, M., et al. (2014) 2014 ESC Guidelines on diagnosis and management of hypertrophic cardiomyopathy: The Task Force for the Diagnosis and Management of Hypertrophic Cardiomyopathy of the European Society of Cardiology (ESC). *Eur Heart J*, 35 (39): 2733–2779. doi:10.1093/eurheartj/ehu284.

Emerick, K.M., Rand, E.B., Goldmuntz, E., et al. (1999) Features of Alagille syndrome in 92 patients: Frequency and relation to prognosis. *Hepatology*, 29 (3): 822–9. doi:10.1002/hep.510290331.

Emerick, K.M., Krantz, I.D., Kamath, B.M., et al. (2005) Intracranial vascular abnormalities in patients with Alagille syndrome. *Gastroenterol Nutr*, 41 (1): 99–107. doi:10.1097/01.MPG.0000162776.67758.2F.

van Engelen, A., Silva Vieira, M., Rafiq, I., et al. (2017) Aortic length measurements for pulse wave velocity calculation: manual 2D vs automated 3D centreline extraction. *J Cardiovasc Magn Reson*, 19 (1). doi:10.1186/s12968-017-0341-y.

Engelfriet, P.M., Duffels, M.G.J., Möller, T., et al. (2007) Pulmonary arterial hypertension in adults born with a heart septal defect: the Euro Heart Survey on adult congenital heart disease. *Heart (British Cardiac Society)*, 93 (6): 682–7. doi:10.1136/hrt.2006.098848.

Englert, C., Grabhorn, E., Burdelski, M., et al. (2006) Liver transplantation in children with Alagille syndrome: Indications and outcome. *Pediatr Transplant*, 10 (2): 154–8. doi:10.1111/j.1399-3046.2005.00432.x.

Eshoo, S., Semsarian, C., Ross, D.L., et al. (2010) Left Atrial Phasic Volumes Are Modulated by the Type Rather Than the Extent of Left Ventricular Hypertrophy. *J Am Soc Echocardiogr*, 23 (5): 538–544. doi:10.1016/j.echo.2010.01.022.

Esmaily Moghadam, M., Bazilevs, Y., Hsia, T.-Y., et al. (2011) A comparison of outlet boundary treatments for prevention of backflow divergence with relevance to blood flow simulations. *Comput Mech*, 48 (3): 277–291. doi:10.1007/s00466-011-0599-0.

Etienne, A., Botnar, R.M., Van Muiswinkel, A.M.C., et al. (2002) “Soap-Bubble” visualization and quantitative analysis of 3D coronary magnetic resonance angiograms. *Magn Reson Med*, 48 (4): 658–666. doi:10.1002/mrm.10253.

Farhad, H., Seidelmann, S.B., Vigneault, D., et al. (2017) Left Atrial structure and function in hypertrophic cardiomyopathy sarcomere mutation carriers with and without left ventricular hypertrophy. *J Cardiovasc Magn Reson*, 19 (1). doi:10.1186/s12968-017-0420-0.

Feigl, E.O. (1983) Coronary physiology. *Physiol Rev*, 63 (1): 1–205. doi:10.1152/physrev.1983.63.1.1.

- Feigl, E.O. (1987) The paradox of adrenergic coronary vasoconstriction. *Circulation*, 76 (4): 737–745. doi:10.1161/01.CIR.76.4.737.
- Feigl, E.O. (1998) Neural control of coronary blood flow. *J Vasc Res*, 35 (2): 85–92. doi:10.1159/000025569.
- Ferreira, P.F., Gatehouse, P.D., Mohiaddin, R.H., et al. (2013) Cardiovascular magnetic resonance artefacts. *J Cardiovasc Magn Reson*, 15 (1): 41. doi:10.1186/1532-429X-15-41.
- Finocchiaro, G., Behr, E.R., Tanzarella, G., et al. (2019) Anomalous Coronary Artery Origin and Sudden Cardiac Death. *JACC: Clinical Electrophysiology*, 5 (4): 516–522. doi:10.1016/j.jacep.2018.11.015.
- Florkow, M., Harana, J.M., van Engelen, A., et al. (2016) An Integrated Software Application for Non-invasive Assessment of Local Aortic Haemodynamic Parameters. *Procedia Comput Sci*, 90: 2–8. doi:10.1016/j.procs.2016.07.002.
- Ford, R.M., Book, W. and Spivey, J.R. (2015) Liver disease related to the heart. *Transplantation Reviews (Orlando, Fla.)*, 29 (1): 33–37. doi:10.1016/j.trre.2014.11.003.
- Frangi, A.F., Niessen, W.J., Vincken, K.L., et al. (1998) “Multiscale vessel enhancement filtering.” In Wells, W.M., Colchester, A. and Delp, S. (eds.) *Medical Image Computing and Computer-Assisted Intervention — MICCAI’98*. Berlin, Heidelberg: Springer Berlin Heidelberg. pp. 130–137. doi:10.1007/BFb0056195.
- Frank, O. (1990) The basic shape of the arterial pulse. First treatise: Mathematical analysis. *J Mol Cell Cardiol*, 22 (3): 255–277. doi:10.1016/0022-2828(90)91460-O.
- Frump, A.L., Bonnet, S., de Jesus Perez, V.A., et al. (2018) Emerging role of angiogenesis in adaptive and maladaptive right ventricular remodeling in pulmonary hypertension. *American Journal of Physiology-Lung Cellular and Molecular Physiology*, 314 (3): L443–L460. doi:10.1152/ajplung.00374.2017.
- Fullerton, D.A., Kirson, L.E., Jones, S.D., et al. (1996) Adenosine is a Selective Pulmonary Vasodilator in Cardiac Surgical Patients. *Chest*, 109 (1): 41–46. doi:10.1378/chest.109.1.41.
- Gabrielli, L., Enríquez, A., Córdova, S., et al. (2012) Assessment of Left Atrial Function in Hypertrophic Cardiomyopathy and Athlete’s Heart: A Left Atrial Myocardial Deformation Study: Left Atrial Function in the Evaluation of Athlete’s Heart. *Echocardiography*, 29 (8): 943–949. doi:10.1111/j.1540-8175.2012.01719.x.
- Gaddum, N.R., Alastruey, J., Beerbaum, P., et al. (2013) A Technical Assessment of Pulse Wave Velocity Algorithms Applied to Non-invasive Arterial Waveforms. *Ann Biomed Eng*, 41 (12): 2617–2629. doi:10.1007/s10439-013-0854-y.
- Galie, N., Humbert, M., Vachiery, J.-L., et al. (2016) 2015 ESC/ERS Guidelines for the diagnosis and treatment of pulmonary hypertension: The Joint Task Force for the Diagnosis and Treatment of Pulmonary Hypertension of the European Society of Cardiology (ESC) and

the European Respiratory Society (ERS): Endor. *European heart journal*, 37 (1): 67–119. doi:10.1093/eurheartj/ehv317.

Gandhi, S.K., Reyes, J., Webber, S.A., et al. (2002) Case report of combined pediatric heart-lung-liver transplantation. *Transplantation*. doi:10.1097/00007890-200206270-00024.

Gersh, B.J., Maron, B.J., Bonow, R.O., et al. (2011) 2011 ACCF/AHA Guideline for the Diagnosis and Treatment of Hypertrophic Cardiomyopathy: Executive Summary. *J Am Coll Cardiol*, 58 (25): 2703–2738. doi:10.1016/j.jacc.2011.10.825.

Giannakudis, J., Röpke, A., Kujat, A., et al. (2001) Parental mosaicism of JAG1 mutations in families with Alagille syndrome. *Eur J Hum Genet*, 9 (3): 209–216. doi:10.1038/sj.ejhg.5200613.

Ginami, G., Neji, R., Rashid, I., et al. (2017) 3D whole-heart phase sensitive inversion recovery CMR for simultaneous black-blood late gadolinium enhancement and bright-blood coronary CMR angiography. *J Cardiovasc Magn Reson*, 19 (1). doi:10.1186/s12968-017-0405-z.

Giulia Gagliardi, M., Crea, F., Polletta, B., et al. (2001) Coronary microvascular endothelial dysfunction in transplanted children. *European Heart Journal*, 22 (3): 254–260. doi:10.1053/euhj.2001.2105.

Gomez, A., Bialostozky, D., Zajarias, A., et al. (2001) Right ventricular ischemia in patients with primary pulmonary hypertension. *J Am Coll Cardiol*, 38 (4): 1137–1142.

Gorman, M.W., Tune, J.D., Richmond, K.N., et al. (2000) Feedforward sympathetic coronary vasodilation in exercising dogs. *J Appl Physiol*, 89 (5): 1892–1902. doi:10.1152/jappl.2000.89.5.1892.

Gorman, M.W. and Feigl, E.O. (2012) Control of Coronary Blood Flow During Exercise. *Exerc Sport Sci Rev*, 40 (1): 37–42. doi:10.1097/JES.0b013e3182348cdd.

Gottrand, F., Clavey, V., Fruchart, J.C., et al. (1995) Lipoprotein pattern and plasma lecithin cholesterol acyl transferase activity in children with Alagille syndrome. *Atherosclerosis*, 115 (2): 233–41.

Gould, K.L., Lipscomb, K. and Hamilton, G.W. (1974) Physiologic basis for assessing critical coronary stenosis. *The American Journal of Cardiology*, 33 (1): 87–94. doi:10.1016/0002-9149(74)90743-7.

Gould, K.L. and Johnson, N.P. (2018) Coronary Physiology Beyond Coronary Flow Reserve in Microvascular Angina. *Journal of the American College of Cardiology*, 72 (21): 2642–2662. doi:10.1016/j.jacc.2018.07.106.

Greil, G.F., Powell, A.J., Gildein, H.P., et al. (2002) Gadolinium-enhanced three-dimensional magnetic resonance angiography of pulmonary and systemic venous anomalies.

Journal of the American College of Cardiology, 39 (2): 335–341. doi:10.1016/S0735-1097(01)01730-2.

Greiner, S., Jud, A., Aurich, M., et al. (2014) Reliability of noninvasive assessment of systolic pulmonary artery pressure by doppler echocardiography compared to right heart catheterization: Analysis in a large patient population. *Journal of the American Heart Association*, 3 (4). doi:10.1161/JAHA.114.001103.

Greyson, C.R. (2008) Pathophysiology of right ventricular failure: *Critical Care Medicine*, 36 (Suppl): S57–S65. doi:10.1097/01.CCM.0000296265.52518.70.

Greyson, C.R. (2010) The right ventricle and pulmonary circulation: basic concepts. *Revista Espanola De Cardiologia*, 63 (1): 81–95.

Grotenhuis, H.B., Westenberg, J.J.M., Steendijk, P., et al. (2009) Validation and reproducibility of aortic pulse wave velocity as assessed with velocity-encoded MRI. *J Magn Reson Imaging*, 30 (3): 521–526. doi:10.1002/jmri.21886.

Grothues, F., Smith, G.C., Moon, J.C.C., et al. (2002) Comparison of interstudy reproducibility of cardiovascular magnetic resonance with two-dimensional echocardiography in normal subjects and in patients with heart failure or left ventricular hypertrophy. *Am J Cardiol*, 90 (1): 29–34.

Gurney, P.T., Yang, P.C., Hargreaves, B.A., et al. (2007) Direct Respiratory Tracking and Motion Correction for Free-Breathing Whole-Heart Coronary Angiography. *Proc Intl Soc Mag Reson Med*, 1 (15): 871.

Habibi, M., Chahal, H., Opdahl, A., et al. (2014) Association of CMR-Measured LA Function With Heart Failure Development. *JACC Cardiovasc Imaging*, 7 (6): 570–579. doi:10.1016/j.jcmg.2014.01.016.

Habibi, M., Lima, J.A.C., Khurram, I.M., et al. (2015) Association of Left Atrial Function and Left Atrial Enhancement in Patients With Atrial Fibrillation: Cardiac Magnetic Resonance Study. *Circ Cardiovasc Imaging*, 8 (2): e002769. doi:10.1161/CIRCIMAGING.114.002769.

Haddad, F., Ashley, E. and Michelakis, E.D. (2010) New insights for the diagnosis and management of right ventricular failure, from molecular imaging to targeted right ventricular therapy. *Current Opinion in Cardiology*. doi:10.1097/HCO.0b013e328335febd.

Harloff, A., Mirzaee, H., Lodemann, T., et al. (2018) Determination of aortic stiffness using 4D flow cardiovascular magnetic resonance - a population-based study. *J Cardiovasc Magn Reson*, 20 (1): 43. doi:10.1186/s12968-018-0461-z.

Harvey, A., Montezano, A.C. and Touyz, R.M. (2015) Vascular biology of ageing—Implications in hypertension. *J Mol Cell Cardio*, 83: 112–121. doi:10.1016/j.yjmcc.2015.04.011.

Hayward, C.S., Adji, A. and O'Rourke, M.F. (2018) Arterial stiffening and arterial dilation as heritable traits caused by defective vital rubber? *Eur Heart J*, 39 (24): 2289–2290. doi:10.1093/eurheartj/ehy231.

Hazirolan, T., Gupta, S.N., Mohamed, M.A., et al. (2005) Reproducibility of black-blood coronary vessel wall MR imaging. *J Cardiovasc Magn Reson*, 7 (2): 409–413.

He, M.-X. and Downey, H.F. (1998) Downregulation of ventricular contractile function during early ischemia is flow but not pressure dependent. *American Journal of Physiology-Heart and Circulatory Physiology*, 275 (5): H1520–H1523. doi:10.1152/ajpheart.1998.275.5.H1520.

He, Y., Pang, J., Dai, Q., et al. (2016) Diagnostic Performance of Self-navigated Whole-Heart Contrast-enhanced Coronary 3-T MR Angiography. *Radiology*, 283 (3): 923. doi:10.1148/radiol.2016152514.

Heineman, F.W. and Grayson, J. (1985) Transmural distribution of intramyocardial pressure measured by micropipette technique. *Am J Physiol*, 249 (6 Pt 2): H1216–1223. doi:10.1152/ajpheart.1985.249.6.H1216.

Henningsson, M., Koken, P., Stehning, C., et al. (2012) Whole-heart coronary MR angiography with 2D self-navigated image reconstruction. *Magn Reson Med*, 67 (2): 437–45. doi:10.1002/mrm.23027.

Henningsson, M., Prieto, C., Chiribiri, A., et al. (2014) Whole-heart coronary MRA with 3D affine motion correction using 3D image-based navigation. *Magnetic Resonance in Medicine*. doi:10.1002/mrm.24652.

Henningsson, M., Hussain, T., Vieira, M.S., et al. (2016) Whole-heart coronary MR angiography using image-based navigation for the detection of coronary anomalies in adult patients with congenital heart disease. *J Magn Reson Imaging*, 43 (4): 947–55. doi:10.1002/jmri.25058.

Henningsson, M., Shome, J., Bratis, K., et al. (2017) Diagnostic performance of image navigated coronary CMR angiography in patients with coronary artery disease. *J Cardiovasc Magn Reson*, 19 (1): 68. doi:10.1186/s12968-017-0381-3.

Henningsson, M., Smink, J., Razavi, R., et al. (2013) Prospective respiratory motion correction for coronary MR angiography using a 2D image navigator. *Magn Reson Med*, 69 (2): 486–494. doi:10.1002/mrm.24280.

Henningsson, M., Smink, J., van Ensbergen, G., et al. (2018) Coronary MR angiography using image-based respiratory motion compensation with inline correction and fixed gating efficiency. *Magn Reson Med*, 79 (1): 416–422. doi:10.1002/mrm.26678.

Heusch, G. (1990) Alpha-adrenergic mechanisms in myocardial ischemia. *Circulation*, 81 (1): 1–13.

- Heusch, G. (2011) The paradox of α -adrenergic coronary vasoconstriction revisited. *J Mol Cell Cardiol*, 51 (1): 16–23. doi:10.1016/j.yjmcc.2011.03.007.
- Hilmi, I., Horton, C.N., Planinsic, R.M., et al. (2008) The impact of postreperfusion syndrome on short-term patient and liver allograft outcome in patients undergoing orthotopic liver transplantation. *Liver Transpl*, 14 (4): 504–8. doi:10.1002/lt.21381.
- Hinojar, R., Varma, N., Child, N., et al. (2015) T1 Mapping in Discrimination of Hypertrophic Phenotypes: Hypertensive Heart Disease and Hypertrophic Cardiomyopathy: Findings From the International T1 Multicenter Cardiovascular Magnetic Resonance Study. *Circ Cardiovasc Imaging*, 8 (12): pii: e003285. doi:10.1161/CIRCIMAGING.115.003285.
- Ho, C.Y. (2009) Hypertrophic Cardiomyopathy: Preclinical and Early Phenotype. *J Cardiovasc Transl Res*, 2 (4): 462–470. doi:10.1007/s12265-009-9124-7.
- Ho, C.Y., Carlsen, C., Thune, J.J., et al. (2009) Echocardiographic Strain Imaging to Assess Early and Late Consequences of Sarcomere Mutations in Hypertrophic Cardiomyopathy. *Circ Cardiovasc Genet*, 2 (4): 314–321. doi:10.1161/CIRCGENETICS.109.862128.
- Ho, C.Y., López, B., Coelho-Filho, O.R., et al. (2010) Myocardial Fibrosis as an Early Manifestation of Hypertrophic Cardiomyopathy. *N Engl J Med*, 363 (6): 552–563. doi:10.1056/NEJMoa1002659.
- Hoffenberg, E.J., Narkewicz, M.R., Sondheimer, J.M., et al. (1995) Outcome of syndromic paucity of interlobular bile ducts (Alagille syndrome) with onset of cholestasis in infancy. *J Pediatr*, 127 (2): 220–4. doi:10.1016/S0022-3476(95)70298-9.
- Hoffman, J.I. and Spaan, J.A. (1990) Pressure-flow relations in coronary circulation. *Physiol Rev*, 70 (2): 331–390. doi:10.1152/physrev.1990.70.2.331.
- Hoit, B.D. and Gabel, M. (2000) Influence of left ventricular dysfunction on the role of atrial contraction: an echocardiographic-hemodynamic study in dogs. *J Am Coll Cardiol*, 36 (5): 1713–1719.
- Hoit, B.D. (2014) Left atrial size and function: role in prognosis. *J Am Coll Cardiol*, 63 (6): 493–505. doi:10.1016/j.jacc.2013.10.055.
- Holland, A.E., Goldfarb, J.W. and Edelman, R.R. (1998) Diaphragmatic and cardiac motion during suspended breathing: preliminary experience and implications for breath-hold MR imaging. *Radiology*, 209 (2): 483–489. doi:10.1148/radiology.209.2.9807578.
- Hsia, T.-Y., Cosentino, D., Corsini, C., et al. (2011) Use of Mathematical Modeling to Compare and Predict Hemodynamic Effects Between Hybrid and Surgical Norwood Palliations for Hypoplastic Left Heart Syndrome. *Circulation*, 124 (11_suppl_1): S204–S210. doi:10.1161/CIRCULATIONAHA.110.010769.

- Hsu, S., Houston, B.A., Tampakakis, E., et al. (2016) Right ventricular functional reserve in pulmonary arterial hypertension. *Circulation*, 133 (24): 13–22. doi:10.1161/CIRCULATIONAHA.116.022082.
- Hu, P., Chan, J., Ngo, L.H., et al. (2011) Contrast-enhanced whole-heart coronary MRI with bolus infusion of gadobenate dimeglumine at 1.5 T. *Magn Reson Med*, 65 (2): 392–398. doi:10.1002/mrm.22706.
- Huber, M.E., Paetsch, I., Schnackenburg, B., et al. (2003) Performance of a new gadolinium-based intravascular contrast agent in free-breathing inversion-recovery 3D coronary MRA. *Magn Reson Med*, 49 (1): 115–121. doi:10.1002/mrm.10350.
- Hudsmith, L.E., Cheng, A.S.H., Tyler, D.J., et al. (2007) Assessment of left atrial volumes at 1.5 Tesla and 3 Tesla using FLASH and SSFP cine imaging. *J Cardiovasc Magn Reson*, 9 (4): 673–679. doi:10.1080/10976640601138805.
- Hussain, T., Lossnitzer, D., Bellsham-Revell, H., et al. (2012) Three-dimensional Dual-Phase Whole-Heart MR Imaging: Clinical Implications for Congenital Heart Disease. *Radiology*, 263 (2): 547–54. doi:10.1148/radiol.12111700.
- Ingles, J., Burns, C., Barratt, A., et al. (2015) Application of Genetic Testing in Hypertrophic Cardiomyopathy for Preclinical Disease Detection. *Circ Cardiovasc Genet*, 8 (6): 852–859. doi:10.1161/CIRCGENETICS.115.001093.
- Inuzuka, R., Seki, M., Sugimoto, M., et al. (2013) Pulmonary Arterial Wall Stiffness and Its Impact on Right Ventricular Afterload in Patients With Repaired Tetralogy of Fallot. *Ann Thorac Surg*, 96 (4): 1435–1441. doi:10.1016/j.athoracsur.2013.05.085.
- Jahnke, C., Paetsch, I., Nehrke, K., et al. (2005) A new approach for rapid assessment of the cardiac rest period for coronary MRA. *J Cardiovasc Magn Reson*, 7 (2): 395–399. doi:10.1081/jcmr-200053616.
- Jahnke, C., Paetsch, I., Achenbach, S., et al. (2006) Coronary MR imaging: breath-hold capability and patterns, coronary artery rest periods, and beta-blocker use. *Radiology*, 239 (1): 71–78. doi:10.1148/radiol.2383042019.
- Janda, S., Shahidi, N., Gin, K., et al. (2011) Diagnostic accuracy of echocardiography for pulmonary hypertension: a systematic review and meta-analysis. *Heart (British Cardiac Society)*, 97 (8): 612–622. doi:10.1136/hrt.2010.212084.
- Johnson, R.K., Premraj, S., Patel, S.S., et al. (2010) Automated analysis of four-dimensional magnetic resonance images of the human aorta. *Int J Cardiovasc Imaging*, 26 (5): 571–578. doi:10.1007/s10554-010-9592-5.
- Jones, C.J., Kuo, L., Davis, M.J., et al. (1995) Regulation of coronary blood flow: coordination of heterogeneous control mechanisms in vascular microdomains. *Cardiovasc Res*, 29 (5): 585–596.

Kamath, B.M., Bason, L., Piccoli, D.A., et al. (2003) Consequences of JAG1 mutations. *J Med Genet*, 40 (12): 891–895. doi:10.1136/jmg.40.12.891.

Kamath, B.M., Spinner, N.B., Emerick, K.M., et al. (2004) Vascular anomalies in Alagille syndrome: a significant cause of morbidity and mortality. *Circulation*, 109 (11): 1354–1358. doi:10.1161/01.CIR.0000121361.01862.A4.

Kamath, B.M., Loomes, K.M. and Piccoli, D.A. (2010a) Medical management of alagille syndrome. *Journal of Pediatric Gastroenterology and Nutrition*. doi:10.1097/MPG.0b013e3181d98ea8.

Kamath, B.M., Munoz, P.S., Bab, N., et al. (2010b) A longitudinal study to identify laboratory predictors of liver disease outcome in alagille syndrome. *J Pediatr Gastroenterol Nutr*, 50 (5): 526–30. doi:10.1097/MPG.0b013e3181cea48d.

Kamath, B.M., Schwarz, K.B. and Hadzić, N. (2010c) Alagille syndrome and liver transplantation. *J Pediatr Gastroenterol Nutr*, 50 (1): 11–5. doi:10.1097/MPG.0b013e3181c1601f.

Kamath, B.M., Podkameni, G., Hutchinson, A.L., et al. (2012a) Renal anomalies in Alagille syndrome: A disease-defining feature. *Am J Med Genet A*, 158A (1): 85–9. doi:10.1002/ajmg.a.34369.

Kamath, B.M., Yin, W., Miller, H., et al. (2012b) Outcomes of liver transplantation for patients with Alagille syndrome: the studies of pediatric liver transplantation experience. *Liver Transpl*, 18 (8): 940–948. doi:10.1002/lt.23437.

Kamath, B.M., Baker, A., Houwen, R., et al. (2018) Systematic Review: the Epidemiology, Natural History and Burden of Alagille Syndrome. *J Pediatr Gastroenterol Nutr*, 67 (2): 148–156. doi:10.1097/MPG.0000000000001958.

Kamath, B.M. and Loomes, K.M. (eds.) (2018) *Alagille Syndrome: Pathogenesis and Clinical Management*. Cham: Springer International Publishing. doi:10.1007/978-3-319-94571-2.

Kato, S., Kitagawa, K., Ishida, N., et al. (2010) Assessment of coronary artery disease using magnetic resonance coronary angiography: A national multicenter trial. *J Am Coll Cardiol*, 56 (12): 983–91. doi:10.1016/j.jacc.2010.01.071.

Kawaji, K., Spincemille, P., Nguyen, T.D., et al. (2014) Direct coronary motion extraction from a 2D fat image navigator for prospectively gated coronary MR angiography: Real-Time 2D Coronary Motion Extraction for Prospective CMRA. *Magnetic Resonance in Medicine*, 71 (2): 599–607. doi:10.1002/mrm.24698.

Keegan, J., Gatehouse, P., Yang, G.-Z., et al. (2002) Coronary artery motion with the respiratory cycle during breath-holding and free-breathing: implications for slice-followed coronary artery imaging. *Magn Reson Med*, 47 (3): 476–481.

Kellenberger, C.J., Yoo, S.-J. and Büchel, E.R.V. (2007) Cardiovascular MR Imaging in Neonates and Infants with Congenital Heart Disease. *RadioGraphics*, 27 (1): 5–18. doi:10.1148/rg.271065027.

Kilner, P.J., Geva, T., Kaemmerer, H., et al. (2010) Recommendations for cardiovascular magnetic resonance in adults with congenital heart disease from the respective working groups of the European Society of Cardiology. *Eur Heart J*, 31 (7): 794–805. doi:10.1093/eurheartj/ehp586.

Kim, H.J., Jansen, K.E. and Taylor, C.A. (2010) Incorporating Autoregulatory Mechanisms of the Cardiovascular System in Three-Dimensional Finite Element Models of Arterial Blood Flow. *Ann Biomed Eng*, 38 (7): 2314–2330. doi:10.1007/s10439-010-9992-7.

Kim, W.Y., Danias, P.G., Stuber, M., et al. (2001) Coronary magnetic resonance angiography for the detection of coronary stenoses. *N Engl J Med*, 345 (26): 1863–1869. doi:10.1056/NEJMoa010866.

King, J.B., Azadani, P.N., Suksaranjit, P., et al. (2017) Left Atrial Fibrosis and Risk of Cerebrovascular and Cardiovascular Events in Patients With Atrial Fibrillation. *J Am Coll Cardiol*, 70 (11): 1311–1321. doi:10.1016/j.jacc.2017.07.758.

Klabunde, R. (2011) *Cardiovascular Physiology Concepts*. 2nd ed. Lippincott Williams & Wilkins. (Google-Books-ID: 27ExgvGnOagC).

Klein, C., Gebker, R., Kokocinski, T., et al. (2008) Combined magnetic resonance coronary artery imaging, myocardial perfusion and late gadolinium enhancement in patients with suspected coronary artery disease. *J Cardiovasc Magn Reson*, 10 (1): 45. doi:10.1186/1532-429X-10-45.

von Knobelsdorff-Brenkenhoff, F. and Schulz-Menger, J. (2012) Cardiovascular magnetic resonance imaging in ischemic heart disease. *J Magn Reson Imaging*, 36 (1): 20–38. doi:10.1002/jmri.23580.

von Knobelsdorff-Brenkenhoff, F. and Schulz-Menger, J. (2015) Role of cardiovascular magnetic resonance in the guidelines of the European Society of Cardiology. *J Cardiovasc Magn Reson*, 18 (1): 6. doi:10.1186/s12968-016-0225-6.

Kowallick, J.T., Kutty, S., Edelmann, F., et al. (2014) Quantification of left atrial strain and strain rate using Cardiovascular Magnetic Resonance myocardial feature tracking: a feasibility study. *J Cardiovasc Magn Reson*, 16 (60). doi:10.1186/s12968-014-0060-6.

Kowallick, J.T., Morton, G., Lamata, P., et al. (2015) Quantification of atrial dynamics using cardiovascular magnetic resonance: inter-study reproducibility. *J Cardiovasc Magn Reson*, 17 (1): 36. doi:10.1186/s12968-015-0140-2.

Kowallick, J.T., Silva Vieira, M., Kutty, S., et al. (2017) Left Atrial Performance in the Course of Hypertrophic Cardiomyopathy: Relation to Left Ventricular Hypertrophy and Fibrosis. *Invest Radiol*, 52 (3): 177–185. doi:10.1097/RLI.0000000000000326.

- Kozlik-Feldmann, R., Hansmann, G., Bonnet, D., et al. (2016) Pulmonary hypertension in children with congenital heart disease (PAH-CHD, PPHVD-CHD). Expert consensus statement on the diagnosis and treatment of paediatric pulmonary hypertension. The European Paediatric Pulmonary Vascular Disease Network, endorsed by ISHLT and DGPK. *Heart*, 102 (Suppl 2): ii42–ii48. doi:10.1136/heartjnl-2015-308378.
- Kramer, C.M., Barkhausen, J., Flamm, S.D., et al. (2013) Standardized cardiovascular magnetic resonance (CMR) protocols 2013 update. *J Cardiovasc Magn Reson*, 15 (1): 91. doi:10.1186/1532-429X-15-91.
- Krissian, K., Carreira, J.M., Esclarin, J., et al. (2014) Semi-automatic segmentation and detection of aorta dissection wall in MDCT angiography. *Med Image Anal*, 18 (1): 83–102. doi:10.1016/j.media.2013.09.004.
- Krowka, M.J., Fallon, M.B., Kawut, S.M., et al. (2016) International liver transplant society practice guidelines: Diagnosis and management of hepatopulmonary syndrome and portopulmonary hypertension. *Transplantation*. doi:10.1097/TP.0000000000001229.
- Kruk, M., Noll, D., Achenbach, S., et al. (2014) Impact of Coronary Artery Calcium Characteristics on Accuracy of CT Angiography. *JACC: Cardiovascular Imaging*, 7 (1): 49–58. doi:10.1016/j.jcmg.2013.07.013.
- Lai, P., Larson, A.C., Bi, X., et al. (2008) A dual-projection respiratory self-gating technique for whole-heart coronary MRA. *J Magn Reson Imaging*, 28 (3): 612–620. doi:10.1002/jmri.21479.
- Landis, J.R. and Koch, G.G. (1977) The measurement of observer agreement for categorical data. *Biometrics*, 33 (1): 159–174.
- Lang, R., Badano, L.P., Mor-Avi, V., et al. (2016) Recommendations for Cardiac Chamber Quantification by Echocardiography in Adults: An Update from the American Society of Echocardiography and the European Association of, Cardiovascular Imaging. *Eur Heart J Cardiovasc Imaging*, 17 (4): 412–412. doi:10.1093/ehjci/jew041.
- Lau, K.D. and Figueroa, C.A. (2015) Simulation of short-term pressure regulation during the tilt test in a coupled 3D–0D closed-loop model of the circulation. *Biomech Model Mechanobiol*, 14 (4): 915–929. doi:10.1007/s10237-014-0645-x.
- Laurent, S., Cockcroft, J., Van Bortel, L., et al. (2006) Expert consensus document on arterial stiffness: methodological issues and clinical applications. *Eur Heart J*, 27 (21): 2588–2605. doi:10.1093/eurheartj/ehl254.
- Lazar, J.M., Flores, A.R., Grandis, D.J., et al. (1993) Effects of chronic right ventricular pressure overload on left ventricular diastolic function. *The American journal of cardiology*, 72 (15): 1179–1182.

- Lee, C.-N., Tiao, M.-M., Chen, H.-J., et al. (2013) Characteristics and Outcome of Liver Transplantation in Children with Alagille Syndrome: A Single-Center Experience. *Pediatrics and neonatology*. doi:10.1016/j.pedneo.2013.09.001.
- Lee, R.T. and Kamm, R.D. (1994) Vascular mechanics for the cardiologist. *J Am Coll Cardiol*, 23 (6): 1289–1295.
- Leiner, T., Katsimaglis, G., Yeh, E.N., et al. (2005) Correction for heart rate variability improves coronary magnetic resonance angiography. *Journal of magnetic resonance imaging: JMRI*, 22 (4): 577–582. doi:10.1002/jmri.20399.
- Leonard, L.D., Chao, G., Baker, A., et al. (2014) Clinical utility gene card for: Alagille Syndrome (ALGS). *Eur J Hum Genet*, 22 (3). doi:10.1038/ejhg.2013.140.
- Lesage, D., Angelini, E.D., Bloch, I., et al. (2009) A review of 3D vessel lumen segmentation techniques: Models, features and extraction schemes. *Med Image Anal*, 13 (6): 819–845. doi:10.1016/j.media.2009.07.011.
- Li, D., Haacke, E.M., Shelton, M.E., et al. (1995) Magnetic resonance imaging of coronary arteries. *Coron Artery Dis*, 6 (5): 368–376.
- Li, L., Krantz, I.D., Deng, Y., et al. (1997) Alagille syndrome is caused by mutations in human Jagged1, which encodes a ligand for Notch1. *Nat Genet*, 16 (3): 243–51. doi:10.1038/ng0797-243.
- Lieberman, J.M., Botti, R.E. and Nelson, A.D. (1984) Magnetic resonance imaging of the heart. *Radiol Clin North Am*, 22 (4): 847–858.
- Lim, D.S., Roberts, R. and Marian, A.J. (2001) Expression profiling of cardiac genes in human hypertrophic cardiomyopathy: insight into the pathogenesis of phenotypes. *J Am Coll Cardiol*, 38 (4): 1175–1180.
- Lindsell, C.E., Shawber, C.J., Boulter, J., et al. (1995) Jagged: A mammalian ligand that activates Notch1. *Cell*, 80 (60): 909–17. doi:10.1016/0092-8674(95)90294-5.
- Lobregt, S. and Viergever, M.A. (1995) A discrete dynamic contour model. *IEEE Trans Med Imaging*, 14 (1): 12–24. doi:10.1109/42.370398.
- Look, D.C. and Locker, D.R. (1970) Time Saving in Measurement of NMR and EPR Relaxation Times. *Rev Sci Instrum*, 41 (2): 250–251. doi:10.1063/1.1684482.
- Lowensohn, H.S., Khouri, E.M., Gregg, D.E., et al. (1976) Phasic right coronary artery blood flow in conscious dogs with normal and elevated right ventricular pressures. *Circ Res*, 39 (6): 760–766. doi:10.1161/01.RES.39.6.760.
- Luo, J., Addy, N.O., Ingle, R.R., et al. (2017) Nonrigid Motion Correction With 3D Image-Based Navigators for Coronary MR Angiography: Nonrigid Motion Correction for Coronary MRA. *Magnetic Resonance in Medicine*, 77 (5): 1884–1893. doi:10.1002/mrm.26273.

Lykavieris, P., Hadchouel, M., Chardot, C., et al. (2001) Outcome of liver disease in children with Alagille syndrome: A study of 163 patients. *Gut*, 49 (3): 431–5. doi:10.1136/gut.49.3.431.

Maintz, D., Aepfelbacher, F.C., Kissinger, K.V., et al. (2004) Coronary MR angiography: comparison of quantitative and qualitative data from four techniques. *AJR. American journal of roentgenology*, 182 (2): 515–521. doi:10.2214/ajr.182.2.1820515.

Makowski, M.R., Wiethoff, A.J., Uribe, S., et al. (2011) Congenital Heart Disease: Cardiovascular MR Imaging by Using an Intravascular Blood Pool Contrast Agent. *Radiology*, 260 (3): 680–688. doi:10.1148/radiol.11102327.

Manes, A., Palazzini, M., Leci, E., et al. (2014) Current era survival of patients with pulmonary arterial hypertension associated with congenital heart disease: A comparison between clinical subgroups. *Eur Heart J*, 35 (11): 716–24. doi:10.1093/eurheartj/ehf072.

Manning, W.J. and Edelman, R.R. (1993) Magnetic resonance coronary angiography. *Magnetic Resonance Quarterly*, 9 (3): 131–151.

Manning, W.J., Li, W. and Edelman, R.R. (1993) A preliminary report comparing magnetic resonance coronary angiography with conventional angiography. *The New England Journal of Medicine*, 328 (12): 828–832. doi:10.1056/NEJM199303253281202.

Maresca, D., Correia, M., Villemain, O., et al. (2018) Noninvasive Imaging of the Coronary Vasculature Using Ultrafast Ultrasound. *JACC: Cardiovascular Imaging*, 11 (6): 798–808. doi:10.1016/j.jcmg.2017.05.021.

Marino, I.R., ChapChap, P., Esquivel, C.O., et al. (1992) Liver transplantation for arteriohepatic dysplasia (Alagille's syndrome). *Transpl Int*, 5 (2): 61–4. doi:10.1007/BF00339217.

Mark, A.L., Abboud, F.M., Schmid, P.G., et al. (1972) Differences in direct effects of adrenergic stimuli on coronary, cutaneous, and muscular vessels. *J Clin Invest*, 51 (2): 279–287. doi:10.1172/JCI106812.

Markl, M., Wallis, W., Brendecke, S., et al. (2010) Estimation of global aortic pulse wave velocity by flow-sensitive 4D MRI. *Magn Reson Med*, 63 (6): 1575–1582. doi:10.1002/mrm.22353.

Markl, M., Wallis, W., Strecker, C., et al. (2012) Analysis of pulse wave velocity in the thoracic aorta by flow-sensitive four-dimensional MRI: Reproducibility and correlation with characteristics in patients with aortic atherosclerosis. *J Magn Reson Imaging*, 35 (5): 1162–1168. doi:10.1002/jmri.22856.

Maron, B.J., Mathenge, R., Casey, S.A., et al. (1999) Clinical profile of hypertrophic cardiomyopathy identified de novo in rural communities. *J Am Coll Cardiol*, 33 (6): 1590–1595.

Maron, B.J. and Maron, M.S. (2013) Hypertrophic cardiomyopathy. *The Lancet*, 381 (9862): 242–255. doi:10.1016/S0140-6736(12)60397-3.

Maron, B.J., Haas, T.S., Maron, M.S., et al. (2014) Left Atrial Remodeling in Hypertrophic Cardiomyopathy and Susceptibility Markers for Atrial Fibrillation Identified by Cardiovascular Magnetic Resonance. *Am J Cardiol*, 113 (8): 1394–1400. doi:10.1016/j.amjcard.2013.12.045.

Maron, M.S. (2012) Clinical Utility of Cardiovascular Magnetic Resonance in Hypertrophic Cardiomyopathy. *J Am Coll Cardiol*, 14 (1): 13. doi:10.1186/1532-429X-14-13.

Marsden, A.L. and Esmaily-Moghadam, M. (2015) Multiscale Modeling of Cardiovascular Flows for Clinical Decision Support. *Applied Mechanics Reviews*, 67 (3): 030804. doi:10.1115/1.4029909.

Mayrovitz, H.N. and Roy, J. (1983) Microvascular blood flow: evidence indicating a cubic dependence on arteriolar diameter. *Am J Physiol*, 245 (6): H1031-1038. doi:10.1152/ajpheart.1983.245.6.H1031.

Maznyczka, A., Sen, S., Cook, C., et al. (2015) The ischaemic constellation: an alternative to the ischaemic cascade—implications for the validation of new ischaemic tests. *Open Heart*, 2 (1): e000178. doi:10.1136/openhrt-2014-000178.

McConnell, M.V., Khasgiwala, V.C., Savord, B.J., et al. (1997) Comparison of respiratory suppression methods and navigator locations for MR coronary angiography. *AJR. American journal of roentgenology*, 168 (5): 1369–1375. doi:10.2214/ajr.168.5.9129447.

McDaniell, R., Warthen, D.M., Sanchez-Lara, P.A., et al. (2006) NOTCH2 Mutations Cause Alagille Syndrome, a Heterogeneous Disorder of the Notch Signaling Pathway. *Am J Hum Genet*, 79 (1): 169–73. doi:10.1086/505332.

McEniery, C.M., Yasmin, Hall, I.R., et al. (2005) Normal vascular aging: Differential effects on wave reflection and aortic pulse wave velocity - The Anglo-Cardiff Collaborative Trial (ACCT). *Journal of the American College of Cardiology*. doi:10.1016/j.jacc.2005.07.037.

Melenovsky, V., Borlaug, B.A., Rosen, B., et al. (2007) Cardiovascular features of heart failure with preserved ejection fraction versus nonfailing hypertensive left ventricular hypertrophy in the urban Baltimore community: the role of atrial remodeling/dysfunction. *J Am Coll Cardiol*, 49 (2): 198–207. doi:10.1016/j.jacc.2006.08.050.

Merkx, M.A.G., Bescós, J.O., Geerts, L., et al. (2012) Accuracy and precision of vessel area assessment: Manual versus automatic lumen delineation based on full-width at half-maximum. *J Magn Reson Imaging*, 36 (5): 1186–1193. doi:10.1002/jmri.23752.

Messroghli, D.R., Moon, J.C., Ferreira, V.M., et al. (2017) Clinical recommendations for cardiovascular magnetic resonance mapping of T1, T2, T2* and extracellular volume: A consensus statement by the Society for Cardiovascular Magnetic Resonance (SCMR)

endorsed by the European Association for Cardiovascular Imaging (EACVI). *J Cardiovasc Magn Reson*, 19 (1): 75. doi:10.1186/s12968-017-0389-8.

Migliavacca, F., Dubini, G. and de Leval, M. (2000) Computational fluid dynamics in paediatric cardiac surgery. *Images in Paediatric Cardiology*, 2 (1): 11–25.

Migliavacca, F. and Dubini, G. (2005) Computational modeling of vascular anastomoses. *Biomechanics and Modeling in Mechanobiology*, 3 (4): 235–250. doi:10.1007/s10237-005-0070-2.

Miyashiro, J.K. and Feigl, E.O. (1995) A model of combined feedforward and feedback control of coronary blood flow. *Am J Physiol*, 268 (2 Pt 2): H895-908. doi:10.1152/ajpheart.1995.268.2.H895.

Miyoshi, H., Mizuguchi, Y., Oishi, Y., et al. (2011) Early detection of abnormal left atrial-left ventricular-arterial coupling in preclinical patients with cardiovascular risk factors: evaluation by two-dimensional speckle-tracking echocardiography. *Eur J Echocardiogr*, 12 (6): 431–439. doi:10.1093/ejechocard/jer052.

Moghari, M.H., Hu, P., Kissinger, K.V., et al. (2012) Subject-specific estimation of respiratory navigator tracking factor for free-breathing cardiovascular MR. *Magnetic Resonance in Medicine*, 67 (6): 1665–1672. doi:10.1002/mrm.23158.

Moghari, M.H., Roujol, S., Henningsson, M., et al. (2014) Three-dimensional heart locator for whole-heart coronary magnetic resonance angiography. *Magn Reson Med*, 71 (6): 2118–26. doi:10.1002/mrm.24881.

Mohiaddin, R.H., Firmin, D.N. and Longmore, D.B. (1993) Age-related changes of human aortic flow wave velocity measured noninvasively by magnetic resonance imaging. *Journal of Applied Physiology*. doi:10.1007/s00330-006-0309-z.

Monge, M.C., Mainwaring, R.D., Sheikh, A.Y., et al. (2013) Surgical reconstruction of peripheral pulmonary artery stenosis in Williams and Alagille syndromes. *The Journal of Thoracic and Cardiovascular Surgery*, 145 (2): 476–481. doi:10.1016/j.jtcvs.2012.09.102.

Monney, P., Piccini, D., Rutz, T., et al. (2015) Single centre experience of the application of self navigated 3D whole heart cardiovascular magnetic resonance for the assessment of cardiac anatomy in congenital heart disease. *Journal of cardiovascular magnetic resonance : official journal of the Society for Cardiovascular Magnetic Resonance*. doi:10.1186/s12968-015-0156-7.

Moon, J.C., Messroghli, D.R., Kellman, P., et al. (2013) Myocardial T1 mapping and extracellular volume quantification: a Society for Cardiovascular Magnetic Resonance (SCMR) and CMR Working Group of the European Society of Cardiology consensus statement. *J Cardiovasc Magn Reson*, 15 (1): 92. doi:10.1186/1532-429X-15-92.

Moyé, D.M., Hussain, T., Botnar, R.M., et al. (2018) Dual-phase whole-heart imaging using image navigation in congenital heart disease. *BMC Medical Imaging*, 18 (1): 36. doi:10.1186/s12880-018-0278-0.

Murali, S., Kormos, R.L., Uretsky, B.F., et al. (1993) Preoperative pulmonary hemodynamics and early mortality after orthotopic cardiac transplantation: the Pittsburgh experience. *American Heart Journal*, 126 (4): 896–904. doi:10.1016/0002-8703(93)90704-d.

Muthurangu, V., Taylor, A., Andriantsimiavona, R., et al. (2004) Novel method of quantifying pulmonary vascular resistance by use of simultaneous invasive pressure monitoring and phase-contrast magnetic resonance flow. *Circulation*, 110 (7): 826–34. doi:10.1161/01.CIR.0000138741.72946.84.

Muzik, O., Paridon, S.M., Singh, T.P., et al. (1996) Quantification of myocardial blood flow and flow reserve in children with a history of Kawasaki disease and normal coronary arteries using positron emission tomography. *J Am Coll Cardiol*, 28 (3): 757–762.

Mynard, J.P. and Nithiarasu, P. (2008) A 1D arterial blood flow model incorporating ventricular pressure, aortic valve and regional coronary flow using the locally conservative Galerkin (LCG) method. *Comm Numer Meth En*, 24 (5): 367–417. doi:10.1002/cnm.1117.

Mynard, J.P., Davidson, M.R., Penny, D.J., et al. (2010) A numerical model of neonatal pulmonary atresia with intact ventricular septum and RV-dependent coronary flow. *Int J Numer Method Biomed Eng*, 26 (1): 843–861. doi:10.1002/cnm.1384.

Mynard, J.P., Penny, D.J. and Smolich, J.J. (2014) Scalability and in vivo validation of a multiscale numerical model of the left coronary circulation. *Am J Physiol Heart Circ Physiol*, 306 (4): H517–H528. doi:10.1152/ajpheart.00603.2013.

Naeije, R. and Badagliacca, R. (2017) The overloaded right heart and ventricular interdependence. *Cardiovasc Res*, 113 (12): 1474–1485. doi:10.1093/cvr/cvx160.

Nagasaka, H., Yorifuji, T., Egawa, H., et al. (2005) Evaluation of risk for atherosclerosis in Alagille syndrome and progressive familial intrahepatic cholestasis: Two congenital cholestatic diseases with different lipoprotein metabolisms. *Journal of Pediatrics*. doi:10.1016/j.jpeds.2004.10.047.

Nagueh, S.F., McFalls, J., Meyer, D., et al. (2003) Tissue Doppler imaging predicts the development of hypertrophic cardiomyopathy in subjects with subclinical disease. *Circulation*, 108 (4): 395–398. doi:10.1161/01.CIR.0000084500.72232.8D.

Nagueh, S.F., Smiseth, O.A., Appleton, C.P., et al. (2016) Recommendations for the Evaluation of Left Ventricular Diastolic Function by Echocardiography: An Update from the American Society of Echocardiography and the European Association of Cardiovascular Imaging. *Eur Heart J Cardiovasc Imaging*, 17 (12): 1321–1360. doi:10.1093/ehjci/jew082.

Nassenstein, K., Breuckmann, F., Hunold, P., et al. (2009) Magnetic resonance coronary angiography: Comparison between a Gd-BOPTA- and a Gd-DTPA-enhanced spoiled

gradient-echo sequence and a non-contrast-enhanced steady-state free-precession sequence. *Acta Radiol*, 50 (4): 406–411. doi:10.1080/02841850902838066.

Negishi, K., Negishi, T., Zardkoohi, O., et al. (2016) Left atrial booster pump function is an independent predictor of subsequent life-threatening ventricular arrhythmias in non-ischaemic cardiomyopathy. *Eur Heart J Cardiovasc Imaging*, 17 (10): 1153–1160. doi:10.1093/ehjci/jev333.

Nehrke, K. and Börnert, P. (2005) Prospective correction of affine motion for arbitrary MR sequences on a clinical scanner. *Magnetic Resonance in Medicine*, 54 (5): 1130–1138. doi:10.1002/mrm.20686.

Nesto, R.W. and Kowalchuk, G.J. (1987) The ischemic cascade: Temporal sequence of hemodynamic, electrocardiographic and symptomatic expressions of ischemia. *The American Journal of Cardiology*, 59 (7): C23–C30. doi:10.1016/0002-9149(87)90192-5.

Nezafat, R., Herzka, D., Stehning, C., et al. (2008) Inflow quantification in three-dimensional cardiovascular MR imaging. *Journal of Magnetic Resonance Imaging*, 28 (5): 1273–1279. doi:10.1002/jmri.21493.

Nguyen, T.D., Spincemaille, P., Cham, M.D., et al. (2008) Free-breathing 3D steady-state free precession coronary magnetic resonance angiography: Comparison of diaphragm and cardiac fat navigators. *Journal of Magnetic Resonance Imaging*, 28 (2): 509–514. doi:10.1002/jmri.21439.

Ni, Y. (2011) “MR Contrast Agents for Cardiac Imaging.” In Bogaert, J., Dymarkowski, S., Taylor, A.M., et al. (eds.) *Clinical Cardiac MRI*. Berlin, Heidelberg: Springer Berlin Heidelberg. pp. 31–51. doi:10.1007/174_2011_360.

Nichols, W.W. (2005) Clinical measurement of arterial stiffness obtained from noninvasive pressure waveforms. *American Journal of Hypertension*. doi:10.1016/j.amjhyper.2004.10.009.

Nichols, W.W., O'Rourke, M.F. and Vlachopoulos, C. (2005) *McDonald's blood flow in arteries; theoretical, experimental and clinical principles*. 5th ed. doi:10.1016/0306-3623(92)90079-Y.

O'Byrne, M.L., Glatz, A.C., Shinohara, R.T., et al. (2015) Effect of center catheterization volume on risk of catastrophic adverse event after cardiac catheterization in children. *Am Heart J*, 169 (6): 823-832.e5. doi:10.1016/j.ahj.2015.02.018.

O'Hanlon, R., Grasso, A., Roughton, M., et al. (2010) Prognostic Significance of Myocardial Fibrosis in Hypertrophic Cardiomyopathy. *J Am Coll Cardiol*, 56 (11): 867–874. doi:10.1016/j.jacc.2010.05.010.

Ohtani, K., Yutani, C., Nagata, S., et al. (1995) High prevalence of atrial fibrosis in patients with dilated cardiomyopathy. *J Am Coll Cardiol*, 25 (5): 1162–1169.

Opotowsky, A.R., Siddiqi, O.K. and Webb, G.D. (2009) Trends in hospitalizations for adults with congenital heart disease in the U.S. *J Am Coll Cardiol*, 54 (5): 460–467. doi:10.1016/j.jacc.2009.04.037.

Oshinski, J.N., Hofland, L., Mukundan, S., et al. (1996) Two-dimensional coronary MR angiography without breath holding. *Radiology*, 201 (3): 737–743. doi:10.1148/radiology.201.3.8939224.

Ovaert, C., Germeau, C., Barrea, C., et al. (2001) Elevated right ventricular pressures are not a contraindication to liver transplantation in Alagille syndrome. *Transplantation*, 72 (2): 345–347. doi:10.1097/00007890-200107270-00034.

Ozier, Y. and Klinck, J.R. (2008) Anesthetic management of hepatic transplantation. *Curr Opin Anaesthesiol*. doi:10.1097/ACO.0b013e3282ff85f4.

Pang, J., Bhat, H., Sharif, B., et al. (2014) Whole-heart coronary MRA with 100% respiratory gating efficiency: Self-navigated three-dimensional retrospective image-based motion correction (TRIM). *Magn Reson Med*, 71 (1): 67–74. doi:10.1002/mrm.24628.

Paraskevaïdis, I.A., Panou, F., Papadopoulos, C., et al. (2009) Evaluation of left atrial longitudinal function in patients with hypertrophic cardiomyopathy: a tissue Doppler imaging and two-dimensional strain study. *Heart*, 95 (6): 483–489. doi:10.1136/hrt.2008.146548.

Partovian, C., Adnot, S., Eddahibi, S., et al. (1998) Heart and lung VEGF mRNA expression in rats with monocrotaline- or hypoxia-induced pulmonary hypertension. *The American Journal of Physiology*, 275 (6): H1948-1956. doi:10.1152/ajpheart.1998.275.6.H1948.

Paugam-Burtz, C., Kavafyan, J., Merckx, P., et al. (2009) Postreperfusion syndrome during liver transplantation for cirrhosis: Outcome and predictors. *Liver Transpl*, 15 (5): 522–529. doi:10.1002/lt.21730.

Paulin, S., von Schulthess, G.K., Fossel, E., et al. (1987) MR imaging of the aortic root and proximal coronary arteries. *AJR Am J Roentgenol*, 148 (4): 665–670. doi:10.2214/ajr.148.4.665.

Pellicori, P., Zhang, J., Lukaschuk, E., et al. (2015) Left atrial function measured by cardiac magnetic resonance imaging in patients with heart failure: clinical associations and prognostic value. *Eur Heart J*, 36 (12): 733–742. doi:10.1093/eurheartj/ehu405.

Pennati, G. (2013) Computational fluid dynamics models and congenital heart diseases. *Frontiers in Pediatrics*, 1. doi:10.3389/fped.2013.00004.

Piao, L., Fang, Y.-H., Parikh, K., et al. (2013) Cardiac glutaminolysis: a maladaptive cancer metabolism pathway in the right ventricle in pulmonary hypertension. *Journal of Molecular Medicine*, 91 (10): 1185–1197. doi:10.1007/s00109-013-1064-7.

Piccini, D., Littmann, A., Nielles-Vallespin, S., et al. (2012) Respiratory self-navigation for whole-heart bright-blood coronary MRI: Methods for robust isolation and automatic segmentation of the blood pool. *Magn Reson Med*, 68 (2): 571–579. doi:10.1002/mrm.23247.

Piccini, D., Monney, P., Sierro, C., et al. (2014) Respiratory Self-navigated Postcontrast Whole-Heart Coronary MR Angiography: Initial Experience in Patients. *Radiology*. doi:10.1148/radiol.13132045.

Pintaske, J., Martirosian, P., Graf, H., et al. (2006) Relaxivity of Gadopentetate Dimeglumine (Magnevist), Gadobutrol (Gadovist), and Gadobenate Dimeglumine (MultiHance) in human blood plasma at 0.2, 1.5, and 3 Tesla. *Invest Radiol*, 41 (3): 213–221. doi:10.1097/01.rli.0000197668.44926.f7.

Ploegstra, M.-J., Brokelman, J.G.M., Roos-Hesselink, J.W., et al. (2018) Pulmonary arterial stiffness indices assessed by intravascular ultrasound in children with early pulmonary vascular disease: prediction of advanced disease and mortality during 20-year follow-up. *European Heart Journal - Cardiovascular Imaging*, 19 (2): 216–224. doi:10.1093/ehjci/jex015.

Png, K., Veyckemans, F., De Kock, M., et al. (1999) Hemodynamic changes in patients with Alagille's syndrome during orthotopic liver transplantation. *Anesth Analg*, 89 (5): 1137–1142. doi:10.1097/00000539-199911000-00011.

Pokreisz, P., Marsboom, G. and Janssens, S. (2007) Pressure overload-induced right ventricular dysfunction and remodelling in experimental pulmonary hypertension: the right heart revisited. *Eur Heart J Suppl*, 9 (H): H75–H84. doi:10.1093/eurheartj/sum021.

Ponio, J.B.D., Wright-Crosnier, C., Groyer-Picard, M.T., et al. (2007) Biological function of mutant forms of JAGGED1 proteins in Alagille syndrome: Inhibitory effect on Notch signaling. *Hum Mol Genet*, 16 (22): 2683–2692. doi:10.1093/hmg/ddm222.

Pushparajah, K., Tzifa, A., Bell, A., et al. (2015) Cardiovascular Magnetic Resonance catheterization derived pulmonary vascular resistance and medium-term outcomes in congenital heart disease. *J Cardiovasc Magn Reson*, 17 (1). doi:10.1186/s12968-015-0130-4.

Rahimtoola, S.H., Ehsani, A., Sinno, M.Z., et al. (1975) Left atrial transport function in myocardial infarction. Importance of its booster pump function. *Am J Med*, 59 (5): 686–694.

Rajiah, P. and Bolen, M.A. (2014) Cardiovascular MR Imaging at 3 T: Opportunities, Challenges, and Solutions. *RadioGraphics*. doi:10.1148/rg.346140048.

Rakowski, H. and Carasso, S. (2007) Quantifying diastolic function in hypertrophic cardiomyopathy: the ongoing search for the holy grail. *Circulation*, 116 (23): 2662–2665. doi:10.1161/CIRCULATIONAHA.107.742395.

Razavi, H., Stewart, S.E., Xu, C., et al. (2013) Chronic effects of pulmonary artery stenosis on hemodynamic and structural development of the lungs. *American Journal of Physiology-*

Lung Cellular and Molecular Physiology, 304 (1): L17–L28.
doi:10.1152/ajplung.00412.2011.

Razavi, R.S., Baker, A., Qureshi, S.A., et al. (2001) Hemodynamic response to continuous infusion of dobutamine in Alagille's syndrome. *Transplantation*, 72 (5): 823–828.
doi:10.1097/00007890-200109150-00014.

Razavi, R., Hill, D.L.G., Keevil, S.F., et al. (2003) Cardiac catheterisation guided by MRI in children and adults with congenital heart disease. *Lancet*, 362 (9399): 1877–1882.
doi:10.1016/S0140-6736(03)14956-2.

Reid, G.J., Webb, G.D., Barzel, M., et al. (2006) Estimates of Life Expectancy by Adolescents and Young Adults With Congenital Heart Disease. *Journal of the American College of Cardiology*. doi:10.1016/j.jacc.2006.03.041.

Reiter, T., Ritter, O., Prince, M.R., et al. (2012) Minimizing Risk of Nephrogenic systemic fibrosis in Cardiovascular Magnetic Resonance. *J Cardiovasc Magn Reson*, 14 (1): 31.
doi:10.1186/1532-429X-14-31.

Rich, S. (2012) Right Ventricular Adaptation and Maladaptation in Chronic Pulmonary Arterial Hypertension. *Cardiol Clin*, 30 (2): 257–269. doi:10.1016/j.ccl.2012.03.004.

van Riel, A.C.M.J., Schuurin, M.J., van Hessen, I.D., et al. (2014) Contemporary prevalence of pulmonary arterial hypertension in adult congenital heart disease following the updated clinical classification. *International journal of cardiology*. doi:10.1016/j.ijcard.2014.04.072.

Roes, S.D., Korosoglou, G., Schär, M., et al. (2008) Correction for heart rate variability during 3D whole heart MR coronary angiography. *Journal of Magnetic Resonance Imaging*, 27 (5): 1046–1053. doi:10.1002/jmri.21361.

Ryan, J.J. and Archer, S.L. (2014) The Right Ventricle in Pulmonary Arterial Hypertension: Disorders of Metabolism, Angiogenesis and Adrenergic Signaling in Right Ventricular Failure. *Circ Res*, 115 (1): 176–188. doi:10.1161/CIRCRESAHA.113.301129.

Saidi, A.S., Kovalchin, J.P., Fisher, D.J., et al. (1998) Balloon pulmonary valvuloplasty and stent implantation. For peripheral pulmonary artery stenosis in Alagille syndrome. *Texas Heart Institute journal / from the Texas Heart Institute of St.Luke's Episcopal Hospital, Texas Children's Hospital*.

Sakuma, H., Ichikawa, Y., Suzawa, N., et al. (2005) Assessment of Coronary Arteries with Total Study Time of Less than 30 Minutes by Using Whole-Heart Coronary MR Angiography. *Radiology*, 237 (1): 316–321. doi:10.1148/radiol.2371040830.

Saleh, M., Kamath, B.M. and Chitayat, D. (2016) Alagille syndrome: clinical perspectives. *Appl Clin Genet*, 9 (1): 75–82. doi:10.2147/TACG.S86420.

Samejima, H., Torii, C., Kosaki, R., et al. (2007) Screening for Alagille syndrome mutations in the JAG1 and NOTCH2 genes using denaturing high-performance liquid chromatography. *Genetic Testing*, 11 (3): 216–227. doi:10.1089/gte.2006.0519.

Sankaranarayanan, R. and Fleming, E.J. (2013) Mimics of Hypertrophic Cardiomyopathy – Diagnostic Clues to Aid Early Identification of Phenocopies. *Arrhythm Electrophysiol Rev*, 2 (1): 36–40. doi:10.15420/aer.2013.2.1.36.

Santamore, W.P. and Dell'Italia, L.J. (1998) Ventricular interdependence: significant left ventricular contributions to right ventricular systolic function. *Prog Cardiovasc Dis*, 40 (4): 289–308.

Scaramucci, J. (1695) “Theoremata familiaria de physico-medicis lucubrationibus Iucta leges mecanicas.” *In De motu cordis, theorema sextum*. pp. 70–81.

Scheffler, K. and Lehnhardt, S. (2003) Principles and applications of balanced SSFP techniques. *Eur Radiol*, 13 (11): 2409–2418. doi:10.1007/s00330-003-1957-x.

Schmidt, E.J., Yoneyama, R., Dumoulin, C.L., et al. (2009) 3D coronary motion tracking in swine models with MR tracking catheters. *Journal of Magnetic Resonance Imaging*. doi:10.1002/jmri.21468.

Schmidt, J.F.M., Buehrer, M., Boesiger, P., et al. (2011) Nonrigid retrospective respiratory motion correction in whole-heart coronary MRA. *Magn Reson Med*, 66 (6): 1541–1549. doi:10.1002/mrm.22939.

Schneider, G., Ballarati, C., Grazioli, L., et al. (2007) Gadobenate dimeglumine-enhanced MR angiography: Diagnostic performance of four doses for detection and grading of carotid, renal, and aorto-iliac stenoses compared to digital subtraction angiography. *J Magn Reson Imaging*, 26 (4): 1020–1032. doi:10.1002/jmri.21127.

Schranz, D., Stopfkuchen, H., Jünger, B.K., et al. (1982) Hemodynamic effects of dobutamine in children with cardiovascular failure. *European Journal of Pediatrics*. doi:10.1007/BF00442069.

Schuster, A., Hor, K.N., Kowallick, J.T., et al. (2016) Cardiovascular Magnetic Resonance Myocardial Feature Tracking: Concepts and Clinical Applications. *Circ Cardiovasc Imaging*, 9 (4): e004077. doi:10.1161/CIRCIMAGING.115.004077.

Scott, A.D., Keegan, J. and Firmin, D.N. (2011) Beat-to-beat respiratory motion correction with near 100% efficiency: a quantitative assessment using high-resolution coronary artery imaging. *Magn Reson Imaging*, 29 (4): 568–578. doi:10.1016/j.mri.2010.11.004.

Seitelberger, R., Guth, B.D., Heusch, G., et al. (1988) Intracoronary alpha 2-adrenergic receptor blockade attenuates ischemia in conscious dogs during exercise. *Circ Res*, 62 (3): 436–442.

- Shah, P.M. (2003) Hypertrophic cardiomyopathy and diastolic dysfunction. *J Am Coll Cardiol*, 42 (2): 286–287. doi:10.1016/S0735-1097(03)00582-5.
- Shea, S.M., Deshpande, V.S., Chung, Y.-C., et al. (2002) Three-dimensional true-FISP imaging of the coronary arteries: improved contrast with T2-preparation. *J Magn Reson Imaging*, 15 (5): 597–602. doi:10.1002/jmri.10106.
- Shechter, G., Devernay, F., Coste-Manière, E., et al. (2003) Three-dimensional motion tracking of coronary arteries in biplane cineangiograms. *IEEE Trans Med Imaging*, 22 (4): 493–503. doi:10.1109/TMI.2003.809090.
- Shen, Y., Goerner, F.L., Snyder, C., et al. (2015) T1 Relaxivities of Gadolinium-Based Magnetic Resonance Contrast Agents in Human Whole Blood at 1.5, 3, and 7 T. *Invest Radiol*, 50 (5): 330–338. doi:10.1097/RLI.0000000000000132.
- Shin, H., Chavan, A., Witthus, F., et al. (2001) Precise determination of aortic length in patients with aortic stent grafts: in vivo evaluation of a thinning algorithm applied to CT angiography data. *Eur Radiol*, 11 (5): 733–738. doi:10.1007/s0033000000681.
- Shirani, J., Pick, R., Roberts, W.C., et al. (2000) Morphology and significance of the left ventricular collagen network in young patients with hypertrophic cardiomyopathy and sudden cardiac death. *J Am Coll Cardiol*, 35 (1): 36–44. doi:10.1016/S0735-1097(99)00492-1.
- Shiwani, H., Brothers, J., Villines, T., et al. (2018) Sudden cardiac death and aborted sudden cardiac death in patients with anomalous aortic origin of a coronary artery (AAOCA) from the inappropriate sinus of Valsalva: a systematic review of the literature. *J Am Coll Cardiol*, 71 (11): A533. doi:10.1016/S0735-1097(18)31074-X.
- Shneider, B.L. (2012) Liver transplantation for alagille syndrome: The jagged edge. *Liver Transplantation*, 18 (8): 878–880. doi:10.1002/lt.23472.
- Silversides, C.K., Bradley, T., Colman, J., et al. (2010) Canadian Cardiovascular Society 2009 Consensus Conference on the management of adults with congenital heart disease: Executive summary. *Can J Cardiol*, 26 (3): 143–150.
- Siniscalchi, A., Dante, A., Spedicato, S., et al. (2010) Hyperdynamic Circulation in Acute Liver Failure: Reperfusion Syndrome and Outcome Following Liver Transplantation. *Transplant Proc*, 41 (4): 1197–1199. doi:10.1016/j.transproceed.2010.03.097.
- Smithson, S., Hall, D., Trachtenberg, B., et al. (2014) Treatment of cardiovascular complications of Alagille syndrome in clinical optimization for liver transplantation. *International Journal of Cardiology*, 176 (2): e37–e40. doi:10.1016/j.ijcard.2014.04.187.
- Sørensen, T.S., Körperich, H., Greil, G.F., et al. (2004) Operator-independent isotropic three-dimensional magnetic resonance imaging for morphology in congenital heart disease: A validation study. *Circulation*. doi:10.1161/01.CIR.0000134282.35183.AD.

Spaan, J.A., Breuls, N.P. and Laird, J.D. (1981a) Diastolic-systolic coronary flow differences are caused by intramyocardial pump action in the anesthetized dog. *Circ Res*, 49 (3): 584–593. doi:10.1161/01.RES.49.3.584.

Spaan, J.A.E., Breuls, N.P.W., Laird, J.D., et al. (1981b) Forward coronary flow normally seen in systole is the result of both forward and concealed back flow. *Basic Res Cardiol*, 76 (5): 582–586. doi:10.1007/BF01908365.

Squires, R.H., Ng, V., Romero, R., et al. (2014) Evaluation of the pediatric patient for liver transplantation: 2014 practice guideline by the American Association for the Study of Liver Diseases, American Society of Transplantation and the North American Society for Pediatric Gastroenterology, Hepatology and Nutrition. *Hepatology*, 60 (1): 362–398. doi:10.1002/hep.27191.

Steadman, R.H. (2004) Anesthesia for liver transplant surgery. *Anesthesiol Clin*, 22 (4): 687–711. doi:10.1016/j.atc.2004.06.009.

Stefanescu Schmidt, A.C., Armstrong, A., Kennedy, K.F., et al. (2017) Prediction of adverse events after catheter-based procedures in adolescents and adults with congenital heart disease in the IMPACT registry. *Eur Heart J*, 38 (26): 2070–2077. doi:10.1093/eurheartj/ehx200.

Stehning, C., Börnert, P., Nehrke, K., et al. (2005) Free-breathing whole-heart coronary MRA with 3D radial SSFP and self-navigated image reconstruction. *Magn Reson Med*, 54 (2): 476–480. doi:10.1002/mrm.20557.

Stillman, A.E., Wilke, N., Li, D., et al. (1996) Ultrasmall superparamagnetic iron oxide to enhance MRA of the renal and coronary arteries: studies in human patients. *J Comput Assist Tomogr*, 20 (1): 51–55.

Stuber, M., Botnar, R.M., Danias, P.G., et al. (1999a) Contrast agent-enhanced, free-breathing, three-dimensional coronary magnetic resonance angiography. *J Magn Reson Imaging*, 10 (5): 790–799.

Stuber, M., Botnar, R.M., Danias, P.G., et al. (1999b) Double-oblique free-breathing high resolution three-dimensional coronary magnetic resonance angiography. *J Am Coll Cardiol*, 34 (2): 524–531. doi:10.1016/s0735-1097(99)00223-5.

Stuber, M., Botnar, R.M., Danias, P.G., et al. (1999c) Submillimeter three-dimensional coronary MR angiography with real-time navigator correction: comparison of navigator locations. *Radiology*, 212 (2): 579–587. doi:10.1148/radiology.212.2.r99au50579.

Subramaniam, P., Knisely, A., Portmann, B., et al. (2011) Diagnosis of alagille syndrome-25 years of experience at King's College Hospital. *J Pediatr Gastroenterol Nutr*, 52 (1): 84–89. doi:10.1097/MPG.0b013e3181f1572d.

Suga, H. (1990) Ventricular energetics. *Physiol Rev*, 70 (2): 247–277. doi:10.1152/physrev.1990.70.2.247.

Suga, H. (2003) Cardiac energetics: from E(max) to pressure-volume area. *Clin Exp Pharmacol Physiol*, 30 (8): 580–585.

Suh, G.-Y., Beygui, R.E., Fleischmann, D., et al. (2014) Aortic Arch Vessel Geometries and Deformations in Patients with Thoracic Aortic Aneurysms and Dissections. *J Vasc Interv Radiol*, 25 (12): 1903–1911. doi:10.1016/j.jvir.2014.06.012.

Sunagawa, K., Maughan, W.L., Burkhoff, D., et al. (1983) Left ventricular interaction with arterial load studied in isolated canine ventricle. *Am J Physiol*, 245 (5 Pt 1): H773-780. doi:10.1152/ajpheart.1983.245.5.H773.

Sunagawa, K., Maughan, W.L. and Sagawa, K. (1985) Optimal arterial resistance for the maximal stroke work studied in isolated canine left ventricle. *Circ Res*, 56 (4): 586–595.

Swoboda, P.P., McDiarmid, A.K., Erhayiem, B., et al. (2016) Assessing Myocardial Extracellular Volume by T1 Mapping to Distinguish Hypertrophic Cardiomyopathy From Athlete's Heart. *J Am Coll Cardiol*, 67 (18): 2189–2190. doi:10.1016/j.jacc.2016.02.054.

Szabó, G., Soós, P., Bährle, S., et al. (2006) Adaptation of the right ventricle to an increased afterload in the chronically volume overloaded heart. *The Annals of Thoracic Surgery*, 82 (3): 989–995. doi:10.1016/j.athoracsur.2006.04.036.

Tandon, A., Hashemi, S., Parks, W.J., et al. (2016) Improved high-resolution pediatric vascular cardiovascular magnetic resonance with gadofosveset-enhanced 3D respiratory navigated, inversion recovery prepared gradient echo readout imaging compared to 3D balanced steady-state free precession readout imaging. *Journal of Cardiovascular Magnetic Resonance*, 18 (1): 74. doi:10.1186/s12968-016-0296-4.

Tangcharoen, T., Jahnke, C., Koehler, U., et al. (2008) Impact of heart rate variability in patients with normal sinus rhythm on image quality in coronary magnetic angiography. *Journal of Magnetic Resonance Imaging*, 28 (1): 74–79. doi:10.1002/jmri.21426.

Tangcharoen, T., Bell, A., Hegde, S., et al. (2011) Detection of Coronary Artery Anomalies in Infants and Young Children with Congenital Heart Disease by Using MR Imaging. *Radiology*, 259 (1): 240–247. doi:10.1148/radiol.10100828.

Taylor, A.M., Jhooti, P., Wiesmann, F., et al. (1997) MR navigator-echo monitoring of temporal changes in diaphragm position: implications for MR coronary angiography. *J Magn Reson Imaging*, 7 (4): 629–636.

Taylor, A.M., Keegan, J., Jhooti, P., et al. (1999) Calculation of a subject-specific adaptive motion-correction factor for improved real-time navigator echo-gated magnetic resonance coronary angiography. *J Cardiovasc Magn Reson*, 1 (2): 131–138.

Taylor, A.M., Dymarkowski, S., Hamaekers, P., et al. (2005) MR coronary angiography and late-enhancement myocardial MR in children who underwent arterial switch surgery for transposition of great arteries. *Radiology*, 234 (2): 542–547. doi:10.1148/radiol.2342032059.

Taylor, C.A. and Figueroa, C.A. (2009) Patient-Specific Modeling of Cardiovascular Mechanics. *Annu Rev Biomed Eng*, 11 (1): 109–134. doi:10.1146/annurev.bioeng.10.061807.160521.

Thomas, L. and Abhayaratna, W.P. (2017) Left Atrial Reverse Remodeling. *JACC Cardiovasc Imaging*, 10 (1): 65–77. doi:10.1016/j.jcmg.2016.11.003.

Tonelli, A.R., Arelli, V., Minai, O.A., et al. (2013) Causes and circumstances of death in pulmonary arterial hypertension. *American Journal of Respiratory and Critical Care Medicine*. doi:10.1164/rccm.201209-1640OC.

Tu, J., Yeoh, G.H. and Liu, C. (2013) *Computational fluid dynamics a practical approach*. 1st ed. Amsterdam; Boston: Elsevier/Butterworth-Heinemann.

Tune, J.D., Gorman, M.W. and Feigl, E.O. (2004) Matching coronary blood flow to myocardial oxygen consumption. *J Appl Physiol (1985)*, 97 (1): 404–415. doi:10.1152/jappphysiol.01345.2003.

Tune, J.D. (2014) *Coronary Circulation*. Colloquium Series on Integrated Systems Physiology: From Molecule to Function to Disease. Granger, D.N. and Granger, J.P. (eds.). Morgan & Claypool.

Turnpenny, P.D. and Ellard, S. (2012) Alagille syndrome: pathogenesis, diagnosis and management. *Eur J Hum Genet*, 20 (3): 251–257. doi:10.1038/ejhg.2011.181.

Tzakis, A.G., Reyes, J., Tepetes, K., et al. (1993) Liver Transplantation for Alagille's Syndrome. *Arch Surg*, 128 (3): 337–339. doi:10.1001/archsurg.1993.01420150093017.

Tzifa, A., Schaeffter, T. and Razavi, R. (2012) MR imaging-guided cardiovascular interventions in young children. *Magn Reson Imaging Clin N Am*, 20 (1): 117–128. doi:10.1016/j.mric.2011.08.011.

Urbano-Moral, J.A., Rowin, E.J., Maron, M.S., et al. (2014) Investigation of Global and Regional Myocardial Mechanics With 3-Dimensional Speckle Tracking Echocardiography and Relations to Hypertrophy and Fibrosis in Hypertrophic Cardiomyopathy. *Circ Cardiovasc Imaging*, 7 (1): 11–19. doi:10.1161/CIRCIMAGING.113.000842.

Uribe, S., Hussain, T., Valverde, I., et al. (2011) Congenital Heart Disease in Children: Coronary MR Angiography during Systole and Diastole with Dual Cardiac Phase Whole-Heart Imaging. *Radiology*, 260 (1): 232–240. doi:10.1148/radiol.11101659.

Valsangiacomo Buechel, E.R., Grosse-Wortmann, L., Fratz, S., et al. (2015) Indications for cardiovascular magnetic resonance in children with congenital and acquired heart disease: an expert consensus paper of the Imaging Working Group of the AEPC and the Cardiovascular Magnetic Resonance Section of the EACVI. *Eur Heart J Cardiovasc Imaging*, 16 (3): 281–297. doi:10.1093/ehjci/jeu129.

- Vardoulis, O., Papaioannou, T.G. and Stergiopoulos, N. (2013) Validation of a novel and existing algorithms for the estimation of pulse transit time: advancing the accuracy in pulse wave velocity measurement. *Am J Physiol Heart Circ Physiol*, 304 (11): H1558–H1567. doi:10.1152/ajpheart.00963.2012.
- Vasanawala, S.S., Chan, F.P., Newman, B., et al. (2011) Combined respiratory and cardiac triggering improves blood pool contrast-enhanced pediatric cardiovascular MRI. *Pediatric Radiology*, 41 (12): 1536–1544. doi:10.1007/s00247-011-2196-y.
- Veselka, J., Anavekar, N.S. and Charron, P. (2017) Hypertrophic obstructive cardiomyopathy. *The Lancet*, 389 (10075): 1253–1267. doi:10.1016/S0140-6736(16)31321-6.
- Vignon-Clementel, I.E., Alberto Figueroa, C., Jansen, K.E., et al. (2006) Outflow boundary conditions for three-dimensional finite element modeling of blood flow and pressure in arteries. *Computer Methods in Applied Mechanics and Engineering*, 195 (29–32): 3776–3796. doi:10.1016/j.cma.2005.04.014.
- Vignon-Clementel, I.E., Marsden, A.L. and Feinstein, J.A. (2010) A primer on computational simulation in congenital heart disease for the clinician. *Progress in Pediatric Cardiology*, 30 (1–2): 3–13. doi:10.1016/j.ppedcard.2010.09.002.
- Vlachopoulos, C., Aznaouridis, K. and Stefanadis, C. (2010) Prediction of Cardiovascular Events and All-Cause Mortality With Arterial Stiffness. A Systematic Review and Meta-Analysis. *Journal of the American College of Cardiology*. doi:10.1016/j.jacc.2009.10.061.
- Vlahakes, G.J., Turley, K. and Hoffman, J.I. (1981) The pathophysiology of failure in acute right ventricular hypertension: hemodynamic and biochemical correlations. *Circulation*, 63 (1): 87–95. doi:10.1161/01.cir.63.1.87.
- Voelkel, N.F., Quaife, R.A., Leinwand, L.A., et al. (2006) Right Ventricular Function and Failure: Report of a National Heart, Lung, and Blood Institute Working Group on Cellular and Molecular Mechanisms of Right Heart Failure. *Circulation*, 114 (17): 1883–1891. doi:10.1161/CIRCULATIONAHA.106.632208.
- Voges, I., Jerosch-Herold, M., Hedderich, J., et al. (2012) Normal values of aortic dimensions, distensibility, and pulse wave velocity in children and young adults: a cross-sectional study. *J Cardiovasc Magn Reson*, 14 (1): 77. doi:10.1186/1532-429X-14-77.
- Vonk-Noordegraaf, A., Haddad, F., Chin, K.M., et al. (2013) Right heart adaptation to pulmonary arterial hypertension: Physiology and pathobiology. *J Am Coll Cardio*, 24;62(25 Suppl):D22-33. doi:10.1016/j.jacc.2013.10.027.
- Vonk Noordegraaf, A., Westerhof, B.E. and Westerhof, N. (2017) The Relationship Between the Right Ventricle and its Load in Pulmonary Hypertension. *J Am Coll Cardio*, 69 (2): 236–243. doi:10.1016/j.jacc.2016.10.047.

- Wang, K.C., Dutton, R.W. and Taylor, C.A. (1999a) Improving geometric model construction for blood flow modeling. *EEE Eng Med Biol Mag.*, 18 (6): 33–39.
- Wang, Y., Riederer, S.J. and Ehman, R.L. (1995) Respiratory motion of the heart: kinematics and the implications for the spatial resolution in coronary imaging. *Magn Reson Med*, 33 (5): 713–719.
- Wang, Y., Vidan, E. and Bergman, G.W. (1999b) Cardiac motion of coronary arteries: variability in the rest period and implications for coronary MR angiography. *Radiology*, 213 (3): 751–758. doi:10.1148/radiology.213.3.r99dc41751.
- Wang, Y., Osborne, M.T., Tung, B., et al. (2018) Imaging Cardiovascular Calcification. *J Am Heart Assoc*, 28;7(13). pii: e008564.. doi:10.1161/JAHA.118.008564.
- Warnes, C.A., Williams, R.G., Bashore, T.M., et al. (2008) ACC/AHA 2008 Guidelines for the Management of Adults With Congenital Heart Disease. *J Am Coll Cardiol*, 52 (23): e143–e263. doi:10.1016/j.jacc.2008.10.001.
- Warnes, C.A. (2009) Adult Congenital Heart Disease. Importance of the Right Ventricle. *J Am Coll Cardio*, 17;54(21):1903-10. doi:10.1016/j.jacc.2009.06.048.
- Wasserman, D., Zemel, B.S., Mulberg, A.E., et al. (1999) Growth, nutritional status, body composition, and energy expenditure in prepubertal children with Alagille syndrome. *J Pediatr*, 134 (2): 172–177.
- Weber, T., Auer, J., O'Rourke, M.F., et al. (2004) Arterial Stiffness, Wave Reflections, and the Risk of Coronary Artery Disease. *Circulation*. doi:10.1161/01.CIR.0000105767.94169.E3.
- Wentland, A.L., Wieben, O., François, C.J., et al. (2013) Aortic pulse wave velocity measurements with undersampled 4D flow-sensitive MRI: comparison with 2D and algorithm determination. *J Magn Reson Imaging.*, 37 (4): 853–859. doi:10.1002/jmri.23877.
- Wentland, A.L., Grist, T.M. and Wieben, O. (2014) Review of MRI-based measurements of pulse wave velocity: a biomarker of arterial stiffness. *Cardiovasc Diagn Ther.*, 4 (2): 193–96. doi:10.3978/j.issn.2223-3652.2014.03.04.
- Westerhof, N., Boer, C., Lamberts, R.R., et al. (2006) Cross-talk between cardiac muscle and coronary vasculature. *Physiol Rev*, 86 (4): 1263–1308. doi:10.1152/physrev.00029.2005.
- Westfall, T.C. and Westfall, D.P. (2011) Chapter 12. Adrenergic Agonists and Antagonists. *Goodman & Gilman's The Pharmacological Basis of Therapeutics, 12e*.
- Williams, L. and Frenneaux, M. (2006) Diastolic ventricular interaction: from physiology to clinical practice. *Nat Clin Pract Cardiovasc Med*, 3 (7): 368–376. doi:10.1038/ncpcardio0584.

Wink, O., Niessen, W.J. and Viergever, M.A. (2000) Fast delineation and visualization of vessels in 3-D angiographic images. *EEE Trans Med Imagin*, 19 (4): 337–346. doi:10.1109/42.848184.

van Wolferen, S.A., Marcus, J.T., Westerhof, N., et al. (2008) Right coronary artery flow impairment in patients with pulmonary hypertension. *Eur Heart J*, 29 (1): 120–127. doi:10.1093/eurheartj/ehm567.

Wong, Y.Y., Ruiters, G., Lubberink, M., et al. (2011) Right Ventricular Failure in Idiopathic Pulmonary Arterial Hypertension Is Associated With Inefficient Myocardial Oxygen Utilization. *Circ Heart Fail*, 4 (6): 700–706. doi:10.1161/CIRCHEARTFAILURE.111.962381.

Wörz, S., von Tengg-Kobligh, H., Henninger, V., et al. (2010) 3-D Quantification of the Aortic Arch Morphology in 3-D CTA Data for Endovascular Aortic Repair. *IEEE Trans Biomed Eng*, 57 (10): 2359–2368. doi:10.1109/TBME.2010.2053539.

Wu, H.H., Gurney, P.T., Hu, B.S., et al. (2013) Free-breathing multiphase whole-heart coronary MR angiography using image-based navigators and three-dimensional cones imaging. *Magn Reson Med*, 69 (4): 1083–93. doi:10.1002/mrm.24346.

Xiao, N., Humphrey, J.D. and Figueroa, C.A. (2013) Multi-scale computational model of three-dimensional hemodynamics within a deformable full-body arterial network. *J Comput Phys*, 244 (1): 22–40. doi:10.1016/j.jcp.2012.09.016.

Yang, H., Woo, A., Monakier, D., et al. (2005) Enlarged left atrial volume in hypertrophic cardiomyopathy: a marker for disease severity. *J Am Soc Echocardiogr*, 18 (10): 1074–1082. doi:10.1016/j.echo.2005.06.011.

Yang, Q., Li, K., Liu, X., et al. (2009) Contrast-Enhanced Whole-Heart Coronary Magnetic Resonance Angiography at 3.0-T. A Comparative Study With X-Ray Angiography in a Single Center. *J Am Coll Cardiol.*, 54 (1): 69–76. doi:10.1016/j.jacc.2009.03.016.

Yang, W., Hanley, F.L., Chan, F.P., et al. (2018) Computational simulation of postoperative pulmonary flow distribution in Alagille patients with peripheral pulmonary artery stenosis. *Congenital Heart Disease*, 13 (2): 241–250. doi:10.1111/chd.12556.

Yang, W.I., Shim, C.Y., Kim, Y.J., et al. (2009) Left Atrial Volume Index: A Predictor of Adverse Outcome in Patients With Hypertrophic Cardiomyopathy. *J Am Soc Echocardiogr*, 22 (12): 1338–1343. doi:10.1016/j.echo.2009.09.016.

Yaylali, Y.T., Kilic-Toprak, E., Ozdemir, Y., et al. (2019) Impaired Blood Rheology in Pulmonary Arterial Hypertension. *Heart, Lung and Circulation*, 28 (7): 1067–1073. doi:10.1016/j.hlc.2018.07.014.

Youssefi, P., Gomez, A., Arthurs, C., et al. (2017) Impact of Patient-Specific Inflow Velocity Profile on Hemodynamics of the Thoracic Aorta. *J Biomech Eng*, 140 (1). doi:10.1115/1.4037857.

Yu, J., Agarwal, H., Stuber, M., et al. (2011) Practical signal-to-noise ratio quantification for sensitivity encoding: Application to coronary MR angiography. *J Magn Reson Imaging*, 33 (6): 1330–1340. doi:10.1002/jmri.22571.

Yun, H., Jin, H., Yang, S., et al. (2014) Coronary artery angiography and myocardial viability imaging: a 3.0-T contrast-enhanced magnetic resonance coronary artery angiography with Gd-BOPTA. *Int J Cardiovasc Imaging*, 30 (1): 99–108. doi:10.1007/s10554-013-0297-4.

Zelt, J.G.E., Chaudhary, K.R., Cadete, V.J., et al. (2019) Medical Therapy for Heart Failure Associated With Pulmonary Hypertension. *Circulation Research*, 124 (11): 1551–1567. doi:10.1161/CIRCRESAHA.118.313650.

Zhang, L., Tian, M., Xue, F., et al. (2018) Diagnosis, Incidence, Predictors and Management of Postreperfusion Syndrome in Pediatric Deceased Donor Liver Transplantation: A Single-Center Study. *Ann Transplant*, 23 (1): 334–344. doi:10.12659/AOT.909050.

Zong, P., Tune, J.D., Setty, S., et al. (2002) Endogenous nitric oxide regulates right coronary blood flow during acute pulmonary hypertension in conscious dogs. *Basic Res Cardiol*, 97 (5). doi:10.1007/s003950200048.

Zong, P., Tune, J.D. and Downey, H.F. (2005) Mechanisms of oxygen demand/supply balance in the right ventricle. *Exp Biol Med (Maywood)*, 230 (8): 507–519. doi:10.1177/153537020523000801.